

# Pushing the boundaries of lithium battery research with atomistic modelling on different scales

Lucy M. Morgan,<sup>†,‡,¶</sup> Michael P. Mercer,<sup>†,§,¶</sup> Arihant Bhandari,<sup>||,¶</sup> Chao Peng,<sup>⊥,¶</sup> Mazharul M. Islam,<sup>‡,¶</sup> Hui Yang,<sup>#,¶</sup> Julian Holland,<sup>||,¶</sup> Samuel W. Coles,<sup>‡,¶</sup> Ryan Sharpe,<sup>‡</sup> Aron Walsh,<sup>#,Ⓜ,¶</sup> Benjamin J. Morgan,<sup>‡,¶</sup> Denis Kramer,<sup>⊥,△,¶</sup> M. Saiful Islam,<sup>‡,¶</sup> Harry E. Hoster,<sup>§,¶</sup> Jacqueline Sophie Edge,<sup>\*,∇,¶</sup> and Chris-Kriton Skylaris<sup>\*,||,¶</sup>

1

<sup>†</sup>*The two authors contributed equally to this review.*

<sup>‡</sup>*Department of Chemistry, University of Bath, Claverton Down, Bath BA2 7AY, UK*

<sup>¶</sup>*The Faraday Institution, Quad One, Harwell Campus, Didcot, OX11 0RA, UK*

<sup>§</sup>*Department of Chemistry, Lancaster University, Bailrigg, Lancaster, LA1 4YB, UK*

<sup>||</sup>*School of Chemistry, University of Southampton, Southampton SO17 1BJ, UK*

<sup>⊥</sup>*School of Engineering, University of Southampton, Southampton SO17 1BJ, UK*

<sup>#</sup>*Department of Materials, Imperial College London, London SW7 2AZ, UK*

<sup>Ⓜ</sup>*Department of Materials Science and Engineering, Yonsei University, Seoul 03722, Korea*

<sup>△</sup>*Faculty of Mechanical Engineering, Helmut-Schmidt University, Holstenhofweg 85, 22043*

*Hamburg, Germany*

<sup>∇</sup>*Department of Mechanical Engineering, Imperial College London, London, SW7 2AZ, UK*

E-mail: [j.edge@imperial.ac.uk](mailto:j.edge@imperial.ac.uk); [c.skylaris@soton.ac.uk](mailto:c.skylaris@soton.ac.uk)

## Abstract

Computational modelling is a vital tool in the research of batteries and their component materials. Atomistic models are key to building truly physics-based models of batteries and form the foundation of the multiscale modelling chain, leading to more robust and predictive models. These models can be applied to fundamental research questions with high predictive accuracy. For example, they can be used to predict new behaviour not currently accessible by experiment, for reasons of cost, safety, or throughput. Atomistic models are useful for quantifying and evaluating trends in experimental data, explaining structure-property relationships, and informing materials design strategies and libraries. In this review, we showcase the most prominent atomistic modelling methods and their application to electrode materials, liquid and solid electrolyte materials, and their interfaces, highlighting the diverse range of battery properties that can be investigated. Furthermore, we link atomistic modelling to experimental data and higher scale models such as continuum and control models. We also provide a critical discussion on the outlook of these materials and the main challenges for future battery research.

# 18 Contents

19	<b>1 Introduction</b>	<b>6</b>
20	<b>2 Methods</b>	<b>14</b>
21	2.1 Method overview . . . . .	14
22	2.1.1 Density Functional Theory . . . . .	14
23	2.1.2 Linear-Scaling DFT . . . . .	17
24	2.1.3 Nudged Elastic Band . . . . .	20
25	2.1.4 Cluster expansion . . . . .	21
26	2.1.5 Lattice gas and Monte Carlo . . . . .	23
27	2.1.6 Molecular Dynamics . . . . .	25
28	2.2 Method Development . . . . .	28
29	2.2.1 Continuum models of electrolyte solutions within Density Functional	
30	Theory . . . . .	28
31	2.2.2 Fitting Potentials for Classical Molecular Dynamics . . . . .	32
32	2.3 Calculating observable properties . . . . .	34
33	2.3.1 Equilibrium voltage . . . . .	34
34	2.3.2 Activity coefficients of electrolytes . . . . .	37
35	2.3.3 Diffusion coefficients . . . . .	37
36	2.3.4 Vibrational and Thermal Properties . . . . .	40
37	<b>3 Anodes</b>	<b>41</b>
38	3.1 Introduction . . . . .	41
39	3.2 Bulk Properties . . . . .	43
40	3.2.1 Graphite structure and Li-graphite stages . . . . .	43
41	3.2.2 Equilibrium potential and measured open circuit voltage . . . . .	44
42	3.2.3 Entropy . . . . .	49
43	3.2.4 Ion diffusion in Li-GIC . . . . .	52

44	3.3	Graphite Surfaces and Interfaces . . . . .	55
45	3.3.1	Possible graphite surfaces and their stability . . . . .	55
46	3.3.2	Surface Effect on Intercalation Energy . . . . .	57
47	3.3.3	The Surface Effect on Li Diffusion . . . . .	59
48	3.3.4	Li deposition on graphite anodes . . . . .	61
49	3.3.5	Solid-Electrolyte Interphase . . . . .	62
50	3.4	C/Si composites . . . . .	66
51	3.5	Outlook and challenges for anodes . . . . .	68
52	<b>4</b>	<b>Electrolytes</b>	<b>71</b>
53	4.1	Introduction . . . . .	71
54	4.2	Liquid Electrolytes . . . . .	75
55	4.2.1	Introduction to liquid electrolyte materials . . . . .	75
56	4.2.2	An introduction to modelling liquid electrolytes . . . . .	76
57	4.2.3	<i>Ab initio</i> modelling of liquid electrolytes . . . . .	77
58	4.2.4	Classical modelling of liquid electrolytes . . . . .	80
59	4.2.5	Bulk Structure and Landscaping . . . . .	82
60	4.2.6	Li-ion Diffusion . . . . .	83
61	4.2.7	Solvation Energies . . . . .	86
62	4.2.8	Activity coefficients of electrolytes . . . . .	86
63	4.2.9	Interfacial Nanostructure of Electrolytes . . . . .	87
64	4.2.10	Outlook and challenges . . . . .	90
65	4.3	Solid Electrolytes . . . . .	92
66	4.3.1	Introduction . . . . .	92
67	4.3.2	Sulfides . . . . .	94
68	4.3.3	Oxides . . . . .	99
69	4.3.4	Interface stability . . . . .	104
70	4.3.5	Outlook and challenges . . . . .	109

71	<b>5 Cathodes</b>	<b>111</b>
72	5.1 Introduction . . . . .	111
73	5.2 Bulk Properties . . . . .	114
74	5.2.1 Crystal Structure and Micro-Structure . . . . .	114
75	5.2.2 Lithium-ion Diffusion . . . . .	116
76	5.2.3 Redox and Electronic Properties . . . . .	120
77	5.2.4 TM Ordering in NMC Layered Oxides . . . . .	123
78	5.2.5 Vibrational and Thermal Properties . . . . .	123
79	5.3 Surfaces . . . . .	125
80	5.4 Interfaces . . . . .	129
81	5.5 Outlook and challenges for cathodes . . . . .	131
82	<b>6 Outlook</b>	<b>133</b>
83	<b>Acknowledgement</b>	<b>137</b>
84	<b>References</b>	<b>137</b>

# 1 Introduction

Lithium-ion (Li-ion) batteries (LiBs) were first commercialised by Sony in 1991.<sup>1</sup> They are ubiquitous in portable electronic devices, are emerging in hybrid and all-electric vehicles,<sup>2</sup> and are starting to play a role in large scale stationary storage.<sup>3</sup> Despite over 30 years of commercialisation and longer for development, not all factors dictating their capacity, performance, safety, and longevity are completely understood. The complexity of battery systems makes it time consuming and impractical to directly measure all of their physical attributes. The grand challenge is to construct a multiscale model, incorporating inputs across length- and time scales that can not only describe, but also predict, changes in behaviour.

To build a truly predictive modelling framework, a physical underpinning to battery models is required, incorporating physically correct descriptions of thermodynamic and kinetic battery behaviour. With sufficient accuracy built in, these models can provide insights on difficult-to-measure internal states, such as degree of Li intercalation and local electrolyte and ionic concentrations, as determined by the nanostructure of the materials used. By contrast, empirical models, which fit a curve to experimental data, are widely used in battery research, but have only a limited physical basis or, in some cases, no physical basis at all. For example, equivalent circuit models, which are widely used in industry, cannot be relied upon to predict battery behaviour over several charge-discharge cycles.

Physics-based continuum models attempt to describe the behaviour of whole cells, for example the widely used Doyle-Fuller-Newman (DFN) model.<sup>4-8</sup> These models need to use drastic simplifications to enable them to run in real time, but their accuracy can be greatly improved by adopting parameters measured using more detailed, microscopic simulations. Atomistic models are key to building truly physics-based models and form the foundation of the multiscale modelling chain, leading to more robust and predictive models.

Atomistic models can also be applied to fundamental research questions with high predictive accuracy. For example, they can be used to predict new behaviour not currently accessible by experiment, for reasons of cost, safety, or throughput. They can be used to op-

112 timise experimental design and use resources more efficiently, determining whether particular  
113 experiments are even worth performing and also provide unique insights into the behaviour  
114 of materials that may not even be accessible, or are impractical to obtain, by experimental  
115 probes. Atomistic models are useful for quantifying and evaluating trends in experimental  
116 data, explaining structure-property relationships and informing materials design strategies  
117 and libraries.

118 With the above in mind, we target this review to the following audiences. Non-atomistic  
119 battery modellers, such as continuum and control modellers, who would benefit from an eas-  
120 ily accessible summary of atomistic methods and how they connect with longer length scale  
121 models. As atomistic models comprise a range of methods, it is also beneficial to summarise  
122 how these interlink, since it is possible to be an expert in one area, whilst being unfamil-  
123 iar with another. For this reason, it is instructive to summarise these different methods in  
124 one place, so that non-specialists can understand these links. Recent developments in these  
125 techniques, such as linear scaling Density Functional Theory (DFT), require summarising  
126 standard DFT techniques. Likewise, longer length scale atomistic techniques can be parame-  
127 terised using *ab initio* data. While DFT and other atomistic methods are widely known and  
128 utilised individually, their other applications and connections to one another are often not  
129 as thoroughly described, nor do these descriptions account for more recent developments.

130 This review also aims to reach those working in the battery area, such as experimen-  
131 tals, who may not be experts in atomistic modelling and want to understand how atomistic  
132 models can help to understand experimental behaviour. Likewise, we show examples of  
133 behaviour currently out of reach with experiments. Similarly, this review is of benefit to  
134 junior researchers new to the battery area, and those who are already familiar with atom-  
135 istic methods but are new to lithium batteries. With these audiences in mind, we have  
136 summarised applications of atomistic methods in lithium-ion batteries and all solid-state  
137 batteries (ASSBs), which represent the most technologically advanced rechargeable battery  
138 systems currently available.

139 The family of atomistic models itself represents a range of different length- and time  
140 scales, from the level of electronic structure calculations through conventional and linear-  
141 scaling DFT, to *ab initio* Molecular dynamics (MD) and on to longer length scale models,  
142 such as classical MD, Monte Carlo (MC), and kinetic Monte Carlo (kMC) calculations, which  
143 are parameterised by force field potentials or *ab initio* data. These techniques, along with re-  
144 cent method developments and battery-specific observable properties, are summarised in the  
145 methods section of this review, section 2.1. Specific applications to anodes, liquid and solid  
146 electrolytes, and cathodes are broken down in the following sections. Links between different  
147 methodologies are emphasised and this review may thus be of particular interest to those  
148 looking, for example, to link DFT calculations to MC calculations, or apply linear-scaling  
149 DFT to MD, bridging possible gaps in nomenclature at different length scales. Atomistic  
150 models linking to *ab initio* calculations are summarised by Van der Ven et al.;<sup>9</sup> also note-  
151 worthy in this area is a review by Shi et al.,<sup>10</sup> and an older review by Franco.<sup>11</sup> A recent  
152 review of method development in the area of hybrid quantum-continuum solvation models  
153 is presented by Herbert.<sup>12</sup>

154 The review covers mechanisms in both the conventional liquid electrolyte based and solid-  
155 state based LiB, as shown schematically in Figure 1. In a single cell of a conventional LiB,  
156 as shown here, the anode, or negative electrode, comprises a copper current collector and the  
157 primary active material is graphite in the vast majority of commercial LiBs. Increasingly,  
158 small amounts of silicon are being added to boost the gravimetric capacity. The electrode  
159 material also comprises a binder, such as polyvinylidene fluoride (PVDF), and sometimes  
160 a small fraction of conductive carbon is added to boost conductivity. The two electrodes  
161 are divided by a separator soaked in an organic electrolyte, which is usually a mixture  
162 of carbonates with dissolved  $\text{LiPF}_6$  salt. The cathode, or the positive electrode, has an  
163 aluminium current collector. Various different types of cathode material are utilised in  
164 commercial LiBs, with the example shown here being the classic “rocking-chair” battery with  
165 a  $\text{LiCO}_2$  cathode.<sup>13</sup> The low conductivity of these transition metal oxides requires addition



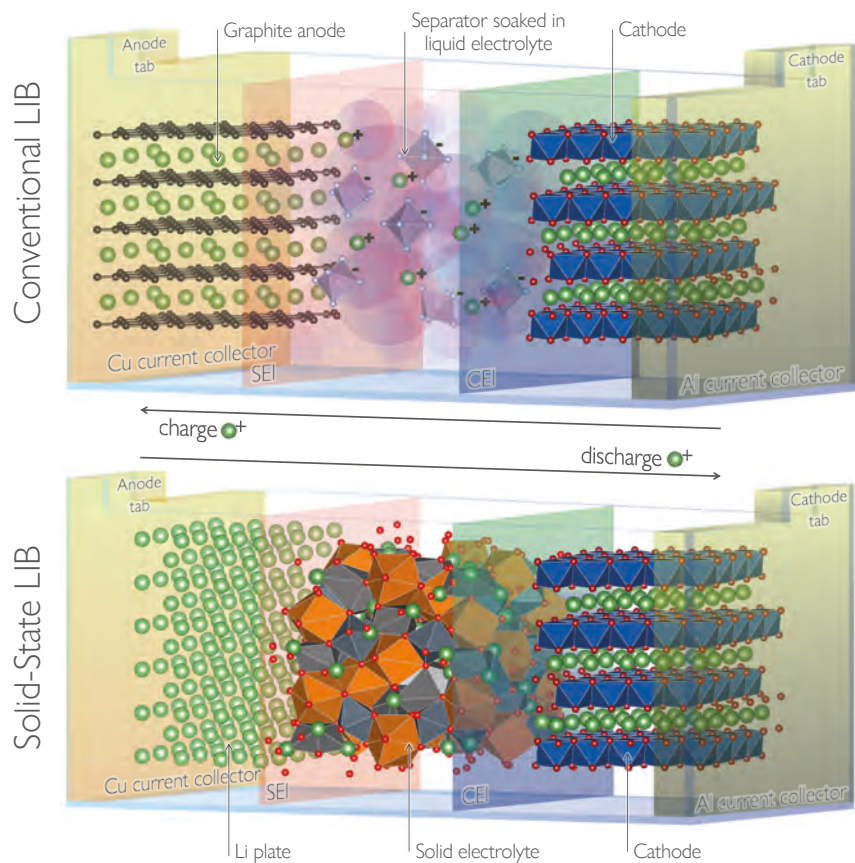


Figure 1: A schematic of a single cell of a conventional, liquid-based lithium-ion battery (LiB) and a solid-state LiB. The conventional LiB comprises an anode composed of a Cu current collector and an active anode material (graphite), a separator soaked in an organic electrolyte, and a cathode composed of a Al current collector and an active cathode material, for example,  $\text{LiCo}_2$ , as shown here. The solid-state LiB comprises a similar cathode, a solid electrolyte, and an anode composed of a Li-ion plate and Cu current collector. The anode-electrolyte interphase (SEI) and cathode-electrolyte interphase (CEI) for both LiBs are represented as pink and blue transparent layers, respectively. The tabs are shown protruding from the top of the current collectors. Both LiB cells show all components as fully lithiated, with directional  $\text{Li}^+$  movement during (dis)charge indicated with arrows.

166 of conductive carbon and, as with the anode material, the active cathode material is held  
167 together with a binder, such as PVDF. When the cell is assembled, the cathode starts fully  
168 lithiated and the anode is completely delithiated. On the first cell charge cycle (also known  
169 as the formation cycle) lithium is removed from the cathode and the anode becomes filled  
170 with lithium while the solid electrolyte interphase (SEI) and cathode electrolyte interphase  
171 (CEI) are formed. While Figure 1 shows both electrodes in a fully lithiated state, Li is  
172 transferred between the electrodes reversibly during (dis)charging, therefore allowing this  
173 system to be rechargeable.

174 Although not yet commercialised, ASSBs are a promising future alternative to conven-  
175 tional liquid electrolyte LiBs. Their anode, or negative electrode, comprises a copper current  
176 collector and either a metallic lithium plate (Li-metal), as shown in Figure 1, or less com-  
177 monly a graphite-based material (Li-ion). As there is no liquid, there is no longer a need  
178 for separators, with the two electrodes being separated by the solid electrolyte material,  
179 shown here with  $\text{Li}_7\text{La}_3\text{Zr}_2\text{O}_2$  (LLZO). The cathode, or positive electrode, has an aluminium  
180 current collector and, as with the conventional LiB, can accommodate various cathode mate-  
181 rials, such as  $\text{LiCo}_2$ . The interfacial regions between the electrodes and the solid electrolyte  
182 are known as the solid-solid interphase, or anode/cathode-solid interphase. Figure 1 shows  
183 both electrodes in a fully lithiated state; however, the Li is transferred between the electrodes  
184 reversibly, as in conventional LiBs.

185 The anodes section, section 3, heavily focuses on graphite, which is still the predominant  
186 anode material in Li-ion cells. The section describes atomistic modelling of bulk graphite,  
187 graphite edges where initial Li-ion insertion occurs, and the Solid-Electrolyte Interphase  
188 (SEI). The bulk modelling discussion includes a direct comparison between experimental  
189 and theoretical thermodynamic parameters, such as the open circuit voltage (OCV) and  
190 entropy, which will also be of interest to battery control modellers. Kinetic predictions  
191 are made and linked to DFT predictions of the influence of graphite edge morphology on  
192 surface states, which may be of interest to those working on battery material development

193 and discovery. Recent work applying linear scaling DFT to complex interfaces will be of  
194 interest to those at the forefront of DFT method development, focusing on the boundary  
195 between atomistic and continuum modelling. Lastly, recent developments in silicides to  
196 boost anode gravimetric capacity, along with their associated challenges, are summarised in  
197 the outlook. Recent reviews in this area include Asenbauer et al.,<sup>14</sup> summarising aspects of  
198 lithiation/delithiation mechanisms and morphological aspects in graphite and silicon oxide  
199 composites, and Zhang et al.,<sup>15</sup> similar in scope but providing a more *ab initio* focus. Here,  
200 our review here covers graphite structure and lithiation/delithiation mechanisms, including  
201 surfaces and interfaces, which have tended to be neglected, although aspects of modelling  
202 the SEI have been reviewed by Wang et al..<sup>16</sup>

203 The liquid electrolyte section, section 4.2, has a strong focus on the development of atom-  
204 istic models, both *ab initio* and force field-based. This includes a pivotal discussion on the  
205 atomic interactions between the components and method development to study electrolytes  
206 via classical MD simulations. This will be of particular interest to those at the forefront of  
207 classical MD method development. Liquid electrolytes are known to be limited by narrow  
208 electrochemical windows, solvent toxicity, and material flammability/safety concerns. The  
209 latter parts of this section describe the atomistic modelling of the bulk structure and land-  
210 scaping, Li-ion diffusion, solvation energies, and activity coefficients of liquid electrolytes,  
211 and the interfacial nanostructure relating to the interface with a solid electrode. These topics  
212 cover the major aspects for improving liquid electrolytes for use in a battery and research  
213 towards circumventing critical safety<sup>17,18</sup> and energy density<sup>19</sup> limitations. The challenges  
214 and potential avenues for solving these issues are summarised in the outlook, including recent  
215 developments to resolve these within the liquid electrolyte family and alternative materials.  
216 Recent reviews in this area include Galiński et al.,<sup>20</sup> summarising the field of ionic liquids,  
217 Wang et al.,<sup>21</sup> reviewing the recent progress in water in salts electrolytes, and Logan and  
218 Dahn,<sup>22</sup> giving some recent developments in conventional electrolytes. Here, our review  
219 covers the continued development of interatomic potentials for liquid electrolytes and a de-

220 scription of the solid electrode-liquid electrolyte interface from the perspective of the liquid,  
221 which is not the conventional frame of reference.

222 Solid state electrolytes (SSEs) are becoming an increasingly popular avenue of research,  
223 motivated by the rise of the electric vehicle (EV).<sup>23</sup> They have been proposed as an alterna-  
224 tive to liquid electrolytes to resolve safety issues pertaining to the flammable organic liquid  
225 electrolytes that are currently used,<sup>17,18</sup> and also as a route to increased energy density.<sup>19</sup>  
226 In the solid electrolyte section, section 4.3, we review a selection of the promising candidate  
227 materials currently being investigated. Each material discussed has a different focus, high-  
228 lighting a range of properties applicable to different SSE materials. In this section, we focus  
229 on four material families, grouping them into sulfide and oxide based SSEs. Sulfide based  
230 SSEs typically have a high Li-ion conductivity and poor electrochemical stability against  
231 Li metal (the anode typically used in combination with SSEs).<sup>24,25</sup>  $\text{Li}_{10}\text{GeP}_2\text{S}_{12}$  (LGPS) is  
232 reviewed, with a focus on how atomistic methods reveal the isotropic ion pathways, while  
233  $\text{Li}_6\text{PS}_5\text{X}$  based Li-argyrodites are focused towards the relationship between ionic conduc-  
234 tivity and anion substitution, as well as atomistic predictions of occupied Li sites. Oxides  
235 typically have a higher electrochemical stability but still suffer from dendrite formation,  
236 amongst other issues.<sup>24</sup> LLZO is also reviewed, with a focus on how multiple atomistic  
237 methods have been applied to probe dendrite formation and ionic transport in the material.  
238 State-of-the-art models of interfaces in oxide nanocomposites are reviewed. Lastly, the chal-  
239 lenges of the SEI are discussed and an outlook to future modelling of SSEs is given. Related  
240 reviews in the area include Zhang et al.,<sup>26</sup> summarising the future directions of ASSBs, and  
241 Gurung et al.,<sup>27</sup> highlighting the advances and challenges in SSEs and ASSBs. Xiao et al.<sup>28</sup>  
242 and others<sup>29,30</sup> provide a more specific review of the SEI. Ceder et al.<sup>31</sup> outlines the prin-  
243 ciples that should be employed when modelling SSEs. Here, our review discusses a broad  
244 range of SSE properties, following the notion that these properties are applicable to range  
245 of materials.

246 The cathodes section, section 5, covers a range of different cathode materials used in a

247 variety of Li-ion cells. This section describes atomistic modelling in the bulk, at the surfaces,  
248 and the Cathode-Electrolyte Interphase (CEI). In discussing bulk modelling, a comparison  
249 of the different cathode crystal structures, micro-structuring, and available diffusion path-  
250 ways within the material are covered, as well as important properties, including redox and  
251 electronic properties, transition metal ordering, and vibrational and thermal properties. Use  
252 of electronic structure methods modelling techniques has been essential for investigating  
253 crystalline structure, so will be of great interest to those who utilise DFT in their research.  
254 Surface structures and morphologies of cathode particles can be difficult to determine using  
255 experimental methods alone, which is where *ab initio* and potentials-based MD can pro-  
256 vide vital insight. As with the SEI, linear-scaling DFT has recently been applied to CEI,  
257 where discussions on CEI will be of interest to those doing state-of-the-art DFT method  
258 development. Related reviews in the area include Ma,<sup>32</sup> summarising modelling Li-ion bat-  
259 tery cathode materials, Yan et al.,<sup>33</sup> focusing on DFT calculations of cathode materials,  
260 and Wang et al.,<sup>34</sup> discussing closing the gap between theoretical and practical capacities  
261 in layered oxide cathode materials. Our review includes a discussion on the CEI, which has  
262 recently been reviewed by Maleki Kheimeh Sari and Li.<sup>35</sup> Here, our review covers thermal,  
263 electronic, dynamic, and structural properties for a range of prominent cathode materials  
264 in terms of both electronic structure methods and potential-based modelling, which have  
265 tended to be more isolated in other reviews.

266 Finally, we provide an outlook on the key remaining challenges for atomistic modelling  
267 of LiBs and promising future directions for resolving them.

## 2 Methods

### 2.1 Method overview

#### 2.1.1 Density Functional Theory

Density Functional Theory (DFT) is amongst the most accurate methods for atomistic simulations of materials, as it is a quantum mechanical method. This means that it is able to simulate the electrons in materials and how they result in all the observable processes and properties of a material. As electrons are microscopic particles, to simulate their properties we need to use the theory of quantum mechanics. However, the computational cost of calculations with this theory is very high, as all the observable properties are obtained from the wave function: a highly complicated function of many variables (proportional to the number of particles we are simulating) and, for exact solution, the computational effort scales exponentially with the number of particles. Approximate wave function based theories with more favourable computational scaling (such as  $\sim N_e^5$  or  $\sim N_e^7$ , where  $N_e$  is the number of electrons in the calculation) have been developed, but the computational effort is still so high that they cannot be applied to molecules with more than a few atoms.

DFT is a reformulation of quantum electronic structure theory, where the central quantity is no longer the wave function, but instead the electronic density,  $\rho(\mathbf{r})$ , which is a comparatively simpler function of only one position variable,  $\mathbf{r}$ . As a result, DFT has lower computational scaling, allowing simulations of much larger systems (up to a few hundred atoms on supercomputers). Another advantage of DFT is that it is formally an exact theory. Due to these two significant advantages, DFT is today the method of choice for most simulations.

DFT was originally developed by Hohenberg and Kohn<sup>36,37</sup> and reformulated by Kohn and Sham<sup>38</sup> into the mathematical description we use today, often called KS-DFT, where the energy of a material is expressed as:

$$E[\rho] = T_{KS}[\rho] + E_{\text{ext}}[\rho] + E_H[\rho] + E_{xc}[\rho]. \quad (1)$$

293 Here all the terms are expressed as functionals of the density and  $T_{KS}[\rho]$  is the kinetic  
 294 energy of the electrons,  $E_{\text{ext}}[\rho]$  is the energy of attraction of the electrons to nuclei (also  
 295 called external potential energy),  $E_H[\rho]$  is the classical (Coulomb) electrostatic energy of  
 296 the electronic density charge distribution (also called Hartree energy), and  $E_{xc}$  describes the  
 297 purely quantum effects of exchange and correlation.

298 DFT calculations are performed in an iterative fashion, with electron density expressed  
 299 as a sum of one-electron wave functions,  $\{\psi_i\}$ , called molecular orbitals (MOs):

$$\rho(\mathbf{r}) = \sum_{i=1}^{N_e} |\psi_i(\mathbf{r})| \quad (2)$$

300 and these MOs are obtained by solving the Kohn-Sham eigenvalue equation:

$$\left[ -\frac{1}{2}\nabla^2 + v_{\text{ext}}(\mathbf{r}) + v_H[\rho](\mathbf{r}) + v_{xc}[\rho](\mathbf{r}) \right] = \varepsilon_i \psi_i(\mathbf{r}). \quad (3)$$

301 As we can see from eqn. 3, the Hartree,  $v_H[\rho]$ , and exchange-correlation,  $v_{xc}[\rho]$ , potentials  
 302 are functionals of the density, thus ultimately functionals of the MOs, which provide the  
 303 solutions of the equation. This equation cannot be solved directly, but must follow an  
 304 iterative procedure called the *self-consistent field (SCF)* process. The simplest SCF method  
 305 is to guess a set of  $\{\psi_i\}$  and use these to build and solve (eqn. 3), obtaining a new set of  
 306  $\{\psi_i\}$  and repeating this process until the  $\{\psi_i\}$  and the energy (eqn. 1) no longer change.

307 KS-DFT is formally an exact theory, but it does not provide an explicit expression for the  
 308 exchange-correlation energy,  $E_{xc}[\rho]$ . The exact exchange-correlation functional is unknown  
 309 or, more precisely, unknowable. Thus a very active area of DFT development is to construct  
 310 approximations of increasing accuracy for  $E_{xc}[\rho]$ . The simplest approximation is the local  
 311 density approximation (LDA), where  $E_{xc}[\rho(\mathbf{r})]$  is expressed as:

$$E_{xc}^{LDA}[\rho(\mathbf{r})] = \int \rho(\mathbf{r})\epsilon_{xc}[\rho(\mathbf{r})] d\mathbf{r} \quad (4)$$

312 The value of  $\epsilon_{xc}$  at some position,  $\mathbf{r}$ , is computed exclusively from the value of  $\rho$  at that  
 313 position. In practice,  $\epsilon_{xc}[\rho(\mathbf{r})]$  describes the exchange and correlation energy per particle of  
 314 a uniform electron gas of density  $\rho$ .<sup>39</sup>

315 In general, the electron density in a molecular system is not spatially uniform, even at  
 316 small volumes of space, limiting the applicability of LDA. More accurate functionals are  
 317 obtained by the inclusion of a density gradient correction, known as the generalised gradient  
 318 approximation (GGA), or semi-local functionals. In the GGA, the functionals depend on  
 319 both the density and the gradient of the density, i.e.  $v_{xc}^{\text{GGA}} = f(\rho, \nabla\rho)$ . Popular examples  
 320 of GGA functionals are Perdew-Wang GGA (PWGGA) (both exchange and correlation),<sup>40</sup>  
 321 Perdew-Burke-Ernzerhof GGA (PBEGGA),<sup>41</sup> and Becke-Lee-Yang-Parr (BLYP).<sup>42,43</sup> Func-  
 322 tionals including contributions from the second derivative of the density are called *meta*-GGA  
 323 functionals.<sup>44</sup>

324 Standard DFT methods fail to describe dispersion effects that are of a non-local electron  
 325 correlation nature. Consequently, DFT methods are often inaccurate for the investigation  
 326 of molecular crystals, adsorption on surfaces, and other systems in which dispersion forces  
 327 due to van der Waals (vdW) gaps between layers play a significant role. Several versions  
 328 of dispersion corrected DFT (DFT-D) approaches are available, e.g. DFT-D2,<sup>45</sup> DFT-D3,<sup>46</sup>  
 329 DFT-D4,<sup>47</sup> DFT-D3BJ,<sup>48,49</sup> etc.

330 GGA functionals, however, still have problems with self interaction. The hybrid func-  
 331 tionals usually offer some improvement over the corresponding pure DFT functionals. Of  
 332 all modern functionals, the B3LYP method is the most popular to date.<sup>43,50</sup> It works well  
 333 both for structural investigations and for the computation of electronic properties.<sup>51</sup> An-  
 334 other popular hybrid functional, PW1PW,<sup>52,53</sup> was parameterised to reproduce structural,  
 335 energetic, and electronic properties of solids. A more recent and popular hybrid functional  
 336 is HSE06, where the correlation part is defined by a PBE functional and a range-separation



337 approach is used for the exchange part.<sup>54</sup>

338 The applicability of the hybrid functionals depends mainly on the type, size, and com-  
339 plexity of the studied systems, as these functionals incur a huge computational cost. An  
340 alternative approach is the DFT+U method, where the effects of strong intra-atomic elec-  
341 tronic correlations are modelled by adding an on-site Coulomb repulsion,  $U$ , and site ex-  
342 change term,  $J$ , to the DFT Hamiltonian.<sup>55-57</sup> Parameters  $U$  and  $J$  can be extracted from  
343 *ab initio* calculations, but are usually obtained semi-empirically. Inspired by the Hubbard  
344 model, the DFT+U method is formulated to improve the ground state description of strongly  
345 correlated systems. The Hubbard Hamiltonian describes the strongly correlated electronic  
346 states (d and f orbitals), while the rest of the valence electrons are treated by normal DFT  
347 approximations.

### 348 2.1.2 Linear-Scaling DFT

349 In conventional DFT, solving the Kohn-Sham eigenvalue equations, eqn. 3, subject to the  
350 required orthonormality constraint, results in a computational cost scaling with the third  
351 power (it is an  $\mathcal{O}(N^3)$  procedure) with the number of atoms,  $N$ . This is demonstrated in the  
352 example of Figure 2, showing the computation time as a function of the number of atoms for  
353 slabs of graphite of increasing size. This unfavourable scaling is the reason why conventional  
354 KS-DFT is practically unfeasible beyond several hundred atoms. However, there are many  
355 grand challenges in materials research, where, due to their inherent complexity, building re-  
356 alistic models requires thousands of atoms, such as simulations of defects, complex structures  
357 of the Solid-Electrolyte Interphase (SEI), and metallic and semiconductor nanoparticles used  
358 in catalysis and battery electrodes, among others. This need for large-scale DFT calcula-  
359 tions has motivated the development of new theoretical methods which can scale linearly  
360 with system size.<sup>58</sup> In these linear-scaling methods, conventional KS-DFT is reformulated in  
361 terms of the one-particle density matrix,  $\gamma$ :

$$\gamma(\mathbf{r}, \mathbf{r}') = \sum_i f_i \psi_i(\mathbf{r}) \psi_i^*(\mathbf{r}'), \quad (5)$$

362 allowing us to exploit the principle of “nearsightedness of electronic matter”,<sup>59</sup> because  
 363 the density matrix decays exponentially with the distance,  $|\mathbf{r} - \mathbf{r}'|$ ,<sup>59</sup> while the MOs,  $\{\psi_i\}$ ,  
 364 are, in general, fully delocalised over the entire electronic system (molecule, nanoparticle,  
 365 slab, etc.) and do not decay. The exponentially-decaying tail of the density matrix can be  
 366 truncated to develop methods with reduced or linear-scaling computational cost. As the  
 367 system size (number of atoms) is increased, it reaches a point where the remaining amount  
 368 of information increases linearly with the size of the system. This can be implemented  
 369 more efficiently with non-orthogonal, localised orbitals,  $\{\phi_\alpha\}$ .<sup>60,61</sup> In this representation, the  
 370 density matrix can be written as:

$$\gamma(\mathbf{r}, \mathbf{r}') = \phi_\alpha(\mathbf{r}) K^{\alpha\beta} \phi_\beta^*(\mathbf{r}'). \quad (6)$$

371 Here, the density kernel matrix,  $\mathbf{K}$ , is a generalisation of the MO occupancies,  $\{f_i\}$ , of  
 372 equation 5, while implicit summation (Einstein convention) is assumed for repeated Greek  
 373 indices.

374 The development of linear-scaling methods has proven to be a very challenging research  
 375 topic, as the goal of developing methods that accommodate the conflicting requirements of  
 376 orbital localisation with high accuracy is extremely difficult to achieve. Recent develop-  
 377 ments towards this goal have made this possible by using a dual resolution approach, where  
 378 both  $\{\phi_\alpha\}$  and  $\mathbf{K}$  are optimised self-consistently during the calculation, while subject to  
 379 localisation constraints.<sup>62–64</sup> The  $\mathcal{O}(N)$  Electronic Total Energy Package (ONETEP),<sup>65</sup> has  
 380 the unique capability of achieving linear-scaling computational cost, while maintaining the  
 381 near-complete basis set accuracy of conventional DFT. The computational efficiency of this  
 382 code is demonstrated on the graphite example in Figure 2, where the linear-scaling behaviour  
 383 can be clearly seen. DFT calculations with tens of thousands of atoms can be performed

384 with ONETEP, opening avenues for simulating realistic models of materials and interfaces in  
 385 lithium-ion batteries (LiBs) with DFT-scale accuracy. ONETEP is being actively developed  
 386 and offers a large and diverse range of capabilities, including: different boundary condi-  
 387 tions, various exchange–correlation functionals, finite electronic temperature methods for  
 388 metallic systems, methods for strongly correlated systems, molecular dynamics, vibrational  
 389 calculations, time-dependent DFT, electronic transport, core loss spectroscopy, implicit sol-  
 390 vation, density of states calculations, and distributed multipole analysis.<sup>65</sup> Recent focus in  
 391 ONETEP is on developing specific electrochemistry tools for battery simulations, aiming to  
 392 develop the first atomistic simulation platform (in particular, the first linear-scaling DFT  
 393 platform) for electrochemistry. Some of these developments are described in this review, in  
 394 subsection 2.2.1.

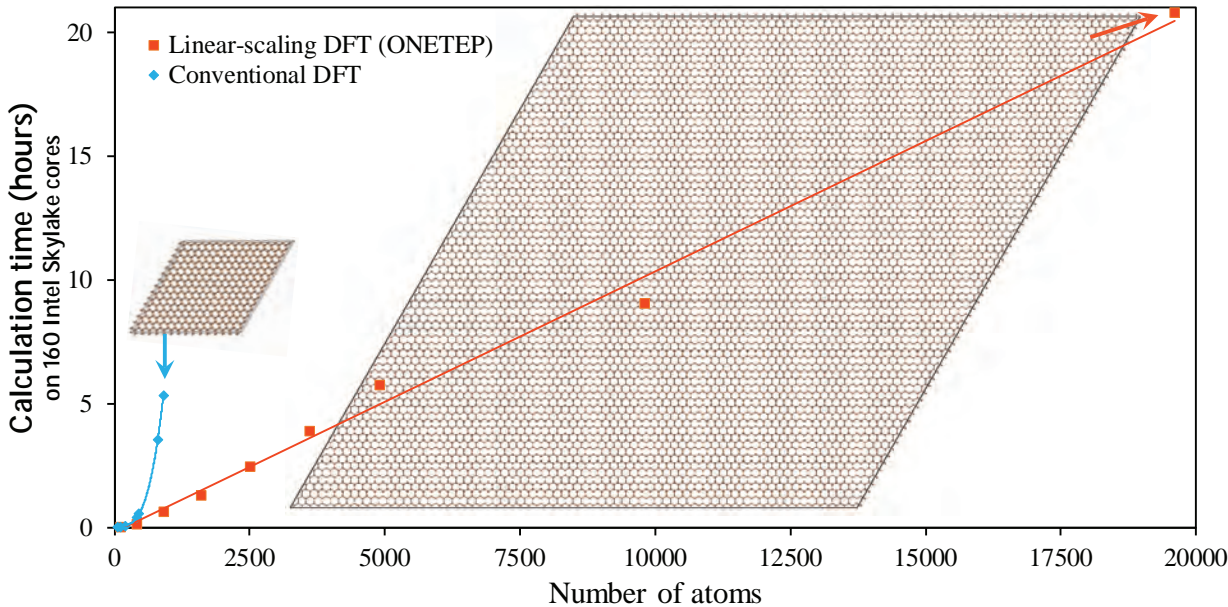


Figure 2: Comparison of the computational time with the number of atoms for slabs of graphite of increasing size using the ONETEP linear-scaling DFT code versus a conventional plane wave DFT code. The computations were performed on the Iridis 5 supercomputer at the University of Southampton on 40 MPI processes, with 4 OpenMP threads each (160 cores in total). Reprinted from Ref. 66, with the permission of AIP Publishing.

395 **2.1.3 Nudged Elastic Band**

396 Nudged elastic band (NEB) theory is a useful method based on transition state theory,  
397 seeking the minimum energy path and the saddle point (or transition state) between two  
398 minima (initial and final states).<sup>67-69</sup> The energy difference between the lowest energy state  
399 and the saddle point is defined as the activation barrier ( $E_a$ ), Figure. 3.<sup>69</sup>

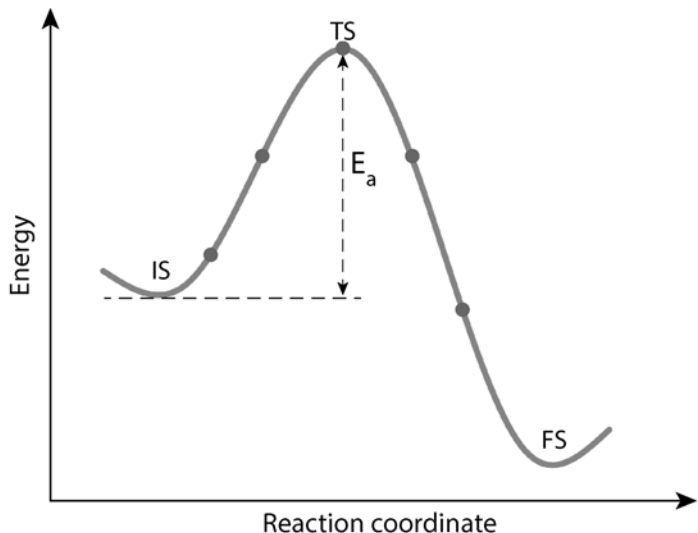


Figure 3: Energy profile of Nudged Elastic Band (NEB) calculation. The IS, TS, and FS are the initial state, transition state and final state, respectively.  $E_a$  denotes the activation barrier along the reaction path. The grey circles are the “images” in the NEB calculation.

400 The NEB approach initially guesses a number of configurations of several possible inter-  
401 mediate “images” that may occur along the reaction coordinate or diffusion path. This set  
402 of images can be created by linear interpolation between the initial and final states. The  
403 NEB algorithm further conducts constrained optimisation and converges those images along  
404 the minimum energy path. Furthermore, fictional spring forces are added between adjacent  
405 images to maintain the spacing and the continuity of the reaction or diffusion path. The  
406 NEB approach is widely applied in the studies of chemical transformations, such as catalytic  
407 reactions or ion diffusion in solid materials. The determined chemical reaction energy bar-  
408 riers can then be used in further, larger time- and length-scale models, such as microkinetic  
409 models.<sup>70,71</sup>

410 **2.1.4 Cluster expansion**

411 The cluster expansion method enables a statistical approach to sample configurational phase  
 412 space at finite temperature.<sup>72-74</sup> This method aims to capture the energetics of mixing two  
 413 or more atoms on a given set of lattice sites, typically with an accuracy close to DFT  
 414 calculations. The approach borrows ideas from the Ising model,<sup>75</sup> where each lattice site is  
 415 assigned as a spin variable to simulate the magnetic properties, but maps site occupancy  
 416 onto spin variables instead.<sup>76</sup> For example, for a binary alloy system with atom types A and  
 417 B, the occupation of each site can be described by a spin-like variable, i.e.  $\sigma_i = +1$ , if the site  
 418 is occupied by atom A, and  $\sigma_i = -1$  if the site is occupied by atom B, as shown in Figure 4.  
 419 A configuration can then be written as  $\sigma = (\sigma_1, \dots, \sigma_n)$ . Accordingly, the energy of each  
 420 configuration can be expressed as:  $E \equiv E(\sigma_1, \dots, \sigma_n)$ .

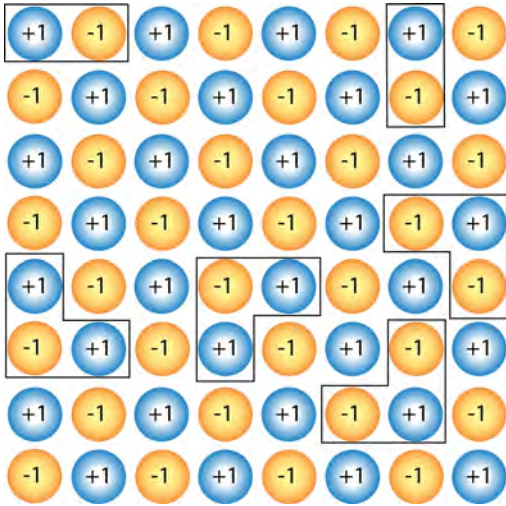


Figure 4: A 2D (8x8) structure including several clusters. +1 and -1 are the lattice sites assigned with different spins.

421 To compute  $E(\sigma)$ , all relevant interactions should be sampled. A set of interactions should  
 422 be considered, such as nearest neighbouring pair interactions, second nearest neighbouring  
 423 pair interactions, triplet interactions, quadruplet interactions, and so on, up to many body  
 424 interactions (Figure 4). Further, all symmetry-equivalent interactions (including transla-  
 425 tions) can be grouped into “clusters ( $\alpha$ )”. Including all relevant cluster interactions, the

426 energy can be expressed as:

$$E_\alpha = \sum_{\alpha} m_\alpha J_\alpha \bar{\Pi}_\alpha(\sigma), \quad (7)$$

427 where  $m_\alpha$  is the multiplicity of the cluster,  $\alpha$ , and can be obtained by considering all the  
 428 point symmetries in the lattice cell.  $J_\alpha$  is the effective cluster interaction (ECI) associated  
 429 with a cluster,  $\alpha$ .  $\bar{\Pi}_\alpha(\sigma)$  is the correlation matrix of normalised spin-products for a particular  
 430 cluster of the entire lattice, obtained via:

$$\bar{\Pi}_\alpha(\sigma) = \frac{1}{Nm_\alpha} \sum_{i \in \alpha} \Pi \sigma_i, \quad (8)$$

431 where  $N$  is the number of parent lattice cells required to generate the configuration  
 432  $\sigma$ . Theoretically, the expansion should include all possible clusters. However, that is not  
 433 practical and one of the key features of cluster expansions is that they usually converge  
 434 quickly after including a handful of terms.<sup>77</sup> Consequently, only a relatively small number  
 435 of DFT calculations are therefore required to parameterise a handful of ECIs. For example,  
 436 if we calculate the energy of an A-B alloy system and consider only four clusters and four  
 437 configurations, the energy of each configuration can be expressed as:

$$\begin{pmatrix} E_1 \\ E_2 \\ E_3 \\ E_4 \end{pmatrix} = \begin{pmatrix} \Pi_1(1) & \Pi_2(1) & \Pi_3(1) & \Pi_4(1) \\ \Pi_1(2) & \Pi_2(2) & \Pi_3(2) & \Pi_4(2) \\ \Pi_1(3) & \Pi_2(3) & \Pi_3(3) & \Pi_4(3) \\ \Pi_1(4) & \Pi_2(4) & \Pi_3(4) & \Pi_4(4) \end{pmatrix} \begin{pmatrix} J_1 \\ J_2 \\ J_3 \\ J_4 \end{pmatrix} \quad (9)$$

438 In principle, the effective interaction coefficients,  $J_\alpha$ , can be obtained via inverting the  
 439 matrix above and using the energies from DFT calculations, but this is not commonly done.  
 440 Rather, a larger training set is generated from DFT and the ECIs are fitted in a least-  
 441 square sense. The set of considered clusters is usually obtained by cross-validation: the  
 442 set of clusters with the highest accuracy for predicting configurations achieves the highest

443 cross-validation score and is selected.

444 Various codes exist to link the results of DFT calculations with cluster expansion codes,  
445 such as the Alloy Theoretic Automated Toolkit (AT-AT),<sup>78-80</sup> the Clusters Approach to  
446 Statistical Mechanics (CASM),<sup>81</sup> *Ab Initio* Random Structure Search (AIRSS),<sup>82</sup> Integrated  
447 Cluster Expansion Toolkit (IceT),<sup>83</sup> and CLuster Expansion in Atomic Simulation Environ-  
448 ment (CLEASE).<sup>84</sup> These codes usually provide a means to fit ECIs and include Monte Carlo  
449 (MC) features to sample phase spaces. They also allow the generation of DFT calculations  
450 to expand the training set. MC methods are explained in the next section.

### 451 2.1.5 Lattice gas and Monte Carlo

452 Lattice gas methods simulate the system state as an array of points.<sup>85</sup> This data structure  
453 is ideally suited to represent periodic, crystalline systems, but extensions to more complex  
454 systems are possible. In atomistic simulations, the array values denote the occupation of  
455 particular sites by certain types of atoms. The evolution of the system state can then be  
456 computed in terms of changes in those array values, i.e. site occupancies.<sup>85</sup>

457 In the Ising Hamiltonian described in the previous section, each site can be in either a +1  
458 or -1 state.<sup>86</sup> This data structure is suited to studying the thermodynamics and kinetics of  
459 binary alloys.<sup>87,88</sup> Simplistically, a LiB intercalation material can be represented as a binary  
460 alloy of lithium atoms and vacancies within an Ising model.<sup>76,89,90</sup>

461 The interaction Hamiltonian describes how the energy of the system depends on the  
462 configuration of the lattice. For a simple interaction model, it is possible to perform a direct  
463 evaluation of the partition function,  $Z$ , via:

$$Z = \sum_i e^{-\beta E_i}, \quad (10)$$

464 where  $E_i$  is the energy of state  $i$ , and  $\beta = 1/kT$  ( $k$  = Boltzmann constant;  $T$  = absolute  
465 temperature). Once  $Z$  is known, the rest of the thermodynamic properties of the system can  
466 easily be determined.<sup>91-93</sup> In a two-level system,<sup>92</sup> the number of states in equation 10 can

467 be reduced to scale linearly with the number of particles in the system, making the sum-  
468 mation computationally tractable.<sup>91–93</sup> Measurable quantities, like the open circuit voltage  
469 (OCV), voltammograms, and partial molar enthalpy and entropy can be simulated.<sup>91–93</sup> This  
470 approach has been applied to lithium intercalation in lithium manganese oxide (LMO)<sup>93</sup> and  
471 graphite,<sup>91,92</sup> as demonstrated in section 3.2.3. The interactions between the particles can  
472 be approximated by taking the average occupation in two levels, allowing ordered structures  
473 like graphite stages to be modelled. This approach represents a step in complexity beyond  
474 the assumption of simple solid solution behaviour, which is still commonly applied in con-  
475 tinuum level models.<sup>94</sup> The approach is closely related to the phase field models applied by  
476 Bazant to systems such as lithium iron phosphate (LFP) and graphite.<sup>95–97</sup>

477 For a more general and realistic interaction Hamiltonian, the number of energy states  
478 precludes direct evaluation of equation 10. In that case, MC methods are useful for calcu-  
479 lating thermodynamic properties. This is true for the Ising model defined in section 2.1.4,  
480 when represented in more than one dimension, as is the case in most practical systems. It is  
481 then more practical to obtain the thermodynamic properties by the Metropolis algorithm.<sup>98</sup>  
482 Following the Markov chain of states, the limiting distribution equals the probability distri-  
483 bution of the thermodynamic ensemble. Properties of interest can be obtained from taking  
484 the average of sampled configurations once the distribution has reached equilibrium.<sup>88</sup>

485 Inputting a chemical potential,  $\mu$ , in the grand canonical ensemble, the ground state  
486 properties of the system are obtained as follows. For a LiB,  $\mu$  represents the chemical  
487 potential of intercalated Li in the host, i.e. the electrode potential, described in section 2.3.1.  
488 Computing the average occupation,  $\langle N \rangle$ , of particles in the system at each  $\mu$  value, therefore  
489 allows the equilibrium potential to be simulated at any input temperature,  $T$ . Along with  
490  $\langle N \rangle$ , the average internal energy,  $\langle E \rangle$ , is a useful parameter to check the convergence of the  
491 simulation results with respect to the system size.<sup>85,89,90,99</sup>

492 Variances can be computed to check the system size convergence and derive experi-  
493 mentally measurable parameters. For example, the configurational component of the heat



494 capacity at constant volume,  $C_V$ , given by:

$$C_V = \frac{\beta}{T} (\langle E^2 \rangle - \langle E \rangle^2) = \frac{\beta}{T} \text{var}(\mathbf{E}), \quad (11)$$

495 where  $\text{var}(\mathbf{E})$  is the variance of  $E$ . The vibrational and electronic components of  $C_V$  must  
496 be determined by other means, such as the approaches outlined in section 2.3.4.

497 It is also possible to determine voltammograms from  $\text{var}(N)$ , as explained by Darling and  
498 Newman and Mercer et al..<sup>89,99</sup> If the covariance of  $U$  and  $N$  is also known, the partial molar  
499 internal energy,  $\partial U/\partial N$  and partial molar entropy  $\partial S/\partial N$  can be obtained, as defined else-  
500 where.<sup>89,90</sup> These parameters can be compared with experimental parameters from “entropy  
501 profiling” or calorimetry<sup>89,91,93,100,101</sup> and input into a dynamic model such as kinetic Monte  
502 Carlo (kMC),<sup>76,99,102,103</sup> or Molecular Dynamics (MD) to describe temperature dependent  
503 behaviour. A review of kMC has recently been published;<sup>104</sup> the technique is also briefly  
504 described by Van der Ven et al..<sup>9</sup> MD is described in the following section.

### 505 2.1.6 Molecular Dynamics

506 MD is an approach which probes the dynamic evolution of a system over time. The crucial  
507 input for these simulations is the potential energy surface (PES), describing the interactions  
508 between atoms. In *ab initio* MD (AIMD), this is described by solving the Schrödinger  
509 equation, whereas in a classical (potentials-based) mechanics framework the interactions are  
510 described using parameterised interatomic potentials. Here, we give an overview of both  
511 frameworks.

512 AIMD is able to capture events that potentials-based MD cannot, including bond break-  
513 ing, and bond formation. AIMD also assumes that the dynamics of particles can be treated  
514 classically and that the equation of motion for all particles can be written as:

$$M_I \ddot{\mathbf{R}}_I = -\nabla_I [\varepsilon_0(\mathbf{R}) + V_{NN}(\mathbf{R})], \quad (12)$$

515 where  $M_I$  is the mass of a given nucleus,  $\mathbf{R}$  denotes all nuclear coordinates,  $\nabla_I$  is the  
 516 Laplacian operator of a given nucleus,  $\varepsilon_0(\mathbf{R})$  represents the ground state energy of the system  
 517 at that given nuclear configuration, and  $V_{NN}(\mathbf{R})$  represents the nuclear-nuclear coulomb  
 518 repulsion at that given nuclear configuration.

519 Most modern techniques use KS-DFT (c.f. section 2.1.1) to solve the Schrödinger equa-  
 520 tion which finds the ground state energy. AIMD can be broadly split up into two main  
 521 categories: Born-Oppenheimer dynamics and Car-Parrinello extended Lagrangean. The  
 522 Born-Oppenheimer dynamics method uses a symplectic integrator to numerically integrate  
 523 the equation of motion in Eq. 12 for each time step. The Car-Perrinello extended Lagrangean  
 524 method gives the Kohn-Sham orbitals an artificial time-dependence. To attain a minimum  
 525 energy with each new  $\mathbf{R}$ , the orbital dynamics are kept at a temperature much lower than  
 526 that of the nuclei, but still high enough for the orbitals to quickly relax as the equation of mo-  
 527 tion proceeds. The new orbitals and their dynamics can then be defined by the Lagrangean  
 528 equation:<sup>105</sup>

$$L = \mu \sum_i f_i \int d\mathbf{r} |\psi_i(\mathbf{r}, t)|^2 + \frac{1}{2} \sum_{I=1}^N M_I \dot{\mathbf{R}}_I^2(t) - E[\psi(t), \mathbf{R}(t)] + \sum_{i,j} \Lambda_{ij} \left[ \int d\mathbf{r} \psi_i^*(\mathbf{r}, t) \psi_j(\mathbf{r}, t) - \delta_{ij} \right], \quad (13)$$

529 where  $\mu$  is an artificial kinetic energy term (discussed further in Refs. 106 and 107),  
 530  $\psi_x(\mathbf{r}, t)$  are the time-dependent Kohn-Sham orbitals, and  $\Lambda_{ij}$  contains a set of Lagrange  
 531 multipliers to implement the orthonormality constraint on the orbitals.

532 Potentials-based MD is not able to capture some of the finer details of the system dy-  
 533 namics that AIMD is able to, however, it is able to reach longer time- and length- scales,  
 534 providing information on long range diffusion properties. In classical potentials-based MD,  
 535 the atomic interactions are described using parameterised interatomic potentials. There are  
 536 multiple forms interatomic potentials can take, with their relevancy and accuracy relating  
 537 to the system and study being conducted. Atoms are either attracted or repelled by one an-

538 other based on their interatomic distance,  $r$ , to reduce their potential energy to a minimum,  
 539  $r_{eq}$ . This is known as a pair-interaction, which can be used to calculate the force,  $\vec{F}$ , acting  
 540 on each atom, given by:

$$\vec{F}_i = \sum_j \vec{\nabla} E(r_{ij}) \quad (14)$$

541 In complex systems, there is a “net effect” of the  $N$  surrounding atoms which can be  
 542 accounted for by calculating the vector summation of each pair interaction contribution.  
 543 Within ionic materials, the pair interactions are dominant and therefore it is computationally  
 544 tractable to truncate the expression after the first term<sup>108</sup> to give an approximation of the  
 545 pair potential. The charged nature of ions forms a coulombic interaction, where the relatively  
 546 slow decay of  $\frac{1}{r}$  as  $r$  increases, gives rise to the long range component of the potential. The  
 547 general term for the total potential can therefore be written as:

$$E(r_{ij}) = \frac{Q_i Q_j}{4\pi\epsilon_0 r_{ij}} + \Phi_{sr}, \quad (15)$$

548 where  $i$  and  $j$  are ions of charge  $Q_i$  and  $Q_j$  at a distance of  $r_{ij}$ , and  $\epsilon_0$  is the permittivity  
 549 of free space.  $\Phi_{sr}$  is used to denote the remaining short-range interactions.

550 For ionic solids, including cathode materials, a common choice for an interatomic po-  
 551 tential is a Coulomb-Buckingham potential,<sup>109</sup> derived from the Born model of the ionic  
 552 solid,<sup>110,111</sup> where the potential energy of the system can be expressed as:

$$E(r_{ij}) = \sum_{ij} \frac{Q_i Q_j}{4\pi\epsilon_0 r_{ij}} + \sum_{ij} A \exp\left(\frac{-r_{ij}}{\rho}\right) - C r_{ij}^{-6}, \quad (16)$$

553 where,  $A$ ,  $\rho$ , and  $C$  are constants.

554 MD simulations can be performed using a range of ensembles, with the most commonly  
 555 used being microcanonical (NVE), canonical (NVT), and isothermal-isobaric (NPT) ensem-  
 556 bles.<sup>112–114</sup> Here, the number of atoms (N), volume (V), energy (E), temperature (T), and  
 557 pressure (P) are conserved within the respective ensembles. Within the NVT and NPT

558 ensembles the energy of endothermic and exothermic processes is exchanged with a ther-  
559 mostat. A variety of thermostat algorithms are available, with some of the most popular  
560 methods including the Nosé-Hoover, Berendsen, and Andersen thermostats.<sup>112-114</sup> For NPT  
561 ensembles, a barostat is also applied to control pressure.

562 The choice between AIMD and potentials-based MD is a trade-off between computational  
563 cost, accuracy, and transferability. AIMD is highly accurate, however, it is computationally  
564 expensive and scales poorly ( $> O(N^3)$ ), making reachable system sizes and timescales rel-  
565 atively small ( $<1000$  atoms,  $\sim 100$  ps). On the other hand, potentials-based MD is less  
566 computationally expensive and can be applied to much larger system sizes, up to millions  
567 of atoms, with longer reachable time scales in the range of nanoseconds. However, the  
568 potentials-based approach is generally less accurate, as developing an interatomic potential  
569 which is sufficiently accurate enough to describe the specific system chemistry is challeng-  
570 ing. The development of interatomic potentials is discussed in greater detail in section 2.2.2.  
571 More recently, development of linear-scaling DFT approaches, as discussed in section 2.1.2,  
572 has worked towards reducing this trade-off.

## 573 **2.2 Method Development**

### 574 **2.2.1 Continuum models of electrolyte solutions within Density Functional The-** 575 **ory**

576 Electrode-electrolyte interfaces are an important part of LiBs and an area of active re-  
577 search.<sup>115,116</sup> The complexity of the structure and formation of electrical double layers at  
578 the interface has hindered the understanding of important electrochemical processes. While  
579 DFT-based electronic structure methods have been successfully used to study the solid-state  
580 physics in the bulk electrodes of LiBs, they are inadequate to describe the liquid state,  
581 which lacks structural order. This has led to rapid development of methods to describe the  
582 electrode-electrolyte interfaces.<sup>117</sup>

583 The liquid state can be described mainly via explicit solvation,<sup>118</sup> implicit solvation,<sup>119</sup>

584 or both.<sup>120</sup> In the former, the surrounding solvent and electrolyte molecules are considered  
 585 at the same level of chemical accuracy as the electrode atoms. The surrounding solvent and  
 586 electrolyte molecules can not only neutralise the excess charge on the electrode surface, but  
 587 also form bonds and adsorb on the electrode surface.<sup>121–123</sup> The addition of a large number of  
 588 solvent and electrolyte molecules to describe the liquid state drastically increases the config-  
 589 uration degrees of freedom. Sampling this large configurational space is computationally  
 590 demanding and often leads to loss of focus on the main region of interest: the interface.  
 591 While consideration of the first bonding layer of explicit solvent and electrolyte molecules  
 592 is necessary to describe the local effects of bonding and electric field,<sup>124</sup> the degrees of free-  
 593 dom of the non-participating solvent and electrolyte molecules far away can be averaged out  
 594 via an implicit model of the electrolyte solution.<sup>125,126</sup> The electrostatic potential in these  
 595 hybrid quantum-continuum models is obtained from the solution of the Poisson-Boltzmann  
 596 equation (P-BE).<sup>127</sup> Recently, many DFT codes have integrated P-BE based continuum  
 597 models.<sup>66,128–135</sup>

598 The continuum electrolyte ions with space-dependent concentrations,  $c_i(\mathbf{r})$ ,  $i = 1 \dots p$ ,  
 599 and charges,  $\{z_i\}$ , create a mobile electrolyte density,  $\rho_{\text{mob}}(\mathbf{r}) = \sum_{i=1}^p z_i c_i(\mathbf{r})$ , which interacts  
 600 with the quantum charge density,  $\rho(\mathbf{r})$ , within a mean-field electrostatic potential,  $\nu(\mathbf{r})$ . This  
 601 effect can be included in standard DFT by extending the standard free energy functional to  
 602 include the mean-field electrostatic potential,  $\nu(\mathbf{r})$ , and the mobile charge concentrations,  
 603  $c_i(\mathbf{r})$ , as:<sup>135</sup>

$$E[\rho(\mathbf{r})] \rightarrow \Omega[\rho(\mathbf{r}), \nu(\mathbf{r}), c_i(\mathbf{r})] \quad (17)$$

604 The variation of the free energy functional with the electrostatic potential,  $\nu(\mathbf{r})$ , gives  
 605 the P-BE:

$$\nabla \cdot [\varepsilon(\mathbf{r}) \nabla \nu(\mathbf{r})] = -4\pi [\rho(\mathbf{r}) + \rho_{\text{mob}}(\mathbf{r})] \quad (18)$$

606 The P-BE not only includes the quantum charge density,  $\rho(\mathbf{r})$ , as in standard DFT  
 607 calculations in vacuum, but also the effect of the solvent in terms of a continuum dielectric  
 608 with permittivity function,  $\varepsilon(\mathbf{r})$ , and mobile charge density of electrolyte ions,  $\rho_{\text{mob}}(\mathbf{r})$ . The  
 609 permittivity function is chosen as a smooth function with value varying from 1 in the quantum  
 610 region to  $\varepsilon^\infty$  in the solvent region:<sup>131</sup>

$$\varepsilon(\mathbf{r}) = 1 + (\varepsilon^\infty - 1) s(\mathbf{r}), \quad (19)$$

611 where  $s(\mathbf{r})$  is a smooth interface function varying from 0 in the quantum region to 1  
 612 in the solvent. Several choices for the interface function have been discussed by Andreussi  
 613 et al..<sup>136</sup> The variation of the free energy functional with ion concentrations,  $c_i(\mathbf{r})$ , gives the  
 614 Boltzmann expression for ionic concentrations:

$$c_i(\mathbf{r}) = c_i^\infty \lambda(\mathbf{r}) \exp\left(-\frac{z_i \nu(\mathbf{r})}{k_B T} + \frac{\mu_i^{\text{ex}}}{k_B T}\right), \quad i = 1 \dots p, \quad (20)$$

615 where  $\{c_i^\infty\}$  and  $\{\mu_i^{\text{ex}}\}$  are the bulk concentrations and excess chemical potentials of  
 616 the electrolyte ions. The mobile charge density of electrolyte ions,  $\rho_{\text{mob}}(\mathbf{r}) = \sum_{i=1}^p z_i c_i(\mathbf{r})$ , is  
 617 shown schematically in Fig. 5. As the interaction with mobile electrolyte charge is purely  
 618 electrostatic and excludes any quantum effects such as Pauli repulsion, there is a problem  
 619 of electrolyte charge accumulating infinitely close to the electrode. In order to prevent this  
 620 problem, the models include an electrolyte accessibility function,  $\lambda(\mathbf{r})$ , which varies from 0  
 621 near the electrode to 1 in the bulk electrolyte region.<sup>133,137,138</sup> One of the ways of defining  
 622 such an accessibility function is as a product of atom-centred interlocking spheres of error  
 623 functions:<sup>135</sup>

$$\lambda(\mathbf{r}) = \prod_k^{n_{\text{atoms}}} \frac{1}{2} \left[ 1 + \operatorname{erf} \left( \frac{|\mathbf{r} - \mathbf{R}_k| - R_k^{\text{solute}}(\rho_e^\lambda) - R_k^{\text{solvent}}}{\sigma} \right) \right], \quad (21)$$

624 where  $\sigma$  is a smearing width ( $0 < \sigma < 0.5 a_0$ ). This description of the ion exclusion region  
 625 derives from a physical picture: the electrolyte ions are moved away from the quantum

$$\nabla \cdot [\varepsilon(\mathbf{r})\nabla v(\mathbf{r})] = -4\pi[\rho(\mathbf{r}) + \rho_{mob}(\mathbf{r})]$$

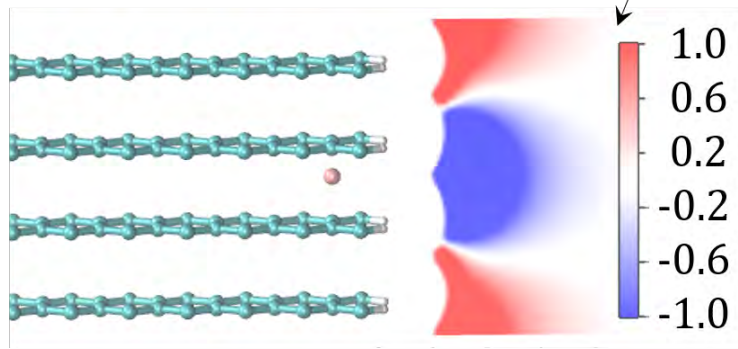


Figure 5: DFT simulation of a lithiated graphite interface in contact with an implicit electrolyte solution, based on the solution of the Poisson-Boltzmann equation. Reprinted with permission from Ref. 135. Copyright 2020 American Chemical Society.

626 electrode, up to a distance that incorporates not only the size of the species but also a  
 627 solvation shell radius around the electrolyte ions. The species size can be described in terms  
 628 of an isoradius of electronic density,  $\rho_e^\lambda$ . The solvation shell radius,  $R_k^{\text{solvent}}$ , depends on the  
 629 solvent and is added to the species size, to calculate the overall radius of interlocking spheres  
 630 for the accessibility function.

631 The electrostatic potential,  $\nu(\mathbf{r})$ , obtained from equation 18 is due to the entire electrode-  
 632 electrolyte interface, where the electrode is treated quantum mechanically and the electrolyte  
 633 solution as a continuum. Variation of the free energy functional with electronic density gives  
 634 the Kohn-Sham equations in the total electrostatic potential, with additional terms for the  
 635 variation of interface function with electronic density.<sup>130,139</sup> Solvation energies are defined  
 636 as:<sup>130,133</sup>

$$\Delta\Omega = \Omega - \Omega_{\text{vac}} - \Omega_{\text{electrolyte}} \quad (22)$$

$$= \Omega[\rho(\mathbf{r}), \{c_i(\mathbf{r})\}, \nu(\mathbf{r})] \quad (23)$$

$$- \Omega[\rho_{\text{vac}}(\mathbf{r}), \{c_i(\mathbf{r})\} = 0, \nu_{\text{vac}}(\mathbf{r})]$$

$$- \Omega[\rho(\mathbf{r}) = 0, \{c_i(\mathbf{r})\} = \{c_i^\infty\}, \nu(\mathbf{r}) = 0],$$

637 where the respective terms can be computed as the total free energy in the electrolyte  
 638 solution, the total free energy in vacuum, and the total free energy of the pure electrolyte.<sup>135</sup>  
 639 The electrolyte effect on solvation energies can be computed as the difference of solvation  
 640 energy in electrolyte at  $\{c_i^\infty\}$  and solvation energy in pure solvent at  $\{c_i^\infty = 0\}$ :

$$\Delta\Delta\Omega = \Delta\Omega[\{c_i^\infty\}] - \Delta\Omega[\{c_i^\infty = 0\}] \quad (24)$$

$$= \Omega - \Omega_{\text{sol}} - \Omega_{\text{electrolyte}}, \quad (25)$$

641 where the respective terms are computed as the total free energy in the electrolyte solu-  
 642 tion,  $\{c_i^\infty\}$ , the total free energy in pure solvent,  $\{c_i^\infty = 0\}$ , and the total free energy of the  
 643 pure electrolyte.

## 644 2.2.2 Fitting Potentials for Classical Molecular Dynamics

645 The development of sufficiently accurate interatomic potentials for a specific chemistry is  
 646 quite challenging. Interatomic potentials are traditionally based on mathematical functions  
 647 that have been parameterised using experimental and/or electronic structure methods de-  
 648 rived data.<sup>109,140</sup> There are a limited number of codes available with the explicit purpose or  
 649 functionality for fitting potentials. Here, we present several available codes and discuss the  
 650 complexities and considerations involved in deriving accurate interatomic potentials.

651 **GULP**,<sup>141</sup> the General Utility Lattice Program, is a widely used code for performing  
 652 a variety of simulation types on materials using boundary conditions.<sup>114</sup> Within this code,  
 653 there is the functionality to fit interatomic potentials to either experimental measurements  
 654 or electronic structure methods data.<sup>142</sup> GULP is capable of simultaneous fitting to multiple  
 655 structures and can also handle core-shell models (which capture polarisation of atoms).

656 **Atomicrex**,<sup>143</sup> **dftfit**,<sup>144</sup> and **potfit**<sup>145,146</sup> are codes designed to fit potentials to elec-  
 657 tronic structure methods data. Each of these codes have different levels of flexibility and



658 their own unique features, however, a joint limitation is the ability to fit empirical potentials  
659 is limited to rigid ions and cannot fit a core-shell model.

660 During the process of developing potentials for  $\text{Li}(\text{Ni}_x\text{Mn}_y\text{Co}_z)\text{O}_2$  (NMC), and its ternary  
661 system  $\text{LiNiO}_2$ , it was found that none of these codes are able to accurately produce poten-  
662 tials for these materials. The complex nature of Ni chemistry in a layered oxide material  
663 is challenging, and to the best of our knowledge, no interatomic potentials exist for  $\text{Ni}^{3+}$ .  
664 Oxide systems are widely described using a Buckingham potential form, as given in equa-  
665 tion 16, and for layered structures, including NMC and its ternary systems, variations of the  
666 Buckingham potentials are presented. Some use rigid ion models,<sup>147–150</sup> others use core-shell  
667 models,<sup>147,151–156</sup> and a mixture of formal and partial charges have been implemented. With  
668 literature in disagreement over which variation of the Buckingham potential is the most  
669 accurate for representing the system, a code capable of fitting different permutations of the  
670 Buckingham potential is needed.

671 Structure and composition of a material are crucial to determine the functional form  
672 of the potential. For example, for a layered structure such as NMC-811, it is crucial to  
673 consider polarisability. Polarisability is described in classical (potentials-based) MD using  
674 a core-shell model. There are predominately two types of core-shell models: the relaxed  
675 (massless shells) model<sup>157</sup> and the dynamic (adiabatic shells) model.<sup>158</sup> The adiabatic shell  
676 model is more widely used in literature, including all core-shell related cited works in this  
677 section,<sup>147,151–156</sup> for calculating long trajectories, as it is less computationally taxing. In the  
678 adiabatic shell model, a fraction of the atomic mass is assigned to the shell. There is no  
679 defined fraction size; however, placing 10 % of the atomic mass on the shell is considered  
680 common practice.<sup>112,113</sup> An additional consideration for using a core-shell model is the sepa-  
681 ration of the formal atomic charge across the core and shell. However, determined numerical  
682 values of the core-shell charge separation are inconsistent.<sup>156,159–162</sup> In some systems, where  
683 there is high polarisability, such as in LMO, the short-range interactions are overwhelmed  
684 by the longer-range coulombic term. In these cases, the system charges can be scaled to

685 increase the influence of the short-range interactions, and are termed partial charges. The  
 686 scaling factor is system dependent therefore no specific value is ideal in all cases, however 60  
 687 % formal charge is commonly adopted.<sup>163</sup>

688 POtential Parameter Optimisation for Force-Fields (PopOff),<sup>164</sup> a code developed within  
 689 the Faraday institution, was specifically created for fitting different permutations of the  
 690 Buckingham potential. It is unique in its ability to consider all the factors discussed above  
 691 (rigid ion/core-shell/charge separation/charge scaling) in a modular design, allowing flexible  
 692 fitting to suit individual systems. The code has been developed in Python, using a training  
 693 set consisting of DFT derived data (*DFT*) and utilising the Large-scale Atomic/Molecular  
 694 Massively Parallel Simulator (LAMMPS).<sup>113</sup> The potential is fitted by minimising the mean  
 695 squared error ( $\chi^2$ ) between the DFT forces,  $F^{DFT}$ , and stress tensors,  $\sigma^{DFT}$ , and those  
 696 produced using the fitted interatomic potential ( $F^{IP}$ ,  $\sigma^{IP}$ ), defined as:

$$\chi^2 = \sum_{i,\alpha}^N \frac{(F_{i,\alpha}^{DFT} - F_{i,\alpha}^{IP})^2}{N_i} + \sum_{\beta} \frac{(\sigma_{\beta}^{DFT} - \sigma_{\beta}^{IP})^2}{6} \quad (26)$$

697 This modular design allows the construction of a Buckingham potential able to accom-  
 698 modate the considerations and complexities of different systems. PopOff also allows for  
 699 individual parameters to be fixed/excluded from the fit, lowering the fit dimensionality and  
 700 computational cost. This is particularly useful for excluding dispersion terms, which are  
 701 known to be zero or close to, for a range of elements.<sup>161,165</sup>

## 702 2.3 Calculating observable properties

### 703 2.3.1 Equilibrium voltage

704 The equilibrium cell voltage,  $E(x)$ , where  $0 < x < 1$  denotes the fraction of sites occupied  
 705 by lithium in the intercalation host, is a fundamental thermodynamic quantity related to  
 706 the energy density of a cell.<sup>9,166,167</sup>  $E(x)$  can be probed through experimental measurements  
 707 of the open circuit voltage (OCV), that is, the voltage between the cathode and anode

708 terminals under zero current flow, assuming that the system has been given sufficient time  
 709 for the OCV to relax to the value of  $E(x)$ . Computationally, the equilibrium cell voltage can  
 710 be modelled through DFT calculations at  $T = 0$  K;<sup>9,166,167</sup> the effect of thermal fluctuations  
 711 can be included by modelling using Monte Carlo (MC) calculations.<sup>89,90</sup>

712 There is a fundamental relationship between the Gibbs free energy of lithium dissolution  
 713 into the host,  $G(x)$ , the chemical potential of Li intercalation in the host,  $\mu(x)$ , and the cell  
 714 voltage  $E(x)$ . Knowledge of  $G(x)$  also provides information about the evolution of the phase  
 715 behaviour dependent on the fraction of intercalated Li,<sup>9,76,167,168</sup> enabling the construction  
 716 of phase diagrams from DFT. The relationships are represented schematically in Figure 6.  
 717 In essence: the tangent to the free energy curve,  $G(x)$ , allows  $\mu(x)$  and hence the cell voltage  
 718 to be obtained. Alternatively, integration of  $\mu(x)$  can be used to derive free energy curves.

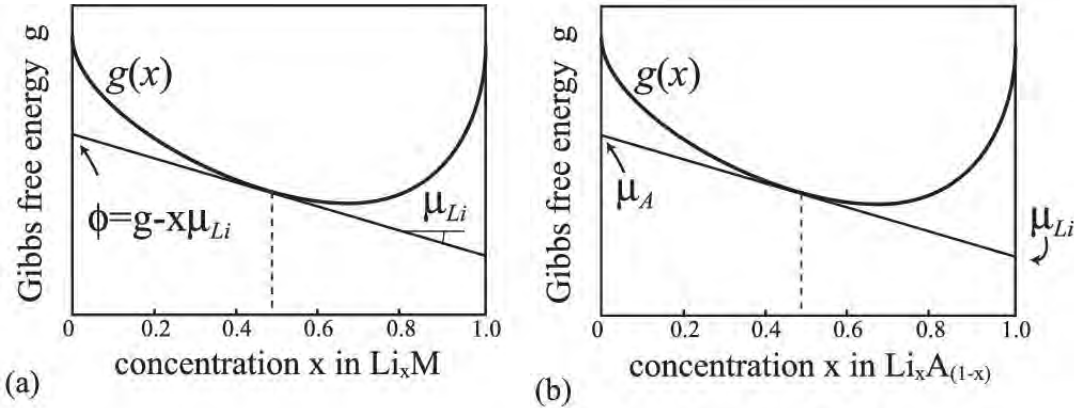


Figure 6: Representation of the connection between the Gibbs free energy,  $G(x)$ , the lithium chemical potential  $\mu(x)$  in (a) an intercalation electrode and (b) an alloy electrode. Reprinted with permission from Ref. 9. Copyright 2020 American Chemical Society.

719 In the case of a Li-ion cell, the equilibrium cell voltage,  $\phi(x)$ , and the chemical potential  
 720 of intercalated Li,  $\mu(x)$ , are related by:

$$\phi(x) = -\frac{\mu(x) - \mu_{\text{Li}}^{\text{ref}}}{nF}, \quad (27)$$

721 where  $\mu_{\text{Li}}^{\text{ref}}$  is the chemical potential of the reference electrode,  $n$  is the number of electrons  
 722 transferred per formula unit of intercalation host ( $n = 1$  for Li-ion cells), and  $F$  is the Faraday

723 constant. The most convenient reference potential, both from the point of view of simulations  
 724 and for comparison with experimental measurements of Li-ion half cells, is the bcc metallic  
 725 Li anode. With a suitable choice of units for all potentials ( $\mu$  expressed in eV per formula  
 726 unit of intercalation host), equation 27 can be written much more simply as:<sup>167</sup>

$$\phi(x) = -\mu(x) \quad (28)$$

727 The intercalated Li chemical potential is defined by:

$$\mu(x) = \left( \frac{\partial \underline{G}(x)}{\partial N_{\text{Li}}} \right)_{p, T, N_{\text{host}}} = \left( \frac{\partial G(x)}{\partial x} \right)_{p, T, N_{\text{host}}}, \quad (29)$$

728 where  $\underline{G}$  is the absolute (i.e. extensive) Gibbs free energy of Li dissolution into the host,  
 729  $p$  is pressure,  $T$  is the absolute temperature, and  $N_{\text{host}}$  and  $N_{\text{Li}}$  are the number of host and  
 730 lithium atoms in the system, respectively. The subscripts  $p$ ,  $T$ , and  $N_{\text{host}}$  will be implicitly  
 731 assumed to be constant from now on and dropped, to simplify notation.

732 Similarly, it is well known that:

$$\frac{\partial G(x)}{\partial x} = \frac{\partial H(x)}{\partial x} - T \frac{\partial S(x)}{\partial x}, \quad (30)$$

733 where  $H(x)$  and  $S(x)$  are the enthalpy and entropy, respectively, per formula unit of host  
 734 material.

735 We can use equations 28, 29, and 30 to get  $\partial G/\partial x = -E_{\text{OCV}}$ , then, taking the derivative  
 736 of the OCV with respect to  $T$  and using the chain rule, we obtain:

$$\frac{\partial S(x)}{\partial x} = \frac{\partial E_{\text{OCV}}(x)}{\partial T} \quad (31)$$

737 and so:

$$\frac{\partial H(x)}{\partial x} = T \frac{\partial E_{\text{OCV}}(x)}{\partial T} - E_{\text{OCV}}(x) \quad (32)$$

738 Due to the units of electron Volts (eV) per formula unit for the potentials  $H(x)$  and  
739  $TS(x)$ , i.e. as in the conversion between equations 27 and 28, the usual factors of  $F$  have  
740 been omitted. In this way it is possible to simulate not only the equilibrium voltage, but split  
741 its contributions into enthalpy and entropy components. Both components can be exper-  
742 imentally measured<sup>91,93,100,169,170</sup> and modelled through MC or mean field methods,<sup>89,91–93</sup>  
743 providing additional properties for model validation purposes and to check the temperature  
744 dependence of those properties is modelled accurately. A good thermodynamic basis can  
745 then be used to derive dynamic properties, as outlined in the subsequent sections.

### 746 2.3.2 Activity coefficients of electrolytes

747 The activity coefficients of electrolytes ( $\gamma_j$ ,  $j = 1 \dots p$ ) describe the thermodynamics of non-  
748 ideal solutions.<sup>171</sup> The activity coefficient of electrolytes can be computed from DFT+P-BE  
749 models, as described in section 2.2.1, by computing the electrolyte effect on solvation energies,  
750  $\Delta\Delta\Omega$ :<sup>130,135</sup>

$$\ln \gamma_j = \frac{\Delta\Delta\Omega_j [\{c_i^\infty\}]}{k_B T}, \quad j = 1 \dots p \quad (33)$$

751 For an electrolyte dissociating into  $p$  species, the mean activity coefficient can be calcu-  
752 lated as:

$$\ln \gamma_{\text{mean}} = \frac{1}{p} \sum_{j=1}^p \ln \gamma_j \quad (34)$$

### 753 2.3.3 Diffusion coefficients

754 The *diffusion coefficient* is a term used to describe the rate of ion transport within a system.  
755 This term, however, has been used in literature to express several forms of diffusion, which  
756 characterise diffusion in a material in different ways. Here, we describe several commonly  
757 used forms of *diffusion coefficient*, in context of where they are used, focusing on bulk  
758 diffusion. Heitjans and Kärger gives a detailed description of diffusion along grain boundaries

759 and along surfaces (chapters 7 and 8).<sup>172</sup>

760 Ionic transport within the electrodes and electrolyte plays a vital role in the kinetics of  
761 a battery. It can be described fundamentally with flux expressions that relate ion fluxes to  
762 chemical or electrochemical potential gradients. This is related by Fick's first law, where the  
763 diffusion flux,  $\mathbf{j}$ , is described using the gradient of the concentration,  $c$ , via:

$$\mathbf{j} = -\mathcal{D}\nabla c, \quad (35)$$

764 where  $\mathcal{D}$  is denoted as the diffusion coefficient tensor or diffusivity tensor and implies  
765 that  $\mathcal{D}$  varies with direction. In general, the diffusion flux and concentration gradient are  
766 not always antiparallel. They are antiparallel for isotropic mediums. Heitjans and Kärger  
767 discusses this in more detail.<sup>172</sup>

768 Steady state methods for measuring diffusion coefficients, like the permeation method, are  
769 directly based on Fick's first law.<sup>173</sup> In non-steady states, the diffusion flux and concentration  
770 vary with time,  $t$ , and position  $x$ , and a balanced equation is necessary. For particles which  
771 undergo no reaction this become the continuity equation:

$$\frac{\partial c}{\partial t} + \nabla \cdot \mathbf{j} = 0 \quad (36)$$

772 Combining equations 35 and 36 leads to Fick's second law, also called the diffusion  
773 equation, which predicts how diffusion causes the concentration to change with time:

$$\frac{\partial c}{\partial t} = \nabla \cdot (\mathcal{D}\nabla c) \quad (37)$$

774 In diffusion studies with trace elements the material composition does not practically  
775 change and  $\mathcal{D}$  is independent of the tracer concentration, presenting a concentration-independent  
776 diffusion coefficient. For diffusion in multiple dimensions Fick's second law becomes:<sup>174</sup>

$$\frac{\partial c}{\partial t} = \mathcal{D}\nabla^2 c \quad (38)$$

777 The temperature dependence of the diffusion coefficient is often described empirically by  
778 an Arrhenius relation:

$$\mathcal{D} = \mathcal{D}_0 \cdot \exp\left(-\frac{E_A}{k_B T}\right), \quad (39)$$

779 where  $E_A$  is the activation energy for the mass transport,  $D_0^T$  is the pre-exponential  
780 factor,  $k_B$  is the Boltzmann constant, and  $T$  is the temperature.

781 From the microscopic point of view, the tracer diffusion coefficient can be defined by the  
782 Einstein-Smoluchowski relation:<sup>175,176</sup>

$$\mathcal{D} = \lim_{t \rightarrow \infty} \frac{\langle r^2(t) \rangle}{2dt}, \text{ where } \langle r^2(t) \rangle = \langle (x(t) - x_0)^2 \rangle, \quad (40)$$

783 where,  $\langle r^2(t) \rangle$  is the mean square displacement (MSD) of the particles after time  $t$  and  
784  $d$  is the dimensionality of the movement. This is also known as the *self diffusion coefficient*  
785 and is the main approach used to calculate the diffusion coefficient in kMC and MD from  
786 the atom trajectories. Van der Ven et al. discusses in greater detail.<sup>9</sup>

787 In atomistic modelling, diffusion coefficients can also be calculated using other approaches,  
788 such as Green-Kubo. The Green-Kubo approach is linked to the Einstein-Smoluchowski re-  
789 lation approach, equation 40. Both approaches assume that particle dynamics can be well  
790 approximated by Brownian motion. As described in equation 40, Brownian motion of inde-  
791 pendent particles can be expressed by the MSD of a particle proportional to time. This can  
792 also be termed as the integral of the velocity. The Green-Kubo approach is derived from the  
793 integration of the velocity (or current) autocorrelation function. Assuming that dynamics  
794 is ergodic, the diffusion coefficient can be calculated using a linear fit to the velocity auto-  
795 correlation function. Averaging is applied to this, for example, a time average for a selected  
796 particle type, a sample average, or an ensemble average.

### 797 2.3.4 Vibrational and Thermal Properties

798 While MD simulates the evolution of a chemical system over time, lattice dynamics is an  
799 approach that models the underlying vibrations. In crystalline solids, extended vibrations  
800 can be described as phonons with a characteristic frequency and wavevector,  $\omega(q)$ . A unit  
801 cell with  $N$  atoms contains  $3N$  phonon modes. The theory of phonons provides a direct  
802 connection between microscopic atomic motion and macroscopic properties including specific  
803 heat capacity, IR and Raman spectra, and thermal expansion.<sup>177–179</sup>

804 While assuming that phonons are harmonic simplifies the theoretical description, it is  
805 necessary to include anharmonic effects to describe phenomena such as heat transport. The  
806 lattice thermal conductivity,  $\kappa$ , depends on the lifetime of each phonon, i.e. how long it  
807 persists before decaying, which is an anharmonic process. Formally, the thermal conductivity  
808 given by the product of the modal heat capacity, ( $C_V$ ), the group velocity,  $v$ , and the phonon  
809 mean free path,  $v \times \tau$  (where  $\tau$  is the phonon lifetime). The macroscopic  $\kappa$  is obtained by  
810 summing over band indices,  $v$ , averaging over wavevectors,  $q$ , and normalising by the unit  
811 cell volume:

$$\kappa = \frac{1}{NV_0} \sum_{qv} C_{V,qv} v_{qv} \otimes v_{qv} \tau_{qv}, \quad (41)$$

812 where  $N$  is the number of unit cells in the crystal (number of wavevectors in the Brillouin  
813 zone summation) and  $V_0$  is the volume of the crystallographic unit cell.

814 The heat capacity and group velocity can be extracted from the harmonic phonons, which  
815 are readily accessible from calculations based on electronic structure methods or potentials-  
816 based potential methods. The lifetime of each phonon mode is more demanding to compute  
817 and is often performed within a many-body perturbation theory expansion of phonon-phonon  
818 interactions. One approximation is to consider only the leading term of three-phonon cre-  
819 ation and annihilation.<sup>180</sup> However, higher-order processes may limit the lifetimes, depending  
820 on the material and temperature. There are a range of packages available to compute the



821 terms in equation 41 including PHONO3PY<sup>180</sup> (recently applied to LiCoO<sub>2</sub> and NMC cath-  
822 odes),<sup>181,182</sup> ALAMODE,<sup>183</sup> and SHENGBTE.<sup>184</sup>

## 823 **3 Anodes**

### 824 **3.1 Introduction**

825 Critical to the success of lithium-ion batteries (LiBs) was the development of graphite-based  
826 anodes. Graphite proved to be ideal for this application, due to its low (de)-intercalation  
827 potential, only slightly higher than that of metallic lithium, and high theoretical gravimetric  
828 capacity of 372 mAh g<sup>-1</sup>. However, many key degradation mechanisms in present-day LiBs  
829 that lead to their eventual failure, including cracking/reformation of the solid-electrolyte  
830 interphase (SEI) and lithium plating, are still intimately connected with graphite-based  
831 anodes.<sup>185,186</sup> The understanding of these mechanisms is still far from complete and leads  
832 to complex, non-linear degradation behaviour that is difficult to predict,<sup>187</sup> motivating the  
833 development of multiscale models with a descriptive and predictive capability. A critical  
834 starting point for these models is a physically accurate atomistic description of the graphite  
835 and its interface with organic electrolytes.

836 The possibility to form Li-graphite intercalation compounds (Li-GICs), also known as  
837 “stages”, up to a stoichiometry of LiC<sub>6</sub>, was known in 1975, albeit at that time it was only  
838 possible to form them by heat treating powders.<sup>188–190</sup> Initial attempts to electrochemi-  
839 cally intercalate lithium into graphite resulted in co-intercalation of the organic solvent and  
840 exfoliation of the graphite.<sup>191</sup> In 1983, Yazami and Touzain reported the first successful  
841 intercalation into graphite using a solid polymer electrolyte.<sup>192</sup> Fong et al. found that re-  
842 versible lithium intercalation could be achieved in liquid organic electrolytes using ethylene  
843 carbonate (EC) as part of the solvent, which finally enabled the formation of a stable SEI on  
844 the graphite surface.<sup>193</sup> Mixtures of EC and dimethyl carbonate (DMC) were developed by  
845 Tarascon and Guyomard in 1993<sup>194</sup> and present-day graphite-based LiBs are still primarily

846 based on this electrolyte mixture. The key challenge was finding a solvent chemistry that  
847 provided sufficient ionic conductivity, did not decompose significantly at the  $\sim 4$  V cathode  
848 potential, while also avoiding co-intercalation into the graphite and producing a stable SEI  
849 on its surface. Further incremental improvements in performance have since been achieved  
850 through additional additives and, more recently, the inclusion of small amounts of silicon in  
851 the anode as a secondary material.

852 This section predominantly focuses on graphite, since it remains the primary anode elec-  
853 trode material in the majority of commercial lithium ion (Li-ion) cells.<sup>14</sup> Here, the experi-  
854 mentally confirmed Li-graphite stages and the nomenclature necessary for atomistic models  
855 of bulk behaviour are defined. Atomistic modelling in the graphite bulk is outlined, in-  
856 cluding both thermodynamic and kinetic properties. The key graphite surfaces relevant  
857 to understanding the initial intercalation are described, then moving to modelling at the  
858 graphite edges and the interface with the electrolyte. Throughout, it is shown how these  
859 models enable quantitative understanding of the physical mechanisms of Li intercalation  
860 in the graphite bulk, the initial insertion at the graphite edges, and the interface between  
861 graphite and the electrolyte. Along the way, the key experimentally observable parameters  
862 are outlined, showing success stories of atomistic models to not only quantify and describe  
863 those parameters but to also predict new behaviour. In some cases, quantitative disagree-  
864 ment between model and experimental observations is also informative and can create new  
865 research directions. Work linking atomistic and continuum models is presented in the case  
866 of the technologically important SEI. Given the emerging importance of C/Si and C/SiO<sub>x</sub>  
867 composites in commercial anode materials, some of the challenges in atomistic modelling of  
868 Si and related materials are summarised at the end. In the outlook, key remaining challenges  
869 are presented for modelling not only graphite, but also next generation materials such as  
870 silicides. Challenges related to metallic Li formation on graphite anodes, and the use of  
871 metallic Li as an anode material, are also summarised in the outlook.

## 872 3.2 Bulk Properties

### 873 3.2.1 Graphite structure and Li-graphite stages

874 Graphite possesses a layered structure with carbon atoms forming a network of hexagons in  
875 each layer. The carbon atoms located within one layer are covalently bonded to each other,  
876 whereas the weak interlayer binding arises from the dispersion or van der Waals (vdW)  
877 interactions.<sup>76,188,189,189,195–197</sup> The lowest energy stacking of the carbon layers is AB stacked  
878 (Figure 7b), but synthesised graphite structures also contain a small amount of rhombohedral  
879 (ABC-stacked) domains.<sup>198</sup>

880 Li-graphite stages, also known as lithium-graphite intercalation compounds (Li-GICs),  
881 are lithium concentration-dependent structures of various stoichiometries.<sup>188,189,195,197,199</sup> In  
882 Li-GICs, Li atoms form a 2D hexagonal ( $\sqrt{3} \times \sqrt{3}$ )R 30 ° superstructure, with Li atoms  
883 sitting directly above each other, as shown in Figure 7a. The stage number,  $n$ , denotes the  
884 number of graphene layers between each lithium-filled layer.<sup>188,195,197,200</sup> The experimentally  
885 confirmed stages adopt different stackings in the carbon host lattice, as shown in Figure 7.  
886 The standard nomenclature for GICs<sup>189</sup> denotes the carbon stacking and Li occupancies:  
887 periodic carbon layer stackings along the [001] axis are designated by uppercase letters  
888 separated by Greek lowercase letters, if Li is intercalated between planes. For instance, fully  
889 lithiated Stage I  $\text{LiC}_6$  ( $x = 1$ ) adopts  $A\alpha A\alpha A\alpha$  stacking.<sup>170,197,201</sup> Here  $\alpha$  denotes a lithium  
890 filled layer and  $x$  is the fraction of Li in  $\text{Li}_x\text{C}_6$  ( $0 \leq x \leq 1$ ).

891 Li-GICs vary not only in their lithium concentrations, but also in their carbon stackings.  
892 The current consensus of all known stages, including their carbon stackings and lithium  
893 stoichiometries, is tabulated in Table 1.

894 Experimental observation of these stages relies largely on probing the average interlayer  
895 carbon spacing through diffraction measurements. Probing the lithium orderings of Li-  
896 GICs through experimental techniques remains very difficult,<sup>71,91,197,207–209</sup> but as shown in  
897 section 3.2.3, atomistic techniques shed light on these orderings.

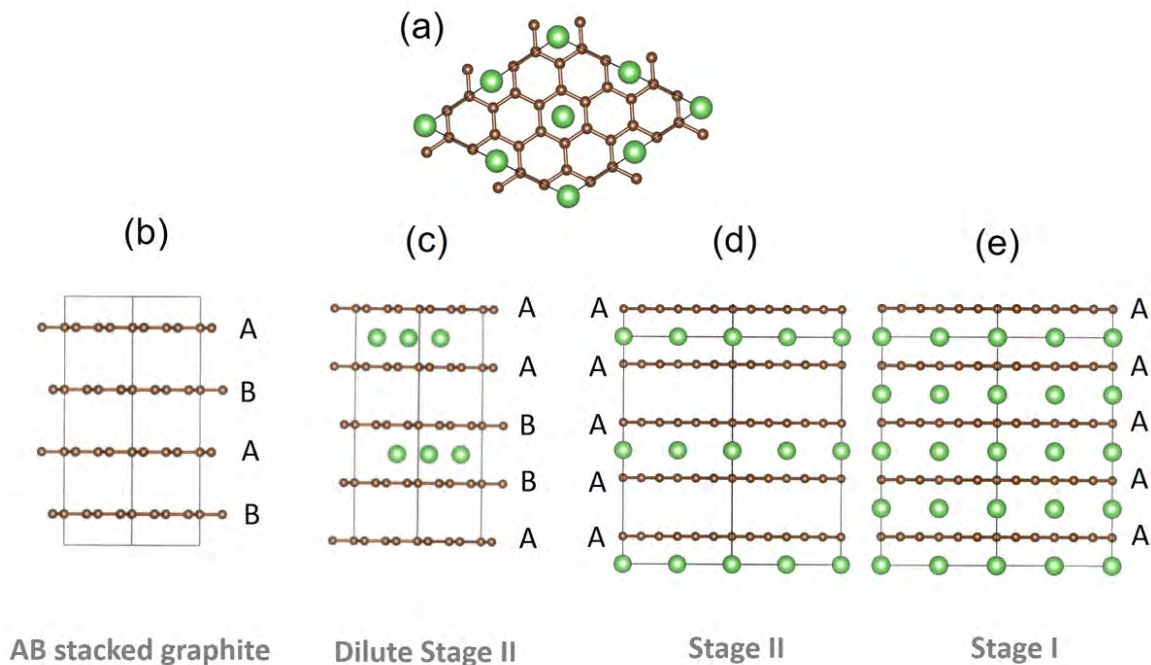


Figure 7: Structural representations of different carbon stackings in experimentally confirmed stages of graphite. (a) Top down view of carbon and lithium arrangements in Stages I and II. (b-e): side views, showing the layers occupied with Li and carbon stackings in (b) empty AB stacked graphite, (c)  $A\alpha AB\beta B$  stacked dilute Stage II, with  $\beta$  indicating a lithium layer translated with respect to  $\alpha$ , (d)  $A\alpha AA\alpha A$  Stage II and (e)  $A\alpha$  stacked Stage I. Green represent Li atoms, while the brown indicate C atoms. Reproduced from Ref. 71 - Published by The Royal Society of Chemistry.

898 Thermodynamic and kinetic properties of Li-GICs have been studied by considering  
 899 various structures of  $\text{LiC}_{6n}$  using Density Functional Theory (DFT),<sup>70,76,196,196,210–216</sup> mean  
 900 field,<sup>91,92,217</sup> canonical and grand canonical Monte Carlo (MC),<sup>76,218,219</sup> and kinetic Monte  
 901 Carlo (kMC) simulation techniques.<sup>76,102,103,214,220</sup> The rest of the section outlines electronic  
 902 structure based studies of experimentally measurable bulk thermodynamic properties, before  
 903 describing atomistic modelling of kinetic properties.

### 904 3.2.2 Equilibrium potential and measured open circuit voltage

905 Knowledge of the correct phase behaviour of an intercalation electrode is an important  
 906 pre-requisite to building a dynamic model of the intercalation process. One of the most

Table 1: Overview of carbon stackings and stoichiometries of Li-graphite stages from the literature, where Latin characters denote carbon stackings and Greek characters denote Li-filled layers.<sup>188,189,195,197,200,202–206</sup>

Stage	Stacking	$x$ in $\text{Li}_x\text{C}_6$
Stage I	$A\alpha A\alpha$	$x = 1$ ( $\text{LiC}_6$ )
Stage II	$A\alpha AA\alpha A$	$x = 0.5$ ( $\text{LiC}_{12}$ )
Dilute Stage II (IID)	$A\alpha AB\beta B$	$x \approx 0.33$ ( $\text{LiC}_{18}$ )
Stage III	$A\alpha AB/A\alpha ABA\alpha AC$	$x \approx 0.22$ ( $\text{LiC}_{27}$ )
Stage IV	Unknown	$x \approx 0.17$ ( $\text{LiC}_{36}$ )
Dilute Stage I (ID)	AB	$x \approx 0.083$ ( $\text{LiC}_{72}$ )
Graphite	AB	$x = 0$

907 directly measurable observables is the experimental open circuit voltage (OCV), which is  
 908 related to the equilibrium potential determinable from atomistic methods (c.f. Methods  
 909 section 2.3.1). The OCV is an important input parameter in continuum models and is also  
 910 used in control models, for example, to determine the state of charge of a battery within a  
 911 Battery Management System (BMS).<sup>221</sup> Inputting a polynomial fit to the experimental OCV  
 912 at an arbitrary temperature without physical meaning could lead to incorrect predictions of  
 913 temperature-dependent behaviour in these models. Therefore, to attain predictive, dynamic  
 914 models on longer length scales, atomistic models of the OCV and equilibrium potential are  
 915 important and can contribute to physically more robust and more predictive temperature  
 916 dependence in continuum and control models.<sup>9,166</sup>

917 In any intercalation electrode, ordered phases give rise to steps in the OCV. In the  
 918 lithium-graphite system, the ordered stages described in section 3.2.1 therefore give rise  
 919 to characteristic features in OCV versus  $x$  curves<sup>195,200</sup> as shown in Figure 8. The influ-  
 920 ence of the Li-graphite stages on the measured OCV at  $T \approx 25$  °C has been well charac-  
 921 terised,<sup>195,199,200,207–209,222–224</sup> although a more thorough study of the temperature dependence  
 922 of the OCV has only been conducted more recently.<sup>71</sup> Each OCV plateau represents a dif-  
 923 ferent two-phase equilibrium. At zero Kelvin, there is no contribution from configurational  
 924 entropy and each step represents a sudden transition between two different two-phase equi-  
 925 libria. This is the behaviour that can be captured using DFT code. The cluster expansion

926 framework, described in more detail in the Methods section 2.1.4, allows the accuracy of  
 927 DFT to be retained to explore configurational degrees of freedom. Thermal fluctuations can  
 928 be included by determining effective cluster interactions (ECIs) from fitting DFT data and  
 929 using these as parameters within an MC method (section 2.1.5). The entropy contribution  
 930 at temperature,  $T > 0$  K has the effect of smoothing out those steps,<sup>71,91,217,225</sup> which is  
 931 caused by some limited single phase solubility around the stoichiometric composition. This  
 932 can be seen in experimentally measured OCV profiles at  $T \approx 300$  K, such as the ones shown  
 933 in Figure 8.

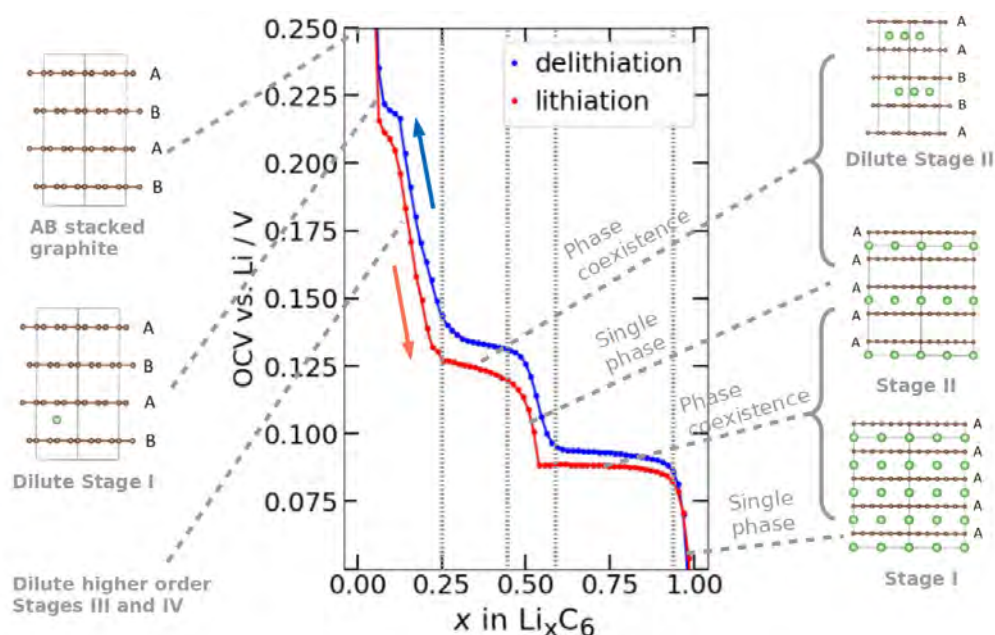


Figure 8: Illustration of OCV features of lithium in graphite using experimental data from ref. 91. Lithiation and delithiation behaviour is overlaid; labelled stages are linked to the lithiation profile, which is closer to the true equilibrium potential. Reproduced from Ref. 71 - Published by The Royal Society of Chemistry.

934 The equilibrium potential versus  $x$  can be modelled through atomistic techniques. For  
 935 example, Li-graphite phase diagrams were constructed and the equilibrium potential was  
 936 modelled by Persson et al.<sup>76</sup> They performed a cluster expansion of Li degrees of freedom  
 937 from total energy DFT calculations, by fixing the carbon stacking degrees of freedom. Those  
 938 degrees of freedom represent the host lattice stackings in the experimentally confirmed stages  
 939 shown in Figure 7. Typically, different cluster expansions are performed in Li-vacancy lattices

940 of the respective hosts,<sup>71,76,196</sup> to account for carbon stacking degrees of freedom with the  
941 result from a more recent work<sup>71</sup> represented in Figure 9a. Within this work, AA, AABB,  
942 and AB stackings of the host lattice were considered, representing all stages of order up  
943 to II (c.f. Figure 7). Reference states at  $x = 0$  and  $x = 1$  were used in AB and AA  
944 stackings, respectively, to linearly correct the free energy and thus obtain the formation  
945 energies at each lithium concentration. The convex hull over all stackings represents the  
946 lowest energy structure for a given  $x$  value. A common tangent construction between the  
947 different stackings represents two-phase coexistence. The slope of the resultant ground state  
948 free energy profile,  $dG(x)/dx$ , (equation 29) equals the intercalated Li chemical potential,  
949  $\mu$ , where  $-\mu$  is equivalent to the equilibrium potential at  $T = 0$  K, as represented more  
950 generally in Figure 6 and the surrounding discussion in the Methods section.

951 The phase behaviour of the lithium-graphite system, and therefore the voltage profile,  
952 is sensitive to the vdW interactions between the carbon planes.<sup>76,210,211</sup> Conventional DFT  
953 approaches without accounting for vdW interactions do not correctly reproduce the structure  
954 and energetics of graphite and Li-GICs<sup>76,210,211</sup> (Figure 9b). Therefore, vdW-corrected DFT  
955 approaches, for example DFT-D2<sup>45</sup> and DFT-D3,<sup>47</sup> are important for correctly describing  
956 the phase behaviour and dynamics of graphite and Li-GICs. Persson et al. considered the  
957 vdW interaction as a constant.<sup>76</sup> This approximation can accurately describe the step height  
958 at  $x = 0.5$  (the height difference represents the difference between the chemical potentials  
959 in the Stage I-Stage II and Stage II-Stage IID coexistence regions). The simulated voltage  
960 profile Figure 9b (blue line), shows that the constant vdW interaction results in a systematic  
961 error in the voltage scale.

962 Voltage profiles like the ones shown in Figure 9b represent the ground state behaviour,  
963 at  $T = 0$  K. As an additional step, cluster expansions can be used to parameterise an MC  
964 simulation (section 2.1.5) and therefore include thermal fluctuations. The lithium-graphite  
965 phase diagram, Figure 9c, has been constructed by performing a combination of canonical  
966 and grand canonical MC simulations at different temperatures.<sup>76</sup>

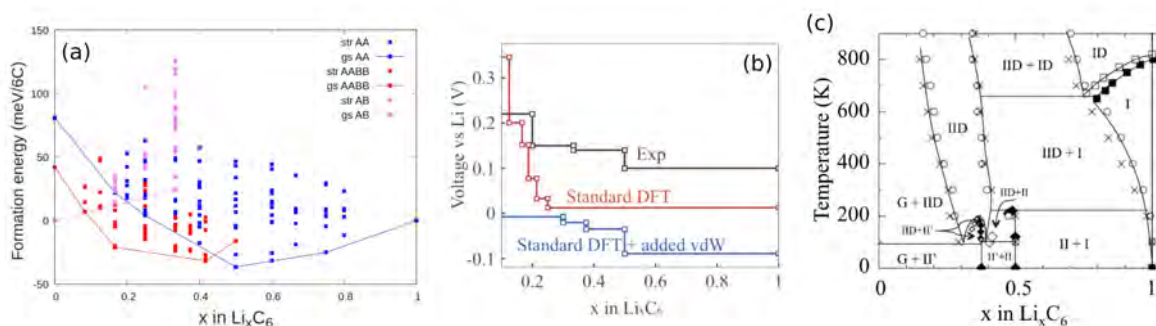


Figure 9: (a) Formation energies of lithium in graphite performed with different carbon stackings. All calculated structures are denoted “str” while the “gs” represent the ground state structures in each of the three carbon stackings: AB, AAB, AA. (b) Phase diagram of lithium in graphite, determined by performing Monte Carlo calculations parameterised by effective cluster interactions from Density Functional Theory calculations. (c) zero kelvin equilibrium potential profiles dependent on different levels of van der Waals corrections. (a) Reproduced from Ref. 71 - Published by The Royal Society of Chemistry; (b-c) Reprinted with permission from Ref. 76. Copyright 2010 American Chemical Society.

967 The experimental OCV and the theoretical equilibrium potential are often, erroneously,  
 968 considered to be equivalent. However, the OCV refers to the measured cell voltage without  
 969 any external current and drifts with time. With sufficient time, it is often assumed the  
 970 OCV will eventually relax to the equilibrium potential, but meta-stable states can occur  
 971 that show no variation over experimental time scales of hours or even days.<sup>71,226,227</sup> The  
 972 true equilibrium potential, as defined in equation 29, is a thermodynamic quantity and  
 973 is not history-dependent.<sup>9,71</sup> Experimentally, a hysteresis of the measurable OCV between  
 974 lithiation and delithiation is observed for Li/graphite half cells<sup>71,170,195,200,206,207,223,228,229</sup> as  
 975 shown in Figure 8. Hysteresis is observed even after several hours of relaxation time and  
 976 for  $T > 298$  K, clearly demonstrating that the measured OCV is not a simple function  
 977 of the thermodynamic ground state. Hysteresis therefore poses an interesting challenge to  
 978 atomistic modellers.

979 It was recently shown that (de)-lithiation hysteresis in graphite is intimately connected  
 980 with disorder in Stage II configurations and appears to be associated with a different carbon  
 981 stacking pathway in each cycling direction.<sup>71</sup> Notably, energetic barriers to translate between



982 ground state configurations, as determined through climbing image nudged elastic band (CI-  
 983 NEB) calculations (Methods section 2.1.3), do not explain the hysteresis in graphite. Non-  
 984 ground state configurations are involved in the delithiation direction. Understanding that  
 985 behaviour requires the configurational entropy of Li/vacancy arrangements to be quantified,  
 986 which is explained in more detail in the next section.

### 987 3.2.3 Entropy

988 The internal energy of intercalation electrodes arises largely from electrostatic interactions  
 989 between the constituents. Those interactions can be well approximated by DFT. An atom-  
 990 istic description of the entropic behaviour of intercalation electrodes,  $S(x)$ , is also needed to  
 991 correctly model thermal behaviour at  $T > 0$  K. The partial molar entropy,  $dS(x)/dx$ , is an  
 992 experimentally accessible quantity, which can be probed by monitoring how the OCV, de-  
 993 scribed in the previous section, varies with temperature (equation 31, c.f. refs. 71,91,93,100,  
 994 169,170,230 for further details).  $S(x)$  is a sum of configurational, vibrational, and electronic  
 995 components.<sup>169,225</sup> For lithium in graphite, the electronic component can be neglected and  
 996 the vibrational component can be well approximated by assigning a Debye temperature to  
 997 all of the vibrational modes,<sup>169,225</sup> or by computing phonon spectra from electronic structure  
 998 methods<sup>196,231</sup> (c.f. section 2.3.4). The quantity that shows the greatest difference with  
 999 lithium concentration,  $x$ , is the configurational entropy of Li/vacancy arrangements,  $S_{\text{config}}$ .  
 1000 Because of the staging phenomena described in section 3.2.1,  $S_{\text{config}}$  strongly deviates from  
 1001 ideal solid solution behaviour for Li in graphite.

1002 The partial molar entropy  $dS(x)/dx$  is difficult to interpret atomistically and so integra-  
 1003 tion is required to get  $S_{\text{config}}$ :

$$\int_{x'=0}^{x'=x} \left( \frac{\partial S_{\text{config}}(x')}{\partial x'} \right) dx' = S_{\text{config}}(x) \approx S(x) - S_{\text{vib}}(x), \quad (42)$$

1004 where  $S_{\text{vib}}$  is the vibrational entropy approximated by Debye temperatures.<sup>169,225</sup> The  
 1005 integration constant is  $S_{\text{config}} = 0$  at  $x = 0$ , because there can be no Li disorder in pure

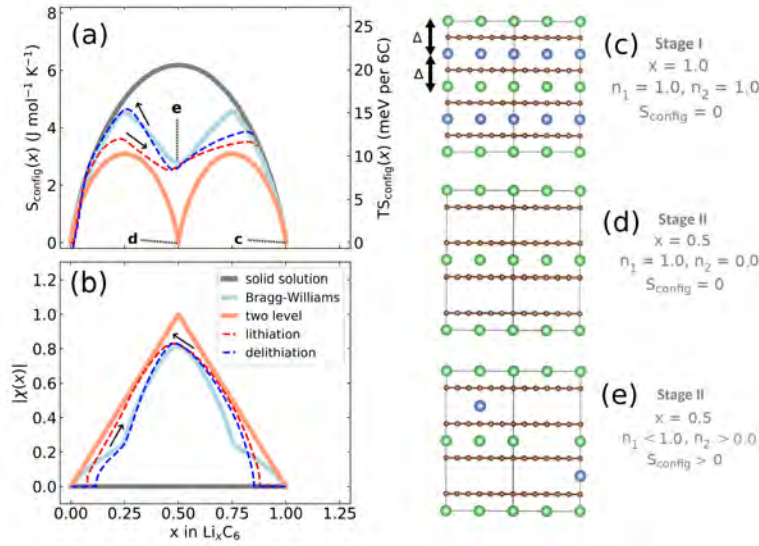


Figure 10: (a) Configurational entropy obtained at  $T = 320$  K: *dark grey solid line*: ideal solid solution; *light blue solid line*: Bragg-Williams solution; *orange solid line*: sequential two level solid solution; *red dashed line*: experimental lithiation; *blue dashed line*: experimental delithiation. (b) Order parameter  $|\chi|$ , as described in the main text, labelled as in (a). In (a), select points (c-e) are indicated and schematic representations of the lattice occupations of Li in levels  $n_1$  (green balls) and  $n_2$  (blue balls) are shown on the right. Reproduced from Ref. 71 - Published by The Royal Society of Chemistry.

1007 Dashed lines in Figure 10a denote post-processed experimental data obtained during  
 1008 lithiation and delithiation using equation 42 from ref. 71. Qualitatively, this shows more  
 1009 configurational Li disorder, i.e. larger entropy, is obtained during delithiation than lithiation.  
 1010 The lithium arrangements can be split into sublattice occupancies  $n_1$  and  $n_2$  arranged in  
 1011 alternate planes, as shown visually in Figure 10c-e. Each sublattice occupancy is linked to  
 1012 the degree of lithiation,  $x$ , via  $x = (n_1 + n_2)/2$ .

1013 Solid lines in Figure 10a-b indicate three hypothetical cases. The orange solid line denotes  
 1014 solid solution (random) filling of Li into one of the sublattices for  $x < 0.5$ , followed by  
 1015 solid solution filling of the other sublattice, resulting in two maxima. Note that  $S_{\text{config}}$   
 1016 is zero in Stage II at  $x = 0.5$  (c.f. Figure 10d). The dark grey line shows the result  
 1017 for an ideal solid solution, if Li were to fill all available sites at random, i.e.  $n_1 = n_2$   
 1018 for all  $x$ . The blue solid line is the solution to a Bragg-Williams model,<sup>91,217</sup> assuming

1019 only nearest neighbour repulsive pairwise lithium interactions between planes of  $\Delta = 75$   
1020 meV and no in-plane interactions. That model allows a direct evaluation of the partition  
1021 function (c.f. equation 10) by enumerating through all possible arrangements of Li atoms  
1022 on the two sublattices for a given  $x$  within the canonical ensemble. The out-of-plane Li-  
1023 Li interactions are treated within a mean field (non-local) approximation to simplify the  
1024 computation (details and formulae in refs. 91,92,217).

1025 The Bragg-Williams model produces a behaviour in  $S_{\text{config}}(x)$  between that expected  
1026 for the solid solution and sequential two level filling. At  $x = 1$ , there is a net repulsion  
1027 on each Li atom of  $2\Delta$ , as represented in Figure 10c. At  $x = 0.5$ , one of the sublattices  
1028 becomes preferentially filled, as represented schematically in Figure 10e. In contrast, a  
1029 perfect Stage II structure as predicted by sequential two level filling (Figure 10d), would  
1030 result in  $S_{\text{config}}(0.5) = 0$ .

1031 These results can be understood within the framework of order parameters.<sup>81</sup> The relevant  
1032 staging order parameter,  $\chi(x) = n_1 - n_2$ , is shown in Figure 10b. Formally,  $\chi(x)$  takes values  
1033 between  $-1$  and  $+1$ , but only the absolute value is meaningful in this case. If  $|\chi(x)| = 1$ ,  
1034 then only one layer is filled with Li, representing maximal staging order. If  $\chi(x) = 0$ , both  
1035 sublattices are occupied with equal probability, maximising disorder and hence no staging  
1036 order is observed.

1037 Greater interlayer Li disorder is observed during delithiation below  $x = 0.5$ . The Li  
1038 ordering, as described by the order parameter, closely follows the Bragg-Williams model.  
1039 This is expected if the host lattice remains in a metastable AA stacking. The lithiation  
1040 behaviour shows a configurational entropy closer to solid solution filling of half the sites,  
1041 which would be expected in AABB stacking, since only half the interlayers (i.e. those locally  
1042 adopting AA or BB stacking) provide favourable Li insertion sites. As shown in Figure 9a,  
1043 this is the ground state stacking configuration for  $x < 0.5$ .

1044 The wider implication of these results is that the transformations between the stackings in  
1045 graphite, and possible stacking dynamics in other layered intercalation hosts, deserve more

1046 attention. These phase transformations not only create a challenge from a cell diagnosis  
1047 point-of-view, they could also be partially responsible for mechanical degradation, fracture,  
1048 unstable interfaces and loss of active material. Phase transformations should be described  
1049 in a rigorous way in continuum models. It is not sufficient to approximate the guest ions as  
1050 an ideal solid solution as, for instance, done in the popular Doyle-Fuller-Newman (DFN)-  
1051 type models. As shown from the methods presented in this section, atomistic techniques  
1052 enable guest orderings to be quantified by means of order parameters, which is information  
1053 inaccessible through experiment alone. Synergies between models of host and guest ion  
1054 orderings with appropriate experimental characterisation will enable a new generation of  
1055 modelling tools that can predict these phenomena with greater accuracy.<sup>9,232</sup>

1056 As shown in the next section, orderings in Li-GICs have implications for the dynamics  
1057 of Li intercalation as well.

### 1058 **3.2.4 Ion diffusion in Li-GIC**

1059 Having outlined the use of atomistic techniques to evaluate observable thermodynamic prop-  
1060 erties of anodes and, in particular, graphite, this section focuses on the computation of bulk  
1061 dynamic properties by DFT and kMC approaches.

1062 Li diffusivity is similar for stage I and stage II Li-GICs,<sup>76</sup> with the probable Li migration  
1063 pathways for  $\text{LiC}_{6n}$  illustrated in Figure 11.<sup>210</sup> These pathways were determined from DFT  
1064 calculations within a CI-NEB approach. Here, Li diffusion across the graphite layers through  
1065 a carbon hexagon hollow (H) are denoted as the through-plane pathway. The in-plane or  
1066 two-dimensional Li migration along the crystallographic *ab* plane occurs either by a bridge  
1067 (B) migration pathway, where Li passes through a rectangle of carbon atoms of subsequent  
1068 layers, or a top (T) migration pathway, where Li passes in between two congruent carbon  
1069 atoms.

1070 Diffusion proceeds in the aforementioned through-plane pathways and in-plane pathways  
1071 via the Frenkel and vacancy mechanisms, respectively. Thinius et al. showed that Li diffu-

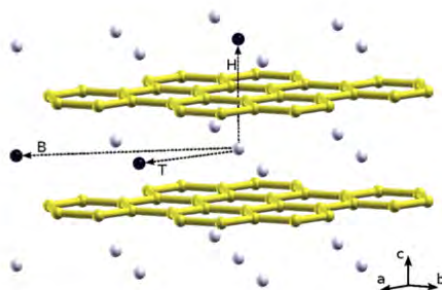


Figure 11: Li migration pathway in  $\text{LiC}_6$ . In the through-plane pathway, lithium migrates through a carbon hexagon hollow (H) along the crystallographic  $c$  direction. The in-plane pathways are denoted as bridge (B) and top (T). Reprinted (adapted) with permission from Ref. 210. Copyright 2014 American Chemical Society.

1072 sion along the crystallographic  $c$  direction is kinetically prohibited, due to a large activation  
 1073 energy barrier.<sup>210</sup> The calculated activation energy for this migration pathway is extremely  
 1074 high (8.00 – 8.23 eV), therefore, the Boltzmann probability for diffusion through pristine  
 1075 graphene planes is negligible at  $T = 300$  K. It is therefore likely that diffusion in the  $c$   
 1076 direction occurs via grain boundaries.<sup>216</sup> In contrast, the activation energy for Li diffusion  
 1077 in the crystallographic  $ab$  plane is much lower (0.42 – 0.52 eV), showing that in Li-GICs, Li  
 1078 diffuses mostly within the intercalation layers.<sup>210</sup> In the literature, DFT-based theoretical  
 1079 investigations provide the same qualitative trends for ion diffusion mechanisms in Li-GICs  
 1080 and the calculated activation barriers vary slightly, but are within the same order of magni-  
 1081 tude.<sup>215,216,233,234</sup>

1082 In order to gain insights into the Li diffusion process in graphite, far from equilibrium and  
 1083 under fast charging conditions, Garcia et al. simulated a range of compositions between stage  
 1084 I and IV, i.e. dilute Stage I.<sup>211</sup> Their study determined reduced activation barriers in the  
 1085 in-plane migration pathways (0.2 – 0.32 eV), which is attributed to the presence of a higher  
 1086 number of electrons compared to  $\text{Li}^+$  ions, occurring at the very beginning of the lithiation  
 1087 cycle during fast charging conditions. This extra charge increases the interlayer spacing in  
 1088 the diffusion layer and adjacent channels, increasing the Li diffusivity.<sup>211</sup> Ji et al. investigated

1089 the anisotropic strain effects on lithium diffusion in graphite anodes using DFT and kMC  
 1090 simulations.<sup>214</sup> According to their study, the activation energy for Li diffusion in unstrained  
 1091  $\text{Li}_x\text{C}_{6n}$  is 0.48 eV. The tensile strain along the direction perpendicular to the graphite planes  
 1092 facilitates in-plane Li diffusion by reducing the energy barrier and vice versa.<sup>214</sup>

1093 Gavilán-Arriazu et al. have recently simulated the dynamic properties of lithium inter-  
 1094 calation in graphite using kMC.<sup>102,103,220</sup> These models considered exchange of Li with the  
 1095 solution on one side of a slab (Figure 12), with only interplanar Li transport allowed, based on  
 1096 the diffusion barrier arguments presented above. Energetic barriers for Li exchange into/out  
 1097 of the graphite were calculated assuming Butler-Volmer kinetics, based on experimental ex-  
 1098 change current density data. Interplanar diffusion barriers were computed using random  
 1099 walk theory, based on experimental data in the dilute limit. Respective barriers of 0.655 eV  
 1100 and 0.370 eV for exchange and interplanar diffusion were obtained. This approach enabled  
 1101 the simulation of several different dynamic properties dependent on lithium concentration,  
 1102  $x$ ,<sup>102,102</sup> sweep direction,<sup>102</sup> and temperature,<sup>103</sup> with a few of these highlighted in Figure 13.  
 1103 Additionally, the importance of metastable Daumas-Hérold orderings in Stage II configura-  
 1104 tions<sup>220</sup> and clogging of lithium at the interface<sup>102</sup> leading to slow Li insertion kinetics were  
 1105 identified as important challenges limiting the kinetics of the lithium (de)insertion processes.

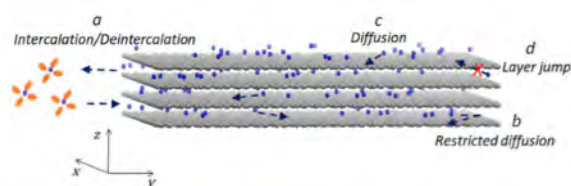


Figure 12: Representation of insertion and diffusion of lithium in graphite in a kinetic Monte Carlo model. Reproduced from Ref. 103 - Published by the Journal of The Electrochemical Society.

1106 Having described modelling of the thermodynamics and bulk Li diffusion in graphite, the  
 1107 following section will focus on another important aspect for a multiscale model: the structure  
 1108 and dynamics of the graphite edges.

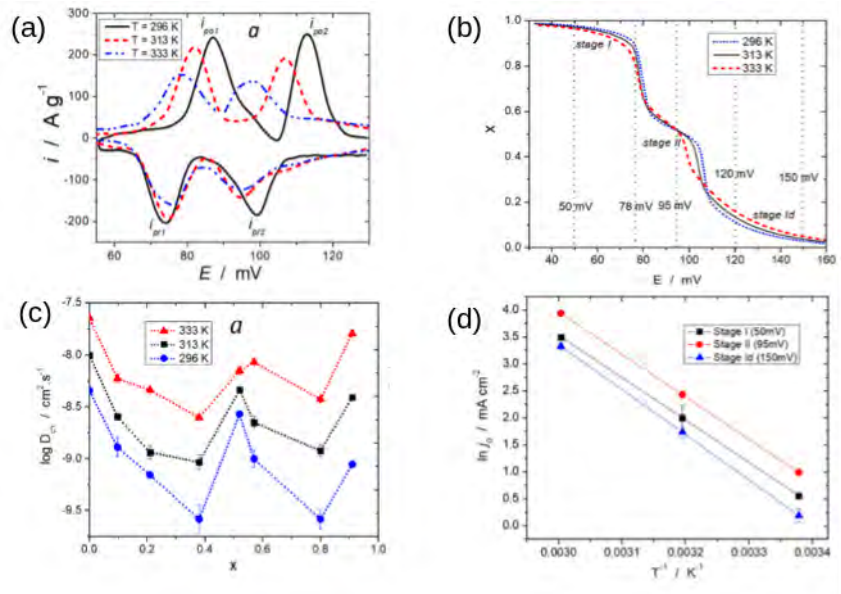


Figure 13: Effect of temperature on the dynamic behaviour of lithium insertion in graphite. (a) voltammograms (b) voltage profiles (isotherms) (c) diffusion coefficients, (d) exchange current density. insertion and diffusion of lithium in graphite in kMC model. Reproduced from Ref. 103 - Published by the Journal of The Electrochemical Society.

### 1109 3.3 Graphite Surfaces and Interfaces

#### 1110 3.3.1 Possible graphite surfaces and their stability

1111 As discussed above, investigating the bulk properties of lithium is key to understanding Li  
 1112 intercalation kinetics and (dis)charging rates in graphite. However, Li exchange occurs be-  
 1113 tween the graphite surfaces and the electrolyte, hence a multiscale model needs to include  
 1114 these phenomena. Addressing the surface properties of graphite would improve the under-  
 1115 standing of (dis)charging behaviours at graphite anodes and possibly suggest how to enhance  
 1116 the (dis)charging rates.

1117 As shown in Figure 14 and section 3.2, graphite consists of multiple stacked graphene  
 1118 layers. One of the exposed surfaces is the basal plane or the (001) surface, which has been  
 1119 widely investigated in both the theoretical and experimental studies.<sup>76,210,234–236</sup> In contrast,  
 1120 the non-basal planes attract less attention, due to their complicated edge morphology. Re-  
 1121 cently, experimental studies characterised the SEI formation and growth along the graphite

1122 edges as opposed to the basal plane,<sup>237,238</sup> indicating the importance of the graphite non-  
1123 basal plane for facilitating Li intercalation.

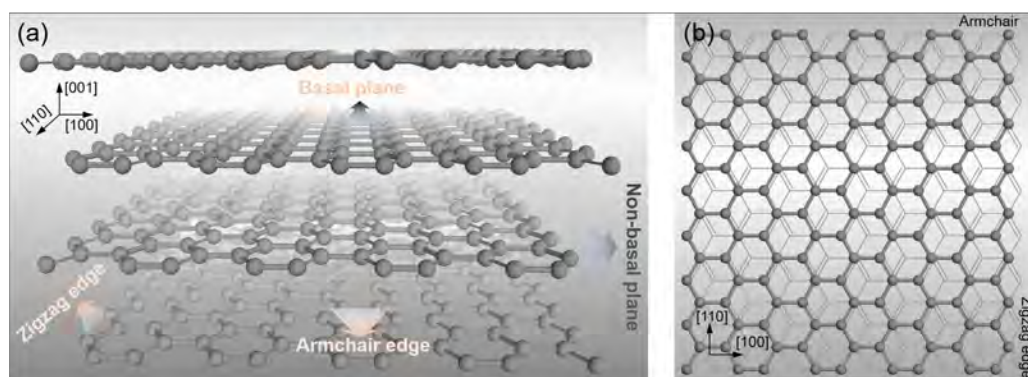


Figure 14: (a) structures of the basal plane and the non-basal plane of graphite. The latter plane consists of different edges of graphites, such as armchair edge and zigzag edge. (b) topological geometries of graphite edges.

1124 Thinius et al. investigated the stability of various low index graphite surface planes in-  
1125 cluding the (001), (110), and (100) planes. The calculations were performed using dispersion  
1126 corrected DFT approaches.<sup>46,48</sup> The surface energies of these planes were found to go in the  
1127 order  $(001) < (110) < (100)$ ,<sup>239</sup> indicating that the (001) surface (the basal plane) is the most  
1128 energetically favourable. However, this plane does not favour Li intercalation, due to the  
1129 high diffusion barrier required for Li to go through the carbon hexagon,<sup>76,210</sup> as highlighted  
1130 in the previous section on ion diffusion in Li-GICs (sec 3.2.4. Li intercalation of graphite  
1131 particles must therefore proceed either via defects in the (001) plane or via the non-basal  
1132 planes.

1133 The (100) surface consists of nanoribbons with a zigzag edge, whereas the (110) surface  
1134 adopts an armchair conformation. The relatively unstable surface planes, such as the (100)  
1135 plane, can be stabilised by various procedures, including chemisorption of oxygen atoms.<sup>240</sup>  
1136 It was found that the oxygen functional groups not only stabilise the graphite edges, but are  
1137 also critical for the formation of the SEI layer near the edge, thereby preventing graphite  
1138 exfoliation.<sup>241</sup> Investigating those non-basal planes and their effects on Li intercalation are  
1139 therefore important and are addressed in the following section.



### 1140 3.3.2 Surface Effect on Intercalation Energy

1141 Understanding the nature of Li intercalation in graphite is important for optimisation of the  
1142 anode material. As described above, Li intercalation in the bulk of graphite has been widely  
1143 investigated.<sup>76,210,234,235,242</sup> Experimental Li diffusivities in graphite have been reported, rang-  
1144 ing from  $10^{-6} - 10^{-14} \text{ cm}^2 \text{ s}^{-1}$ .<sup>234,243-245</sup> However, DFT calculations<sup>76</sup> based on bulk graphite  
1145 indicate that Li diffusion coefficients based on the AABB and AA stacked graphite are around  
1146  $10^{-7} \text{ cm}^2 \text{ s}^{-1}$  and decrease slightly with increasing Li concentration.<sup>76</sup> The variability be-  
1147 tween reported experimental diffusion coefficients arises from a combination of the staging  
1148 dynamics and the anisotropy of Li diffusion (through versus into the basal plane). There  
1149 is also a difference between the surface morphologies of different types of graphite, i.e. the  
1150 proportion of zigzag and armchair edges and their surface chemical terminations, implying  
1151 possible differences between the electronic behaviour and charge transfer kinetics dependent  
1152 on edge morphology and termination. Therefore, investigation beyond the bulk properties  
1153 of graphite is necessary to optimise the overall rate performance of graphite electrodes. As  
1154 described in section 3.3, the basal plane is relatively inert towards Li intercalation.<sup>216</sup> The  
1155 non-basal plane, consisting of different edge morphology, attracts more attention due to  
1156 observations of Li intercalation and SEI growth.<sup>237,238</sup> Uthaisar and Barone studied the Li  
1157 adsorption and diffusion on the edged graphene system using DFT.<sup>246</sup> The graphene edges  
1158 were found to affect not only Li adsorption but also the diffusion coefficient. Narrower  
1159 graphite nanoribbons showed faster delithiation behaviour than the larger sized graphene,  
1160 due to the topological effect of graphene edges. This highlights that an in-depth knowl-  
1161 edge of interface effects is needed to understand Li intercalation rate and enable rational  
1162 optimisation of the battery performance.

1163 From an atomistic perspective, the surface and edge morphology of anode materials  
1164 were found to have a strong impact on Li binding energies.<sup>246,247</sup> Through investigating Si  
1165 nano-structures, Chan and Chelikowsky found that Li has higher binding energies at the  
1166 bulk site compared to the edge, requiring a higher energy cost of Li migration from the

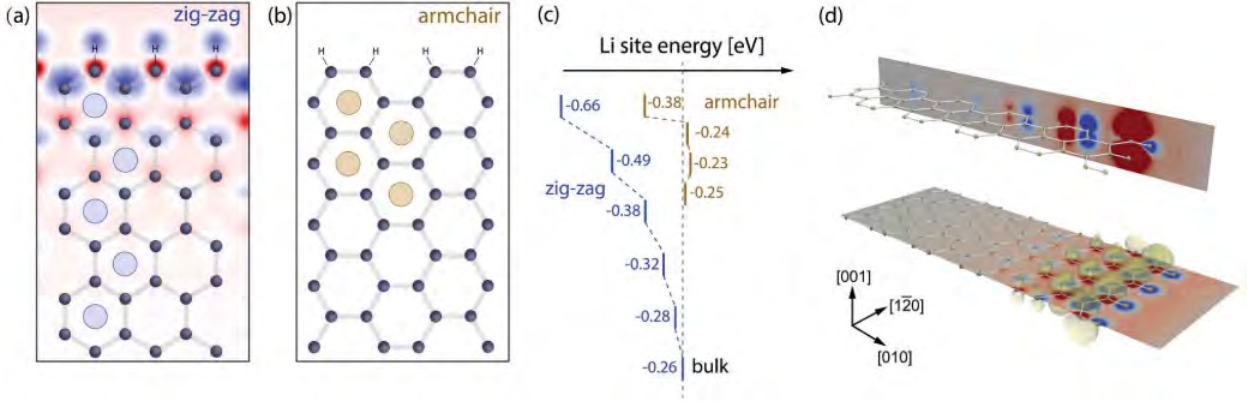


Figure 15: Structures of the zigzag-edged graphite (a) and the armchair-edged graphite (b). (c) shows the energy profile of Li adsorption in edged graphite. (d) is the spin densities of zigzag-edged graphite. The iso-surface value is  $0.0002 \text{ e} \text{ \AA}^{-3}$ . Reproduced from Ref. 70 with permission from The Royal Society of Chemistry.

1167 bulk towards the edge.<sup>248</sup> In graphite anode materials, however, Leggesse et al. reported  
 1168 that the edged graphite systems showed remarkably enhanced Li binding energies and high  
 1169 Li mobility along graphite edges.<sup>247</sup> Peng et al. recently quantified the edge effects on Li  
 1170 intercalation in graphite.<sup>70</sup> In their work, different edged graphites at dilute Li concentration  
 1171 were comprehensively investigated using DFT calculations. Interestingly, they found the  
 1172 unique topological electronic structures near the edges, particularly near the zigzag edge,  
 1173 induced distinct intercalation energies of Li in graphite. Figure 15c shows the Li adsorption  
 1174 energies at the armchair-edged and the zigzag-edged graphite, respectively. The adsorption  
 1175 energy,  $E_{\text{ads}}$ , is expressed as:

$$E_{\text{ads}} = E_{\text{Li|Graphite}} - E_{\text{Graphite}} - E_{\text{Li}}, \quad (43)$$

1176 where  $E_{\text{Li|Graphite}}$ ,  $E_{\text{Graphite}}$ , and  $E_{\text{Li}}$  are the energies of Li adsorption in graphite, the  
 1177 pristine graphite, and one Li in body-centred cubic (bcc) Li metal, respectively. At the  
 1178 armchair edge, from the energy profile (c.f. Figure 15), the adsorption energy of Li is the  
 1179 lowest at the edge site (-0.38 eV). With Li penetrating into the bulk, the adsorption energy  
 1180 decreases rapidly to -0.24 eV at the sub-surface site and becomes -0.26 eV at the bulk  
 1181 site. The topological geometry of the armchair edge promotes Li adsorption relative to the

1182 graphite bulk.

1183 At the zigzag edge, the edge effect becomes even stronger, due to the existence of the  
1184 surface state which consists of  $C - p_z$  orbitals emerging from the zigzag edge.<sup>249,250</sup> Figure  
1185 15c shows that Li achieves a much lower adsorption energy of -0.66 eV at the zigzag edge  
1186 site, indicating the strong binding of Li at the edge. The edge effect in the zigzag system  
1187 is much stronger than that at the armchair edge and additionally penetrates into the bulk,  
1188 indicated by the gradual decrease in magnitude of the Li adsorption energy from the edge  
1189 to the bulk.

1190 The zigzag edge displays completely different spin densities contributed by the  $p_z$  orbitals  
1191 perpendicular to the graphene planes, as shown in Figure 15a-b.<sup>70,247,249,250</sup> These spin den-  
1192 sities consist of the unpaired electrons accumulating on the edged carbons. The amplitude  
1193 of this topological surface state gradually diminishes over a few bond distances beneath the  
1194 surface. It is this surface state that interacts with Li at the zigzag edge and favours its  
1195 adsorption. In summary, the graphite edges show stronger interactions with Li than those  
1196 in the bulk. The effect is especially pronounced at the zigzag edge, strongly stabilising Li  
1197 binding due to the topological surface states.

### 1198 **3.3.3 The Surface Effect on Li Diffusion**

1199 As Li obtains higher binding energies at the graphite edge, due to the specific topological  
1200 structure of graphite edges,<sup>70,247</sup> it's worth examining the impact of those edges on Li diffu-  
1201 sion. In bulk graphite, the diffusion barrier of Li jumping from one site to another is around  
1202 0.4 eV at the dilute limit.<sup>210</sup> Li, however, exhibits completely different diffusion kinetics at  
1203 graphite edges in contrast to those in the bulk.<sup>70,247</sup>

1204 Peng et al. show the energy profile of Li diffusion from the graphite edge towards the bulk  
1205 at dilute Li concentration, Figure 16. In the armchair-edged graphite, Li has to overcome  
1206 an energy barrier of 0.43 eV to move from site 1 to site 2 and a 0.42 eV barrier to further  
1207 move from site 2 to site 3. The direct jump from site 1 to site 3 has to overcome an energy

1208 barrier of 0.58 eV and is therefore less favourable. In contrast, for bulk diffusion, Li needs to  
1209 overcome a  $\sim 0.43$  eV barrier to move to either adjacent site. The higher diffusion barrier at  
1210 the armchair edge is caused by the compensation of Li adsorption energy at the edge site.  
1211 At the zigzag edge, Li obtains two different diffusion pathways. Li diffusion from the edge  
1212 (site 1) to the subsurface (site 3), where the diffusion barrier is 0.48 eV. In contrast, there is  
1213 only a 0.21 eV activation barrier for Li diffusion along the edge sites (site 1 to site 2), which  
1214 is much lower. This indicates that Li is extremely mobile at the zigzag edge, which can be  
1215 verified by the stronger flux connecting the edge sites compared to diffusion towards the bulk  
1216 (c.f. Figure 16). Due to the surface effect identified at the zigzag edge, Li favours diffusion  
1217 along the edge direction within the first sub-surface sites, as the diffusion barrier (0.41 eV)  
1218 is still lower than the barrier to moving Li into the bulk (0.49 eV). Markov chain analysis  
1219 was conducted in Peng et al.'s study to examine Li diffusion from the armchair edge and the  
1220 zigzag edge to a bulk site 20 Å below the edge surface (see Figure 16c). They demonstrated  
1221 that Li diffusion from the armchair edge to the bulk site is around one order of magnitude  
1222 faster than its diffusion from the zigzag edge to the bulk, due to the strong binding of Li at  
1223 the zigzag edge that generates a deep potential well for Li.<sup>70</sup>

1224 On the basis of these studies, it was shown that the graphite edges have strong ef-  
1225 fects not only on the Li intercalation energies but also on its diffusion kinetics close to  
1226 the edge.<sup>70,247</sup> The effect is pronounced at the zigzag edge.<sup>241,251,252</sup> Thus much more slug-  
1227 gish (de)intercalation kinetics are expected at that edge, compared to the armchair edge.  
1228 Strategies including promoting growth of armchair edge over zigzag edge during synthesis  
1229 of graphite nanomaterials and tuning the edge properties by chemical doping to improve Li  
1230 diffusion rate towards the bulk could be useful to enhance Li (dis)charging rate for graphite  
1231 anodes.<sup>253–255</sup> These studies can also offer some universal insights for investigating the inter-  
1232 face effects of other materials such as the cathode. Prior to Li intercalation into graphite,  
1233 the Li desolvation process is also an important step affecting the overall (dis)charging rate.  
1234 However, due to the complicated solid-liquid interface, addressing the graphite interaction

1235 with the electrolyte is an extremely challenging aspect for both modelling and experiment,  
 1236 as discussed in the following sections. We discuss the effect of that interface on Li plating  
 1237 and aspects related to the SEI in the following sections.

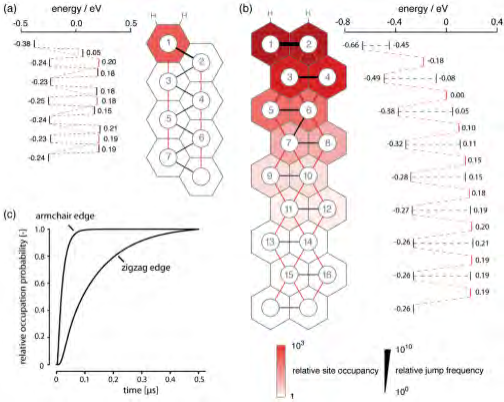


Figure 16: Li diffusion at (a) the armchair-edged and (b) the zigzag-edged graphite. The hexagons indicate lattice sites and the colours show occupancy probability relative to that in the bulk. The width of the lines connecting sites implies the jump frequencies. (c) shows the occupation probability for Li to occupy a site approximately 20 Å below the graphite edge, relative to the steady-state value after being introduced at time zero at the edge. Reproduced from Ref. 70 with permission from The Royal Society of Chemistry.

1238 **3.3.4 Li deposition on graphite anodes**

1239 Apart from intercalation of Li ions into the graphite anode, Li ions can also deposit on surface  
 1240 of graphite in the form of metallic Li dendrites, which can grow during battery operation and  
 1241 cause internal short-circuits. Several situations for the deposition of Li metal on the graphite  
 1242 anode have been identified, as shown schematically in Figure 17.<sup>256</sup> A “normal” intercalation  
 1243 mechanism is shown in Figure 17a. When the voltage of the graphite electrode drops below  
 1244 0 V with respect to Li/Li<sup>+</sup>, deposition of Li<sup>+</sup> ions on the graphite surface, as metallic Li,  
 1245 becomes thermodynamically possible, as shown in Figure 17b. The thermodynamic criterion  
 1246 can be satisfied when the overpotential,  $\eta_{int}$ , is larger than the equilibrium voltage of the  
 1247 stage II to stage I phase transition ( $\sim 85$  mV). Deposition becomes kinetically feasible when  
 1248 the overpotential for the intercalation reaction ( $\eta_{int}$ ) becomes larger than the intercalation  
 1249 voltage ( $\sim 85$  mV), so that the graphite voltage drops below 0 V with respect to Li/Li<sup>+</sup>.

1250 The overpotential originates from mass transfer limitations in the electrolyte region near the  
1251 graphite edge, as shown schematically in Figure 17c. Li plating can be triggered upon local  
1252 salt depletion in the electrolyte,  $c_l \rightarrow 0$ , if liquid diffusion is slow compared to intercalation.  
1253 Solid-state diffusion between the graphite edge and the bulk, as shown schematically in  
1254 Figure 17d, also contributes to this overpotential. Li plating can occur when intercalated  
1255  $\text{Li}^+$  ions saturate the graphite edge ( $c \rightarrow 1$ ) and block further insertion, if diffusion from  
1256 surface to the bulk is slow compared to Li insertion at the edge. A combination of both  
1257 effects can result in Li deposition on the graphite surface.

1258 A recent DFT study by Peng et al. has shown that in a vacuum environment: (1) Li  
1259 deposition is more favourable near the graphite edges rather on the basal plane, (2) the energy  
1260 barrier for Li deposition at the zigzag edge (only) increases with the degree of lithiation of  
1261 the graphite, (3) chemical doping of nitrogen can increase the energy barrier and can possibly  
1262 suppress the Li deposition on graphite anode on the zigzag edge.<sup>257</sup> More advanced models  
1263 for DFT simulations in the presence of an electrolyte under applied potential (cf. (sec. 2.2.1  
1264 and Ref. 258)), have the potential to shed more light on the Li deposition phenomenon in  
1265 experimental conditions.

### 1266 3.3.5 Solid-Electrolyte Interphase

1267 The SEI is an important component of the rechargeable Li-ion battery and is formed from  
1268 deposition of the decomposition products of the electrolyte and solvent on the anode surface.  
1269 The SEI allows transport of  $\text{Li}^+$  ions but blocks the transfer of electrons, thereby stopping  
1270 further electrolyte decomposition reactions.<sup>259,260</sup> Here we discuss aspects of the SEI related  
1271 to our discussion of Li-ion diffusion energy barrier in bulk and graphite surfaces. A recent  
1272 comprehensive review on the atomistic modelling of the SEI describes several other aspects  
1273 of the SEI in detail:<sup>16</sup>

- 1274 • Electrolyte and solvent reduction mechanisms, including: prediction of the reduction  
1275 voltage for each solvent and electrolyte species, the effect of the electrolyte solvation

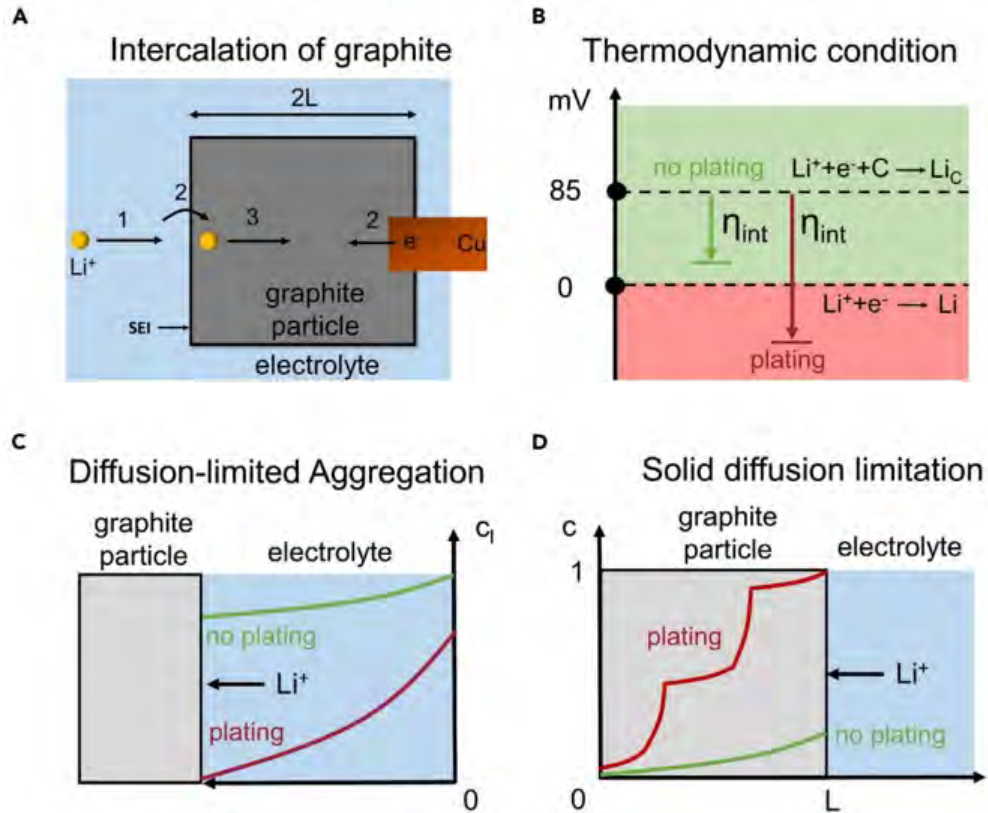


Figure 17: (a) 2D schematic of intercalation of a graphite particle. Three sequential steps take place during charging at the graphite anode: (1)  $\text{Li}^+$  transport in electrolyte toward the reaction site; (2)  $\text{Li}^+$  intercalation into a graphite particle (including de-solvation and migration through the SEI); and (3)  $\text{Li}^+$  solid diffusion within the graphite particle. (b) Thermodynamic criterion for Li plating (cell voltage,  $U < 0$  V versus  $\text{Li}/\text{Li}^+$ ). The green and red arrows illustrate the required overpotentials to drive the insertion reaction at small current/fast insertion kinetics and large current/slow insertion kinetics. (c) 1D schematic of diffusion-limited aggregation resulting from electrolyte transport limitations. The green and red curves illustrate the  $\text{Li}^+$  salt concentration profile in the electrolyte. (d) 1D schematic of solid diffusion-limitation mechanism. The green and red curves illustrate the  $\text{Li}^+$  concentration profile in the graphite particle. Reprinted from Ref. 256, with permission from Elsevier.

1276 structure, the effect of anode surface termination, and the dynamic buildup of the  
1277 nanometer thick SEI layer.

1278 • Modification of the SEI by electrolyte additives and prediction of new electrolyte ad-  
1279 ditives.

1280 • Correlation of the SEI properties with battery performance, including: the electron  
1281 insulating properties of the inorganic components in the SEI, the ionic conductivity  
1282 of the SEI components, Li-ion desolvation at the SEI/electrolyte interface, chemical  
1283 stability of the SEI components, and mechanisms of SEI growth and battery aging.

1284 • The use of coatings to artificially design the SEI.

1285 One way to describe the SEI is via the implicit continuum models described in sec. 2.2.1.  
1286 Applying their DFT + implicit electrolyte model on an armchair edge of 1634-atom graphite  
1287 slab in contact with a 0.5 M  $\text{LiPF}_6$  in EC solution, Dziedzic et al. calculated that a Li atom  
1288 is 2.34 eV more stable at the graphite edge than in the electrolyte solution.<sup>135</sup> Similarly,  
1289 Haruyama et al. found favourable energetics for Li intercalation from the electrolyte solu-  
1290 tion into the graphite edge.<sup>261</sup> They also studied the variation in energy as a function of  
1291 Li distance from the graphite edge, as shown in figure 18. In Haruyama et al.'s model, Li  
1292 intercalation is accompanied by an electron gain from the external circuit. This was imple-  
1293 mented using a grand canonical version of electronic DFT, where the number of electrons in  
1294 the electrode can change subject to fixed electrode potential. Correspondingly, the appropri-  
1295 ate thermodynamic quantity to represent this ensemble is the grand potential,  $\Omega = A - \mu_e N_e$ ,  
1296 which is plotted on the y axis for several different constant chemical potentials of electrons,  
1297  $\mu_e$ . Two illustrative cases include: (a) the potential of zero charge (PZC), which is the  
1298 electrochemical potential of a charge-neutral Li-graphite system, and (b) the equilibrium  
1299 potential (c.f. sections 2.3.1 and 3.2.2), where the net change in the grand potential for  
1300 the intercalation reaction becomes zero. Haruyama et al.'s simulations estimate an energy



1301 barrier of around 0.6 eV for Li intercalation into the graphite edge, which is close to the  
 1302 experimental measurements from impedance spectroscopy.<sup>262</sup>

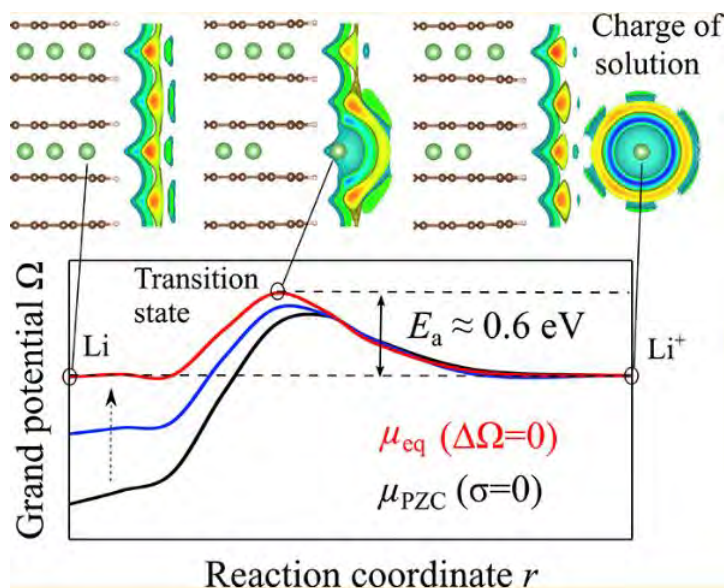


Figure 18: Profiles of grand potential  $\Omega$  as a function of the Li-position during Li-intercalation process at the interface between graphite edge and an implicit electrolyte solution. The simulation is performed at conditions of constant chemical potential of electrons  $\mu_e$  (constant electrode potentials similar to experiments). Reprinted with permission from Ref. 261. Copyright 2018 American Chemical Society.

1303 Another way to describe the SEI is via explicit consideration of SEI components. Shi et al.  
 1304 performed a direct calculation of Li-ion transport in the  $\text{Li}_2\text{CO}_3$  component of the SEI,<sup>263</sup>  
 1305 via DFT-based CI-NEB calculations (section 2.1.3). Two mechanisms for  $\text{Li}^+$  diffusion were  
 1306 considered, namely, the knock-off and direct hopping mechanisms, which were found to  
 1307 have energy barriers of 0.31 eV and 0.54 eV respectively, as shown in Figure 19. The Li  
 1308 self-diffusion coefficient was calculated to be  $1.1 \times 10^{-7} \text{ cm}^2 \text{ s}^{-1}$  and  $8.4 \times 10^{-12} \text{ cm}^2 \text{ s}^{-1}$   
 1309 respectively. Estimating the formation energy of corresponding defects in the lattice of  
 1310  $\text{Li}_2\text{CO}_3$  as a function of voltage, the total activation energy barrier for Li-ion diffusion was  
 1311 predicted to be in the 0.67–1.07 eV range for the knock-off mechanism and in the 0.92–1.32  
 1312 eV range for the direct-hopping mechanism.

1313 The predicted values of the Li-ion diffusion energy barrier by both the implicit and the  
 1314 explicit models described above are significantly higher than that in the bulk of graphite,

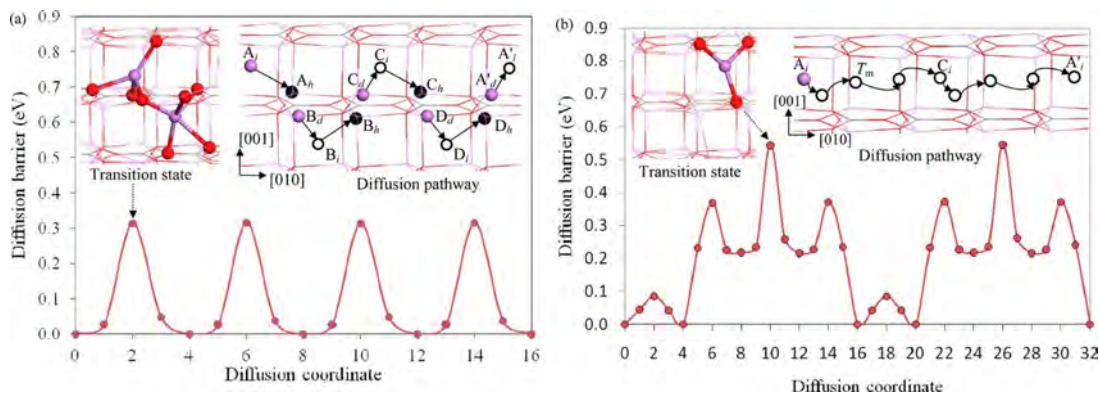


Figure 19: Energy barrier for Li-ion transport in the SEI via (a) knock-off and (b) direct hopping mechanisms. Reprinted with permission from Ref. 263. Copyright 2012 American Chemical Society.

1315 which is reported to be between 0.2-0.5 eV (c.f. section 3.2.4).<sup>76,210,211</sup> This indicates a  
 1316 limiting role of the SEI in determining overall kinetics of Li-ion diffusion and the overall  
 1317 rate-capability of Li-ion batteries.

### 1318 3.4 C/Si composites

1319 Use of anode materials capable of electrochemically alloying with lithium could allow higher  
 1320 energy densities than are possible with graphite. In particular, silicon, due to its high  
 1321 gravimetric capacity of 4200 mAh g<sup>-1</sup>, has achieved tremendous attention as an anode  
 1322 material.<sup>264</sup> Si has a low electrochemical potential 0.37–0.45 V vs. Li/Li<sup>+</sup>, which is only  
 1323 ~0.27 V higher than graphite.<sup>265</sup> Si is highly abundant, cost effective and non-toxic.<sup>265–267</sup>  
 1324 While pure Si anode materials are not presently viable, present day anode materials combine  
 1325 a small atomic fraction (typically 5-10 at %) of silicon with graphite to boost the gravimetric  
 1326 capacity of the anode.<sup>14</sup> However, there are certain challenges in understanding the behaviour  
 1327 of Si and C/Si composites that are summarised in this section.

1328 The phase diagram of lithium and silicon shows five crystalline intermetallic Zintl-like  
 1329 phases: Li<sub>21</sub>Si<sub>5</sub>, Li<sub>13</sub>Si<sub>4</sub>, Li<sub>7</sub>Si<sub>3</sub>, Li<sub>12</sub>Si<sub>7</sub>, and LiSi.<sup>268</sup> However, LiSi is not accessible under  
 1330 electrochemical conditions, since it is synthesised under high pressure, and the stoichiometry  
 1331 of Li<sub>21</sub>Si<sub>5</sub> is disputed, with a mixed Li<sub>21</sub>Si<sub>5</sub>/Li<sub>22</sub>Si<sub>5</sub> phase also proposed.<sup>269</sup> Under electro-

1332 chemical conditions, metastable phases with compositions  $\text{Li}_{15}\text{Si}_4$ <sup>270</sup> and amorphous  $\text{Li}_x\text{Si}_y$   
1333 can be formed.<sup>271</sup> It has been proposed that a different reaction pathway between these  
1334 phases during lithiation and delithiation contributes to the observed charge/discharge hys-  
1335 teresis in lithium silicides and C/Si composites.<sup>270</sup> In particular, Jiang et al. found that the  
1336 crystalline phase  $\text{Li}_{15}\text{Si}_4$  is accessed during lithiation, but the lattice undergoes an amor-  
1337 phisation process during delithiation, with the latter step being rate determining.<sup>270</sup> This  
1338 limits the utility of ground state DFT calculations for understanding the Li-Si system under  
1339 operating battery conditions, and is therefore a challenge for multiscale modelling.

1340 An additional challenge is the volume expansion. Upon full lithiation, the volume of Si  
1341 can expand to more than three times its original volume, which means the Si electrodes do  
1342 not retain their morphology during prolonged cycling or, even worse, some particles become  
1343 detached from the electrode assembly.<sup>265,267,272</sup> This volume expansion/contraction during  
1344 cycling also leads to severe cracking and degradation of the SEI. It is for mainly these  
1345 reasons that pure Si anodes are not currently commercially viable and must be combined  
1346 with graphite. Several strategies have been proposed to change the morphology to miti-  
1347 gate these issues, including development of different Si robust nanostructures (0D or hollow  
1348 nanoparticles, 1D nanowires, 2D film-like Si, and 3D Si structures),<sup>265</sup> and the development  
1349 of composites (Si/carbon composites, Si/polymer composites, Si alloys, and Si/metal oxide  
1350 composites).<sup>14</sup> While modelling the complex nature of the degradation pathways of the Si,  
1351 Si-composites and their SEIs is presently out of reach of atomistic methods, these techniques  
1352 nonetheless emerge as natural tools for high-throughput screening of different promising an-  
1353 ode materials.<sup>273</sup> These approaches can also tell experimentalists the most promising part  
1354 of the parameter space in which to perform more extensive, time consuming, and sometimes  
1355 costly characterisation.

1356 A more comprehensive overview of the application of mesoscale models to challenging  
1357 composite systems is presented by Franco et al., with the volume averaging approach high-  
1358 lighted perhaps being particularly applicable to Si and C/Si systems.<sup>232</sup> Particularly for

1359 carbon anodes in combination with Si or silicon suboxide (SiO<sub>x</sub>), collectively referred to as  
1360 C/Si or C/SiO<sub>x</sub>, it may presently be necessary to sacrifice some details of the atomic level de-  
1361 scription to enable these systems to be tractably modelled at either mesoscale or continuum  
1362 levels. Regarding the dynamic and metastable behaviour described above, kMC would be a  
1363 natural technique to bridge length scales and include different time scale dynamic events, as  
1364 explained in a recent review dedicated to this technique.<sup>104</sup>

### 1365 3.5 Outlook and challenges for anodes

1366 Graphite remains the predominant anode material in most Li-ion cells, due to its suitably  
1367 high capacity of 372 mAh g<sup>-1</sup>, an operating potential close to 0 V vs. Li/Li<sup>+</sup>, and its  
1368 compatibility with liquid organic electrolytes. Alternative materials that form solid solutions  
1369 with lithium (including silicides) presently do not have sufficient long term structural stability  
1370 to be used as the primary anode material, requiring them to be composites with graphite.  
1371 The development of graphite-based anodes has relied upon not only understanding staging  
1372 formation in bulk, but also upon the development and understanding of a stable SEI and its  
1373 implications of that SEI for cell longevity and (de)intercalation rate behaviour.

1374 Advancements in developing all solid-state batteries (ASSBs) have resulted in additional  
1375 research of Li metal anodes, as reviewed by Fang et al.,<sup>274</sup> and Li et al..<sup>275</sup> In this section,  
1376 we have summarised the safety and degradation challenges caused by lithium plating on  
1377 graphite anodes. The use of Li metal as the anode for LiBs and ASSBs still face similar issues  
1378 regarding redeposition of metallic Li as dendrites and consumption of cyclable lithium.<sup>274,275</sup>

1379 Many aspects of modelling the bulk behaviour of lithium (de)insertion graphite are well  
1380 understood. As shown in this section, challenging aspects like quantifying the Li ion ordering  
1381 with lithiation fraction can only be obtained by combining experimental observations with  
1382 atomistic models. However, there are challenges with atomistic modelling in anodes that  
1383 hinder improvements in capacity, rate performance, safety and durability of the anode itself  
1384 and, consequently, full Li-ion cells. In addition, there are challenges with transferring insights

1385 from atomistic modelling in a scalable form to models on different length and time scales,  
1386 while maintaining physical integrity. These outstanding challenges are:

- 1387 • The role of metastable phases in the kinetics of staging behaviour. New theoretic-  
1388 cal frameworks should be developed to understand the connectivity between different  
1389 phases and the effect of this on the path dependency of measurable behaviour like the  
1390 OCV. These distinct pathways also have implications for mechanical degradation and  
1391 fracture. A promising approach in this direction is the semi-grand canonical framework  
1392 developed by Van der Ven et al., Van der Ven et al. describing layered transitions in  
1393 cathodes<sup>9,231,276,277</sup> that could also be applicable to graphite anodes and other candi-  
1394 date materials like silicides.
- 1395 • The role of the configurational, vibrational and electronic entropy of lithium insertion.  
1396 Longer length scales, i.e. continuum models, still assume that the entropy follows  
1397 an ideal solid solution behaviour. The importance of configurational entropy to the  
1398 phase transitions of lithium in graphite was highlighted in previous sections.<sup>71,91,225</sup> One  
1399 promising extension would be to use the results from MC calculations to parameterise  
1400 a phase field model, such as those developed by Bazant,<sup>95</sup> Guo et al.<sup>96</sup> and Bai et al.,<sup>97</sup>  
1401 with a more realistic Hamiltonian and thus include entropy effects in a rigorous way.
- 1402 • Regarding dynamics, kMC approaches with an empirical Hamiltonian show promise,<sup>102–104,220</sup>  
1403 but are limited by the length and time scale of the properties that can currently be  
1404 modelled. A possible solution would be to develop an effective cluster interaction  
1405 Hamiltonian linking with a linear scaling DFT code, such as ONETEP. Parellelisation  
1406 of the kMC calculations could be achieved by exploiting recently developed graphical  
1407 processing unit (GPU) architectures.

1408 Superior models of surface and interface effects are needed. This includes development  
1409 of a physically rigorous version of the Butler-Volmer equation, which is valid for electron  
1410 transfer but is conventionally assumed to be valid too for ionic transfer in Li-ion batteries.

1411 The current models of the interface are too simplistic or represent an ideal situation instead of  
1412 dealing with the complex reality of the SEI. A systematic coarse-graining approach involving  
1413 multi-length- and multi-time-scale physics can help in understanding the complex nature of  
1414 the SEI and its influence on performance of Li-ion batteries. Controlling and improving the  
1415 properties of SEI is crucial to improve the overall rate capability of Li-ion batteries, as that  
1416 interface is the bottleneck for Li-ion diffusion.

1417 Regarding graphite, atomistic modelling can be used to predict systematic modifications  
1418 to the edge morphology or the use of dopants on the graphite edge,<sup>70,253,254</sup> or tuning of  
1419 the interlayer carbon spacing<sup>214</sup> to enable systematic tuning of the rate performance. This  
1420 approach has the potential to lead to more robust interfaces and strategies to tune the anode  
1421 voltage and dynamics, thus tuning nucleation barriers and mitigating the risk of lithium  
1422 plating.<sup>257</sup> In this regard, it should be pointed out that decoupling the rate performance of  
1423 different graphite edges is still a great challenge from experiment and therefore this finding  
1424 represents a success for atomistic modelling.

1425 We highlight that there are still outstanding challenges regarding modelling metastable  
1426 behaviour, volume expansion and degradation in solid solution materials such as silicides.  
1427 So far, high-throughput atomistic modelling techniques have provided a predictive tool to  
1428 suggest anode materials that are promising for more extensive experimental characterisation.  
1429 However, composite materials such as C/Si and C/SiO<sub>x</sub>, which are increasingly being used in  
1430 commercial anodes, are presently challenging to model on the atomistic scale. In this regard,  
1431 an extension to mesoscale modelling, such as a volume averaged approach as suggested by  
1432 Franco et al., could be a promising way to model challenging materials such as composites,  
1433 in which each component experiences different degrees of volume expansion.<sup>232</sup>

## 1434 4 Electrolytes

### 1435 4.1 Introduction

1436 Electrolytes are a medium for the transport of charged ionic species, i.e.  $\text{Li}^+$ , between the  
1437 electrodes.<sup>278,279</sup> While the electrons flow through the outer circuit, an equal ionic current  
1438 flows through the electrolyte to balance the charge. Electrolytes can be categorised into two  
1439 groups: liquid and solid, both of which have their benefits and drawbacks. Liquid electrolytes  
1440 are currently used in commercial lithium-ion batteries (LiBs) and offer high conductivities,  
1441 but have safety concerns.<sup>280–282</sup> Solid electrolytes are a safer alternative that are approaching  
1442 commercialisation and can potentially reach higher energy densities.<sup>283</sup> There are several  
1443 key aspects to the design of either liquid or solid electrolytes in LiBs: their electrochemical  
1444 stability window,<sup>2,284</sup> ionic conductivity,<sup>285,286</sup> electric double layers,<sup>278,287</sup> solid-electrolyte  
1445 interphase (SEI),<sup>288,289</sup> and safety, which are all discussed in the following sections.<sup>290,291</sup>

1446 **Electrochemical stability window** An electrolyte can be safely used within its elec-  
1447 trochemical stability window, which defines the voltage range outside of which it can be  
1448 oxidised or reduced.<sup>2</sup> The electrochemical stability window is schematically depicted in Fig-  
1449 ure 20, showing the electronic energy levels in the electrodes and electrolyte of a battery  
1450 cell. If the anode electrochemical potential,  $\mu_A$ , is above the lowest unoccupied molecu-  
1451 lar orbital (LUMO) of the electrolyte, the electrolyte will be reduced. Conversely, if the  
1452 cathode electrochemical potential,  $\mu_C$ , is below the highest occupied MO (HOMO) of the  
1453 electrolyte, the electrolyte will be oxidised. Therefore, the electrochemical potentials,  $\mu_A$   
1454 and  $\mu_C$ , should lie within the energy gap,  $E_g$ , between the LUMO and the HOMO of the  
1455 electrolyte, constraining the open circuit voltage (OCV),  $V_{\text{oc}}$ , of a battery cell, such that:<sup>2</sup>

$$eV_{\text{oc}} = \mu_A - \mu_C \leq E_g, \quad (44)$$

1456 where  $e$  is the elementary charge, i.e. the magnitude of the charge on an electron.

1457 The energy gap,  $E_g$ , for an aqueous electrolyte is  $\sim 1.3$  eV, severely limiting the OCV,

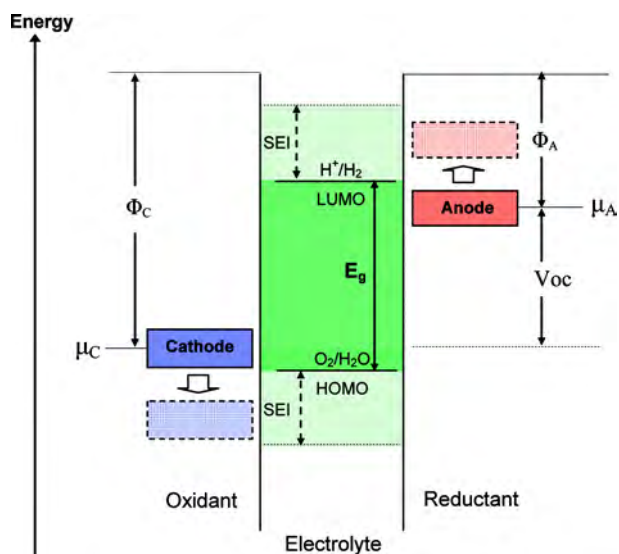


Figure 20: Schematic open circuit energy diagram of an aqueous electrolyte.  $\Phi_A$  and  $\Phi_C$  are the anode and cathode work functions.  $E_g$  is the electrochemical stability window of the electrolyte. If  $\mu_A >$  lowest unoccupied molecular orbital (LUMO) and/or  $\mu_C <$  highest occupied MO (HOMO), the electrolyte would be thermodynamically unstable and its usage would require kinetic stability through the formation of a solid-electrolyte interphase (SEI) layer. Reprinted with permission from Ref. 2. Copyright 2010 American Chemical Society.

1458  $V_{oc}$ . In order to obtain a higher OCV, non-aqueous electrolytes with larger  $E_g$  have been used  
 1459 in LiBs.<sup>2,290</sup> A good summary of electrochemical stability windows of different classes of non-  
 1460 aqueous electrolytes including (organic and inorganic) liquids, solids, ionic liquids, polymers  
 1461 and their combinations is presented by Goodenough and Kim.<sup>2</sup> Commonly used organic  
 1462 liquid electrolytes, such as 1 M LiPF<sub>6</sub> in 1:1 ethylene carbonate (EC) : dimethyl carbonate  
 1463 (DMC), have stability windows between  $\sim 1.3$ -5.0 V, while ionic liquids have stability window  
 1464 between  $\sim 1.0$ -5.3 V. A desirable property of solid electrolytes is their larger electrochemical  
 1465 stability window ( $\sim 0.0$ -8.0 V), compared to liquid electrolytes,<sup>2</sup> allowing them to operate  
 1466 within a larger voltage window and thus increase the energy density of the battery.

1467 **Ionic conductivity** High ionic conductivity ( $> 10^{-4}$  S cm<sup>2</sup>) in the electrolyte (liquid  
 1468 or solid) and across the electrode-electrolyte interphase enables a high rate-capability of the  
 1469 overall Li-ion battery.<sup>2,285,286</sup> Generally, the ionic conductivity of liquid electrolytes is higher  
 1470 than that of solid electrolytes. However, new classes of solid materials have been found with  
 1471 ionic conductivity surpassing that of liquids (cf. section 4.3), known as superionic conductors.



1472 The ionic conductivity of commonly used liquid electrolytes is several orders of magnitude  
1473 higher than that in the bulk of electrodes and the electrode-electrolyte interphase.<sup>285</sup>

1474 **Electric double layer** During the charging of an electrode in contact with a liquid elec-  
1475 trolyte, excess charge develops at the electrode surfaces. This triggers the rearrangement of  
1476 electrolyte ions in the electrolyte solution, such that counter-electrolyte charges accumulate  
1477 near the electrode-electrolyte interface, forming an interfacial charge density perturbation, to  
1478 achieve local electroneutrality at the interface. In the classical system of dilute electrolytes,  
1479 electroneutrality is achieved by the formation of a monotonically decaying ‘double layer’.<sup>278</sup>  
1480 The double layers in solid electrolytes cannot be directly observed experimentally, so mod-  
1481 elling can be used to rationalise their effects. Several models of the electric double layer in  
1482 electrochemistry exist, such as Helmholtz, Gouy-Chapman, and Gouy-Chapman-Stern.<sup>279</sup>  
1483 Early models were limited in sophistication: the Helmholtz double layer model suggested  
1484 charge screening by a plane of counter-charged electrolyte ions near the electrode surface,  
1485 resembling a capacitor. In contrast, the Gouy-Chapman model screens charge via a diffuse  
1486 layer of electrolyte ions, decaying monotonically to their bulk concentration value, where the  
1487 electric potential will fall to zero. The Gouy-Chapman-Stern model accounted for discrepan-  
1488 cies encountered by including both a Helmholtz layer of counter charge, as well as a diffuse  
1489 layer of electrolyte ions, as shown schematically in figure 21(a). These continuum models of  
1490 electrolyte ions are also being integrated with quantum mechanical methods, such as Density  
1491 Functional Theory (DFT) (c.f. section 2.2.1). Bhandari et al. recently implemented such  
1492 a hybrid quantum-continuum model to achieve electroneutrality in simulations of charged  
1493 electrochemical interfaces, based on a modified Poisson-Boltzmann equation (PBE).<sup>66</sup>

1494 At the interface between solid electrolytes and electrodes, a similar decay in charge is  
1495 observed. However, in this case, the charge carrier is the charge vacancy. Maier discuss the  
1496 theory of this decay in detail<sup>292</sup> and new continuum models continue to be developed for  
1497 solid electrolytes.<sup>293–296</sup> Swift et al. present a model for formation of the double layer in solid-  
1498 solid electrochemical interfaces, based on the Poisson-Fermi-Dirac equation. The resulting

1499 space charge layer of point defects in a solid electrolyte material is shown schematically in  
 1500 figure 21(b). However, this study only accounts for the effect of correlations between ions  
 1501 by limiting the concentration of defects in the interfacial layer to be below a certain value.

1502 At higher concentrations, screening of electrodes changes markedly in liquids, with a new  
 1503 regime emerging when the Debye screening length is of roughly equal value to the ionic  
 1504 diameter. In this regime, charge is screened by means of exponentially damped oscillations  
 1505 of counter-ions and co-ions, in an ordered interfacial structure known as overscreening;<sup>297</sup>  
 1506 a structure that has previously been observed experimentally for liquids.<sup>298–301</sup> In 2021,  
 1507 Dean et al. became the first to propose the existence of a similar oscillatory decay at solid  
 1508 electrolyte grain boundaries.<sup>302</sup>

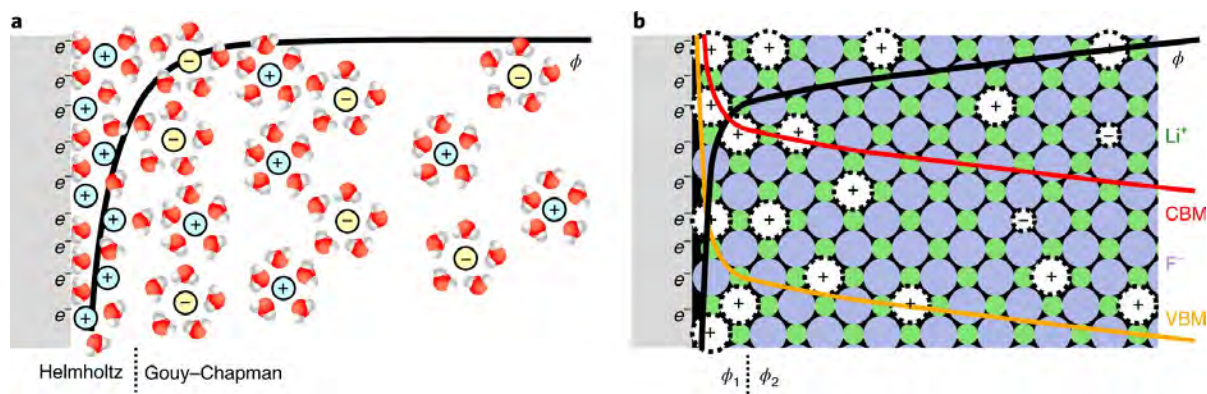


Figure 21: Schematic comparing the double layer formed at the solid–liquid and solid–solid electrochemical interfaces. (a) For the solid–liquid interface, excess electrons on the electrode are balanced by increased density of solvated positive ions in the liquid electrolyte.  $\phi$  is the electrostatic potential and is mediated by the Helmholtz layer, followed by exponential decay in the diffuse layer (described by Gouy–Chapman theory). (b) For the solid–solid interface, excess electrons on the electrode are balanced by increased density of positive point defects in the solid electrolyte. Electronic band bending occurs in the solid electrolyte.  $\phi_1$  and  $\phi_2$  are the electrostatic potentials next to and further from the interface. Electronic band-bending is shown via the valence-band maximum (VBM), also known as the highest occupied molecular orbital (HOMO), and conduction-band minimum (CBM), also known as the lowest unoccupied molecular orbital (LUMO). Reproduced with permission from Springer Nature: Ref. 287, Copyright 2021.

1509 **Solid-electrolyte interphase** The “interface” described above is basically a two-dimensional  
 1510 surface between the electrode and electrolyte. In LiBs, the electrolyte reacts irreversibly and  
 1511 decomposes on the electrode surfaces, leading to the formation of a distinct phase, several

1512 nanometres thick, between the electrode and the electrolyte, known as the SEI.<sup>288</sup> The ability  
1513 to form a stable interphase, which is both ionically conducting and electronically insulating,  
1514 is an important criterion for the selection of an electrolyte material. The electron insulating  
1515 property of the SEI is important, to stop further decomposition of the electrolyte on the  
1516 electrode.<sup>2,290</sup> High ionic conductivity through the SEI is important, otherwise this can form  
1517 a bottleneck for the overall rate capability of LiBs.<sup>16,291</sup> While the SEI was originally discov-  
1518 ered in liquid electrolytes, its rate-limiting behaviour is now also observed in all-solid-state  
1519 batteries (ASSBs).<sup>289</sup>

1520 The two major classes of electrolyte materials, solid and liquid electrolytes, are discussed  
1521 separately. We focus on the atomistic modelling of different types of liquid and solid elec-  
1522 trolytes and their battery related properties. For the liquid electrolyte section, this includes  
1523 the bulk structure, diffusion properties, solvation energies, and activity coefficients of dif-  
1524 ferent solvents. For the solid electrolyte section, there is a particular emphasis on the ion  
1525 transport mechanisms, material stability, and the electrode-electrolyte interfaces. Finally,  
1526 we discuss the individual challenges and outlook for future atomistic modelling of both liquid  
1527 and solid electrolytes.

## 1528 4.2 Liquid Electrolytes

### 1529 4.2.1 Introduction to liquid electrolyte materials

1530 The most widely used liquid electrolyte in Li-ion batteries is  $\text{LiPF}_6$  in a solvent, which  
1531 is typically a mix of two or more solvents, for example EC, DMC, propylene carbonate  
1532 (PC), or ethyl methyl carbonate (EMC), in order to achieve the competing objectives of  
1533 dissolution of a high concentration of salt, low viscosity, and high dielectric constant at  
1534 typical operational temperatures.<sup>22,194,290,291,303</sup> Cyclic carbonates (EC, PC) have a higher  
1535 dielectric constant but also high viscosity, while “linear” carbonates (DMC, EMC) have  
1536 low viscosity but also a low dielectric constant. For that reason, mixtures of solvents are  
1537 often used to optimise performance in a specific application.<sup>22,194,304</sup> However, in the last

1538 two decades there has been continued innovation in electrolyte mixtures, including ionic  
1539 liquids<sup>305</sup> and salt in water-based systems.<sup>306</sup> This section will touch on both traditional  
1540 and emergent electrolyte solvents.

#### 1541 4.2.2 An introduction to modelling liquid electrolytes

1542 The modelling of liquid electrolytes for conventional batteries is a broad and diverse field.  
1543 Over the past 20-30 years, atomistic modelling has helped to shape the fundamental physics  
1544 of liquids, determining a new physical basis and validating decades-old pen and paper theories  
1545 of concentrated electrolytes.<sup>307-310</sup> Here, we focus on the development of liquid electrolyte  
1546 models and the considerations needed when modelling these materials, before moving on to  
1547 their applications in measuring different properties.

1548 Atomistic modelling of liquid electrolytes can be broadly separated into *ab initio* and  
1549 classical (potentials-based) Molecular Dynamics (MD) modelling (c.f. section 2.1.6). These  
1550 are complementary techniques which can be used to aid each other. For example, *ab initio*  
1551 calculations are able to provide information on the electron distribution, required for param-  
1552 eterising the non-bonded components of force fields used in classical MD. Classical MD can  
1553 also be used to provide the starting conditions for DFT calculations. *Ab initio* and classical  
1554 methods can also be combined in quantum mechanics/molecular mechanics (QM/MM) stud-  
1555 ies, where the larger system is treated classically with a smaller sub-region being modelled  
1556 using *ab initio* methods. For example, a study by Fujie et al. used the “Red Moon” method  
1557 to investigate the formation of the SEI at the metallic electrode.<sup>311</sup>

1558 In this section, we first discuss the separate design and use of *ab initio* and classical MD  
1559 methods, followed by their application to determine properties in the bulk liquid electrolyte.  
1560 Finally, we discuss the application of atomistic methods to SEI investigations, from the  
1561 perspective of the liquid electrolyte (complementary to the solid-focused SEI discussion given  
1562 in section 3.3.5).

### 1563 4.2.3 *Ab initio* modelling of liquid electrolytes

1564 *Ab initio* calculations on liquid electrolytes provide critical information that can be used  
1565 to explain their behaviour in experimental applications. For many years, DFT calculations  
1566 (c.f. section 2.1.1) have been used to provide information on the electrochemical stability  
1567 of solvents.<sup>312</sup> Modelling the electrochemical stability allows more complex effects to be  
1568 decoupled, which is not possible through experimental techniques, and these models have  
1569 aided the understanding of the functional form of the LUMO and HOMO, opening routes  
1570 to raise the stability window by design. Computational models were further developed in  
1571 2011 when Ong et al. used a combined MD and DFT approach to model the electrochemical  
1572 stability window of several ionic liquids with a higher degree of accuracy than previously  
1573 seen.<sup>313</sup> This methodology has since been widely used in studying the stability of various  
1574 ions in solution, with many key studies being based on the initial work of Vuilleumier and  
1575 Sprik.<sup>314</sup> Here, the authors modelled the ionisation of sodium and silver using *ab initio* MD  
1576 (AIMD), which was later extended to model fluctuations in the coordination shells,<sup>315</sup> and  
1577 then to model copper<sup>316</sup> ions and the redox of molecular species.<sup>317</sup> However, the applicability  
1578 of any such method is somewhat dependent on the solvent. This point was made clear by  
1579 Lynden-Bell on the subject of the difficulties of applying Marcus theory to ionic liquids,  
1580 where long range electrostatic interactions may become important.<sup>318</sup> This type of modelling  
1581 is important, as single atom events cannot easily be viewed in isolation, experimentally.

1582 *Ab initio* modelling using DFT provides a parameter-free approach to simulating the  
1583 properties of liquid electrolytes. For example, Ganesh et al. demonstrated the use of AIMD of  
1584 liquid electrolytes, using the PBE-generalised gradient approximation (PBE-GGA) exchange-  
1585 correlation functional to calculate the statistical and dynamic properties.<sup>319</sup> They performed  
1586 simulations of LiPF<sub>6</sub> at 310 K and 400 K in EC and PC at densities comparable with typical  
1587 experimental compositions. They observed a spontaneous decomposition of LiPF<sub>6</sub> into Li<sup>+</sup>  
1588 and PF<sub>6</sub><sup>-</sup> and a coordination number of 4 for solvated Li<sup>+</sup>, similar to experimental observa-  
1589 tions. The plots of the radial distribution function (RDF) of Li-ion with the carbonyl oxygen

1590 of EC and PC are shown in Figure 22. The Li-O (carbonyl) near-neighbour distance in PC  
 1591 is found to be  $\sim 1.94$  Å at 310 K and  $\sim 1.90$  Å at 400 K, quite close to the experimentally  
 1592 measured distance of  $\sim 2.04$  Å by time of flight neutron scattering experiments.<sup>320</sup> The Li-O  
 1593 (carbonyl) peak for EC is  $\sim 1.92$  Å at 310 K and  $\sim 1.90$  Å at 400 K, which is quite close to  
 1594 that for PC. Comparatively, a classical MD simulation predicted a Li-O (carbonyl) peak at  
 1595  $\sim 1.70$  Å.<sup>321</sup> The Li-O=C bond angle distribution is shown in the inset of Figure 22. The  
 1596 center of the distribution for PC is at  $140^\circ$  which is in agreement with the experimentally  
 1597 measured value of  $138^\circ$ .<sup>320</sup> Here, the distribution for EC is predicted to be similar to that  
 1598 for PC. Calculations using classical MD simulation also predict EC and PC to have similar  
 1599 distributions, though at a much higher Li-O=C angle  $\sim 160^\circ$  for both solvents.<sup>321</sup>

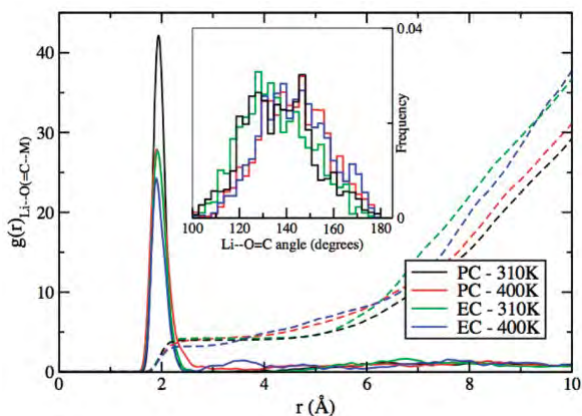


Figure 22: Partial radial distribution function of Li-ion with the carbonyl oxygen of EC and PC along with the partial-density weighted integral (dashed lines) which equals the Li-ion coordination number. In both electrolytes, the Li-O (carbonyl) distance is  $\sim 2$  Å and the first-solvation shell of Li-ion has 4 EC or PC molecules, consistent with the experiments. The inset shows the histogram of the Li-O=C angle. Reprinted with permission from Ref. 319. Copyright 2011 American Chemical Society.

1600 Perhaps the most enticing possibility regarding *ab initio* methods at interfaces is to study  
 1601 the liquid-electrode interfacial behavior. The physics of such a study are, however, complex  
 1602 and therefore trade-offs in functional choice and solvent model may need to be made, in order  
 1603 to make calculations feasible. Lespes and Filhol used an implicit solvent model to study the  
 1604 interfacial electrochemistry of lithium EC solutions.<sup>322</sup>

1605 While AIMD is free from the effects of arbitrary parameters and is highly accurate, a

1606 major limitation of this approach is the high computational cost, restricting the reachable  
1607 time- and length-scales to just tens of pico-seconds and between hundreds (conventional  
1608 DFT) and thousands of atoms (linear-scaling DFT approaches, c.f. section 2.1.2), resulting  
1609 in inaccuracies and irregularities in the calculations.

1610 When considering the impacts of small length scales, the critical issue is the introduc-  
1611 tion of spurious long- to medium-range correlations of atoms and molecules. As liquids do  
1612 not exhibit long-range order, the presence of periodic images that are located at exactly a  
1613 cell's width in all directions introduces an unphysical correlation. This is observed in the  
1614 modelling of systematically disordered solids in smaller cells.<sup>323</sup> For example, Zhao et al.  
1615 recently revealed that there is a distribution of different, low-symmetry, local motifs in cubic  
1616 halide perovskites, such as tilting and rotations, which are only observed if you allow for  
1617 a larger-than-minimal cell size.<sup>324</sup> Beyond truncating the RDF to a shorter distance than  
1618 is optimal (i.e. half the shortest distance between periodic images), this effect will also in-  
1619 troduce (normally small) inaccuracies in thermodynamic and dynamic quantities.<sup>85,325–327</sup>  
1620 These inaccuracies are of a particular concern in liquid electrolytes, as the electrostatic in-  
1621 teractions between ions gives rise to longer range interactions, even when the Debye length  
1622 is far smaller than the system size.<sup>328</sup>

1623 The short time scales of *ab initio* simulations can, particularly for more viscous liquids,  
1624 lead to highly non-ergodic (fully-sampled) simulations. When snapshots throughout the  
1625 whole trajectory are highly correlated,<sup>329</sup> this can lead to problems for both dynamic and  
1626 equilibrium studies.

1627 Often, neither time correlation nor finite size have a significant detrimental effect on  
1628 the reproducibility of experimental results in *ab initio* studies. However, in specific studies  
1629 where they need to be avoided, or where a quantum description of a liquid electrolyte pro-  
1630 vides no significant advantage over a classical description, it is beneficial to turn towards  
1631 far less computationally expensive potentials-based simulations, allowing larger and longer  
1632 simulations.

#### 1633 4.2.4 Classical modelling of liquid electrolytes

1634 Classical simulation of liquid electrolytes includes classical force field-based MD (c.f. sec-  
1635 tion 2.1.6) and the related field of classical Monte Carlo (MC) (c.f. section 2.1.5). Classical  
1636 MD, also known in solid-state communities as potentials-based MD, is a broad field which  
1637 uses many different types of force fields for different studies. The development of force fields  
1638 for ionic solids is described in section 2.2.2, whereas here we evaluate the force fields used  
1639 for liquid electrolytes and the considerations for developing them. Historically, force fields  
1640 for different electrolyte systems have developed at similar paces. Here, we use the example  
1641 of the development of force fields for ionic liquids.

1642 Electrolyte solvents, from water to molecular solvents and ionic liquids, pose a challenge  
1643 that is not normally present in the solid-state, specifically the need to model covalent bond-  
1644 ing. This is achieved by splitting the potential acting on each atom into bonding and non-  
1645 bonding contributions. The non-bonding component accounts for the effects of electrostatics,  
1646 dispersion, and degeneracy pressure; and the bonding component accounts for the effects of  
1647 covalent bonding. In classical modelling of liquid electrolytes, we are mainly interested in  
1648 the behaviour within the electrolyte’s electrochemical stability window (c.f. section 4.1).  
1649 Therefore, the vast majority of classical studies model bonds with unbreakable, harmonic  
1650 potentials. There are four distinct types of bonded potential:<sup>329,330</sup> bonds, angles, dihedrals,  
1651 and improper dihedrals. These can be traced back to the parameterisation of force fields,  
1652 such as OPLSA-AA,<sup>331,332</sup> and are often parameterised from spectroscopic force constants.  
1653 There are many ways of defining bonded potential types in available codes,<sup>113,330</sup> though  
1654 their discussion is beyond the scope of this review. Atoms which are subject to a bonded  
1655 potential are often wholly, or partially, excluded from non-bonded interactions, though in  
1656 large molecules, non-bonded intramolecular interactions are important. Alternatively, bonds  
1657 can be kept rigid using a constraint algorithm.<sup>333–335</sup>

1658 When developing force fields, generally, it is the non-bonded force field components, in  
1659 particular the partial charges on atoms, which are more frequently varied. A common model



1660 for liquid electrolytes is the OPLS-AA force field.<sup>332</sup> This is a Lennard-Jones potential-  
1661 based force field with an additional coulombic term.<sup>336-339</sup> Further developments can be  
1662 made from this base force field, such as the CP&P force field,<sup>331,340-342</sup> describing a wide  
1663 range of ionic liquid cations and anions. Some non-bonded parameters, particularly charges,  
1664 were varied from OPLS-AA. The charges on the individual molecules are obtained from DFT  
1665 calculations, in this case by use of the charge mapping algorithm CHelpG<sup>331</sup> (though other  
1666 algorithms may also be used.<sup>343-345</sup>)

1667 Electrostatic interactions are important when modelling charged electrolytes, as are the  
1668 effects of polarisability. Often it is advantageous in a non-polarisable force field to scale the  
1669 charge on each ion down from a value of  $1e$ .<sup>346-348</sup> This accounts for the effect of polarisability  
1670 on the strength of electrostatic interactions between ions, which is particularly important  
1671 for transport properties. However, other force fields have been defined to account directly  
1672 for polarisability.<sup>347</sup> As described in section 2.2.2, polarisability can be introduced to a force  
1673 field by the employment of Drude Oscillators (core shell model).<sup>330,346,347</sup> This approach is  
1674 computationally cheap and is core to the polarisable ionic liquid force field developed from  
1675 CL&P by Schröder.<sup>346</sup> A more advanced representation of polarisability can be provided  
1676 by intrinsically polarisable force fields, normally based on the Fumi-Tosi potential.<sup>349</sup> This  
1677 method has been used for molten salts,<sup>350</sup> ionic liquids,<sup>347,351</sup> and lithium salts in molecular  
1678 solvents.<sup>352-354</sup> This provides the best description of polarisability in a classical force field,  
1679 however, there is an associated higher computational cost, and a particular code, such as  
1680 metalwalls,<sup>355</sup>) is often required to implement it.

1681 The development of force fields for metal cations has seen an equal level of discussion  
1682 and interest. These cations can be slightly easier to model, owing to their relative non-  
1683 polarisability.<sup>347,356,357</sup> They are frequently modeled as Lennard-Jones spheres to match the  
1684 potential in the prevailing solvent models (SPC and OPLS-AA). For alkali and alkali earth  
1685 metal cations, a wide range of values of  $\sigma$  (excluded volume) and  $\epsilon$  (interaction strength)  
1686 can be used, as the basic energetics associated with one of these force fields can be recovered

1687 for many pairs of sigma and epsilon values. The choice of which pair of parameters to use is  
1688 normally driven by which property requires the highest degree of accuracy for the targeted  
1689 study.<sup>356</sup> It is worth noting that many force fields used to modeled the electrolytes of specific  
1690 interest to us here, were parameterised for aqueous solutions.<sup>356</sup>

#### 1691 **4.2.5 Bulk Structure and Landscaping**

1692 For structural analysis of liquid electrolytes, analysis of the RDF is the mostly widely used  
1693 approach. Modelling of structural properties in this capacity provide more information-rich  
1694 data compared to scattering, especially in complex systems, and is less labour intensive.  
1695 RDFs can be converted to structure factors by a simple Fourier transform into reciprocal  
1696 space, allowing for easy comparison with experimental structure factors,<sup>348,358–360</sup> subject  
1697 to re-scaling for the specific intensities associated with different atoms. This method has  
1698 been used frequently for a broad array of electrolytes and has seen particular utility for ionic  
1699 liquids, where the large, inhomogenous ion surface can lead to complex patterns, for which  
1700 MD can provide explanation. Modelling of this sort of behaviour has been performed for  
1701 aprotic<sup>361</sup> solvate ionic liquids,<sup>348</sup> imidazolium salts,<sup>359</sup> lithium carbonate solutions,<sup>362</sup> and  
1702 highly concentrated aqueous solvents.<sup>358</sup>

1703 The RDF is closely related to potential of mean force acting on a particle, however, the  
1704 physical relevance of RDFs goes further than this. The mean force describes the changing  
1705 potential landscape acting between particles as they approach one another.<sup>329</sup> Information  
1706 on the potential of mean force is exceptionally challenging to obtain experimentally, which  
1707 is why modelling techniques are frequently used in colloids. As well as being generated from  
1708 a RDF, the potential of mean force can be obtained by direct calculation by use of centre  
1709 of mass pulling, umbrella sampling,<sup>330</sup> or running multiple calculations with ions frozen an  
1710 exact distance apart from one another. When modelling liquid electrolytes, this method is  
1711 also used to study the approach of ions to an electrode, where the energetics associated with  
1712 decoordination from the solvent and coordination to the electrode can be modelled. For

1713 example, Sergeev et al. looked at the approach of oxygen and lithium based species towards  
1714 electrodes.<sup>363</sup> Here, the authors performed MD simulations of the electrode/electrolyte inter-  
1715 faces of a Li-O<sub>2</sub> cathode with an experimentally relevant potential in 1 M dimethyl sulfoxide  
1716 (DMSO) solution of LiPF<sub>6</sub> salt. They find that oxygen anions are effectively pushed out of  
1717 the reaction layer, making the second reduction of superoxide anion hardly probable, indicat-  
1718 ing the main cause of the electrode surface passivation is the presence of lithium superoxide  
1719 near the electrode surface. Sergeev et al. proposes a way to suppress the passivation by shift-  
1720 ing the equilibrium  $\dot{O}_2 + Li^+ \rightleftharpoons LiO_2$  to the side of separately solvated ions, for example,  
1721 by using solvents resulting in lower free energy of the ions.<sup>363</sup>

#### 1722 4.2.6 Li-ion Diffusion

1723 Diffusion (c.f. section 2.3.3) plays a critical role in the operation of liquid electrolytes through  
1724 its impact on conductivity. However, in liquid electrolytes its impact goes deeper, as the  
1725 dielectric constant of liquids consists of both dipolar and ionic contributions. These two con-  
1726 tributions can be obtained by analysis of the dipole orientation and current auto-correlation  
1727 functions using the Einstein-Helfand method. For example, Coles et al. performed this  
1728 analysis on four liquid electrolytes (three in aqueous solvent and one in a common organic  
1729 solvent mixture): aqueous solutions of LiCl, NaI, and lithium bistriflimide (LiTFSI), as well  
1730 as the same LiTFSI salt solvated in an equimolar mixture of dimethoxyethane (DME) and  
1731 1,3-dioxolane (DOL).<sup>328</sup> Here, it was shown that for polar solvents, the dipolar contribution  
1732 is nearly always dominant, with the current making a small corrective contribution which  
1733 could feasibly be neglected (particularly for more dilute systems). For ionic liquids, which  
1734 contain ionic species that can exhibit a net dipole, such as TFSI, both dipolar and ionic  
1735 contributions would be observed. The effect of molecular ions having simultaneous charges  
1736 and dipoles was explored by Schröder, who showed that even more thorough treatment may  
1737 be required to observed the impacts of their interplay.<sup>365</sup> These contributing factors cannot  
1738 be easily/feasibly disentangled experimentally.

1739 The self-diffusion coefficient can be calculated from the slope of the mean-squared dis-  
1740 placement, according to the Stokes-Einstein relation. For example, Ganesh et al. calculated  
1741 the mean-squared displacement of solvated Li-ion in EC and PC solvents from AIMD, as  
1742 shown in Figure 23. For PC, the self-diffusion coefficient is calculated to be  $\sim 0.7 \times 10^{-9}$   
1743  $\text{m}^2 \text{s}^{-1}$  at 310 K while the experimentally measured value of self-diffusion coefficient at 303  
1744 K is  $\sim 0.16 \times 10^{-9} \text{m}^2 \text{s}^{-1}$ .<sup>366</sup> For EC, it is calculated to be  $\sim 1.0 \times 10^{-9} \text{m}^2 \text{s}^{-1}$  at 310 K,  
1745 while the experimentally measured value of self-diffusion coefficient at 313 K is  $\sim 0.21 \times 10^{-9}$   
1746  $\text{m}^2 \text{s}^{-1}$ .<sup>366</sup> At 400 K, the calculated diffusion coefficient for PC increases to  $\sim 3.7 \times 10^{-9}$   
1747  $\text{m}^2 \text{s}^{-1}$ , while it remains the same for EC. It is notable here that the Li-ion diffusion in the  
1748 electrolyte solution is 4-5 orders of magnitude higher than that in the bulk of electrodes, e.g.  
1749 in the graphite anode (cf. section 3.2.4).

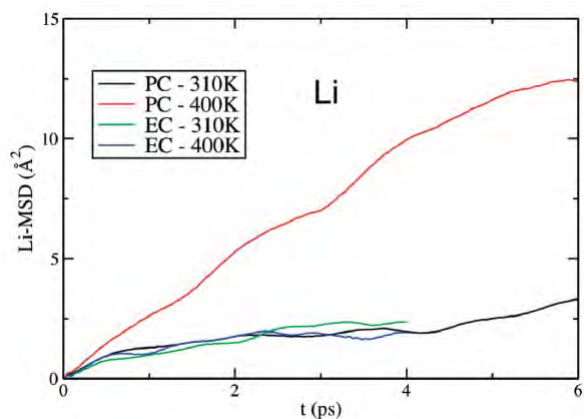


Figure 23: Mean-squared displacement of solvated Li-ion in EC and PC. Reprinted with permission from Ref. 319. Copyright 2011 American Chemical Society.

1750 Investigation of the diffusion of different ions subject to a field gives a sense of the diffusion  
1751 rate of specific ions and also an idea of exchange rates of solvent molecules. This information  
1752 can be obtained using nuclear magnetic resonance (NMR), however, atomistic models can  
1753 provide more detailed data. Strongly coordinated solvents will have diffusion coefficients  
1754 closer to the ions they are coordinated to, whereas less strongly coordinated ligands will  
1755 have diffusion coefficients dissimilar from the coordinating ion.<sup>348,352,367-369</sup> Examples of this  
1756 behaviour can be found in the MD studies of Borodin et al., which looked at diffusion in

1757 lithium solutions of both the common carbonate<sup>352</sup> and ethylene glycol oligomer solvents.<sup>368</sup>  
1758 For the common carbonate, MD predictions of the ion and solvent self-diffusion coefficients  
1759 and conductivity were in good agreement with experiments, with approximately half of the  
1760 charge transported by charged ion aggregates with the other half carried by free ions.<sup>352</sup> The  
1761 self-diffusion coefficients and conductivity predicted by MD for the ethylene glycol oligomer  
1762 solvents were also found to be in good agreement with experimental data.  $\text{Li}^+$  transport was  
1763 found to primarily occur through exchange of TFSI<sup>-</sup> anions in the first coordination shell.<sup>368</sup>  
1764 The 2015 study of Shimizu et al. investigated a number of different lithium glyme solvate  
1765 ionic liquids.<sup>348</sup> Here, the authors found that although MD was unable to yield quantitative  
1766 information about the dynamics of the system, it could provide two important pieces of  
1767 information: the auto-diffusion coefficients of glyme molecules in pure glyme are much larger  
1768 than those of glyme molecules in glyme equimolar mixtures at the same temperature; the  
1769 decrease in the glyme diffusion coefficients is more pronounced in the  $\text{Li}[\text{Ntf}_2] + \text{glyme}$  system  
1770 than in the  $\text{Li}[\text{NO}_3] + \text{glyme}$  mixture.<sup>348</sup> The study of Lesch et al. used MD to investigate  
1771 lithium salts dissolved in aprotic ionic liquids.<sup>367</sup> The authors found that the exchange of  
1772 TFSI anions in and out of the first coordination shell of  $\text{Li}^+$  was faster in  $\text{pyr}_{13}$ -based systems,  
1773 compared to emim-based systems, and that the  $\text{Li}^+$  ion transference number was higher.<sup>367</sup>  
1774 In more complex solvents, such as ionic liquids, the nature of the solvent plays an important  
1775 role too, for instance Borodin and Smith showed the effect of fluorination of ionic liquid  
1776 cations on diffusion behaviour.<sup>369</sup> This sort of study can be directly compared with pulsed  
1777 field gradient NMR experiments of battery materials. This was done, for example, when  
1778 Shimizu et al. studied a LiTFSI-based solvate ionic liquid, which had been proposed as  
1779 a solvent for Lithium Sulfur batteries.<sup>348</sup> The authors found the molecular behaviour of  
1780 solvate ionic liquids to be probed effectively using a combination of MD trajectories and  
1781 structural/aggregation analysis techniques.

### 1782 4.2.7 Solvation Energies

1783 Solvation energies in electrolytes have been widely studied and, though research focus has  
1784 been on aqueous solvation of biomolecules, these techniques can also be used to look at  
1785 solvation of metal ions with organic solvents. Dependent on the exact thermodynamics  
1786 of the system, the solvation energies of ions may be obtained by a number of methods.  
1787 Skarmoutsos et al. combined DFT and MD methods to look at the solvation structures of  
1788 lithium salts in ternary mixtures of different carbonate solvents and showed that different  
1789 solvents were found to dominate at different distances from a central lithium cation, observing  
1790 a particular preference for solvation of lithium by DMC ions over PC and EC, as shown in  
1791 Figure 24. Takeuchi et al. looked even deeper at the energetics behind the direct contact  
1792 between cations and anions in solution.<sup>371</sup> The relative stabilities of the mono-, bi-, and tri-  
1793 dentate coordination structures were assessed with and without solvent, where water, PC,  
1794 and DMC were found to favour the ion pair (CIP)–solvent contact. Vacant sites of  $\text{Li}^+$  cation  
1795 in CIP are solvated with three carbonyl oxygen atoms of PC and DMC solvent molecules,  
1796 and the solvation is stronger for the monodentate CIP than for the multidentate.<sup>371</sup> Such  
1797 detailed analysis is not possible to resolve through experimental techniques.

1798 These are just a few notable studies on solvation energies in liquid electrolytes. A full  
1799 theoretical description of solvation is given by Lazaridis.<sup>372</sup>

### 1800 4.2.8 Activity coefficients of electrolytes

1801 The activity coefficients describe the deviation of actual electrolytes from an ideal mixture  
1802 of substances<sup>171</sup> and can be calculated using DFT+PBE simulations (c.f. section 2.1.1) of  
1803 solutes in electrolyte solutions, as described in sec 2.3.2. The experimental value of bulk  
1804 permittivity of EC is ( $\epsilon^\infty = 90.7$ )<sup>373</sup> and its surface tension is ( $0.0506 \text{ N m}^{-1}$ ).<sup>374</sup> These  
1805 values were used by Dziejcz et al. to calculate the activity coefficient of  $\text{LiPF}_6$  in EC.<sup>135</sup>  
1806 The solvent radius was set to  $R_k^{\text{solvent}} = 10.5 a_0$ , to approximate the size of an EC molecule,  
1807 and the isovalue of solute electronic density, ( $\rho_e^\lambda$ ), is varied to match the experimental activity

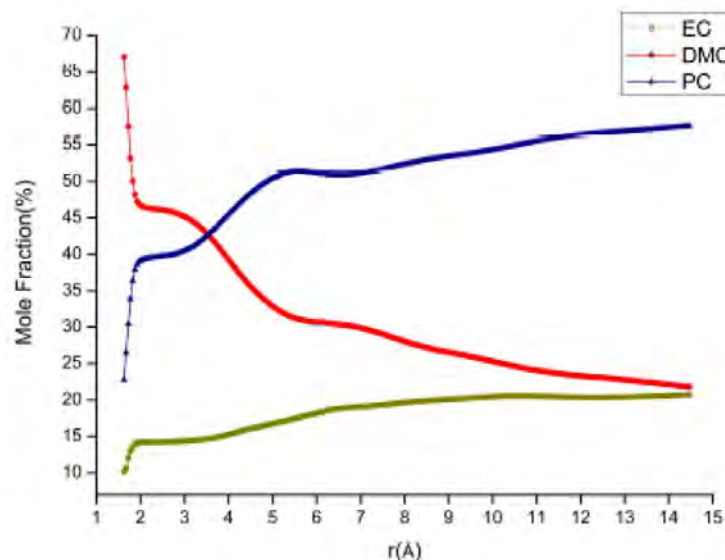


Figure 24: Local mole fractions (%) of ethylene carbonate, propylene carbonate, and dimethyl carbonate as a function of the distance from the lithium cation in the ternary mixture. Reprinted with permission from Ref. 370. Copyright 2015 American Chemical Society.

1808 coefficients. A plot of the computed activity coefficients as a function of the square root of  
 1809 electrolyte concentration is given in Figure 25, along with experimental values from Stewart  
 1810 and Newman.<sup>375</sup> Here, we see a good agreement for  $\rho_e^\lambda = 0.002 e/a_0^3$ . Trends are also plotted  
 1811 from the linearised approximation of PBE, where the solvent radius is reduced to resemble  
 1812 the prediction for point charges from the Debye-Hückel theory.<sup>376</sup> The thermodynamic factor  
 1813 can be obtained from numerically differentiating these curves. This is a novel technique of  
 1814 calculating activity coefficients and thermodynamic factors from hybrid atomistic-continuum  
 1815 methods.

#### 1816 4.2.9 Interfacial Nanostructure of Electrolytes

1817 In sections 3.3 and 5.4, the interfaces between solids and liquids from the perspective of  
 1818 the solid have been discussed. However, the interface from the perspective of the liquid is  
 1819 also of interest. The structure of liquid electrolytes at metallic<sup>377</sup> and charged dielectric<sup>378</sup>  
 1820 interfaces will normally extend away from the interfacial region and can be observed promi-  
 1821 nently for tens of nanometers and, dependent on concentration of the liquid, can either be

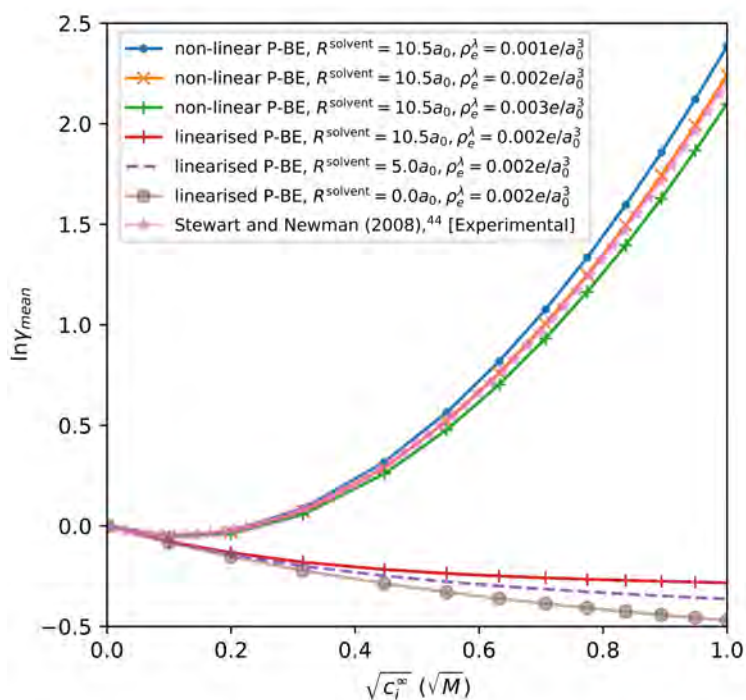


Figure 25: Mean activity coefficients for  $\text{LiPF}_6$  in ethylene carbonate at  $T = 308$  K as a function of concentration and for different values of the atomic electronic density isovalue parameter which determines the extent of the accessibility function. Calculations with the linearised approximation to P-BE are also shown. Reprinted with permission from Ref. 135. Copyright 2020 American Chemical Society.



1822 monotonic or oscillatory, as described in section 4.2. Spectroscopic and surface methods  
1823 used to study the liquid–solid interface are often indirect, requiring specific conditions for  
1824 analysis (e.g. transparency and smoothness), which often constrain the interfaces we can  
1825 study. Computational modelling provides a route to direct and data rich understanding of  
1826 the liquid solid interface.

1827 Concentrated electrolytes and ionic liquids both adopt the characteristic overscreening  
1828 structure at charged interfaces, including electrodes. This structure, comprising oscillations  
1829 of charge decaying into the bulk, is commonly observed.<sup>377,379</sup> Modelling these systems re-  
1830 quires an appropriate electrode model. While interesting information can be gained from  
1831 simulating ions at an electrode with a fixed charge, for example in a high throughput study  
1832 looking at structural changes with electrode surface charge,<sup>379</sup> fixed potential boundary con-  
1833 ditions will provide a more accurate description of the capacitance,<sup>377,380</sup> interfacial struc-  
1834 turing of a liquid electrolyte,<sup>379,381,382</sup> and the decoordination and dechelation dynamics of  
1835 coordinated ions.<sup>383</sup> Though we note that, in light of a recent study by Scalfi et al., this  
1836 field continues to evolve as more nuanced classical electrode models are employed, such as  
1837 the Thomas-Fermi based model proposed by Scalfi et al..<sup>380</sup>

1838 A wide variety of different electrolytes have been studied using fixed potential electrolytes,  
1839 from ionic liquids to concentrated electrolyte. Both nanoporous<sup>381,383–385</sup> and nanoscopically  
1840 rough electrode surfaces have been heavily used.<sup>386</sup> A specific example of interest is the  
1841 work of Borodin and Bedrov, where MD simulations were performed on dilithium ethylene  
1842 dicarbonate ( $\text{Li}_2\text{EDC}$ ) and dilithium butylene dicarbonate ( $\text{Li}_2\text{BDC}$ ), in contact with mixed  
1843 solvent electrolyte (EC:DMC) doped with  $\text{LiPF}_6$ .<sup>387</sup> In this study, the authors examined the  
1844 SEI–electrolyte interface and found an increase of EC and  $\text{PF}_6^-$  molecules and a decrease of  
1845 DMC at the interfacial layer next to the SEI surface, compared to bulk electrolyte concen-  
1846 trations. The activation energies for the  $\text{Li}^+$  solvation–desolvation reaction were estimated  
1847 to be 0.42–0.46 eV for the  $\text{Li}_2\text{EDC}$ –electrolyte and  $\text{Li}_2\text{BDC}$ –electrolyte interfaces.

#### 1848 4.2.10 Outlook and challenges

1849 Liquid electrolytes will likely remain the most prominent form of commercialised electrolyte  
1850 for battery applications in the near future. This is partly due to their monopoly in the  
1851 market and partly due to their low cost, which will continue to drive popularity. Despite  
1852 the overwhelming success of commercial liquid electrolytes, there is still room for further  
1853 performance improvements, with several key issues as limiting factors. Liquid electrolytes  
1854 are known to be limited by narrow electrochemical windows, solvent toxicity, and material  
1855 flammability/safety concerns. There are two potential avenues for solving these issues:

- 1856 • Resolving these limitations within the confines of liquid electrolytes: ionic liquids have  
1857 a large electrochemical window and high thermal stability, and their conductivities  
1858 are similar to those of conventional organic solvent solutions.<sup>305</sup> However, they are  
1859 expensive and there are associated safety concerns.<sup>280,281</sup> A liquid electrolyte alternative  
1860 to this could be in water-in-salt electrolytes. Water-in-salt electrolytes are a novel  
1861 class of electrolytes, which inverts the conventional idea of a salt being dissolved in  
1862 a solvent, with a small amount of water being dissolved in a hygroscopic lithium salt  
1863 to the point where a liquid is obtained,<sup>388,389</sup> analogous to the high concentration  
1864 organic electrolyte solutions described by Yamada et al..<sup>304</sup> These liquids have the  
1865 advantage of being comprised solely of a lithium salt and water, which decreases cost  
1866 and eliminates the toxicity and risk of flammability and thermal runaway traditionally  
1867 associated with organic solvents. The high concentration of salt also leads to a greatly  
1868 expanded electrochemical window of 3 V<sup>306</sup> from the 1.23 V value for dilute aqueous  
1869 solutions. However, the highly concentrated solutions in these electrolytes lead to re-  
1870 crystallisation of the lithium salt and low conductivity, due to the high viscosity of the  
1871 liquid.<sup>389,390</sup>
- 1872 • Replacing liquid electrolytes with solid or soft matter alternatives: despite the suc-  
1873 cess of liquid electrolytes in LiBs, a number of issues have arisen that may prove

1874 impractical to address within the grouping of liquids. Organic liquid electrolytes are  
1875 highly flammable, leading to safety issues, such as thermal runaway, when deployed  
1876 in portable electronic devices and EVs.<sup>17,18,391</sup> These safety issues may have a low fre-  
1877 quency of occurrence, but when used often by a large number of people, they become  
1878 nearly inevitable events, as evidenced by EV and portable device explosions making  
1879 the news headlines.

1880 The use of liquid electrolytes also limits the compatibility with electrode materials and  
1881 thereby limits the maximum energy density of a battery.<sup>19</sup> For example, higher energy  
1882 density lithium sulfur (Li-S) batteries are unstable, due to interactions between the  
1883 liquid electrolyte and the electrodes.<sup>392</sup> Similarly, Li metal anodes cannot be used with  
1884 organic liquid electrolyte solvents without additives,<sup>393</sup> because of dendrite formation  
1885 and capacity loss.<sup>394,395</sup> Due to these concerns, research in recent years has shifted  
1886 to looking at alternatives, such as solid and soft matter-based electrolytes.<sup>26</sup> Solid  
1887 electrolytes are discussed in detail in the next section (c.f. section 4.3) and soft matter  
1888 electrolytes are discussed in detail by Hallinan Jr and Balsara and Popovic.<sup>396,397</sup>

1889 The design of the electrode-electrolyte interfaces affects the capacity and rate capabil-  
1890 ity in LiBs.<sup>288,291</sup> Further work to design better interfaces that are compatible with the  
1891 electrodes, thermodynamically stable, kinetically fast for Li-ion transfer, electronically in-  
1892 sulating, and which lead to minimal loss in performance, will be crucial to progress LiB  
1893 performance.<sup>2,289,290</sup> Atomistic modelling can help in this area by analysing the chemical re-  
1894 actions leading to SEI formation and predicting new materials which form a well-structured  
1895 SEI, conducive to ion transmission.<sup>16</sup> Further details of the formation and function of the  
1896 SEI at the graphite anode are summarised in section 3.3.5.

1897 Liquid electrolytes are complex substances and are therefore difficult to fully capture  
1898 in atomistic models. In recent years, computational capacity has expanded, allowing more  
1899 complex models to be studied. Alongside this, new computational methods have been de-  
1900 veloped under the open source license, allowing research of these materials to become more

1901 accessible.<sup>355,384,387,398</sup> Future advances in computational ability, combined with improved  
1902 experimental studies, provide a framework for high throughput screening of electrolyte ma-  
1903 terials.

1904 Developments in expanding the achievable time and length scales of AIMD will allow  
1905 more complex models to be developed. However, it is still implausible that AIMD will be  
1906 able to simulate whole electrodes/interfaces/battery cells for long enough time and length  
1907 periods to achieve full ergodicity (statistical convergence). Therefore, methods which can  
1908 provide long scale simulations are still needed. In particular, the emerging fields of fitting  
1909 machine learnt potentials for liquid electrolytes,<sup>399–401</sup> and more complex classical models  
1910 which incorporate polarisability<sup>347,355</sup> or bond breaking dynamics.<sup>402,403</sup> This would enable  
1911 simulations of electron transfer, bond formation, and the effect of ion and solvent polaris-  
1912 ability at larger scales and in greater detail.

1913 Atomistic modelling of liquid electrolytes does not necessarily require more computational  
1914 expense to advance. Exploitation of underused physical methods to model liquid systems at  
1915 far lower cost has been explored. One such method, classical DFT, has already been applied  
1916 to model aqueous capacitors<sup>404</sup> and confined ionic liquids.<sup>405</sup> This has the potential to be  
1917 coupled with electronic DFT (c.f. section 2.1.1) to model electron transfer.<sup>406</sup>

1918 It should be emphasised that, for practical use, the interfaces between the liquid elec-  
1919 trolyte and the electrodes are the major limiting factors in terms of performance, stability,  
1920 and safety. Therefore, advancement through electrolyte design is crucial, where the critical  
1921 obstacles discussed here could be resolved by the use of novel, solvents, salts, or electrolyte  
1922 salts. Several articles discuss the challenges of this topic in greater detail.<sup>407–409</sup>

## 1923 **4.3 Solid Electrolytes**

### 1924 **4.3.1 Introduction**

1925 Solid electrolytes have attracted considerable attention as an alternative to highly-flammable  
1926 liquid electrolytes, as they significantly improve device safety and have the potential to im-

1927 prove energy and power densities, while also reducing the cost of synthesis.<sup>283,410–413</sup> An  
1928 ideal solid electrolyte material should possess high electronic resistance, high ionic conduc-  
1929 tivity, outstanding thermal stability, strong electrochemical stability, excellent mechanical  
1930 strength, and reduced interfacial resistance.<sup>414,415</sup> There are three different categories of solid  
1931 electrolytes used in rechargeable batteries:<sup>413</sup> (1) inorganic ceramic electrolytes, (2) organic  
1932 polymer electrolytes, and (3) composite electrolytes.

1933 Solid electrolytes were discovered by Michael Faraday in the early 1830s through research  
1934 on the conduction properties of heated solid silver sulfide ( $\text{Ag}_2\text{S}$ ) and lead fluoride ( $\text{PbF}_2$ ).<sup>416</sup>  
1935 The use of a ceramic-based  $\beta$ -alumina ( $\text{Na}_2\text{O}\cdot 11\text{Al}_2\text{O}_3$ ) in high-temperature sodium-sulfur  
1936 (Na-S) batteries in the 1960s was considered as a milestone in the development of batteries,  
1937 enabled by solid electrolytes.<sup>417</sup> In the 1980s, the Zeolite Battery Research Africa (ZEBRA)  
1938 group developed the “ZEBRA” batteries using  $\text{Na}_2\text{O}\cdot 11\text{Al}_2\text{O}_3$  as the solid electrolyte.<sup>418</sup> So  
1939 far, the Na-S battery has been commercialised in Japan,<sup>419</sup> whereas the ZEBRA battery is  
1940 currently being developed by the General Electric Corporation in the United States.<sup>420</sup>

1941 In 1990, the Oak Ridge National Laboratory synthesised a lithium phosphorus oxynitride  
1942 (LiPON) material,<sup>421,422</sup> opening up the use of inorganic solid-state electrolytes in LiBs.  
1943 Since then, a huge number of inorganic, lithium-ion conductive ceramic materials have been  
1944 developed, including perovskite-type,<sup>423</sup> garnet-type oxides,<sup>424,425</sup> garnet-type sulfides,<sup>426</sup>  
1945 lithium super ionic conductor (LISICON),<sup>427</sup> sodium super ionic conductor (NASICON)-  
1946 like materials,<sup>428</sup> lithium-argyrodite materials,<sup>429</sup> and Li-rich anti-perovskites.<sup>430,431</sup>

1947 Despite recent advancements in crystalline inorganic electrolytes, they are still brit-  
1948 tle and therefore difficult to fit into different battery shapes. Solid-state polymer elec-  
1949 trolytes (SSPEs), due to their high flexibility, can fit into any battery shape and present  
1950 improved safety and stability features compared to crystalline inorganic electrolytes.<sup>413</sup>  
1951 Since 1980, various high molecular weight, dielectric polymer hosts were investigated for  
1952 LiBs as high conductivity electrolytes, such as poly(ethylene oxide) (PEO),<sup>432</sup> polyacry-  
1953 lonitrile (PAN),<sup>433,434</sup> poly(vinylidene fluoride) (PVDF),<sup>435–437</sup> poly(methyl methacrylate)

1954 (PMMA),<sup>438,439</sup> and poly(vinylidene fluoride-hexa-fluoropropylene) (PVDF-HFP).<sup>440–442</sup>

1955 The ionic conductivities of most polymer electrolytes are significantly lower than those of  
1956 both oxide solid electrolytes and liquid electrolytes.<sup>443</sup> A possible solution to this limitation is  
1957 to create composites by integrating nanoscale, highly conductive, inorganic, particulate fillers  
1958 into the polymer electrolyte material.<sup>413</sup> This enhances the ionic conductivity and improves  
1959 the mechanical strength and stability of the SSPEs, including the interfacial stability.<sup>444</sup>  
1960 Here, heterogeneous doping increases the ionic conductivity as a result of increasing inter-  
1961 facial regions between an inert solid phase, such as silica, alumina, or boron oxide particles,  
1962 and an electrolyte.<sup>445</sup> A wide range of inorganic solid composite electrolytes have previously  
1963 been studied, based on oxides ( $\text{Li}_2\text{O}:\text{Al}_2\text{O}_3$ ,<sup>446</sup>  $\text{Li}_2\text{O}:\text{B}_2\text{O}_3$ ,<sup>447–449</sup>) hydrides ( $\text{LiBH}_4:\text{SiO}_2$ ,<sup>450</sup>)  
1964 halides ( $\text{LiI}:\text{Al}_2\text{O}_3$ ,<sup>451</sup>  $\text{LiI}:\text{SiO}_2$ ,<sup>452</sup>  $\text{LiF}:\text{Al}_2\text{O}_3$ ,<sup>453</sup>) and sulfides ( $\text{Li}_2\text{S}:\text{SiS}_2$ .<sup>454</sup>)

1965 Over the last decade, a limited number of candidates with high ionic conductivities ( $>1$   
1966  $\text{mS cm}^{-1}$ ) have arisen as potential competitors to liquid electrolytes.<sup>455–463</sup> Figure 26 presents  
1967 the ionic conductivities of most currently known solid electrolytes.<sup>26</sup>

1968 In this section, we review atomistic modelling investigations into the structure-property  
1969 relationships in selected solid-state electrolytes:  $\text{Li}_{10}\text{GeP}_2\text{S}_{12}$  (LGPS), lithium argyrodites,  
1970 and  $\text{Li}_7\text{La}_3\text{Zr}_2\text{O}_{12}$  (LLZO), belonging to the inorganic solid ceramic electrolyte type, and  
1971  $\text{Li}_2\text{O}:\text{B}_2\text{O}_3$  materials, belonging to the oxide-based solid composite type. A particular focus  
1972 is given to the ion transport mechanism in those materials, which is important for reaching  
1973 high conductivities, a key property of battery materials. Finally, we take a more detailed  
1974 look at the interface of solid electrolytes with the electrodes, and discuss the challenges and  
1975 outlook for future atomistic modelling investigations.

### 1976 4.3.2 Sulfides

1977 There are a substantial number of computational studies of sulfides which largely relate  
1978 to a recent emergence of newly discovered crystalline sulfide superionic conductors. Sul-  
1979 fides also tend to have comparatively lower intrinsic electrochemical and chemical stability,

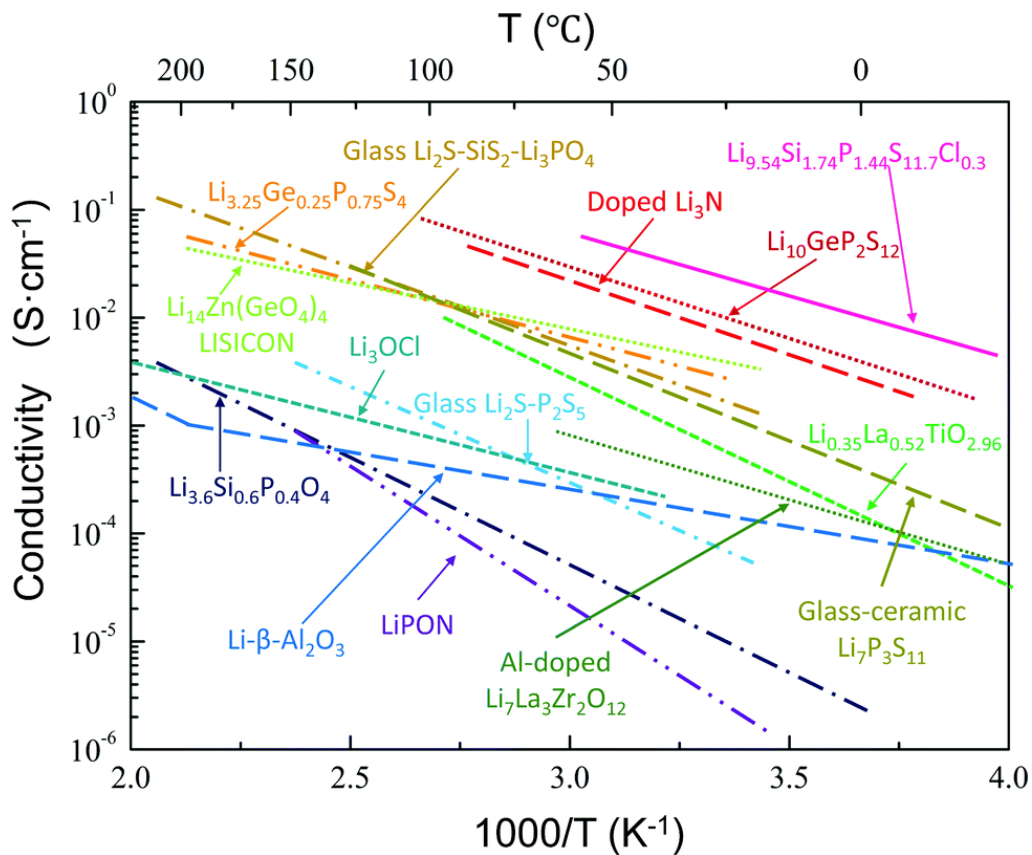


Figure 26: Ion conductivity of several well-known solid lithium ion conductors, including glass and crystalline conductors. Reproduced from Ref. 26 - Published by The Royal Society of Chemistry.

1980 which has stimulated interest in understanding the interfacial interactions within batteries.<sup>28</sup>  
1981 The sulfide group encompasses a range of sulfide-based solid electrolytes, including glass  
1982 ceramics,<sup>464</sup> argyrodites,<sup>465</sup> and thio-LISICONs.<sup>466</sup> Some of the most promising solid elec-  
1983 trolytes to emerge in recent years include LGPS,<sup>286,467,468</sup> and the Li-argyrodite ( $\text{Li}_6\text{PS}_5\text{X}$ ,  
1984  $\text{X}=\text{Cl,Br,I}$ )<sup>429,469-473</sup> families of superionic conductors.

1985 **LGPS** A study by Kamaya et al. reports that LGPS can reach high room temperature  
1986 ionic conductivities of  $12 \text{ mS cm}^{-1}$ , comparable to that of commercial liquid electrolytes ( $\sim$   
1987  $10 \text{ mS cm}^{-1}$ ).<sup>286</sup> The authors also determined that diffusion in LGPS is anisotropic, where  
1988  $c$  directional motion is predominant over the  $ab$  plane, with an overall energy barrier for Li  
1989 diffusion being  $0.24 \text{ eV}$ , with later reports measuring  $0.22 \text{ eV}$ .<sup>474</sup> Using AIMD, Mo et al. later  
1990 determined the average direction energy barriers of  $0.17 \text{ eV}$  along the  $c$  channel and  $0.28 \text{ eV}$   
1991 in the cross channel ( $ab$  plane),<sup>468</sup> with Xu et al. showing the Li migration mechanism is  
1992 through cooperative motion, instead of the initially determined single hop mechanism.<sup>475</sup>  
1993 More recently, Adams and Prasada Rao predicted the presence of additional Li sites using  
1994 MD, which would allow diffusion along the  $ab$  plane.<sup>476</sup> These sites could change not only  
1995 the Li occupancies in the  $c$  channel, but also provide a diffusion mechanism involving the  $ab$   
1996 plane, opening up the possibility of cross-channel diffusion. The presence of these additional  
1997 sites were later confirmed experimentally using single crystal X-ray Diffraction (XRD).<sup>477</sup>

1998 More recently, Bhandari and Bhattacharya also investigated the lithium diffusion dimen-  
1999 sionality in LGPS by performing a DFT study of the lithium diffusion energy barrier, using  
2000 the nudged elastic band (NEB) method.<sup>467</sup> In this study, the authors took into account  
2001 the fractional occupancies leading to variable  $c$  channel Li populations, variable chemical  
2002 environments surrounding Li, and all possible migration mechanisms. The authors found  
2003 that lithium diffusion is neither purely  $c$  directional nor purely along the  $ab$  plane, but there  
2004 exists a correlated mechanism of motion along  $c - ab$  which critically controls the degree  
2005 of anisotropy of Li diffusion in LGPS. The energy barriers for different mechanisms of Li-  
2006 diffusion, shown in Figure 27, suggest that correlated hopping has the lowest energy barrier.



2007 Bhandari and Bhattacharya further performed a statistical average of all diffusion energy  
 2008 barriers, taking into account the formation energy of various Li configurations and predicting  
 2009 an overall energy barrier of 239 meV,<sup>467</sup> which is in close agreement with experiments.<sup>286</sup>  
 2010 Thus, the DFT approach not only explained the overall diffusivities and energy barriers,  
 2011 but also gave insight into the underlying mechanism behind the fast Li diffusion in LGPS,  
 2012 resolving the discrepancy about the anisotropy of Li diffusion in this compound.

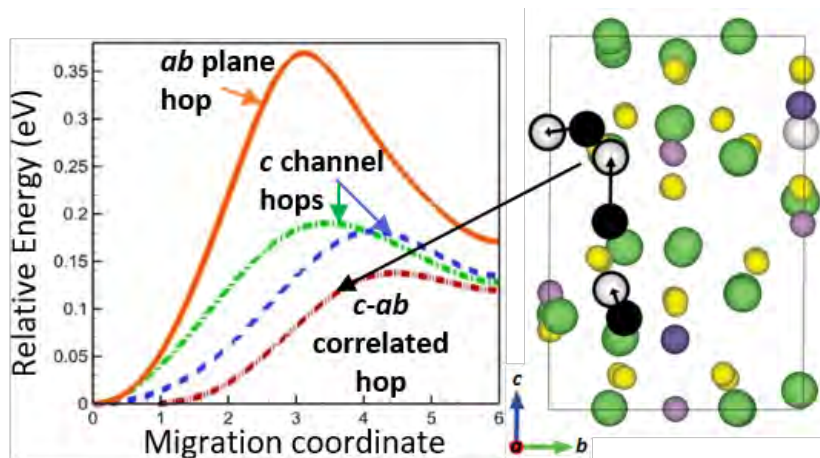


Figure 27: Energy barrier for Li-ion diffusion in the solid electrolyte,  $\text{Li}_{10}\text{GeP}_2\text{S}_{12}$  (LGPS), calculated using the nudged elastic band (NEB) method. Reprinted with permission from Ref. 467. Copyright 2016 American Chemical Society.

2013 **Lithium argyrodites**,  $\text{Li}_6\text{PS}_5\text{X}$  ( $X = \text{Cl}, \text{Br}, \text{I}$ ), can reportedly reach ionic conductivities  
 2014 of up to  $10^{-2} \text{ S cm}^{-1}$ .<sup>470</sup> While  $\text{Li}_6\text{PS}_5\text{Cl}$  and  $\text{Li}_6\text{PS}_5\text{Br}$  exhibit high ionic conductivities of  
 2015  $10^{-3} \text{ S cm}^{-1}$  at room temperature,  $\text{Li}_6\text{PS}_5\text{I}$  has considerably lower conductivities of  $10^{-6}$   
 2016  $\text{ S cm}^{-1}$ .<sup>478</sup> The difference of three orders of magnitude is surprising, as the identical crystal  
 2017 structures suggest the same Li diffusion pathways exist in all systems. Another intriguing  
 2018 aspect is that the conductivity trend runs counter to other families of solid electrolytes,  
 2019 such as LGPS, where larger, more polarisable and less electronegative anions are linked with  
 2020 increased ionic conductivities.<sup>479</sup>

2021 Understanding which properties and mechanisms influence the conductivity is essential  
 2022 to obtaining higher ionic conductivities and improving battery performance. Material stoi-  
 2023 chiometry, anion/cation disorder, and doping, have all been shown to influence conductivity.

2024 The effect of these can be difficult to deconvolve experimentally in many materials, as they  
2025 are intrinsically coupled. This is where computational analysis can provide vital insight,  
2026 allowing deconvolution of coupled properties and the roles they play in the diffusion process.

2027 A particularly interesting aspect of the Li-argyrodites is the diffusion topology, comprising  
2028 of interconnected  $\text{Li}_6\text{S}$  cages, with anions arranged at 4a, 4c, and 16e Wyckoff positions  
2029 and Li arranged over a tetrahedra, with sites labelled as type 1, 2, 4, and 5.<sup>480</sup> Lithium  
2030 mainly occupies type 5 tetrahedral sites in  $x(\text{Li})=6$  argyrodites, with occupation of non-  
2031 type 5 sites only recently observed experimentally.<sup>481,482</sup> Computational studies, however,  
2032 have previously predicted occupation of non-type 5 sites, showing lithium distributed over  
2033 tetrahedral types 5, 2, and 4.<sup>470,483,484</sup>

2034 Li hopping within these cages, while effectively barrierless, does not contribute to long-  
2035 range diffusion. In fact, a combination of inter-cage and intra-cage hopping is needed, with  
2036 occupation of non-type 5 sites and transitions between all adjacent site types, to achieve  
2037 long-range diffusion. This is shown schematically in Figure 28, showing the connectivity  
2038 between the Li tetrahedral sites. AIMD simulations have shown that cation and anion  
2039 substitution,<sup>429,481</sup> anion site disorder,<sup>482,484</sup> and lithium concentration<sup>485-487</sup> all influence  
2040 the ionic conductivity.

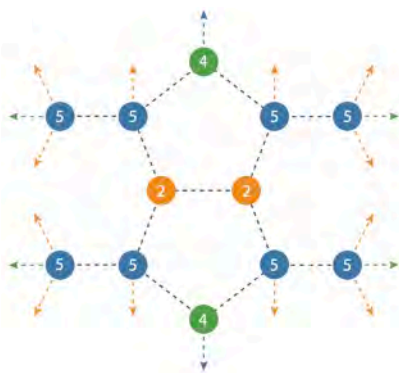


Figure 28: (a) Possible Li diffusion pathways in Li-argyrodites, involving type 2, 4, and 5 tetrahedra for long-range diffusion. Reprinted with permission from Ref. 484. Copyright 2020 American Chemical Society.

2041 The influence of anion substituent concentration on conductivity is currently uncertain,

2042 with research by De Klerk et al. determining excess Cl in  $\text{Li}_5\text{PS}_4\text{Cl}_2$ , resulting in similar con-  
2043 ductivities to  $\text{Li}_6\text{PS}_5\text{Cl}$ ,<sup>429</sup> in contrast to research by Yu et al. and Feng et al., who concluded  
2044 that excess Cl improved Li conductivity.<sup>487,488</sup> Yu et al. determined the highest conductivity  
2045 was produced by  $\text{Li}_{5.7}\text{PS}_{4.7}\text{Cl}_{1.3}$  ( $6.4 \text{ mS cm}^{-1}$ ),<sup>486,488</sup> while Feng et al. determined this to  
2046 be  $\text{Li}_{5.3}\text{PS}_{4.3}\text{Cl}_{1.7}$  ( $17 \text{ mS cm}^{-1}$ ).<sup>487</sup> Feng et al., however, presented alternative, or coupled,  
2047 reasoning for this increased conductivity. Drawing from previous studies,<sup>473,489</sup> they pro-  
2048 posed that the increased Cl content amplified the anion disorder in the system, which is the  
2049 underpinning cause of the higher conductivities.

### 2050 4.3.3 Oxides

2051 **LLZO** Cubic  $\text{Li}_7\text{La}_3\text{Zr}_2\text{O}_{12}$  (c-LLZO) has a high Li-ion conductivity of  $10^{-4} \text{ S cm}^{-1}$ ,<sup>490</sup> a  
2052 high shear modulus of 59 GPa,<sup>491</sup> and the largest thermodynamic stability window with  
2053 reference to lithium metal<sup>24,492,493</sup> of current solid electrolyte materials (c.f. section 4.3.4).  
2054 However, at low temperatures ( $< 150^\circ\text{C}$ ), c-LLZO is not stable and transitions to the less  
2055 conductive tetragonal LLZO (t-LLZO) phase.<sup>494</sup> Attempts have been made to retain the  
2056 more desirable c-LLZO by Al doping on lithium sites, with some success.<sup>494,495</sup>

2057 Lithium dendrite growth has been shown to be a challenge in solid-electrolytes. For  
2058 LLZO, dendrite growth has caused short circuits in the cells after relatively short peri-  
2059 ods.<sup>496,497</sup> Cheng et al. observed this growth directly and found that the process occurs  
2060 mostly through grain boundaries.<sup>498</sup> Recently, Kim et al. confirmed these observations and  
2061 investigated the use of an interlayer buffer, to restrict Li propagation through grain bound-  
2062 aries.<sup>499</sup>

2063 There has been a wide effort to understand dendrite formation through modelling.<sup>500-502</sup>  
2064 For example, Tian et al. used DFT to investigate dendrite growth through analysis of c-LLZO  
2065 and t-LLZO bulk and slab surface energies, via the total density of states (TDOS).<sup>501</sup> The  
2066 authors found that t-LLZO forms at the surface of bulk c-LLZO, even with Al-doping,<sup>503,504</sup>  
2067 and that extra states appear in the band gap for the slab structures, which do not appear

2068 in the bulk, potentially allowing electrons to be trapped on the surface of LLZO. Electrons  
 2069 localised primarily around  $\text{Li}^+$  and  $\text{La}^{3+}$  ions on the surface lead to the nucleation of lithium  
 2070 metal, which can result in lithium growth through grain boundaries and pores in the LLZO,  
 2071 eventually forming dendrites,<sup>496</sup> as shown in Figure 29. This analysis was also conducted on  
 2072 LiPON, where no electron trapping was found to occur, indicating that LiPON could be a  
 2073 suitable coating to prevent dendrite and t-LLZO formation (c.f. section 4.3.4).

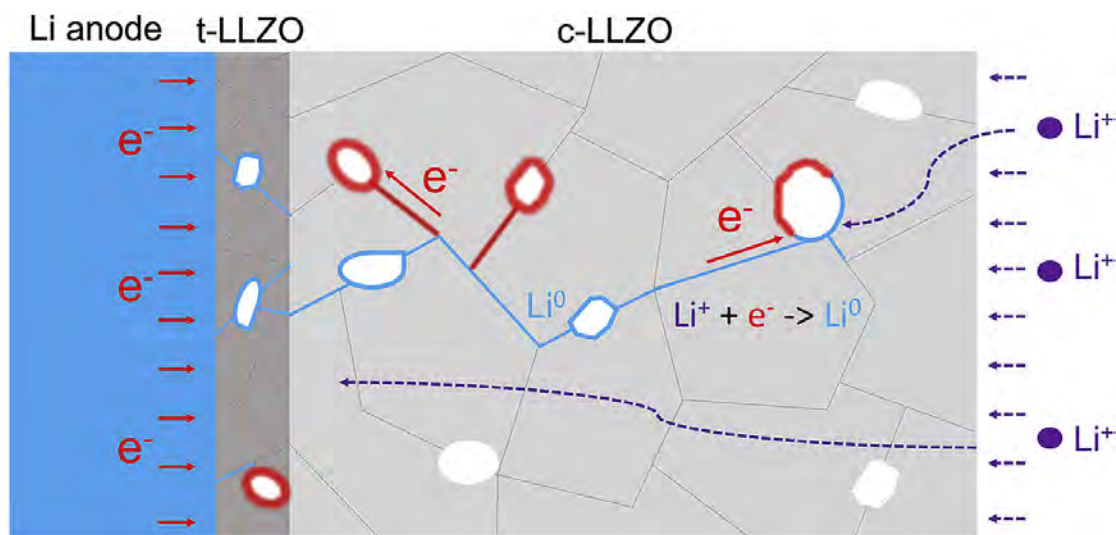


Figure 29: Schematic showing Li metal formation (blue) along grain boundaries and pores, due to electron accumulation (red) combining with  $\text{Li}^+$  as they move through the electrolyte. Reprinted from Ref. 501, Copyright 2018, with permission from Elsevier.

2074 Gao et al. attributed the dendrite growth mechanism to the under-coordination of Zr  
 2075 present on some of the stable interfaces of LLZO with Li,<sup>502</sup> leading to inhomogenous Li  
 2076 depletion, which has been linked to Li metal deposition and dendrite formation.<sup>505-509</sup> It  
 2077 is unclear whether the suggested cause by Gao et al. is complementary evidence of Tian  
 2078 et al.'s electron trapping theory or a separate cause of interface dendrite growth. However,  
 2079 the papers do differ on their choice of surface. Tian et al. used Li and La rich surfaces,  
 2080 which were determined to be more stable by Thompson et al., who used DFT to investigate  
 2081 6 different LLZO slabs for the (100) and (110) planes.<sup>510</sup> By contrast, Gao et al. drew upon  
 2082 results presented in several methods<sup>500,510,511</sup> and performed DFT calculations on a wider  
 2083 range of surfaces, finding (100) and (001) surfaces to be the most stable. The findings of these

2084 studies agree that Li and La rich surfaces are the most stable. However, Gao et al. calculated  
2085 the interface formation energies of the Li-LLZO interfaces using the CALYPSO interface  
2086 structure prediction method<sup>512</sup> and determined the Zr-rich surfaces to be the most stable  
2087 at this interface.<sup>513</sup> Experimental observations corroborate these findings, also determining  
2088 that the formation of Zr-rich surfaces to be a cause of interfacial degradation.<sup>508</sup>

2089 Experimental measurements have suggested a non-uniform distribution of current on the  
2090 surfaces as a possible cause of dendrite growth.<sup>506,514</sup> Non-uniform current distribution pro-  
2091 duces random, local spikes in current density for short periods of time, leading to a reduction  
2092 of Li at these sites. Squires et al. used DFT to model the electronic conductivity in LLZO to  
2093 probe the importance of the surface current to dendrite formation.<sup>515</sup> The authors determined  
2094 that at room temperature, bulk c-LLZO was found to have negligible electron/electron-hole  
2095 concentrations, indicating that bulk defects are not a significant factor in dendrite growth.  
2096 However, these models did not account for other forms of defects, such as grain boundary  
2097 and surface effects.

2098 Understanding Li-ion migration is key to improving battery conductivity. Xu et al.  
2099 analysed the Li-ion migration path through LLZO using DFT with the NEB method (c.f.  
2100 section 2.1.3).<sup>516</sup> Two migration paths were observed, depending on Li concentration. Low  
2101  $\text{Li}_x$  ( $\text{Li}_5\text{La}_3\text{Zr}_2\text{O}_{12}$ ) led to a higher energy, single hop migration path, whereas higher  $\text{Li}_x$   
2102 ( $\text{Li}_7\text{La}_3\text{Zr}_2\text{O}_{12}$ ) led to a lower energy, two hop migration path. Using potentials-based MD  
2103 (c.f. section 2.1.6), Burbano et al. further investigated the Li-ion transport mechanisms by  
2104 comparing ionic conductivity in t-LLZO and c-LLZO.<sup>517</sup> The authors found that the longer  
2105 time scale of potentials-based MD allowed the observation of a large sample of diffusion  
2106 events in both LLZO structural forms. Diffusion events in t-LLZO were less common and  
2107 involved exactly 8 Li ions, which corresponds to the cyclic movement of Li ions around the  
2108 12 octahedral and tetrahedral ring sites in t-LLZO. This cyclic mechanism results in no net  
2109 long-range diffusion of Li and hampers the ability of t-LLZO to conduct ions. AIMD (c.f.  
2110 section 2.1.6) investigations of the transport mechanism in LLZO have also been conducted.

2111 However, the shorter time scale led to some key disagreements about the transport mecha-  
2112 nism in c-LLZO.<sup>517–519</sup> Resolving Li-ion migration through LLZO experimental measurement  
2113 is challenging, due to the complexity of the system coupled with the need to observe the  
2114 processes during active (dis)charge. Here, atomistic modelling has provided insights difficult  
2115 to obtain experimentally.

2116 DFT calculations have determined that Al doping reduces the energy barrier for Li-ions to  
2117 move between octahedral and tetrahedral sites, increasing the ionic conductivity.<sup>520,521</sup> More  
2118 recent work by Bonilla et al., using potentials-based MD, supports this conclusion, finding  
2119 increased conductivity in t-LLZO, due to the Al forcing Li ions into previously inaccessible  
2120 tetrahedral sites.<sup>522</sup> The authors also found that Al doping in c-LLZO led to a slight decrease  
2121 in conductivity. They attributed this to the tendency for Al to “trap” Li ions close to the  
2122 dopant.

2123 **Oxide Nanocomposites** Due to attractive mechanical, electrical, optical, and mag-  
2124 netic properties, nanocomposite oxide materials represent a new generation of advanced  
2125 materials.<sup>445,447</sup> They often show enhanced conductivity, compared to single-phase ceramic  
2126 oxides, making them suitable candidates as electrolytes for future ASSBs. For example,  
2127  $\text{Li}_2\text{O}:\text{B}_2\text{O}_3$ <sup>447–449</sup> and  $\text{Li}_2\text{O}:\text{Al}_2\text{O}_3$  nanocomposites<sup>446</sup> have higher ionic conductivities than  
2128 nanocrystalline  $\text{Li}_2\text{O}$ , although  $\text{B}_2\text{O}_3$  and  $\text{Al}_2\text{O}_3$  are insulators. The ionic conductivity shows  
2129 a maximum at about 50 % of  $\text{B}_2\text{O}_3/\text{Al}_2\text{O}_3$  content. This surprising behaviour was attributed  
2130 to the increased fraction of structurally disordered interfacial regions and the enhanced sur-  
2131 face area of the nanosized particles.<sup>447</sup> The oxide nanocomposites contain three types of in-  
2132 terfaces, as presented in Figure 30 (a): interfaces between the ionic conductor grains (green  
2133 lines), between the insulator grains (black lines), and between the ionic conductor and the  
2134 insulator grains (red lines). The latter can lead to surprising effects in the conductivity of  
2135 composite materials. In this case, the highly conducting interface region can act as a bridge  
2136 between two  $\text{Li}_2\text{O}$  grains not in direct contact with each other, opening up additional paths  
2137 for Li ions. The conductivity enhancement in the interfacial regions may have different ori-

2138 gins, e.g. the formation of space charge layers, an enhanced concentration of dislocations, or  
2139 defects, or the formation of new phases.

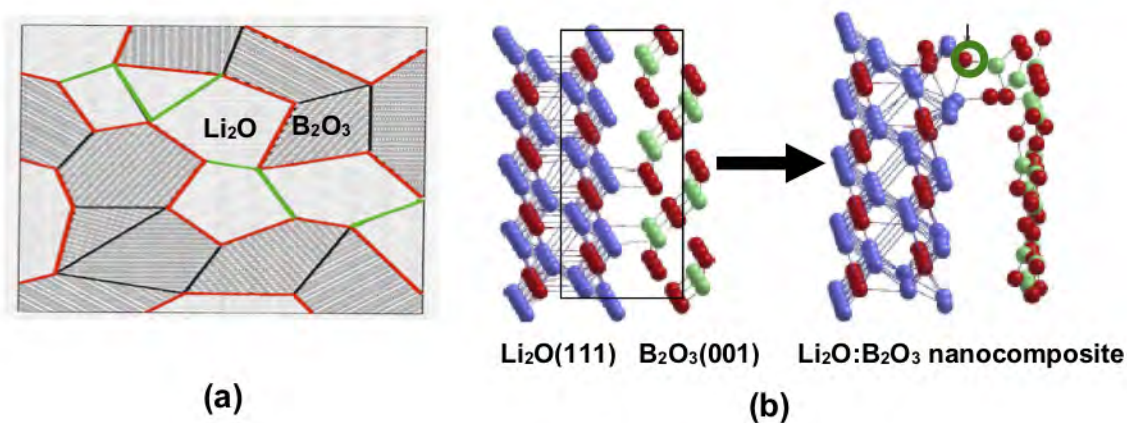


Figure 30: (a) Schematic diagram of  $\text{Li}_2\text{O}$  and  $\text{B}_2\text{O}_3$  interface (b) Atomistic model of  $\text{Li}_2\text{O}:\text{B}_2\text{O}_3$  nanocomposite. Reproduced with permission from Ref. 523 Copyright IOP Publishing. All rights reserved.

2140 Islam et al. studied the interface of  $\text{Li}_2\text{O}:\text{B}_2\text{O}_3$  nanocomposite, by modelling a combi-  
2141 nation of two favorable surfaces of  $\text{Li}_2\text{O}$  and  $\text{B}_2\text{O}_3$  using HF/DFT Hybrid approach.<sup>523,524</sup>  
2142 After full structural optimisation, it was observed that Li–O bonds are weakened, while B–O  
2143 bonds are formed simultaneously at the boundary between the two surfaces, Figure 30 (b).  
2144 An oxygen atom from the  $\text{Li}_2\text{O}$  surface (marked by a green circle) is pulled from the surface  
2145 layer towards a neighbouring boron atom of the  $\text{B}_2\text{O}_3$  surface. This preference of oxygen  
2146 bonding with B (or Al in  $\text{Li}_2\text{O}:\text{Al}_2\text{O}_3$ ) plays a key role in generating low-coordinated Li.  
2147 As a consequence of this dislocation, the coordination of a Li atom in the second layer is  
2148 reduced from four to three.

2149 The defect properties were investigated in the interface region. It was observed that the  
2150 removal of surface oxygen from  $\text{Li}_2\text{O}$  is responsible for the increased vacancy defect concentra-  
2151 tion in  $\text{Li}_2\text{O}:\text{B}_2\text{O}_3$  (or  $\text{Li}_2\text{O}:\text{Al}_2\text{O}_3$ ) nanocomposite materials. Therefore, the nanocomposites  
2152 of ionic compounds (containing weakly bound and therefore mobile cations) with highly co-  
2153 valent compounds (with strong metal- or nonmetal-oxygen bonds) are promising candidates

2154 for high ionic conductivity. The model calculations showed that the most likely mechanism  
2155 for  $\text{Li}^+$  migration was in a zigzag pathway, rather than in a straight line along a direction  
2156 parallel to the interface plane.

2157 The average calculated activation energy for  $\text{Li}^+$  migration in the  $\text{Li}_2\text{O}:\text{B}_2\text{O}_3$  interface  
2158 ( $0.28 \text{ eV}$ )<sup>523,524</sup> is similar to the experimental values of bulk  $\text{Li}_2\text{O}$  ( $0.31 \text{ eV}$ ),<sup>447</sup>  $\text{Li}_2\text{O}:\text{B}_2\text{O}_3$   
2159 ( $0.34 \pm 0.04 \text{ eV}$ ),<sup>449</sup> and  $\text{Li}_2\text{O}:\text{Al}_2\text{O}_3$  ( $0.30 \pm 0.02 \text{ eV}$ )<sup>446</sup> nanocomposites. According to  
2160 the defect formation energies, the interface region of  $\text{Li}_2\text{O}:\text{B}_2\text{O}_3$  nanocomposites contains  
2161 higher concentrations of both Li vacancies and Frenkel defects than bulk  $\text{Li}_2\text{O}$  and  $\text{Li}_2\text{O}$  sur-  
2162 faces.<sup>523,524</sup> Therefore, the experimentally observed enhanced Li mobility in the  $\text{Li}_2\text{O}:\text{B}_2\text{O}_3$   
2163 interface region is thermodynamically and not kinetically controlled. The models proposed in  
2164 this study allowed a direct simulation of the defect formation and ion mobility at the atomic  
2165 scale, without any experimental input. They provide a deep insight into the local bonding  
2166 situation at the interface of oxide nanocomposites, which is difficult to obtain from experi-  
2167 ments. State-of-the-art synchrotron techniques, like hard x-ray photoelectron spectroscopy  
2168 (HAXPES), could possibly shed light on this challenge.<sup>525,526</sup>

#### 2169 **4.3.4 Interface stability**

2170 Experimental investigations of solid electrolyte interfaces are often challenging, making atom-  
2171 istic modelling a vital tool.<sup>29</sup> The interfacial stability properties of solid electrolyte materials  
2172 in contact with an electrode are best described by the electrochemical stability window, de-  
2173 fined by Zhu et al. as the range of voltages under which the interface configuration, a mixture  
2174 of electrode (Li) and the solid electrolyte, does not undergo a decomposition reaction.<sup>492</sup>

2175 It has been widely reported in both experiment<sup>527,528</sup> and theory<sup>468</sup> that certain solid elec-  
2176 trolytes have an electrochemical stability window with reference to a Li anode of between 0–5  
2177 V.<sup>286,527,529</sup> Mo et al. reported a 3.6 eV band gap from a DFT calculation (c.f. section 2.1.1)  
2178 for LGPS,<sup>468</sup> attributing the higher solid electrolyte stability observed to the passivation  
2179 phenomenon forming an interphase layer at the interface of the anode-electrolyte.<sup>530</sup> More



2180 recent work by Zhu et al. has questioned this high stability window, using DFT to demon-  
2181 strate that the stability windows, particularly of sulfides, are far smaller than originally  
2182 thought (Figure 31).<sup>24</sup>

2183 A smaller thermodynamic window increases the importance of the interphase layer forma-  
2184 tion. Zhu et al. determined that a range of solid electrolytes are unstable with respect to Li  
2185 metal at low and high voltages, with the exception of LLZO, which appears to be kinetically  
2186 stabilised at low voltages, due to an unfavourable reduction energy of -0.02 eV per atom.  
2187 Any potential outside of the thermodynamic stability window results in decomposition into  
2188 lithium binary compounds, unless otherwise kinetically stabilised. This is problematic for  
2189 germanium- and titanium-containing compounds, as they form electronically conductive al-  
2190 loys upon decomposition.<sup>24</sup> This renders the proposed passivation process impossible,<sup>24,468</sup>  
2191 as this degradation process would be sustained throughout the bulk cycling, severely lim-  
2192 iting the efficacy of these materials as electrolytes. Such degradation can also increase  
2193 interfacial resistance.<sup>531,532</sup> Other solid electrolytes face different problems. As explained in  
2194 section 4.3.3, LLZO forms the far less ionically conductive tetragonal LLZO at the surface.  
2195 The Li-LiPON and Li-argyrodite interfaces were reported to degrade favourably, forming an  
2196 ionically conductive and electronically insulating interphase consisting of Li<sub>2</sub>O, Li<sub>2</sub>S, Li<sub>3</sub>P,  
2197 Li<sub>3</sub>N, and LiI.<sup>24</sup>

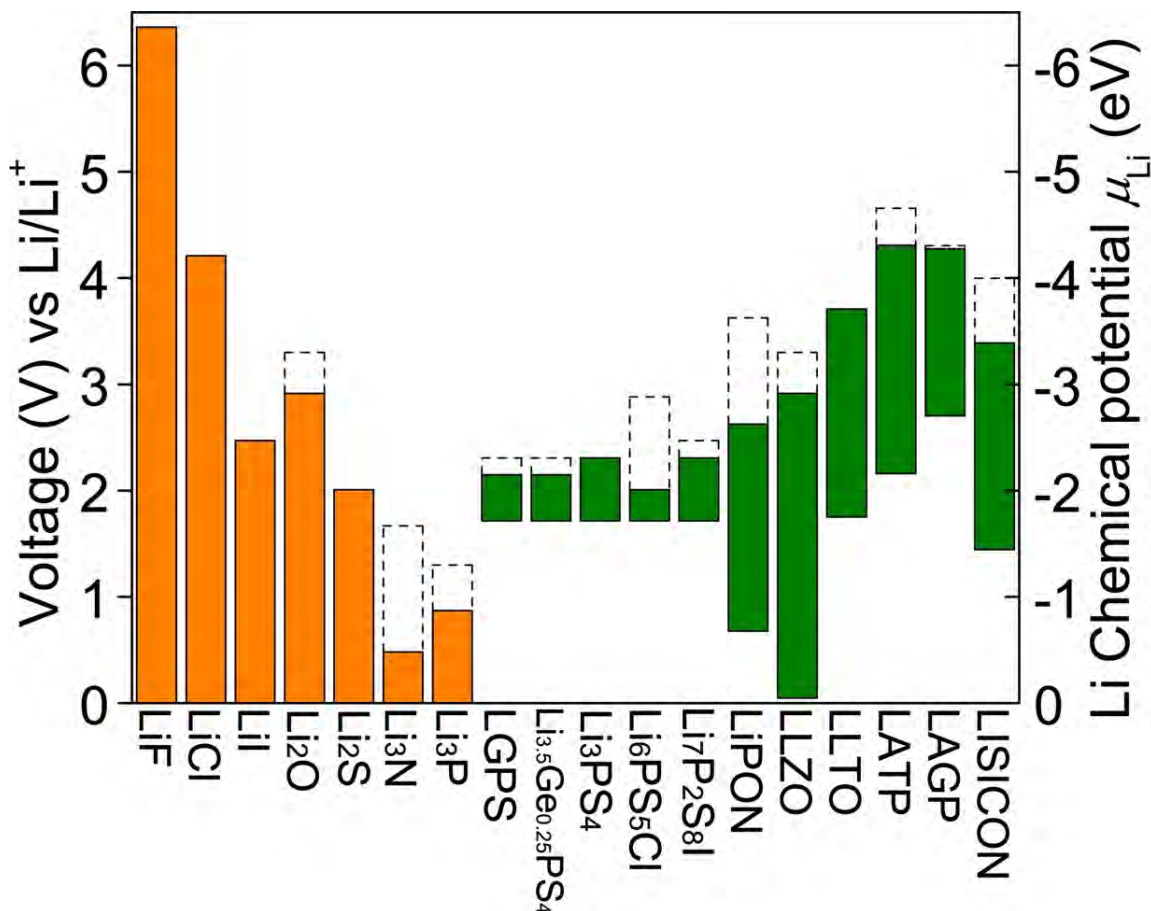


Figure 31: A comparison of the voltage stability windows for a selection of solid electrolytes (green) and the binary compounds that often form upon decomposition of the solid electrolyte (orange). The dashed line represents the oxidation potential to fully delithiate the material. Reprinted with permission from Ref. 24. Copyright 2015 American Chemical Society.

2198 Further study by Zhu et al. sought to investigate the mechanism behind the degrada-  
 2199 tion/instability at the surface.<sup>492</sup> In order to probe these mechanisms, the authors calculated  
 2200 the chemical and electrochemical stability of several solid electrolytes (LGPS, LLZO, LiPON,  
 2201 NASICON-type, lithium lanthanum titanate oxide (LLTO)) as well as the equilibrium con-  
 2202 ditions at the interfaces. Examining the cathode-electrolyte interface, using lithium cobalt  
 2203 oxide (LCO) as the cathode, a similar pattern emerged: oxides were found to be far more  
 2204 stable than their sulfide counterparts. However, LLTO and lithium aluminum titanium  
 2205 phosphate (LATP) had the best electrochemical stability against LCO.

2206 Studies looking into the interfacial resistance have been conducted,<sup>30,533-535</sup> with the

2207 main source of resistance attributed to the electric double layer, which, in liquid electrolytes,  
 2208 consists of a capacitance and diffusion layer (c.f. section 4.1).<sup>30</sup> Tateyama et al. used the  
 2209 CALYPSO method<sup>512,513</sup> to find low-energy surfaces to probe the interface. The lithium  
 2210 chemical potential of these stable interfaces in the Helmholtz layer, corresponding to the  
 2211 negative of the Li ion vacancy formation energy, was determined. These energies correspond  
 2212 to lithium moving from the electrode to the electrolyte, with the vacant lithium sites becom-  
 2213 ing a potential source of interfacial resistance. Okuno et al. use DFT calculations to compare  
 2214 the interfacial resistances of sulfide and oxide based solid electrolytes with LCO cathodes.<sup>533</sup>  
 2215 The Li vacancy formation energy and ion exchange across various interfaces were calculated.  
 2216 It was found that sulfide-based electrolytes had a higher interfacial resistance, due to the  
 2217 presence of more sites with a low vacancy formation energy on the surface. The authors also  
 2218 found the interfacial resistance to be dependent on the orientation of the crystals at the inter-  
 2219 face. Interfacial resistance is a major impediment to the commercialisation of ASSBs. The  
 2220 cause of this phenomenon has been elucidated through atomistic simulation of the interface  
 2221 and has provided direction to future SSE development.

2222 A study by Lepley and Holzwarth used DFT to investigate the interface energies between  
 2223 the Li electrode and the compounds that make up the interphase layer of the electrolyte.<sup>536</sup>  
 2224 They defined the interface energy as:

$$\gamma_{ab}(\Omega) = \frac{E_{ab}(\Omega, A, n_a, n_b) - n_a E_a - n_b E_b}{A}, \quad (45)$$

2225 where  $\Omega$  is the interface configuration of atoms,  $E_{ab}$  is the energy of the complete system,  
 2226  $E_x$  is the bulk energy per formula unit and  $A$  is the surface energy. Because the interface  
 2227 energy is intensive, calculating larger systems will give a converging value for  $\gamma_{ab}$ ,

$$\lim_{\Omega_s \rightarrow \Omega} [\gamma_{ab}(\Omega_s)] = \gamma_{ab}(\Omega), \quad (46)$$

2228 where  $\Omega_s$  is the atomic configuration in a sample of the interface volume. Because the

2229 exact matching of lattice constants between interfaces is unlikely, a semi-coherent interface is  
2230 considered, meaning lattice strain needed to be taken into account. Using the lowest overall  
2231 lattice energy structure and explicitly accounting for the lattice strain, the most probable  
2232 interfaces could be found. The Li/Li<sub>3</sub>PO<sub>4</sub>, Li/Li<sub>2</sub>O and Li/Li<sub>2</sub>S interfaces were found to be  
2233 stable and the Li/Li<sub>3</sub>PS<sub>4</sub> interface was found to be unstable.<sup>536</sup>

2234 In response to the apparent poor stability of most solid electrolytes, many studies have  
2235 attempted to simulate the effect of coating the electrolyte with an oxide layer.<sup>501,537,538</sup> As  
2236 discussed in section 4.3.3, Tian et al. identified LiPON as a suitable coating material for  
2237 LLZO, by comparing the bulk and surface density of states.<sup>501</sup> The authors found no extra  
2238 states on the surface structure, so concluded that no electron trapping would occur (the pri-  
2239 mary mechanism that they attributed to dendrite formation). Recently, Sang et al. proposed  
2240 an artificial interphase layer between the Li anode and the solid electrolyte, composed of a  
2241 Li<sub>3ab</sub>N<sub>a</sub>X<sub>b</sub> compound, where  $X$  is a halide.<sup>539</sup> This material was investigated computationally  
2242 by screening stable and metastable structures using the USPEX structure prediction  
2243 software.<sup>540,541</sup> The dynamic stability of the stable structures was found by analysing the  
2244 phonon frequency spectrum by using PHONO3PY.<sup>180,542,543</sup> The temperature-dependant ionic  
2245 transport properties were found using AIMD (c.f. section 2.1.6).

2246 Phase diagrams for various atomic configurations were then constructed using cluster  
2247 expansion, implemented through the Alloy Theoretic Automated Toolkit (AT-AT) (c.f. sec-  
2248 tion 2.1.4).<sup>80,544</sup> Through these various computational techniques, Sang et al. found that  
2249 Li<sub>6</sub>NCl<sub>3</sub> has the most favourable properties for use with sulfide-based solid electrolytes, such  
2250 as LGPS.<sup>539</sup> Authors such as Tian et al. and Sang et al. have leveraged the insights gained  
2251 through atomistic simulation to predict viable coatings for the SSE. This level of insight  
2252 would be near-impossible to obtain experimentally, due to the inherent difficulty in probing  
2253 interfaces and the inability to access the same depth of knowledge about electronic struc-  
2254 ture. These findings demonstrate the critical role atomistic simulation plays when addressing  
2255 modern material science problems.

### 2256 4.3.5 Outlook and challenges

2257 The drive for the development of commercialised ASSBs has been intense, with the EV indus-  
2258 try at the forefront of promoting this.<sup>23</sup> Although ASSBs can offer high gravimetric energy  
2259 density (250 Wh kg<sup>-1</sup>) and volumetric energy density (700 Wh L<sup>-1</sup>), along with improved  
2260 safety over conventional liquid electrolytes, the slow ionic diffusion can impair fast discharge  
2261 and charge performance. With solid electrolytes intended to replace both the separator and  
2262 liquid electrolyte in conventional LiBs,<sup>545</sup> there are still multiple challenges which need to  
2263 be overcome for this to be viable. In recent years, there have been breakthroughs in the  
2264 discovery of new solid electrolytes, such as Li<sub>9.54</sub>Si<sub>1.74</sub>P<sub>1.44</sub>S<sub>11.7</sub>Cl<sub>0.3</sub>,<sup>546</sup> which exhibit ionic  
2265 conductivity competitive with that of organic liquid electrolytes. The improved performance  
2266 of these materials is enabled by interfacial coatings or buffer layers and micro-structure  
2267 engineering solutions at the electrode/electrolyte interfaces.<sup>547</sup>

2268 ASSBs are currently not capable of reliable cycling at current densities > 0.6 mA cm<sup>-2</sup>.<sup>411,548</sup>  
2269 The current density and stability is limited by: poor electrode/electrolyte physical contact,  
2270 leading to particle cracking and interface delamination, formation and propagation of Li  
2271 dendrites, chemical and electrochemical stability, and high interfacial resistance.<sup>411</sup> There  
2272 are several critical issues related to the pairing of solid electrolytes with cathode and anode  
2273 materials, which need to be addressed for long-term battery operation:

- 2274 • The limited system sizes of atomistic modelling are not sufficient to capture lattice  
2275 relaxation, which would allow a coherent (completely matched) interface to form. This  
2276 amplifies the effects of lattice strain in the model, particularly in cases where periodic  
2277 boundary conditions are used.<sup>536</sup> The lattice strain energy can be calculated and fac-  
2278 tored into bulk scale calculations, but it is not as accurate as explicitly calculating  
2279 dislocation defects that naturally relieve lattice strain.<sup>549,550</sup>
- 2280 • Dendrite formation has been a notable problem for even the most physically robust elec-  
2281 trolytes (c.f. section 4.3.3). Modelling of dendrite formation mechanisms has yielded

2282 some contradictory results, due to incomplete models of the interface.<sup>500–502</sup> However,  
2283 a more detailed understanding requires modelling of larger systems, encompassing the  
2284 interface and bulk regions of both materials. This incurs a high computational cost  
2285 not currently reachable through electronic structure methods methods. Further de-  
2286 velopment of the linear-scaling DFT approach (c.f. section 2.1.2) may allow a more  
2287 complete, multiscale approach.

- 2288 • The system size limitations in DFT modelling also hinder the modelling of the full  
2289 electric double layer, which is also applicable to liquid electrolytes. Comparatively, in  
2290 solid electrolytes the double layer is less understood. For example, Tateyama et al. were  
2291 only able to successfully model the initial capacitance layer at the interface (Helmholtz  
2292 layer).<sup>30</sup>
- 2293 • Interfacial resistance presents an interesting challenge, as it can be introduced through  
2294 multiple mechanisms:<sup>535</sup> electric double layer,<sup>30</sup> surface crystal orientation,<sup>533</sup> and pro-  
2295 duction issues, such as poor wettability.<sup>534</sup> Strong collaboration between theorists and  
2296 experimentalists will be needed, in order to make informed improvements to current  
2297 interfacial structures.

2298 The interface is the primary source of dendrite formation, lattice mismatch, and inter-  
2299 facial resistance in solid electrolytes. The interface also presents opportunities for atomistic  
2300 modelling, with the growing popularity of coatings that try to address the shortcomings of  
2301 popular solid electrolytes.<sup>29,499,551–564</sup> For example, Tian et al.’s solution to dendrite growth  
2302 in LLZO by utilising a LiPON coating<sup>501</sup> (c.f. section 4.3.3). Understanding how effective  
2303 coatings are at addressing the aforementioned issues is essential.<sup>501,537,538</sup> A very recent re-  
2304 view by Kim et al. presents a detailed insight into the challenges and future prospects of  
2305 solid-state Li-metal batteries, which we have touched upon here.<sup>547</sup>

## 2306 5 Cathodes

### 2307 5.1 Introduction

2308 As mentioned in our Introduction (section 1), lithium-ion batteries (LiBs) became promising  
2309 applications in 1979 when Goodenough and Mizushima successfully demonstrated  $\text{LiCoO}_2$   
2310 as a cathode.<sup>565</sup> Since then, LiBs have become instrumental in portable electronics, such  
2311 as mobile phones, and electric vehicles,<sup>566–570</sup> largely attributed to their high energy den-  
2312 sity.<sup>285,412,417,571–579</sup> Due to the high abundance and low material cost, sodium-ion batteries  
2313 have also received increased attention, especially for grid storage applications.<sup>580–584</sup> Re-  
2314 gardless of the application, the discovery of new materials and the optimisation of current  
2315 chemistries for improved performance is crucial for the next generation of rechargeable bat-  
2316 teries. With that in mind, it is known that the energy density of the cathode material is the  
2317 limiting factor in improving battery performance, thus current research is largely focused  
2318 on exploring cathode chemistries. These include layered oxides ( $\text{LiMO}_2$ ,  $M=\text{Co,Mn,Ni}$ ),  
2319 spinel oxides ( $\text{LiM}_2\text{O}_4$ ), olivine phosphates ( $\text{LiFePO}_4$ ), disordered rock-salts, ( $\text{Li}_2\text{MnO}_2\text{F}$ ),  
2320 and other compounds, such as silicates.<sup>585,586</sup>

2321 Layered transition metal (TM) oxides ( $\text{LiMO}_2$ ,  $M=\text{Co,Mn,Ni,etc.}$ ) are commonly con-  
2322 sidered to be the first generation of cathode materials in commercial LiBs. These materials  
2323 possess a theoretical specific capacity of  $270 \text{ mAh g}^{-1}$ . However, their practical capacity is  
2324 generally limited to below  $200 \text{ mAh g}^{-1}$ .<sup>587</sup>  $\text{LiCoO}_2$  held high capacities but the material was  
2325 problematic due to capacity fading, low abundance, and the high cost of cobalt and geopolit-  
2326 ical issues, including ethical concerns, making large scale applications impractical.<sup>588</sup> There  
2327 is also considerable instability in the  $\text{LiCoO}_2$  structure, caused by the extraction of Li during  
2328 cycling, which results in undesirable phase transitions from O3-type to O6-type  $\text{Li}_x\text{CoO}_2$  and  
2329 O1-type  $\text{CoO}_2$ .<sup>589,590</sup> Other layered oxides also pose their own challenges, such as  $\text{Li}_x\text{NiO}_2$   
2330 presenting capacity fade and poor safety,<sup>591</sup> and  $\text{Li}_x\text{Mn}_2\text{O}_4$  presenting low capacity.<sup>592</sup> An  
2331 emerging alternative to solve some of these challenges is using a combination of the TMs. In

2332 2000, Paulsen et al. presented  $\text{Li}_{2/3}[\text{Ni}_{1/3}\text{Mn}_{2/3}]\text{O}_2$ ,<sup>593,594</sup> with  $\text{Li}[\text{Ni}_x\text{Mn}_{1-2x}\text{Co}_z]\text{O}_2$  (NMC)  
2333 presented by the authors in 2001.<sup>595</sup> Partially replacing Co in  $\text{LiCoO}_2$  with Ni and Mn to  
2334 obtain layered  $\text{Li}[\text{Ni}_x\text{Mn}_y\text{Co}_z]\text{O}_2$ ,<sup>566</sup> where  $x + y + z = 1$ , shows improved electrochemical  
2335 performance, while also reducing material cost and improving stability.<sup>596</sup> These layered ox-  
2336 ides are commonly termed as NMC, with the subsequent numbering relating to the ratio  
2337 between the cations.

2338 A huge benefit of combining these TMs is the ability to tune the TM composition to  
2339 optimise aspects including capacity, (dis)charging rate, electrochemical stability, and lifetime,  
2340 with the potential of reaching capacities  $> 220 \text{ mAh g}^{-1}$ .<sup>597</sup> Some NMC compositions are  
2341 already used commercially, with industry focus shifting from NMC111 to higher Ni containing  
2342 compositions including NMC442, NMC532, and NMC622.<sup>598</sup> These compositions, however,  
2343 still contain 20 % or more Co. A great deal of research is working towards reducing the Co  
2344 content even further, with compositions such as NMC811 ( $\text{Li}[\text{Ni}_{0.8}\text{Mn}_{0.1}\text{Co}_{0.1}]\text{O}_2$ ) showing  
2345 promise as future commercial materials for applications, such as in long-range electric vehicles  
2346 (EVs).<sup>599</sup> These Ni-rich NMC compositions are also considered to be the cathode of choice  
2347 for future all-solid-state LiBs.<sup>587</sup>

2348 Recently, research into further improving the capacity of these materials by inserting  
2349 lithium into the TM cation sites has attracted considerable attention. This has lead to  
2350 a new generation of cathode materials termed “Li-rich” or lithium excess. The increased  
2351 capacities of these materials arises from invoking redox chemistry on both the TM and oxide  
2352 ions, as opposed to just TM ions in traditional oxide-based intercalation compounds.<sup>600–608</sup>  
2353 These Li-rich cathodes, including  $\text{Li}_{1+x}\text{Ni}_y\text{Co}_z\text{Mn}_{(1-x-y-z)}\text{O}_2$  layered oxide, can reach high  
2354 capacities of  $> 300 \text{ mAh g}^{-1}$ . However, synthesis of these materials has proven to be difficult  
2355 and work is ongoing to improve synthesis techniques.<sup>609</sup>

2356 There has also been growing interest in disordered intercalation structures, especially  
2357 disordered rock-salt structures. They were initially disregarded as cathodes, as their struc-  
2358 ture appeared to limit lithium diffusion. However, recent research has shown that lithium



2359 diffusion can be facile in some disordered materials, provided that there is enough of a  
2360 lithium excess to allow the formation of an uninterrupted percolating network of channels  
2361 involving no face-sharing TM ions.<sup>601,610,611</sup> There have been several examples reported,  
2362 including  $\text{Li}_{1.2}\text{Ni}_{0.33}\text{Ti}_{0.33}\text{Mo}_{0.13}\text{O}_2$ ,<sup>611</sup>  $\text{Li}_{1.2}\text{Ti}_{0.4}\text{Mn}_{0.4}\text{O}_2$ ,<sup>612</sup>  $\text{Li}_4\text{Mn}_2\text{O}_5$ ,<sup>613-615</sup>  $\text{Li}_3\text{NbO}_4$ -based  
2363 systems,<sup>616-618</sup> and oxyfluorides, where some of the anion sites are occupied by  $\text{F}^-$  rather than  
2364  $\text{O}^{2-}$ , such as  $\text{Li}_2\text{MnO}_2\text{F}$ ,<sup>619-621</sup>  $\text{Li}_2\text{VO}_2\text{F}$ ,<sup>622-628</sup> and  $\text{Li}_2\text{Mn}_{2/3}\text{Nb}_{1/3}\text{O}_2\text{F}$ .<sup>629</sup> These materials  
2365 can be difficult to synthesise, however, as Mn-rich 3D TM compounds tend to form ordered  
2366 phases, such as  $\text{LiMnO}_2$  or  $\text{Li}_2\text{MnO}_3$ , high energy mechano-chemical ball-milling methods  
2367 have been utilised to counter this.<sup>613,620,630</sup> These materials are able to reach very high en-  
2368 ergy storage capacities of  $300 \text{ mAh g}^{-1}$ ,<sup>631</sup> which is attributed to the ability to perform both  
2369 cationic and anionic redox.<sup>628,631,632</sup> These materials typically show less first cycle hysteresis  
2370 than other Li-rich compounds, thought to be because the structure already resembles that  
2371 of the Li-rich materials after they undergo cation disorder on cycling.

2372 Knowledge of the broad structural and electrochemical properties of cathode materials  
2373 can be obtained from various experimental methods. However, detailed insight into, for  
2374 example, TM configurations, vibrational and thermal properties, and atomistic diffusion  
2375 mechanisms, is challenging and, in some cases, not resolvable using experimental techniques.  
2376 This is where atomistic modelling can provide greater insight. In this section, we explore  
2377 a range of cathode material properties, using several Li-ion materials, to highlight different  
2378 properties and the considerations needed to gain the most desirable electrochemical perfor-  
2379 mance. We describe which atomistic modelling methods are used to investigate the discussed  
2380 properties and the importance of modelling in this context. Using a range of promising cath-  
2381 ode materials (layered oxides, spinel oxides, polyanions, and disordered rock-salt oxides and  
2382 oxyfluorides) to aid in the discussion, we first look at the different cathode crystal structures  
2383 and the effects of micro-structuring. We then discuss some of the bulk material properties,  
2384 including ion diffusion, redox and electronic properties, TM ordering, and vibration and ther-  
2385 mal properties. Finally, we consider the surfaces and interfaces of these cathode materials,

2386 with an outlook to current and future challenges in the atomistic modelling of cathodes.

## 2387 5.2 Bulk Properties

### 2388 5.2.1 Crystal Structure and Micro-Structure

2389 **Crystal structure.** Cathode materials consist of a range of different crystal structures, with  
2390 some of the most promising LiCoO<sub>2</sub> based materials adopting the  $\alpha$ -NaFeO<sub>2</sub> structure, with  
2391 alternating layers of [CoO<sub>2</sub>]<sup>-</sup> and Li<sup>+</sup>. In LiBs, the cathode is a limiting factor, as the amount  
2392 of lithium that can be reversibly extracted and re-inserted (cycled) directly influences the bat-  
2393 tery capacity, with the Fermi energy linked to the cell voltage.<sup>586</sup> Thermo-chemical stability  
2394 and high energy density are also important considerations, with several promising candidates  
2395 for future battery materials. These include mixed-metal layered oxides (NMC), spinel oxides  
2396 (LiMn<sub>2</sub>O<sub>4</sub>), polyanion materials(LiFePO<sub>4</sub>,<sup>412,567,571,579</sup> Li<sub>2</sub>FeSiO<sub>4</sub>,<sup>633-635</sup> LiFeSO<sub>4</sub>F<sup>636</sup>), and  
2397 disordered rock-salt oxides and oxyfluorides (Li<sub>2</sub>MnO<sub>2</sub>F<sup>619,628,631,632,637</sup>). The crystal struc-  
2398 tures of these cathode materials are presented in Figures 32 and 33, where these materials  
2399 are described in more detail.

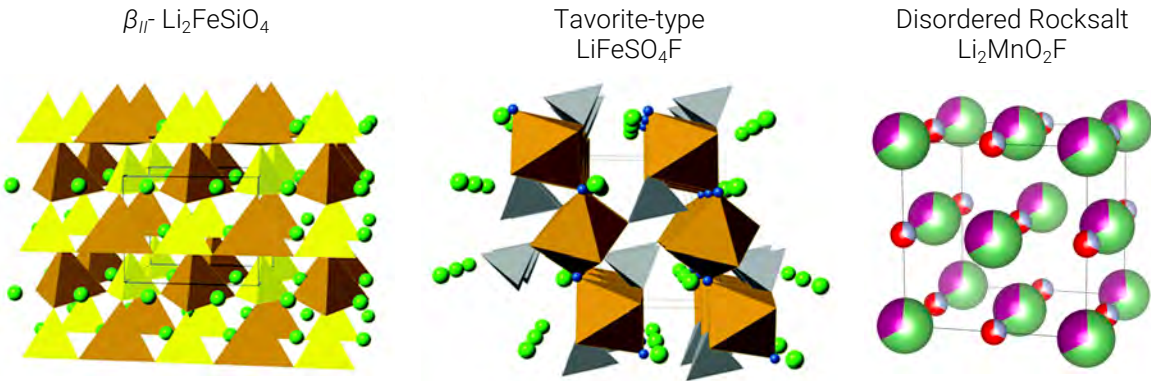


Figure 32: Representative crystal structures of  $\beta_{II}$ -Li<sub>2</sub>FeSiO<sub>4</sub>, tavorite-type LiFeSO<sub>4</sub>F, and disordered rock-salt Li<sub>2</sub>MnO<sub>2</sub>F cathode materials for lithium-ion batteries. Li<sup>+</sup> ions are shown in green spheres, O in red, Mn in mauve, and F in grey. Fe–O polyhedra are shown in brown, SiO<sub>4</sub> tetrahedra in yellow, and SO<sub>4</sub> tetrahedra in grey.

2400 Some TM oxides are stable in various structural forms, such as lithium manganese oxide  
2401 (LMO), which has been synthesised with layered,<sup>638</sup> spinel,<sup>639</sup> and rock-salt structures.<sup>640</sup>

2402 For intercalation-type cathodes used in LiBs, the structural framework is expected to remain  
2403 relatively unchanged, with only small changes from lattice expansion/contraction. However,  
2404 phase transitions can occur during the cycling process. For example, during cycling, a phase  
2405 transition can occur from the  $\text{LiMn}_2\text{O}_4$  spinel structure to the  $\text{LiMnO}_2$  rock-salt structure,  
2406 partially due to oxygen evolution.<sup>641</sup> Phase transitions between layered and spinel struc-  
2407 tures are also widely observed.<sup>642</sup> For example, Reed et al. investigated the layered to spinel  
2408 phase transitions in  $\text{Li}_x\text{MnO}_2$  using Density Functional Theory (DFT) modelling (c.f. sec-  
2409 tion 2.1.1).<sup>643</sup> Their investigation determined that partially lithiated layered  $\text{Li}_x\text{MnO}_2$  tran-  
2410 sitions to spinel in a two-stage process. Firstly, a large percent of Mn and Li ions quickly  
2411 occupy tetrahedral sites, to form a meta-stable intermediate. Then, a more complex, coordi-  
2412 nated rearrangement of Mn and Li occurs to form spinel. Interestingly, this behaviour is in  
2413 contrast to  $\text{Li}_x\text{CoO}_2$  and understanding the reasons for this could prove useful for creating  
2414 Mn-based cathode materials.

2415 **Micro-Structuring.** It is clear that control over bulk structure has an impact on the  
2416 material's performance, as many properties are dependent on shape and size.<sup>644</sup> The struc-  
2417 tural and micro-structural properties of a material are also vital to the cycling stability of a  
2418 cathode. For example, reducing the particle size of  $\text{LiFePO}_4$  to the nanometre scale is shown  
2419 to increase the electrochemical performance, compared to equivalent, but larger, particles, by  
2420 reducing transport path lengths.<sup>645-647</sup> Selective structuring can also provide mechanical ben-  
2421 efits, for example, where forces acting on the functional cathode during cycling, as the lattice  
2422 expands and contracts with lithium intercalation, can cause plastic deformation and extin-  
2423 guish desirable activities. Ledwaba et al. modelled diffusion-induced stress in layered-spinel  
2424 LMO composites, revealing structural resilience, enabled by flexing of a porous structure.<sup>648</sup>  
2425 In this study, Ledwaba et al. found the yield stress of the bulk material was 11.35 GPa,  
2426 whilst the nanoporous material subjected to an equivalent strain experienced a stress of 4.32  
2427 GPa. In fact, it has been proposed that a  $\beta\text{-MnO}_2$  host should be symmetrically porous and  
2428 heavily twinned to maximise the cathode's electrochemical properties.<sup>649</sup> Further to this, in-

2429 tergrowing structures of two polymorphs of  $\text{MnO}_2$ ,  $\beta\text{-MnO}_2$  and Ramsdellite- $\text{MnO}_2$ ,<sup>650</sup> has  
2430 been shown to enhance cell performance,<sup>651</sup> due to reduction in stresses and facile diffusion  
2431 in more open structure of Ramsdellite- $\text{MnO}_2$ .

## 2432 5.2.2 Lithium-ion Diffusion

2433 As discussed in section 2.3.3, Li-ion diffusion coefficients can be calculated using multiple  
2434 techniques, including *ab initio* Molecular Dynamics (MD), classical (potentials-based) MD,  
2435 and Monte Carlo (MC). Diffusion coefficients, although important experimentally and for  
2436 parameterising continuum models, are not the only ion transport property of interest on  
2437 the atomistic scale. Properties such as atomistic diffusion mechanisms, hopping frequencies,  
2438 and activation energy barriers are all vital to understanding Li-ion transport and (dis)charge  
2439 rate behaviour. This is of particular interest for investigating the effects of grain-boundaries  
2440 and interfaces on the migration routes and mechanisms. For example, in  $\text{LiCoO}_2$ , Moriwake  
2441 et al. determined that the activation energy,  $E_a$ , for Li migration *along* a twin boundary is  
2442 0.20 eV, smaller than that in the bulk, while the  $E_a$  *across* a twin boundary is 0.4 eV.<sup>652</sup>  
2443 This demonstrates the influence of grain-boundaries on the kinetic properties.

2444 Computational techniques can provide information regarding a material's diffusion be-  
2445 haviour, which cannot be fully understood through experiments alone. For example, Dixit  
2446 et al. compared Li and Na diffusion in  $\text{Li}_{0.25}\text{FePO}_4$  and  $\text{Na}_{0.25}\text{FePO}_4$ , respectively, by calcu-  
2447 lating the potential and free energy diffusion barriers and determining the nuclear quantum  
2448 effects (NQEs) of the Li ions.<sup>653</sup> Their calculations found that Li diffusion was faster than  
2449 Na diffusion, which is in agreement with experiments. However, the authors also determined  
2450 that the NQEs for Li-ions were higher than those for Na-ions and that the quantum be-  
2451 haviour of the Li-ions was unusual. This information would not be possible to resolve using  
2452 current experimental methods.

2453 The cathode crystal structure determines the available diffusion pathways in the material.  
2454 DFT calculations<sup>654,655</sup> and classical MD using a core-shell model<sup>656</sup> show  $\text{Li}_x\text{FePO}_4$  is an

## Dimensionality of the Li<sup>+</sup> ion transport

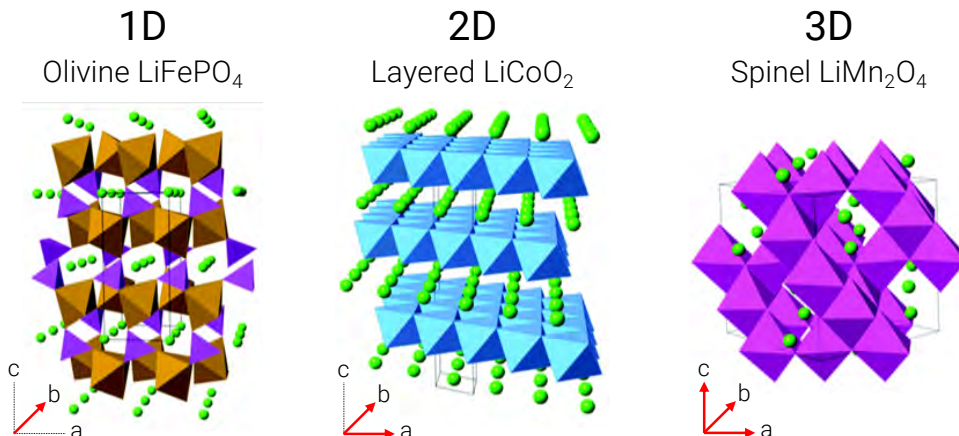


Figure 33: Dimensionality of the Li<sup>+</sup> ion diffusion in LiFePO<sub>4</sub>, LiCoO<sub>2</sub>, and LiMn<sub>2</sub>O<sub>4</sub>. Figure edited and reproduced with permission from Ref. 586 - Published by The Royal Society of Chemistry.

2455 olivine based structure which hosts Li over an interstitial network that has one-dimensional  
2456 connectivity, i.e. 1-D diffusion, along the *b* lattice vector of the orthorhombic cell.<sup>657</sup> Li<sub>*x*</sub>CoO<sub>2</sub>  
2457 is a layered compound that accommodates Li ions within octahedral sites forming two-  
2458 dimensional triangular lattices, resulting in 2-D diffusion, along the *b* and *c* lattice vector  
2459 of the orthorhombic cell.<sup>658</sup> The spinel form of Li<sub>*x*</sub>Mn<sub>2</sub>O<sub>4</sub> has both tetrahedrally and octa-  
2460 hedrally coordinated Li interstitial sites, forming a three-dimensional network and resulting  
2461 in 3-D diffusion, along all lattice vectors.<sup>659,660</sup> These different diffusion pathways can be  
2462 seen in Figure 33. The 1-D diffusion pathways in Li<sub>*x*</sub>FePO<sub>4</sub> are not actually exactly one  
2463 dimensional. Although they travel solely along the *b* lattice vector, the pathways themselves  
2464 are curved, as shown in Figure 34, as originally predicted by Islam et al. using atomistic  
2465 modelling,<sup>656</sup> before later being observed experimentally.<sup>661</sup>

2466 Chemical diffusion coefficient of Li in an intercalation compound often has a strong  
2467 dependence on Li concentration and crystal structure. The combination of DFT cluster  
2468 expansion Hamiltonians with kinetic Monte Carlo (kMC) simulations, as described in sections  
2469 2.1.4 and 2.1.5 revealed that the Li diffusion coefficients of TM oxides (and sulfides) are  
2470 very sensitive to the Li concentration and also to the degree of cation ordering.<sup>77,662–665</sup> For

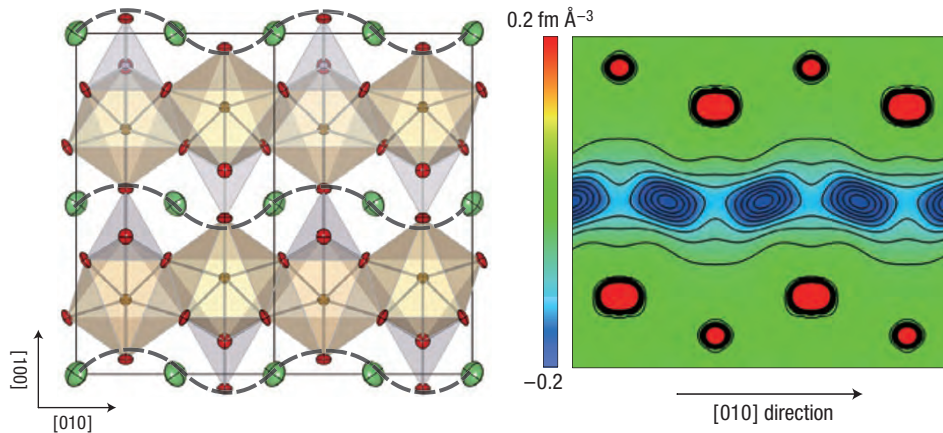


Figure 34: Anisotropic harmonic lithium vibration in  $\text{LiFePO}_4$ . Expected curved one-dimensional continuous chains of lithium motion are drawn as dashed lines to show how the motions of Li atoms evolve from vibrations to diffusion. Two-dimensional contour map sliced on the  $(001)$  plane at  $z = 0.5$ ; lithium delocalises along the curved one-dimensional chain along the  $[010]$  direction, whereas Fe, P, and O remain near their original positions. Adapted by permission from Springer Nature: Ref. 661, Copyright 2008.

2471 example, Van der Ven et al. shows the calculated Li diffusion coefficients for the layered (2D)  
 2472 and spinel (3D) forms of  $\text{Li}_x\text{TiS}_2$  as a function of Li concentration.<sup>9,662,663,665</sup> This is presented  
 2473 in Figure 35, along with the structural images and vacancy mechanisms highlighted. Here it  
 2474 can be seen that not only do the Li diffusion coefficients differ by orders of magnitude, but  
 2475 the shape of the diffusion/Li concentration relation is very different. This shows how the  
 2476 crystal structure, and thus the active diffusion pathways, plays a crucial role in determining  
 2477 the concentration dependence of the diffusion coefficients in these materials.

2478 We have already eluded that diffusion is sensitive to the Li-ion concentration. However,  
 2479 the exact relation is through the activation barriers. Early DFT studies<sup>658,666</sup> of  $\text{Li}_x\text{CoO}_2$   
 2480 systems showed that the lithium diffusion was predominately through a divacancy mecha-  
 2481 nism, when  $0 \leq x < 1$ . However, at infinite vacancy dilutions diffusion is through a single  
 2482 vacancy mechanism.<sup>586</sup> There are two hopping mechanisms at play here; oxygen dumbbell  
 2483 hops and tetrahedral site hops. Oxygen dumbbell hopping occurs when there is a single  
 2484 vacancy and a Li-ion has to travel between two occupied adjacent lithium sites to reach the  
 2485 vacant lithium site. Tetrahedral site hopping occurs when there are divacant or trivacant

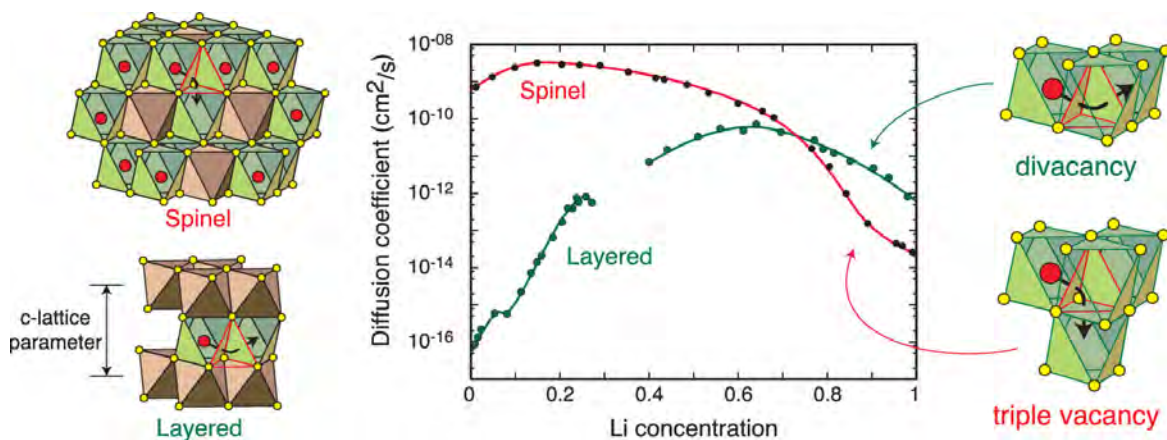


Figure 35: Chemical diffusion coefficient of Li in an intercalation compound often has a strong dependence on Li concentration and crystal structure. Reprinted with permission from Ref. 9. Copyright 2020 American Chemical Society.

2486 sites, i.e. when one or both of the adjacent lithium sites are vacant.<sup>666</sup> Oxygen dumbbell  
 2487 hopping has a significantly lower migration barrier energy compared to tetrahedral site hop-  
 2488 ping, which highlights the sensitivity of the activation barrier to the lithium concentration.  
 2489 Experimental studies of mixed-TM layered oxides, such as  $\text{Li}(\text{Ni}_{0.5}\text{Mn}_{0.5})\text{O}_2$ , have reported  
 2490 site exchange between Li and Ni ( $\sim 8\text{-}12\%$ ).<sup>667</sup> DFT has been used to aid in understanding  
 2491 the effects of site-exchange on Li-ion mobility.<sup>668,669</sup> (De)intercalation of lithium in the ma-  
 2492 terial changes the distances between the layers. As Li is removed from the structure, there  
 2493 is a reduced “barrier” between the oxygen layers which start to repel one another. By calcu-  
 2494 lating the activation energy as a function of the distance between the O layers on either side  
 2495 of the Li layers, a trend between increased O layer separation and lower activation energy is  
 2496 seen.<sup>668,669</sup>

2497 In addition to the crystal structure and available diffusion pathways, doping the cathode  
 2498 material can also influence the material properties, including ion diffusion. NMC cathodes  
 2499 are effectively  $\text{LiCoO}_2$  doped with Ni and Mn. As previously mentioned in section 5.1,  
 2500 introducing Ni and Mn into the system to form a mixed-TM layered oxide increases the  
 2501 diffusion/conductivity and electrochemical performance. There are very few detailed com-  
 2502 putational studies of mixed-TM oxides due to their complexities. An illustration of this is the

2503 complexities which arise from TMs, such as Fe, Ni, Co, and Mn, which exhibit localised oxi-  
2504 dation states. This can be further complicated, or influenced by, TM ordering. For instance,  
2505 Lee and Persson investigated the effects of TM disorder on the electrochemical properties  
2506 of  $\text{Li}_x\text{Ni}_{0.5}\text{Mn}_{1.5}\text{O}_4$  using cluster expansion and MC methods (c.f. sections 2.1.4 and 2.1.5).  
2507 The authors determined a correlation between Li vacancy ordering and TM ordering.<sup>670</sup> Hao  
2508 et al. found similar evidence for  $\text{Li}_x(\text{Mn}_y\text{Ni}_{1-y})_2\text{O}_4$ .<sup>671</sup> These also have an effect on the diffu-  
2509 sion properties of the material. TM ordering in NMC cathodes is discussed in more detail in  
2510 section 5.2.4. Using experimental techniques, Capsoni et al. found that doping the cationic  
2511 sublattice of spinel  $\text{LiMn}_2\text{O}_4$  with as low as 1 %  $\text{Ga}^{3+}$  significantly modifies the temper-  
2512 ature of the conductivity drop associated with Jahn-Teller (JT) distortion, preventing the  
2513 transition observed near room temperature.<sup>672</sup> This allows for a wider temperature window  
2514 for the higher conductivity phase. DFT using generalised gradient approximation (GGA) or  
2515 its variant GGA+U (c.f. section 2.1.1), was also employed to analyse the effect of doping  
2516  $\text{LiMn}_2\text{O}_4$  on the JT distortion. In this study, Singh et al. found that doping with Cr and Mg  
2517 also suppressed the JT distortion and thus the associated temperature of the conductivity  
2518 drop.<sup>673</sup>

### 2519 5.2.3 Redox and Electronic Properties

2520 The cathode operates by the deintercalation of  $\text{Li}^+$  on charging, and the reinsertion of  $\text{Li}^+$   
2521 on discharging. The charge is balanced by the oxidation and reduction of the TM ion, e.g.  
2522  $\text{LiCo}^{3+}\text{O}_2 \rightleftharpoons \text{Li}_{1-x}\text{Co}^{4+}\text{O}_2 + x\text{Li}^+ + xe^-$ . The role of TM redox in LiBs has been well  
2523 known since the first publications by Goodenough on  $\text{LiCoO}_2$  as an intercalation electrode  
2524 in 1980.<sup>565</sup> Although various classes of compounds have been investigated over the years, the  
2525 overall mechanism of TM redox is broadly similar. The three major classes of oxide cathodes,  
2526 (layered,<sup>565</sup> polyanion,<sup>674</sup> and spinel<sup>675</sup>) all function via a TM redox couple. The specific  
2527 capacity of most LiB cathode materials is limited by the number of electrons per TM cation  
2528 that can participate in the redox reaction. However, the recent discovery of oxygen redox



2529 reactivity,  $O^{2-} \rightarrow (O_2)^{n-}$ , in Li-excess cathode materials<sup>600,602–607,609,619,676–690</sup> has prompted  
2530 further investigation.

2531 DFT has been pivotal in shedding light on this phenomenon, in conjunction with a range  
2532 of experimental techniques. DFT can be used to analyse the atomic charge and electronic  
2533 structure of each ground state, enabling the charge compensation during delithiation to be  
2534 correctly attributed during simulated charging. Yao et al. were able to propose a sequence  
2535 of redox events for delithiation of  $Li_xMn_2O_5$ ;<sup>614</sup> first, cationic redox,  $Mn^{3+}/Mn^{4+}$ , dominates  
2536 for  $Li_xMn_2O_5$ , when  $4 \geq x > 2$ . Then anionic redox,  $O^{2-}/O^{1-}$ , dominates for  $Li_xMn_2O_5$ ,  
2537 when  $2 \geq x > 1$ . Finally, mixed cationic ( $Mn^{4+}/Mn^{5+}$ ) and anionic ( $O^{2-}/O^{1-}$ ) redox for  
2538  $Li_xMn_2O_5$ , when  $1 \geq x \geq 0$ . Meanwhile, fluorinated materials such as  $Li_2Mn_{2/3}Nb_{1/3}O_2F$ <sup>629</sup>  
2539 and  $Li_2MnO_2F$ <sup>619</sup> were found to exhibit some overlap between the redox processes, suggest-  
2540 ing that the substitution of O by F favours lower Mn oxidation states, therefore leading  
2541 to more redox overlap with oxygen. DFT has also been used to establish the band struc-  
2542 ture for cathode materials, determining which TM orbitals hybridise more with the O(2p)  
2543 orbitals<sup>679,691</sup> and to identify hole states.<sup>684,692</sup>

2544 In a combined experimental and computational study, Gent et al. observed a strong  
2545 correlation between anion redox, cation migration and open circuit voltage (OCV) hysteresis  
2546 in Li-rich layered oxides.<sup>604</sup> Hong et al. offered an explanation for the strong coupling between  
2547 anion redox and structural disordering in Li rich layered oxides; they found local stabilisation  
2548 of short  $\sim 1.8$  Å metal-oxygen  $\pi$  bonds and  $\sim 1.4$  Å O-O dimers during oxygen redox.<sup>693</sup>

2549 Seo et al. showed that anion redox chemistry is heavily dependent on the anion nearest-  
2550 neighbour coordination environment.<sup>603</sup> In particular, they described how more Li-O-Li con-  
2551 figurations lead to more potentially labile oxygen electrons, resulting in enhanced O redox  
2552 chemistry, as shown in Figure 36. A similar result was found with  $Li_2MnO_2F$ ; those oxygens  
2553 coordinated to at least five Li (e.g.  $OLi_5Mn$ ) in the fully lithiated state were the first to oxi-  
2554 dised, whereas those coordinated to three or fewer (e.g.  $OLi_3Mn_3$ ) did not undergo oxidation  
2555 at all. This showcased a more continuous variation in the O-redox potential, dependent on

2556 the number of Li coordinated to a given  $O^{2-}$  ion.<sup>619</sup> Recent computational screening work on  
 2557 layered oxide cathodes using hybrid DFT has reported trends in O-redox activity associated  
 2558 with the electrostatic (Madelung) energy at oxygen sites.<sup>694</sup>

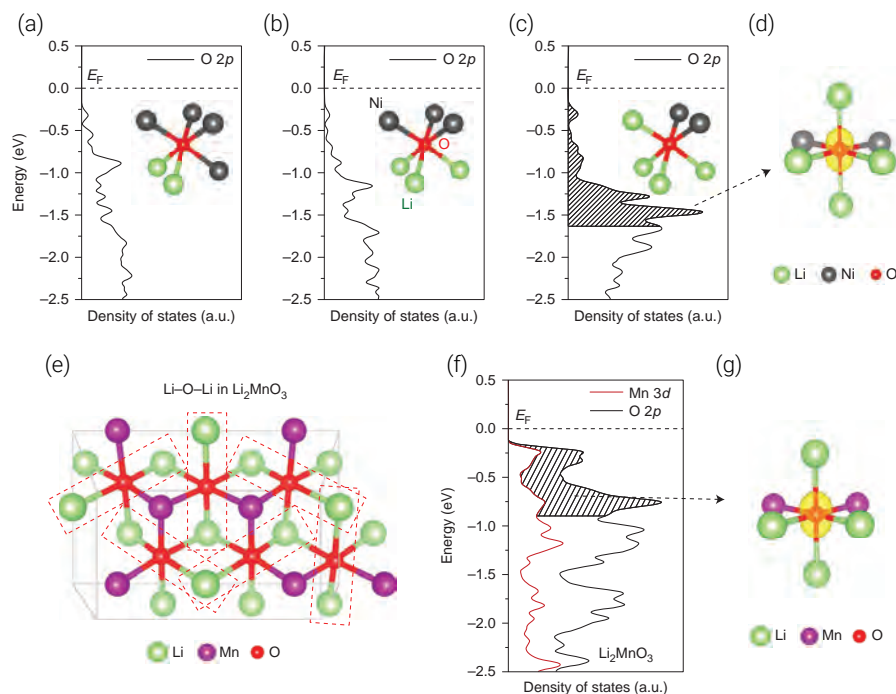


Figure 36: Effect of local atomic environments on the electronic states of O ions in (a-d) cation-mixed layered LiNiO<sub>2</sub> and (e-g) Li<sub>2</sub>MnO<sub>3</sub>. Cation mixing introduces various local environments around oxygen. Projected density of states (pDOS) of the O 2p orbitals of O atoms in cation-mixed layered LiNiO<sub>2</sub> coordinated by (a) two Li and four Ni, (b) three Li and three Ni, and (c) four Li and two Ni. (d) gives the isosurface of the charge density (yellow) around the oxygen coordinated by four Li and two Ni, in the energy range of 0 to -1.64 eV. (e) gives an illustration of Li-O-Li configurations in Li<sub>2</sub>MnO<sub>3</sub>, with (f) giving the related pDOS of the O 2p orbitals and Mn 3d orbitals, and (g) giving the isosurface of the charge density (yellow) around the oxygen, in the energy range of 0 to -0.9 eV. Adapted by permission from Springer Nature: Ref. 603, Copyright 2016.

2559 Chen and Islam investigated delithiation and kinetic processes in Li<sub>2</sub>MnO<sub>3</sub> using hybrid  
 2560 DFT and found that Li extraction is charge-compensated by oxidation of the oxide anion,  
 2561 so that the overall delithiation reaction involves lattice oxygen loss.<sup>681</sup> Localised holes on  
 2562 oxygen ( $O^-$ ) are formed at the first step but, due to their instability, lead to oxygen dimers  
 2563 (O-O is approximately 1.3 Å) and eventually to the formation of molecular O<sub>2</sub>. This then  
 2564 facilitates Mn migration to the octahedral site in the vacant Li layer, leading to a spinel-like

2565 structure. DFT has also been used to show the formation of  $O_2$  at high states of charge in  
2566  $Li_2MnO_2F$ <sup>619</sup> and  $Li_{1.2}Ni_{0.13}Co_{0.13}Mn_{0.54}O_2$ ,<sup>608</sup> agreeing with experimental resonant inelastic  
2567 X-ray scattering (RIXS) data, and to report superoxide formation in  $Li_2VO_2F$ , in agreement  
2568 with electron paramagnetic resonance (EPR) spectroscopy studies.<sup>628</sup>

#### 2569 **5.2.4 TM Ordering in NMC Layered Oxides**

2570 Cation/anion ordering also plays a vital role in the properties/activity of a material, such  
2571 as the physical and electrochemical properties. A topical illustration of this is the NMC  
2572 cathode materials, where recent experimental studies show that spin interaction of the TM  
2573 ions is a major challenge.<sup>597,695</sup> The varying compositions, charge distributions, and elec-  
2574 tron negativities of the TMs lead to a mixture of valence states, where Ni can exist as  $Ni^{2+}$ ,  
2575  $Ni^{3+}$ , and  $Ni^{4+}$ , Co can exist as  $Co^{3+}$  and  $Co^{4+}$ , and Mn exists as  $Mn^{4+}$ .<sup>695</sup> The interac-  
2576 tions between these mixed valence states poses a challenge to the identification of ground  
2577 states. As NMC materials, such as NMC811, emerge as front runners for commercialisation,  
2578 research into their specific chemistry has become of great interest. Recently, several com-  
2579 putational studies have been performed to analyse the influence of TM valence states on  
2580 the stability and structure-property relationships of NMC materials, which are challenging  
2581 to resolve experimentally.<sup>696-699</sup> Sun and Zhao analysed five NMC compositions, observing  
2582 that random arrangements of TMs present similar thermodynamic states, which is in con-  
2583 tradiction with experiments identifying that TM spin interactions vary the stability of any  
2584 NMC composition.<sup>696</sup>

#### 2585 **5.2.5 Vibrational and Thermal Properties**

2586 An important contribution to the thermodynamic properties at finite temperature is the  
2587 vibrational partition function, which can be evaluated by calculating the material's normal  
2588 modes of lattice vibrations. A number of researchers have theoretically addressed the vibra-  
2589 tional contribution to the material thermodynamic properties in LiBs, especially in NMC

2590 cathodes.<sup>181,182,700</sup> There are several works studying cathode materials beyond NMC. Shang  
2591 et al. employed DFT phonon calculations with a mixed-space approach to probe the lattice  
2592 dynamics and finite-temperature thermodynamic properties of olivine structure  $\text{LiMPO}_4$  (M  
2593 = Mo, Fe, Co, Ni).<sup>701</sup> The authors reported that  $\text{LiMPO}_4$  structures from Mn, Fe, Co, to  
2594 Ni show increasing zero-point vibrational energy, but a diminishing vibrational contribution  
2595 to the Gibbs energy, due to the decreasing phonon densities of state at the low frequency re-  
2596 gion of  $\text{LiMPO}_4$ . Recently, lattice dynamics studies have been expanded to solid electrolytes,  
2597 aiding in the discovery of lithium fast-ion conductors.<sup>702</sup>

2598 Two major approaches have been developed to compute lattice thermal conductivity;  
2599 by solving the Boltzmann transport equation (BTE) using anharmonic lattice dynamics  
2600 and through MD simulations. Puligheddu et al. compared lattice thermal conductivity  
2601 values from these two methods and found a satisfactory agreement.<sup>703</sup> The comparison used  
2602 empirical potentials and took into account the effects of both fourth order phonon scattering  
2603 and temperature-dependent phonon frequencies, reporting the different effects of quantum  
2604 and classical statistics.

2605 Using BTE within the relaxation-time approximation, Mattila and Karttunen reported  
2606 the highly anisotropic lattice thermal conductivities in isotopic  $\text{LiCoO}_2$ , close to the values  
2607 in Yang et al.'s work,<sup>181,182</sup> and illustrated the effect of the alkali metal atom by replacing  
2608 Li by Na.<sup>704</sup> The authors explained this through the significantly shorter phonon lifetimes  
2609 in  $\text{LiCoO}_2$ . They found that in-plane lattice thermal conductivities in  $\text{NaCoO}_2$  are  $\sim 0.7$   
2610 times larger than that in  $\text{LiCoO}_2$  at room temperature, since the former has significantly  
2611 longer phonon life times. While Feng et al. report much lower thermal conductivity values  
2612 by including four-phonon scattering, using a different functional, the local density approxi-  
2613 mation (LDA), for exchange and correlation.<sup>705</sup> They also investigated the thermal transport  
2614 reduction during delithiation (charging) due to reduced phonon velocities and increasing an-  
2615 harmonicity. Furthermore, grain-boundary effects reduced thermal transport and suppressed  
2616 thermal conductivities in polycrystals are well reproduced when grain sizes were reduced down

2617 to several nm in either BTE or MD simulations.<sup>155</sup>

2618 The thermal conductivity investigation can be also performed on anodes and many other  
2619 materials.<sup>706,707</sup> Recently, a high-throughput study was reported for 37 binary rock-salt and  
2620 zinc blende material systems, in which the authors highlight the importance of high-order  
2621 phonon-phonon interactions based on harmonic calculations.<sup>708</sup> Modelling heat transport  
2622 using DFT calculations is complex but essential due to the difficulties inherent in preparing  
2623 high-quality samples for experimental measurements.

### 2624 5.3 Surfaces

2625 Surface structures and morphologies of cathode particles are difficult to determine using  
2626 experimental methods alone and thus computational investigations can provide vital in-  
2627 sights.<sup>709</sup> Both *ab initio* and potentials-based MD have been extensively used to investigate  
2628 the surfaces and morphologies of layered oxides, spinel oxides, and olivine phosphates, which  
2629 will be briefly discussed here. These techniques have also been used to investigate cathode  
2630 materials in sodium-ion batteries, which is covered in more detail in Ref. 586.

2631 With oxides at the forefront of the battery revolution, it is unsurprising that there have  
2632 been many DFT and potentials-based MD studies into layered  $\text{LiCoO}_2$ ,  $\text{LiMn}_2\text{O}_4$  spinel,  
2633  $\text{MnO}_2$ -type and related materials, looking at properties including the surfaces, nanostruc-  
2634 tures, and morphologies.<sup>710–717</sup> Surface energies for low-index layered  $\text{LiCoO}_2$  surfaces, as a  
2635 function of external Li and O chemical potentials, revealed the (0001) and  $(10\bar{1}4)$  surfaces  
2636 were present for all reasonable values of Li and O chemical potentials, whereas the  $(01\bar{1}2)$   
2637 surface was only stable under oxidising conditions.<sup>710</sup> Studies into the low-index surface  
2638 facets of  $\text{LiMn}_2\text{O}_4$  determine the (111) surface to be the most stable. This is due to the site  
2639 exchange of under-coordinated Mn on the surface, which exhibit a cubo-octahedral type, pre-  
2640 dominately comprising  $\{111\}$  surfaces.<sup>715</sup> Other studies show that the Mn-terminated (111)  
2641 surfaces undergo surface reconstruction, indicating instead that the Li-terminated (001) sur-  
2642 face has the lowest energy.<sup>714</sup>

2643 It has also been shown that electronic spin state transitions occur on the surfaces of sto-  
2644 ichiometric  $\text{LiCoO}_2$ . Here Qian et al. found that the trivalent Co ions at the surface adopt  
2645 an intermediate spin state if they are square-pyramidally coordinated and a high spin state  
2646 if they are pseudo-tetrahedrally coordinated. This highlighted the effect of low-coordinated  
2647 geometries at the particle surface on the  $\text{Co}^{3+}$ - $\text{Co}^{4+}$  redox potential.<sup>718</sup> Hong et al. investi-  
2648 gated the surface properties of  $\text{LiCoO}_2$  nanoplatelets and their chemical modifications with  
2649  $\text{Al}^{3+}$ , using combined experimental and theoretical approaches.<sup>719</sup> Their models also showed  
2650 the electronic structures of several  $\text{LiCoO}_2$  surface facets are different from those of the bulk,  
2651 attributing this to the altered spin states of surface  $\text{Co}^{3+}$  atoms. The authors found splitting  
2652 of the Co 3d-O 2p states, which were linked with high-spin-state  $\text{Co}^{3+}$  at the surface. Partial  
2653 substitution of  $\text{Co}^{3+}$  by  $\text{Al}^{3+}$  was found to increase the ratio of low-spin-state  $\text{Co}^{3+}$  at the  
2654 surface, resulting in a distinct change in the intensity ratio of the split Co 3d-O 2p states.

2655 When exposed to certain environmental conditions,  $\text{LiCoO}_2$  releases Co cations, a known  
2656 toxicant. Abbaspour-Tamijani et al. has applied DFT (with different functionals) and ther-  
2657 modynamics modelling to study the  $\text{LiCoO}_2$  surface transformations.<sup>720</sup> They assessed how  
2658 the calculated predictions for ion release depend on aspects of the structural surface model.  
2659 Here, the authors propose a generalised scheme for predicting a threshold pH at which Co  
2660 release becomes favourable, providing information that could be used to inform macroscopic  
2661 contaminant fate models. More recently, these authors have furthered this investigation in  
2662 cation dissolution at the  $\text{LiCoO}_2$  surface, finding that at a pH of 7, 16 % of surface Co  
2663 undergoes dissolution.<sup>720</sup>

2664 Phase transitions in cathode materials can have negative effects on the desirable proper-  
2665 ties. However, there are circumstances where use of different structural phases are beneficial.  
2666 For example, post-modification of Li-rich layered material surfaces to form a spinel  $\text{LiMn}_2\text{O}_4$   
2667 membrane, i.e. encapsulating the layered particle, has shown enhanced related rate capabil-  
2668 ity and cycling stability.<sup>148,721,722</sup> More significantly, insertion of a spinel component<sup>723</sup> or the  
2669 formation of platelets<sup>724</sup> on layered-layered composites of NMC cathodes, yields a high spe-

2670 cific capacity ( $\sim 250 \text{ mAh g}^{-1}$ ) and can partly correct for voltage fade.<sup>148</sup> Phase transitions  
2671 can also be a negative consequence of particle surface stress. Warburton et al. investigated  
2672 the particle fracturing in  $\text{LiMn}_2\text{O}_4$  caused by stress through the delithiation process.<sup>725</sup> Using  
2673 DFT, the authors provide a good understanding of the stress buildup at the surface during  
2674 delithiation, demonstrating that the delithiation of near-surface layers contribute towards  
2675 the buildup, leading to a  $\text{LiMn}_2\text{O}_4/\text{Li}_{0.5}\text{Mn}_2\text{O}_4$  low-voltage phase transition, Figure 37. The  
2676 authors also investigate if there is an orientation preference, concluding that cracks due to  
2677 tensile stress buildup are not likely to orient preferentially in the [001] direction, because the  
2678 stresses act in the plane of the (001) surface.<sup>725</sup> This shows that an in-depth understanding of  
2679 the electrochemical processes of cathode materials, at the atomistic scale, is urgently needed,  
2680 especially for more complex chemistries like NMC. A recent study on the NMC surfaces by  
2681 Liang et al. looked at the surface segregation and anisotropy using DFT+U calculations.<sup>726</sup>  
2682 In this study, the authors looked at surface stability, morphology, and elastic anisotropy, all  
2683 related to the degradation of Li-ion batteries. Ni surface segregation predominantly occurs  
2684 on the (100), (110), and (104) nonpolar surfaces, showing a tendency to form a rock-salt  
2685 NiO domain on the surface, due to severe Li-Ni exchange. The findings of this study showed  
2686 that an uneven deformation is more likely to form in particles which have been synthesised  
2687 under low oxygen conditions, leading to crack generation and propagation.<sup>726</sup>

2688 The surface structures of  $\text{LiFePO}_4$  exhibit a complex and uneven topology due to the  
2689 size difference of  $\text{Li}^+$ ,  $\text{Fe}^{2+}$ , and  $\text{PO}_4^{3-}$ . The majority of terminating surfaces undergo  
2690 fairly considerable relaxation, which makes predictions based on rigid terminations unre-  
2691 liable. Although  $\text{LiFePO}_4$  can be synthesised in multiple morphologies exposing different  
2692 surfaces,<sup>646,727</sup> studies on the (010) surfaces are particularly interesting. This surface is nor-  
2693 mal to the most facile pathway for lithium ion conduction,<sup>728</sup> reducing the diffusion path  
2694 lengths for lithium at the surface, enhancing the electrochemical performance of the cath-  
2695 ode. DFT calculation of the diffusion pattern and energy landscape of lithium in  $\text{LiFePO}_4$   
2696 showed that the energy barrier for the Li diffusion along (010) is lower than along the other

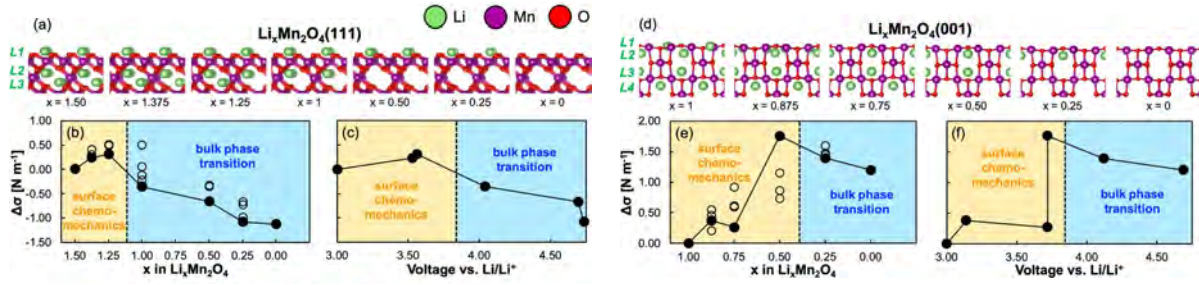


Figure 37: Surface stress evolution upon delithiation of lithium manganese oxide (LMO) surfaces. Low energy structures of the (a) LMO(111) and (d) LMO(001) surfaces at different  $\text{Li}^+$  contents. Differential surface stresses of (b) LMO(111) and (e) LMO(001) as a function of the  $\text{Li}^+$  content for various  $\text{Li}^+$  configurations. The filled circles in (b,e) represent the most energetically stable structures for a given stoichiometry. The unfilled circles in (b,e) denote metastable lithium configurations. Differential surface stresses of (c) LMO(111) and (f) LMO(001) as a function of the cell voltage. The dashed lines correspond to the calculated equilibrium potential of 3.84 V vs  $\text{Li}/\text{Li}^+$  between LMO and  $\text{L}_{0.5}\text{MO}$ . The yellow-shaded regions correspond to surface-dominated mechanics from the near-surface delithiation. The blue-shaded regions correspond to surface phases that are thermodynamically inaccessible because they become stable only at voltages above the equilibrium potential. Reprinted with permission from Ref.<sup>725</sup> Copyright 2020 American Chemical Society.

2697 directions, e.g. (100), indicating that the Li diffusion in  $\text{LiFePO}_4$  is one dimensional.<sup>729</sup>  
 2698 Understanding processes such as the lithium (de)intercalation on the  $\text{LiFePO}_4$  (010) surface  
 2699 is important for developing effective approaches for further improving the material's rate  
 2700 performance. Using DFT calculations, Xu et al. found that the extraction of Li from the  
 2701 surface layer has a significant effect on the work function of the  $\text{LiFePO}_4$  (010) surface, pro-  
 2702 viding evidence for whether Li atoms are present in the outermost layer of  $\text{LiFePO}_4$  (010)  
 2703 surface or not.<sup>730</sup> Here, the authors also calculate the redox potential and formation energies  
 2704 for extracting Li from different (010) surface layers. They find that extracting lithium from  
 2705 the outer surface layers has the lowest redox potential and formation energy, indicating that  
 2706 it is energetically favorable to extract Li first from the surface layer. Xu et al. propose a  
 2707 new method that surface work functions can be used for providing insight into the lithium  
 2708 (de)intercalation on the  $\text{LiFePO}_4$  (010) surface.<sup>730</sup>

2709 Zhang et al. used a combined experimental and computational (DFT) approach to inves-  
 2710 tigate the preferential cation doping on the surface of  $\text{LiFePO}_4$  and its effect on properties.<sup>731</sup>



2711 The authors found that, for all chosen dopants, there were increased ratios of  $\text{Fe}^{3+}/\text{Fe}^{2+}$  ox-  
2712 idation on the particle surfaces, while the core atoms remained closer to that of the pristine,  
2713 undoped material. This indicates that the dopants are predominantly pushed to the particle  
2714 surfaces during phase formation. This disparity in distribution of dopant across the core and  
2715 surface results in improved conductivities.<sup>731</sup> *ab initio* MD simulations with X-ray Diffrac-  
2716 tion (XRD) and microscopy experiments on the  $\text{LiFePO}_4$  cathode show Li-ions migrating  
2717 along the surface, facilitated by solvent molecules.<sup>732</sup> This work establishes fluid-enhanced  
2718 surface diffusion as a key factor in tuning phase transformation in anisotropic solids.

## 2719 5.4 Interfaces

2720 Although the cathode-electrolyte interphase (CEI) is thinner than the SEI at the anode,  
2721 it is still quite complex in structure and composition.<sup>115,733</sup> DFT-based simulations can  
2722 provide insight into adsorption trends,<sup>734</sup> reaction pathways and energetics,<sup>735,736</sup> and mi-  
2723 gration barriers for Li-ion transfer,<sup>737</sup> etc. The electrolyte in a Li-ion battery is typically a  
2724 Li salt, for example  $\text{LiPF}_6$  in an organic carbonate solvent, such as ethylene carbonate (EC),  
2725 propylene carbonate (PC), diethyl carbonate (DEC) or dimethyl carbonate (DMC). The  
2726  $\text{LiPF}_6$  electrolyte reacts with trace amounts of moisture to form hydrofluoric acid (HF),<sup>735</sup>  
2727 which is highly corrosive and reacts with the cathode surface to form fluoride-based prod-  
2728 ucts.<sup>736</sup> The organic carbonate solvent also reacts with the cathode surface to form a series  
2729 of decomposition products.<sup>738</sup> The adsorption of solvent-decomposition and fluoride-based  
2730 products is the first step in the series of reactions that lead to the formation of the CEI.  
2731 The decomposition reaction of cyclic organic carbonate solvents proceeds via ring opening,  
2732 having an energy barrier predicted via climbing image nudged elastic band (CI-NEB) calcu-  
2733 lations (sections 2.1.1 and 2.1.3) to be around 0.62 eV on (100)  $\text{LiMn}_2\text{O}_4$  surfaces,<sup>716</sup> over  
2734 1 eV on (101 $\bar{4}$ )  $\text{LiCoO}_2$  surfaces,<sup>738</sup> and around 0.29 eV on (101 $\bar{4}$ )  $\text{Li}(\text{Ni},\text{Mn},\text{Co})\text{O}_2$  sur-  
2735 faces.<sup>739</sup> While experimental studies on the composition of the CEI have shown the presence  
2736 of both solvent-decomposition and fluoride-based products on most oxide cathodes, such as

2737  $\text{LiMn}_2\text{O}_4$ ,  $\text{LiNiO}_2$ ,  $\text{LiCoO}_2$  and  $\text{LiNi}_{0.8}\text{Co}_{0.2}\text{O}_2$ , no solvent reaction or solvent decomposition  
2738 products are detected on  $\text{LiFePO}_4$ .<sup>733,740</sup> Recent calculations of adsorption energies based  
2739 on DFT have shown that adsorption preference of HF over EC leads to the entire  $\text{LiFePO}_4$   
2740 nano-particle being covered by fluoride-based products, further leading to their dominant  
2741 presence in the CEI.<sup>734</sup> DFT simulations have also been used to design suitable coatings in  
2742 order to prevent cathode degradation.<sup>736</sup> These calculations can shortlist effective candidate  
2743 materials to guide experiments. Thus, atomistic methods can not only provide the neces-  
2744 sary insights needed in order to explain experimental observations, but also suggest novel  
2745 solutions for mitigating cathode degradation.

2746 Apart from the complexity of structure of the CEI, another challenge is understanding  
2747 Li-ion migration at the CEI, impacting the rate capability of LiBs. Li-ion conductivity in  
2748 bulk electrolyte is around  $1 \text{ S cm}^{-1}$  (c.f. section 4) which is several orders of magnitude  
2749 higher than that in bulk electrode materials (c.f. sections 3.2.4 and 5.2.2) (around  $10^{-7}$ –  
2750  $10^{-2} \text{ S cm}^{-1}$ ).<sup>285,665</sup> However, the complex structure of the CEI and uncertainty about the  
2751 mechanism of Li-ion transfer across it has hindered the understanding of kinetics at the in-  
2752 terface. Recent NEB calculations on the  $\text{LiFePO}_4$  cathode have estimated an energy barrier  
2753 of 756 meV, for Li to move from a near-surface solvated cluster to a sub-surface vacancy  
2754 in the  $\text{LiFePO}_4$  cathode material.<sup>737</sup> Due to preferential adsorption of fluoride on  $\text{LiFePO}_4$   
2755 surfaces,<sup>733,734</sup> the energy barrier has been found to decrease to 410 meV in the presence  
2756 of fluoride. Nevertheless, the interfacial energy barrier is higher than that in bulk cathode  
2757 material, which is estimated to be around 270–290 meV.<sup>654,741</sup> This highlights a rate-limiting  
2758 behaviour of the interface in the overall Li-ion diffusion process in LiBs. This study moti-  
2759 vates further investigation on other cathode electrolyte interfaces, especially with recently  
2760 developed advanced methods for characterising the interface, as described in section 2.2.1.

## 2761 5.5 Outlook and challenges for cathodes

2762 Lowering the cost, increasing capacity, and improving the sustainability of battery materials  
2763 is becoming more critical, as we move towards large-scale deployment of LiBs for applications  
2764 such as EVs.<sup>568</sup> Here, we highlight some of the outstanding challenges for cathodes and how  
2765 atomistic modelling can provide insights and suggest solutions.

2766 Ni-rich NMC layered oxides are favorite candidates for cathode materials, due to their  
2767 high gravimetric and volumetric energy densities.<sup>742</sup> However, these materials have three  
2768 critical challenges: cycle instability, thermal instability, and air instability. These are all  
2769 linked with the instability of Ni<sup>3+</sup> and Ni<sup>4+</sup> at the surface/interface. Other cathode materials,  
2770 such as oxyfluorides, have worked towards solving some of these issues, however, there are  
2771 still outstanding surface and interfacial challenges, for which atomistic modelling is vital:

2772 • In Ni-rich NMC, the unstable Ni<sup>3+</sup> and Ni<sup>4+</sup> react aggressively with the electrolyte  
2773 to form thick CEI layers and cause Ni and Mn dissolution. The dissolute TMs then  
2774 migrate to the anode and cause electrolyte decomposition, leading to thick SEI layers  
2775 which limit the battery cyclability.<sup>743,744</sup> CEI and SEI formation are crucial challenges  
2776 to be overcome for both conventional and solid-state batteries. Although electrochem-  
2777 ical spectroscopic techniques have been used to obtain molecular scale information,  
2778 further detail, which cannot be resolved using current experimental techniques, is  
2779 needed to gain more reliable information.<sup>745</sup> For example, deconvoluting impedance  
2780 components in two-terminal electrochemical impedance spectroscopy (EIS) data that  
2781 have similar time constants is challenging.<sup>746</sup> Half-cell measurements can be used to  
2782 study the impedance of the two electrodes separately, but this does not fully reflect  
2783 the processes occurring in a full-cell battery at different states of (dis)charge.<sup>747</sup> This  
2784 is where atomistic modelling can provide the fundamental understanding and can be  
2785 used to guide further experiments.

2786 • Phase transitions at the surface of cathode materials occur at a high state of charge

2787 and affect the surface reactivity, resulting in increased TM dissolution and CEI/SEI  
2788 formation. The effect of this is rapid capacity fading during cycling.<sup>748</sup> Co-free Li-  
2789 rich layered oxides, such as  $\text{Li}[\text{Li}_{0.2}\text{Mn}_{0.6}\text{Ni}_{0.2}]\text{O}_2$ , are appealing due to their low cost  
2790 and high capacities ( $300 \text{ mAh g}^{-1}$ ).<sup>749,750</sup> However, these materials undergo layered to  
2791 spinel transitions due to low octahedral site stability of  $\text{Mn}^{3+}$ , leading to voltage decay  
2792 during cycling and Mn dissolution,<sup>751</sup> making these materials challenging to employ  
2793 as a practical cathode. Atomistic insight into the mechanisms involved in these phase  
2794 transitions, gained through *ab initio* and potentials-based MD methods, can provide  
2795 the detail and understanding needed to prevent these phase transitions from occurring.

2796 • Some cathode materials show reversible O-redox, with lower voltage hysteresis and,  
2797 where  $\text{O}_2$  is formed, it reincorporates into the lattice.<sup>619</sup> In contrast, other materials  
2798 show irreversible O-redox, with  $\text{O}_2$  lost from the surface,<sup>608,681,752</sup> leading to unwanted  
2799 side reactions with the electrolyte. The formation and potential loss of molecular  $\text{O}_2$   
2800 is likely to be heavily dependent on local structure. In the case of  $\text{Li}_2\text{MnO}_2\text{F}$ , DFT  
2801 showed that  $\text{O}_2$  is formed only in O-Li rich areas, not in O-Mn rich areas.<sup>619</sup> Meanwhile,  
2802 other oxyfluorides, such as  $\text{Li}_2\text{VO}_2\text{F}$ , do not show molecular  $\text{O}_2$  formation at all, but  
2803 instead form superoxides on charging.<sup>628</sup>

2804 It is challenging to model disordered systems as, by their very nature, they can have  
2805 an almost infinite arrangement of atoms. Use of computational techniques, such as cluster  
2806 expansion, to generate low energy structures of disordered rock-salts, is a promising route  
2807 to more realistic DFT studies.<sup>621</sup>

2808 As discussed in sections 2.2.2 and 4.2.4, more careful considerations of the factors/parameters  
2809 to include when fitting interatomic potentials for a system is key to improving the quality  
2810 of research conducted through potentials-based modelling. It is commonplace to reuse po-  
2811 tentials from literature sources, without determining how they were fitted, which can lead  
2812 to inaccuracies in the calculations performed. For example, if the potentials for a cathode  
2813 material were fitted only to lattice parameters, elastic constants, and the bulk modulus, then

2814 the potential would not be accurately representative of the cathode redox properties. If prop-  
2815 erties such as the dielectric constant were included, then redox chemistry would be better  
2816 represented. In effect, interatomic potentials in literature are not necessarily transferable to  
2817 different types of study. It is not feasible to fit to every material property, however, a broader  
2818 range of properties, most relevant to the study being conducted, is required. There are tools  
2819 in development<sup>142,143,145,164</sup> aiming to make this potential fitting process more accessible to  
2820 atomistic modellers, with the ability to fit to a larger range of parameters. However, there  
2821 is still a need for improved transparency in the publication of studies using interatomic po-  
2822 tentials. Use of machine learning to develop potentials has also shown to be a promising  
2823 avenue. Deringer et al. recently published a progress update, showing how machine learn-  
2824 ing is improving interatomic potentials by “learning” from electronic-structure data, giving  
2825 increased accuracy in approximating material properties.<sup>753</sup>

2826 In-depth insight into the elemental distribution, electronic structure, and crystalline  
2827 structure under electrochemical conditions is challenging to achieve experimentally. Atom-  
2828 istic techniques, including DFT and MD, are well suited to provide the insight needed for  
2829 these properties. However, future research and development of cathode materials will re-  
2830 quire collaborative efforts, involving the disciplines of chemistry, physics, material science,  
2831 nanoscience/nanotechnology, and computational modelling/simulation.<sup>116</sup>

## 2832 6 Outlook

2833 In this review, we have introduced the key methods deployed in battery modelling at the  
2834 atomistic scale (section 2.1) in lithium-ion batteries (LiBs) and solid-state batteries (ASSBs),  
2835 which are collectively called lithium batteries. We have summarised progress in this field,  
2836 covering models for anodes, liquid and solid electrolytes, and cathodes. Outlooks specific to  
2837 these components are summarised as follows: anodes, in section 3.5; liquid electrolytes, in  
2838 section 4.2.10; solid electrolytes, in section 4.3.5; and cathodes, in section 5.5.

2839 There are several notable developments in atomistic methods for lithium batteries which  
2840 need to be addressed. These include development of a semi-grand canonical framework, incor-  
2841 porating order parameters, with initial promising work developed by Van der Ven et al.,<sup>9,231</sup>  
2842 the expansion of the linear scaling Density Functional Theory (DFT) codes,<sup>58,62,65</sup> to link up  
2843 with kinetic Monte Carlo (kMC), the inclusion of entropy effects by parameterising a phase  
2844 field model (such as those developed by Bazant)<sup>95–97</sup> using results obtained from Monte Carlo  
2845 (MC) calculations, development of more accurate force field potentials, and parallelisation  
2846 to speed up MC calculations on longer length scales.

2847 Alongside deepening our understanding of atomic structure and processes, atomistic mod-  
2848 els can be used to aid the design of new materials with improved capacity, rate capability,  
2849 and stability. Atomistic modelling approaches have been shown to be strong tools to de-  
2850 velop novel nanostructures and composites, understand dynamics and phase behaviour, and  
2851 could identify novel interfaces to accommodate volume expansion in solid solution materials,  
2852 such as silicides. Promising areas for future work include tuning the morphology and com-  
2853 position of graphite edges<sup>70,253,254</sup> and interlayer spacings<sup>214</sup> to aid intercalation, improved  
2854 understanding of the phase behaviour and dynamics of silicides as anode materials,<sup>270</sup> and  
2855 investigation of the emerging class of Li-rich cathode materials.<sup>606,607,609</sup>

2856 We have identified several outstanding challenges for further work. For example, certain  
2857 anode and cathode materials show pronounced hysteresis between charge and discharge cy-  
2858 cles.<sup>71,226,270,754–756</sup> This results in a difference between expected equilibrium potentials from  
2859 atomic-scale calculations and the experimentally measurable open circuit voltage (OCV),  
2860 which creates ambiguity when using the measured OCV in longer length scale models, like  
2861 control models for battery management systems. Future kinetic models must therefore ac-  
2862 count for metastable behaviour that can persist over experimental time scales of hours or  
2863 even days.<sup>226</sup> The next generation of models should consider the connectivity between differ-  
2864 ent phase transformations, with the framework developed by Van der Ven et al. highlighted  
2865 above being one promising solution that is potentially transferable to a variety of material

2866 types.

2867 Flammable liquid electrolyte materials currently dominate the commercial market. De-  
2868 velopment of safer, non-flammable, electrolyte materials is key to addressing safety concerns  
2869 and accidents resulting from attempts to confine increasing energy densities into smaller  
2870 volumes and into geometries that are challenging to thermally manage. More work is needed  
2871 to investigate potential avenues for resolving these issues, including alternative liquid elec-  
2872 trolytes,<sup>17,18,391</sup> such as water-in-salt electrolytes,<sup>388,389</sup> and replacing liquid electrolytes with  
2873 solid or soft matter alternatives.<sup>23,547</sup> Advancements in electrolyte design are crucial, where  
2874 critical obstacles could be resolved through new novel electrolyte salts and solvents. De-  
2875 velopment and open source accessibility of atomistic scale models, combined with improved  
2876 experimental studies, provide a framework for high throughput screening of electrolyte ma-  
2877 terials.<sup>355,384,387,398</sup>

2878 More work is needed to incorporate heterogeneities formed during material synthesis and  
2879 battery degradation,<sup>757-759</sup> such as point defects<sup>89,93,287,515,698</sup> and grain boundaries,<sup>302,499,760</sup>  
2880 into atomistic models and to determine their effect on battery performance. Modelling of  
2881 the complex behaviour at interfaces, such as the solid-electrolyte interphase (SEI) in LiBs  
2882 and lattice mismatch in ASSBs, is a prominent challenge which requires further investiga-  
2883 tion. Atomistic models have already provided insight into particular aspects of degradation,  
2884 leading to design of more robust materials, but the development of a universal framework  
2885 for simulating degradation mechanisms and their interactions would be of great benefit and  
2886 is still beyond current capabilities. In order for such a framework to be truly multiscale,  
2887 significant work is needed to connect the modelling scales, linking atomistic to continuum  
2888 modelling and on to longer length scales, such as control models, as well as forming closer  
2889 links with experiments at all scales.

2890 As we have seen throughout this review, different atomistic modelling approaches can be  
2891 used individually to gain insight into different aspects and properties of LiB materials, across  
2892 the wide range of time and length scales encompassing atomistic modelling. When combined

2893 into multiscale modelling (MSM) approaches, these techniques can provide a more complete  
2894 interpretation of the material(s).<sup>10,11,232</sup> A popular approach has been to combine DFT cal-  
2895 culations of activation energies of different events, which are then used to implement kMC  
2896 simulations.<sup>104</sup> DFT calculations of the migration mechanisms and activation barriers of Li-  
2897 ions have also been combined with classical MD studies of Li-ion diffusion to gain a more  
2898 complete analysis of the dynamic properties in LiB materials.<sup>761,762</sup> Quantum mechanical  
2899 techniques, such as DFT, are also increasing being used to parameterise larger scale tech-  
2900 niques, for example classical MD.<sup>143–145,164,753</sup> The key consideration when designing MSM  
2901 approaches is to reproduce the phenomena that dictate the natural behaviour and evolution  
2902 of the material in given conditions. Thorough reviews, which focus more on the MSM aspect  
2903 of LiB research, have recently been published by Franco et al.<sup>232</sup> and Shi et al.<sup>10</sup> kMC  
2904 in particular has been highlighted as a natural technique to bridge length scales, naturally  
2905 including different time scale dynamic events.<sup>104</sup> In this review, we have instead focused on  
2906 the individual contributions of atomistic techniques, the understanding of which is key to  
2907 building MSM approaches. However, the full complexity of composite materials, such as  
2908 C/Si, may only be accessible by bridging atomistic techniques to MSM such as via phase  
2909 field methods, volume-averaged approaches, or mesostructurally-resolved models.<sup>10,11,95,232</sup>

2910 This review has focused almost entirely on lithium batteries, given that they currently  
2911 comprise the most technologically advanced rechargeable battery systems that are commer-  
2912 cialised at scale. However, atomistic modelling applied to LiBs also improves understanding  
2913 of batteries that could be based on more environmentally-friendly or Earth-abundant ma-  
2914 terials, such as sodium. Solid state models of intercalation, applied to LiBs, are directly  
2915 transferable to other intercalation chemistries. The understanding of interfaces in batteries  
2916 with other chemistries is even less developed than in LiBs. However, the modelling frame-  
2917 works highlighted in this review, such as the linear-scaling DFT framework, could also be  
2918 applied to improve understanding of these interfaces.



## 2919 Acknowledgement

2920 The authors thank the Faraday Institution (<https://faraday.ac.uk/>; EP/S003053/1), grant  
2921 number FIRG003, for funding, and Dr. Maxim Zyskin for his discussions. We also thank  
2922 Mr. Amir Kosha Amiri for his graphical design expertise in constructing and formatting the  
2923 figures, as well as Dr. Felix Hanke and Dr. Victor Milman from BIOVIA for their comments  
2924 and suggestions.

## 2925 References

- 2926 (1) Zeng, X.; Li, M.; Abd El-Hady, D.; Alshitari, W.; Al-Bogami, A. S.; Lu, J.; Amine, K.  
2927 Commercialization of lithium battery technologies for electric vehicles. *Advanced En-*  
2928 *ergy Materials* **2019**, *9*, 1900161.
- 2929 (2) Goodenough, J. B.; Kim, Y. Challenges for rechargeable Li batteries. *Chemistry of*  
2930 *Materials* **2010**, *22*, 587–603.
- 2931 (3) Kubiak, P.; Cen, Z.; López, C. M.; Belharouak, I. Calendar aging of a 250 kW/500  
2932 kWh Li-ion battery deployed for the grid storage application. *Journal of Power Sources*  
2933 **2017**, *372*, 16–23.
- 2934 (4) Doyle, M.; Fuller, T. F.; Newman, J. Modeling of galvanostatic charge and discharge  
2935 of the lithium/polymer/insertion cell. *Journal of the Electrochemical society* **1993**,  
2936 *140*, 1526.
- 2937 (5) Fuller, T. F.; Doyle, M.; Newman, J. Simulation and optimization of the dual lithium  
2938 ion insertion cell. *Journal of the Electrochemical Society* **1994**, *141*, 1.
- 2939 (6) Fuller, T. F.; Doyle, M.; Newman, J. S. Relaxation Phenomena in Lithium-Ion-  
2940 Insertion Cells. *Journal of The Electrochemical Society* **1994**, *141*, 982.

- 2941 (7) Doyle, M.; Newman, J. The use of mathematical modeling in the design of  
2942 lithium/polymer battery systems. *Electrochimica Acta* **1995**, *40*, 2191–2196.
- 2943 (8) Newman, J.; Thomas-Alyea, K. E. *Electrochemical Systems*; Wiley-Interscience, 2004;  
2944 Vol. 3; pp 1–647.
- 2945 (9) Van der Ven, A.; Deng, Z.; Banerjee, S.; Ong, S. P. Rechargeable Alkali-Ion Battery  
2946 Materials: Theory and Computation. *Chemical Reviews* **2020**, *120*, 6977–7019.
- 2947 (10) Shi, S.; Gao, J.; Liu, Y.; Zhao, Y.; Wu, Q.; Ju, W.; Ouyang, C.; Xiao, R. Multi-  
2948 scale computation methods: Their applications in lithium-ion battery research and  
2949 development. *Chinese Physics B* **2016**, *25*, 018212.
- 2950 (11) Franco, A. A. Multiscale modelling and numerical simulation of rechargeable lithium  
2951 ion batteries: concepts, methods and challenges. *Rsc Advances* **2013**, *3*, 13027–13058.
- 2952 (12) Herbert, J. M. Dielectric continuum methods for quantum chemistry. *Wiley Interdis-  
2953 ciplinary Reviews: Computational Molecular Science* **2021**, 1–73.
- 2954 (13) Scrosati, B. Lithium Rocking Chair Batteries: An Old Concept? *Journal of The  
2955 Electrochemical Society* **1992**, *139*, 2776–2781.
- 2956 (14) Asenbauer, J.; Eisenmann, T.; Kuenzel, M.; Kazzazi, A.; Chen, Z.; Bresser, D. The  
2957 success story of graphite as a lithium-ion anode material – fundamentals, remaining  
2958 challenges, and recent developments including silicon (oxide) composites. *Sustainable  
2959 Energy & Fuels* **2020**, 10.1039.D0SE00175A.
- 2960 (15) Zhang, H.; Yang, Y.; Ren, D.; Wang, L.; He, X. Graphite as anode materials: Fun-  
2961 damental mechanism, recent progress and advances. *Energy Storage Materials* **2021**,  
2962 *36*, 147–170.
- 2963 (16) Wang, A.; Kadam, S.; Li, H.; Shi, S.; Qi, Y. Review on modeling of the anode solid

- 2964 electrolyte interphase (SEI) for lithium-ion batteries. *npj Computational Materials*  
2965 **2018**, *4*.
- 2966 (17) Shepherd, K.; Siddiqui, F. A driverless Tesla crashed and burned for four hours, police  
2967 said, killing two passengers in Texas. *Washington Post*
- 2968 (18) Pfrang, A.; Kriston, A.; Ruiz, V.; Lebedeva, N.; di Persio, F. *Emerging Nanotechnolo-*  
2969 *gies in Rechargeable Energy Storage Systems*; Elsevier Inc., 2017; pp 253–290.
- 2970 (19) Liu, L.; Xu, J.; Wang, S.; Wu, F.; Li, H.; Chen, L. Practical evaluation of energy  
2971 densities for sulfide solid-state batteries. *eTransportation* **2019**, *1*, 100010.
- 2972 (20) Galiński, M.; Lewandowski, A.; Stepniak, I. Ionic liquids as electrolytes. *Electrochimica*  
2973 *acta* **2006**, *51*, 5567–5580.
- 2974 (21) Wang, Y.; Meng, X.; Sun, J.; Liu, Y.; Hou, L. Recent Progress in “Water-in-Salt”  
2975 Electrolytes Toward Non-lithium Based Rechargeable Batteries. *Frontiers in Chem-*  
2976 *istry* **2020**, *8*.
- 2977 (22) Logan, E.; Dahn, J. Electrolyte Design for Fast-Charging Li-Ion Batteries. *Trends in*  
2978 *Chemistry* **2020**, *2*, 354–366.
- 2979 (23) Woods, L. Technological Advancements in Solid State Batteries for Electric Vehicles,  
2980 2020 Report - Toyota is the Pioneer of Solid-state Battery Research and Development  
2981 with a Lion’s Share of Patent Ownership. 2021.
- 2982 (24) Zhu, Y.; He, X.; Mo, Y. Origin of Outstanding Stability in the Lithium Solid Elec-  
2983 trolyte Materials: Insights from Thermodynamic Analyses Based on First-Principles  
2984 Calculations. *ACS Applied Materials & Interfaces* **2015**, *7*, 23685–23693.
- 2985 (25) Zhang, Q.; Cao, D.; Ma, Y.; Natan, A.; Aurora, P.; Zhu, H. Sulfide-Based Solid-State  
2986 Electrolytes: Synthesis, Stability, and Potential for All-Solid-State Batteries. *Advanced*  
2987 *Materials* **2019**, *31*, 1901131.

- 2988 (26) Zhang, Z.; Shao, Y.; Lotsch, B.; Hu, Y. S.; Li, H.; Janek, J.; Nazar, L. F.; Nan, C. W.;  
2989 Maier, J.; Armand, M.; Chen, L. New horizons for inorganic solid state ion conductors.  
2990 *Energy & Environmental Science* **2018**, *11*, 1945–1976.
- 2991 (27) Gurung, A.; Pokharel, J.; Baniya, A.; Pathak, R.; Chen, K.; Lamsal, B. S.;  
2992 Ghimire, N.; Zhang, W.-H.; Zhou, Y.; Qiao, Q. A review on strategies addressing  
2993 interface incompatibilities in inorganic all-solid-state lithium batteries. *Sustainable*  
2994 *Energy & Fuels* **2019**, *3*, 3279–3309.
- 2995 (28) Xiao, Y.; Wang, Y.; Bo, S. H.; Kim, J. C.; Miara, L. J.; Ceder, G. Understanding  
2996 interface stability in solid-state batteries. *Nature Reviews Materials* **2020**, *5*, 105–126.
- 2997 (29) Xu, L.; Tang, S.; Cheng, Y.; Wang, K.; Liang, J.; Liu, C.; Cao, Y.-C.; Wei, F.; Mai, L.  
2998 Interfaces in Solid-State Lithium Batteries. *Joule* **2018**, *2*, 1991–2015.
- 2999 (30) Tateyama, Y.; Gao, B.; Jalem, R.; Haruyama, J. Theoretical picture of positive elec-  
3000 trode–solid electrolyte interface in all-solid-state battery from electrochemistry and  
3001 semiconductor physics viewpoints. *Current Opinion in Electrochemistry* **2019**, *17*,  
3002 149–157.
- 3003 (31) Ceder, G.; Ong, S. P.; Wang, Y. Predictive modeling and design rules for solid elec-  
3004 trolytes. *MRS Bulletin* **2018**, *43*, 782–788.
- 3005 (32) Ma, Y. Computer simulation of cathode materials for lithium ion and lithium batteries:  
3006 A review. *Energy & Environmental Materials* **2018**, *1*, 148–173.
- 3007 (33) Yan, L.-M.; Su, J.-M.; Sun, C.; Yue, B.-H. Review of the first principles calculations  
3008 and the design of cathode materials for Li-ion batteries. *Advances in Manufacturing*  
3009 **2014**, *2*, 358–368.
- 3010 (34) Wang, L.; Chen, B.; Ma, J.; Cui, G.; Chen, L. Reviving lithium cobalt oxide-based

- 3011 lithium secondary batteries-toward a higher energy density. *Chemical Society Reviews*  
3012 **2018**, *47*, 6505–6602.
- 3013 (35) Maleki Kheimeh Sari, H.; Li, X. Controllable cathode–electrolyte interface of  
3014  $\text{Li}[\text{Ni}_{0.8}\text{Co}_{0.1}\text{Mn}_{0.1}]\text{O}_2$  for lithium ion batteries: a review. *Advanced Energy Materi-*  
3015 *als* **2019**, *9*, 1901597.
- 3016 (36) Parr, R. G.; Yang, W. *Density-Functional Theory of Atoms and Molecules (Interna-*  
3017 *tional Series of Monographs on Chemistry)*; Oxford University Press, USA, 1994.
- 3018 (37) Hohenberg, P.; Kohn, W. Inhomogeneous Electron Gas. *Phys. Rev.* **1964**, *136*, B864–  
3019 B871.
- 3020 (38) Kohn, W.; Sham, L. J. Self-Consistent Equations Including Exchange and Correlation  
3021 Effects. *Phys. Rev.* **1965**, *140*, A1133–A1138.
- 3022 (39) Dirac, P. A. M. Note on Exchange Phenomena in the Thomas Atom. *Mathematical*  
3023 *Proceedings of the Cambridge Philosophical Society* **1930**, *26*, 376–385.
- 3024 (40) Perdew, J. P.; Wang, Y. Accurate and simple analytic representation of the electron-  
3025 gas correlation energy. *Phys. Rev. B* **1992**, *45*, 13244–13249.
- 3026 (41) Perdew, J. P.; Burke, K.; Ernzerhof, M. Generalized Gradient Approximation Made  
3027 Simple. *Phys. Rev. Lett.* **1996**, *77*, 3865–3868.
- 3028 (42) Becke, A. D. Density-functional exchange-energy approximation with correct asymp-  
3029 totic behavior. *Phys. Rev. A* **1988**, *38*, 3098–3100.
- 3030 (43) Lee, C.; Yang, W.; Parr, R. G. Development of the Colle-Salvetti correlation-energy  
3031 formula into a functional of the electron density. *Phys. Rev. B* **1988**, *37*, 785–789.
- 3032 (44) Perdew, J. P.; Kurth, S.; Zupan, A.; Blaha, P. Accurate density functional with correct  
3033 formal properties: A step beyond the generalized gradient approximation. *Physical*  
3034 *review letters* **1999**, *82*, 2544.

- 3035 (45) Grimme, S. Semiempirical GGA-type density functional constructed with a long-range  
3036 dispersion correction. *Journal of Computational Chemistry* **2006**, *27*, 1787–1799.
- 3037 (46) Grimme, S.; Antony, J.; Ehrlich, S.; Krieg, H. A consistent and accurate ab initio  
3038 parametrization of density functional dispersion correction (DFT-D) for the 94 ele-  
3039 ments H-Pu. *The Journal of Chemical Physics* **2010**, *132*, 154104.
- 3040 (47) Caldeweyher, E.; Bannwarth, C.; Grimme, S. Extension of the D3 dispersion coefficient  
3041 model. *The Journal of Chemical Physics* **2017**, *147*, 034112.
- 3042 (48) Grimme, S.; Ehrlich, S.; Goerigk, L. Effect of the damping function in dispersion  
3043 corrected density functional theory. *Journal of Computational Chemistry* **2011**, *32*,  
3044 1456–1465.
- 3045 (49) Johnson, E. R.; Becke, A. D. A post-Hartree-Fock model of intermolecular interactions:  
3046 Inclusion of higher-order corrections. *The Journal of Chemical Physics* **2006**, *124*,  
3047 174104.
- 3048 (50) Becke, A. D. Density-functional thermochemistry. III. The role of exact exchange. *The*  
3049 *Journal of Chemical Physics* **1993**, *98*, 5648–5652.
- 3050 (51) Cramer, C. J. *Essentials of computational chemistry: theories and models*; John Wiley  
3051 & Sons, 2013.
- 3052 (52) Bredow, T.; Gerson, A. R. Effect of exchange and correlation on bulk properties of  
3053 MgO, NiO, and CoO. *Phys. Rev. B* **2000**, *61*, 5194–5201.
- 3054 (53) Islam, M. M.; Bredow, T.; Gerson, A. Electronic properties of oxygen-deficient and  
3055 aluminum-doped rutile TiO<sub>2</sub> from first principles. *Phys. Rev. B* **2007**, *76*, 045217.
- 3056 (54) Heyd, J.; Scuseria, G. E.; Ernzerhof, M. Hybrid functionals based on a screened  
3057 Coulomb potential. *The Journal of Chemical Physics* **2003**, *118*, 8207–8215.

- 3058 (55) Dudarev, S. L.; Botton, G. A.; Savrasov, S. Y.; Humphreys, C. J.; Sutton, A. P.  
3059 Electron-energy-loss spectra and the structural stability of nickel oxide: An LSDA+U  
3060 study. *Phys. Rev. B* **1998**, *57*, 1505–1509.
- 3061 (56) Dudarev, S. L.; Liechtenstein, A. I.; Castell, M. R.; Briggs, G. A. D.; Sutton, A. P.  
3062 Surface states on NiO (100) and the origin of the contrast reversal in atomically  
3063 resolved scanning tunneling microscope images. *Phys. Rev. B* **1997**, *56*, 4900–4908.
- 3064 (57) Anisimov, V. I.; Aryasetiawan, F.; Liechtenstein, A. I. First-principles calculations  
3065 of the electronic structure and spectra of strongly correlated systems: the **LDA+U**  
3066 method. *Journal of Physics: Condensed Matter* **1997**, *9*, 767–808.
- 3067 (58) Goedecker, S. Linear scaling electronic structure methods. *Reviews of Modern Physics*  
3068 **1999**, *71*, 1085–1123.
- 3069 (59) Prodan, E.; Kohn, W. Nearsightedness of electronic matter. *Proceedings of the Na-*  
3070 *tional Academy of Sciences* **2005**, *102*, 11635–11638.
- 3071 (60) Galli, G.; Parrinello, M. Large scale electronic structure calculations. *Phys. Rev. Lett.*  
3072 **1992**, *69*, 3547–3550.
- 3073 (61) Hernández, E.; Gillan, M. J. Self-consistent first-principles technique with linear scal-  
3074 ing. *Phys. Rev. B* **1995**, *51*, 10157–10160.
- 3075 (62) Skylaris, C. K.; Haynes, P. D.; Mostofi, A. A.; Payne, M. C. Introducing ONETEP:  
3076 Linear-scaling density functional simulations on parallel computers. *Journal of Chem-*  
3077 *ical Physics* **2005**, *122*, 1–10.
- 3078 (63) Gillan, M. J.; Bowler, D. R.; Torralba, A. S.; Miyazaki, T. Order-N first-principles  
3079 calculations with the conquest code. *Computer Physics Communications* **2007**, *177*,  
3080 14–18.

- 3081 (64) Mohr, S.; Ratcliff, L. E.; Genovese, L.; Caliste, D.; Boulanger, P.; Goedecker, S.;  
3082 Deutsch, T. Accurate and efficient linear scaling DFT calculations with universal ap-  
3083 plicability. *Physical Chemistry Chemical Physics* **2015**, *17*, 31360–31370.
- 3084 (65) A., P. J. C. The ONETEP linear-scaling density functional theory program. *J. Chem.*  
3085 *Phys.* **2020**, *152*, 174111.
- 3086 (66) Bhandari, A.; Anton, L.; Dziejczak, J.; Peng, C.; Kramer, D.; Skylaris, C.-K. Electronic  
3087 structure calculations in electrolyte solutions: Methods for neutralization of extended  
3088 charged interfaces. *The Journal of Chemical Physics* **2020**, *153*, 124101.
- 3089 (67) Jónsson, H.; Mills, G.; Jacobsen, K. W. Nudged elastic band method for finding  
3090 minimum energy paths of transitions. *Classical and Quantum Dynamics in Condensed*  
3091 *Phase Simulations* **1998**, 385–404.
- 3092 (68) Henkelman, G.; Uberuaga, B. P.; Jónsson, H. A climbing image nudged elastic band  
3093 method for finding saddle points and minimum energy paths. *The Journal of chemical*  
3094 *physics* **2000**, *113*, 9901–9904.
- 3095 (69) Henkelman, G.; Jónsson, H. Improved tangent estimate in the nudged elastic band  
3096 method for finding minimum energy paths and saddle points. *The Journal of chemical*  
3097 *physics* **2000**, *113*, 9978–9985.
- 3098 (70) Peng, C.; Mercer, M. P.; Skylaris, C.-K.; Kramer, D. Lithium intercalation edge effects  
3099 and doping implications for graphite anodes. *Journal of Materials Chemistry A* **2020**,  
3100 *8*, 7947–7955.
- 3101 (71) Mercer, M. P.; Peng, C.; Soares, C.; Hoster, H. E.; Kramer, D. Voltage hysteresis  
3102 during lithiation/delithiation of graphite associated with meta-stable carbon stackings.  
3103 *J. Mater. Chem. A* **2021**, *9*, 492–504.



- 3104 (72) Sanchez, J. M.; Ducastelle, F.; Gratias, D. Generalized cluster description of multi-  
3105 component systems. *Physica A: Statistical Mechanics and its Applications* **1984**, *128*,  
3106 334–350.
- 3107 (73) De Fontaine, D. Cluster approach to order-disorder transformations in alloys. *Solid*  
3108 *state physics* **1994**, *47*, 33–176.
- 3109 (74) Blum, V.; Zunger, A. Mixed-basis cluster expansion for thermodynamics of bcc alloys.  
3110 *Physical Review B* **2004**, *70*, 155108.
- 3111 (75) Gallavotti, G. *Statistical mechanics: A short treatise*; Springer Science & Business  
3112 Media, 2013.
- 3113 (76) Persson, K.; Hinuma, Y.; Meng, Y. S.; Van der Ven, A.; Ceder, G. Thermodynamic  
3114 and kinetic properties of the Li-graphite system from first-principles calculations. *Phys.*  
3115 *Rev. B* **2010**, *82*, 125416.
- 3116 (77) Van der Ven, A.; Ceder, G.; Asta, M.; Tepesch, P. D. First-principles theory of ionic  
3117 diffusion with nondilute carriers. *Phys. Rev. B* **2001**, *64*, 184307.
- 3118 (78) van de Walle, A. Multicomponent multisublattice alloys, nonconfigurational entropy  
3119 and other additions to the Alloy Theoretic Automated Toolkit. *Calphad* **2009**, *33*,  
3120 266–278.
- 3121 (79) van de Walle, A.; Asta, M. D.; Ceder, G. The Alloy Theoretic Automated Toolkit: A  
3122 User Guide. *Calphad* **2002**, *26*, 539–553.
- 3123 (80) van de Walle, A.; Ceder, G. Automating first-principles phase diagram calculations.  
3124 *Journal of Phase Equilibria* **2002**, *23*, 348–359.
- 3125 (81) Natarajan, A. R.; Thomas, J. C.; Puchala, B.; Van der Ven, A. Symmetry-adapted or-  
3126 der parameters and free energies for solids undergoing order-disorder phase transitions.  
3127 *Phys. Rev. B* **2017**, *96*, 134204.

- 3128 (82) Pickard, C. J.; Needs, R. J. Ab initio random structure searching. *Journal of Physics:*  
3129 *Condensed Matter* **2011**, *23*, 053201.
- 3130 (83) Ångqvist, M.; Muñoz, W. A.; Rahm, J. M.; Fransson, E.; Durniak, C.; Rozyczko, P.;  
3131 Rod, T. H.; Erhart, P. ICET – A Python Library for Constructing and Sampling Alloy  
3132 Cluster Expansions. *Advanced Theory and Simulations* **2019**, *2*, 1900015.
- 3133 (84) Chang, J. H.; Kleiven, D.; Melander, M.; Akola, J.; Garcia-Lastra, J. M.; Vegge, T.  
3134 CLEANSE: a versatile and user-friendly implementation of cluster expansion method.  
3135 *Journal of Physics: Condensed Matter* **2019**, *31*, 325901.
- 3136 (85) Binder, K.; Landau, D. P. *A Guide to Monte-Carlo Simulations in Statistical Physics,*  
3137 *Third Edition*; Cambridge University Press: Cambridge, UK, 2009.
- 3138 (86) Lee, T. D.; Yang, C. N. Statistical Theory of Equations of State and Phase Transitions.  
3139 II. Lattice Gas and Ising Model. *Phys. Rev.* **1952**, *87*, 410–419.
- 3140 (87) Mercer, M. P.; Hoster, H. E. Ultrahigh vacuum and electrocatalysis - The powers of  
3141 quantitative surface imaging. *Nano Energy* **2016**, *29*, 394–413.
- 3142 (88) Oviedo, O.; Reinaudi, L.; Garcia, S.; Leiva, E. *Underpotential Deposition: From Fun-*  
3143 *damentals and Theory to Applications at the Nanoscale*; Monographs in Electrochem-  
3144 *istry*; Springer International Publishing, 2015.
- 3145 (89) Mercer, M. P.; Finnigan, S.; Kramer, D.; Richards, D.; Hoster, H. E. The influence  
3146 of point defects on the entropy profiles of Lithium Ion Battery cathodes: a lattice-gas  
3147 Monte Carlo study. *Electrochimica Acta* **2017**, *241*, 141–152.
- 3148 (90) Kim, S.-W.; Pyun, S.-I. Thermodynamic and kinetic approaches to lithium intercala-  
3149 tion into a  $\text{Li}_{1-\delta}\text{Mn}_2\text{O}_4$  electrode using Monte Carlo simulation. *Electrochimica Acta*  
3150 **2001**, *46*, 987–997.

- 3151 (91) Mercer, M. P.; Otero, M.; Ferrer-Huerta, M.; Sigal, A.; Barraco, D. E.; Hoster, H. E.;  
3152 Leiva, E. P. Transitions of lithium occupation in graphite: A physically informed  
3153 model in the dilute lithium occupation limit supported by electrochemical and ther-  
3154 modynamic measurements. *Electrochimica Acta* **2019**, *324*, 134774.
- 3155 (92) Leiva, E. P. M.; Perassi, E.; Barraco, D. Shedding Light on the Entropy Change Found  
3156 for the Transition Stage II  $\rightarrow$  Stage I of Li-Ion Storage in Graphite. *Journal of The*  
3157 *Electrochemical Society* **2017**, *164*, A6154–A6157.
- 3158 (93) Schlueter, S.; Genieser, R.; Richards, D.; Hoster, H. E.; Mercer, M. P. Quantifying  
3159 structure dependent responses in Li-ion cells with excess Li spinel cathodes: matching  
3160 voltage and entropy profiles through mean field models. *Physical Chemistry Chemical*  
3161 *Physics* **2018**, *20*, 21417–21429.
- 3162 (94) Haftbaradaran, H.; Song, J.; Curtin, W.; Gao, H. Continuum and atomistic models of  
3163 strongly coupled diffusion, stress, and solute concentration. *Journal of Power Sources*  
3164 **2011**, *196*, 361–370.
- 3165 (95) Bazant, M. Z. Thermodynamic stability of driven open systems and control of phase  
3166 separation by electro-autocatalysis. *Faraday Discussions* **2017**, *199*, 423–463.
- 3167 (96) Guo, Y.; Smith, R. B.; Yu, Z.; Efetov, D. K.; Wang, J.; Kim, P.; Bazant, M. Z.;  
3168 Brus, L. E. Li Intercalation into Graphite: Direct Optical Imaging and Cahn–Hilliard  
3169 Reaction Dynamics. *The Journal of Physical Chemistry Letters* **2016**, *7*, 2151–2156.
- 3170 (97) Bai, P.; Cogswell, D. A.; Bazant, M. Z. Suppression of Phase Separation in LiFePO<sub>4</sub>  
3171 Nanoparticles During Battery Discharge. *Nano Letters* **2011**, *11*, 4890–4896.
- 3172 (98) Metropolis, N.; Rosenbluth, A. W.; Rosenbluth, M. N.; Teller, A. H.; Teller, E. Equa-  
3173 tion of State Calculations by Fast Computing Machines. *The Journal of Chemical*  
3174 *Physics* **1953**, *21*, 1087–1092.

- 3175 (99) Darling, R.; Newman, J. Dynamic Monte Carlo Simulations of Diffusion in  $\text{Li}_y\text{Mn}_2\text{O}_4$ .  
3176 *Journal of The Electrochemical Society* **1999**, *146*, 3765–3772.
- 3177 (100) Thomas, K. E.; Newman, J. Heats of mixing and of entropy in porous insertion elec-  
3178 trodes. *Journal of Power Sources* **2003**, *119-121*, 844 – 849.
- 3179 (101) Zhang, X.-F.; Zhao, Y.; Patel, Y.; Zhang, T.; Liu, W.-M.; Chen, M.; Offer, G. J.;  
3180 Yan, Y. Potentiometric measurement of entropy change for lithium batteries. *Phys.*  
3181 *Chem. Chem. Phys.* **2017**, *19*, 9833–9842.
- 3182 (102) Gavilán-Arriazu, E.; Pinto, O.; López de Mishima, B.; Barraco, D.; Oviedo, O.;  
3183 Leiva, E. Kinetic Monte Carlo applied to the electrochemical study of the Li-ion  
3184 graphite system. *Electrochimica Acta* **2020**, *331*, 135439.
- 3185 (103) Gavilán-Arriazu, E. M.; Mercer, M. P.; Pinto, O. A.; Oviedo, O. A.; Barraco, D. E.;  
3186 Hoster, H. E.; Leiva, E. P. M. Effect of Temperature on The Kinetics of Electrochemical  
3187 Insertion of Li-Ions into a Graphite Electrode Studied by Kinetic Monte Carlo. *Journal*  
3188 *of The Electrochemical Society* **2020**, *167*, 013533.
- 3189 (104) Gavilán-Arriazu, E. M.; Mercer, M. P.; Barraco, D. E.; Hoster, H. E.; Leiva, E. P. M.  
3190 Kinetic Monte Carlo simulations applied to Li-ion and post Li-ion batteries: a key  
3191 link in the multi-scale chain. *Progress in Energy* **2021**, *3*, 042001.
- 3192 (105) Car, R.; Parrinello, M. Unified Approach for Molecular Dynamics and Density-  
3193 Functional Theory. *Physical Review Letters* **1985**, *55*, 2471–2474.
- 3194 (106) Tuckerman, M. E.; Parrinello, M. Integrating the Car–Parrinello equations. I. Basic  
3195 integration techniques. *The Journal of Chemical Physics* **1994**, *101*, 1302–1315.
- 3196 (107) Grossman, J. C.; Schwegler, E.; Draeger, E. W.; Gygi, F.; Galli, G. Towards an  
3197 assessment of the accuracy of density functional theory for first principles simulations  
3198 of water. *The Journal of Chemical Physics* **2004**, *120*, 300–311.

- 3199 (108) Harding, J. H. Computer simulation of defects in ionic solids. *Reports on Progress in*  
3200 *Physics* **1990**, *53*, 1403–1466.
- 3201 (109) Buckingham, R. A. The classical equation of state of gaseous helium, neon and argon.  
3202 *Proceedings of the Royal Society of London. Series A. Mathematical and Physical*  
3203 *Sciences* **1938**, *168*, 264–283.
- 3204 (110) Born, M.; Mayer, J. On the Lattice Theory of Ionic Crystals. *Zeitschrift für Physik*  
3205 **1932**, *75*, 1–18.
- 3206 (111) Mayer, J. E. Dispersion and Polarizability and the Van der Waals Potential in the  
3207 Alkali Halides. *The Journal of Chemical Physics* **1932**, *1*, 270.
- 3208 (112) Todorov, I. T.; Smith, W.; Trachenko, K.; Dove, M. T. DL\_POLY\_3: new dimen-  
3209 sions in molecular dynamics simulations via massive parallelism. *Journal of Materials*  
3210 *Chemistry* **2006**, *16*, 1911–1918.
- 3211 (113) Plimpton, S. Fast Parallel Algorithms for Short-Range Molecular Dynamics. *Journal*  
3212 *of Computational Physics* **1995**, *117*, 1 – 19.
- 3213 (114) Gale, J. D. GULP: A computer program for the symmetry-adapted simulation of  
3214 solids. *Journal of the Chemical Society, Faraday Transactions* **1997**, *93*, 629–637.
- 3215 (115) Gauthier, M.; Carney, T. J.; Grimaud, A.; Giordano, L.; Pour, N.; Chang, H.-H.;  
3216 Fenning, D. P.; Lux, S. F.; Paschos, O.; Bauer, C.; Maglia, F.; Lupart, S.; Lamp, P.;  
3217 Shao-Horn, Y. The Electrode-Electrolyte Interface in Li-ion Batteries: Current Under-  
3218 standing and New Insights. *The Journal of Physical Chemistry Letters* **2015**, 4653—  
3219 -4672.
- 3220 (116) Yu, X.; Manthiram, A. Electrode–electrolyte interfaces in lithium-based batteries.  
3221 *Energy & Environmental Science* **2018**, *11*, 527–543.

- 3222 (117) Jinnouchi, R.; Kodama, K.; Morimoto, Y. Electronic structure calculations on elec-  
3223 trolyte–electrode interfaces: Successes and limitations. *Current Opinion in Electro-*  
3224 *chemistry* **2018**, *8*, 103–109.
- 3225 (118) Hansen, M. H.; Rossmeisl, J. PH in Grand Canonical Statistics of an Electrochemical  
3226 Interface. *Journal of Physical Chemistry C* **2016**, *120*, 29135–29143.
- 3227 (119) Sakong, S.; Naderian, M.; Mathew, K.; Hennig, R. G.; Groß, A. Density functional  
3228 theory study of the electrochemical interface between a Pt electrode and an aqueous  
3229 electrolyte using an implicit solvent method. *Journal of Chemical Physics* **2015**, *142*.
- 3230 (120) Skyner, R. E.; McDonagh, J. L.; Groom, C. R.; Van Mourik, T.; Mitchell, J. B. A  
3231 review of methods for the calculation of solution free energies and the modelling of  
3232 systems in solution. *Physical Chemistry Chemical Physics* **2015**, *17*, 6174–6191.
- 3233 (121) Kang, J.; Wei, S. H.; Zhu, K.; Kim, Y. H. First-principles theory of electrochemical  
3234 capacitance of nanostructured materials: Dipole-assisted subsurface intercalation of  
3235 lithium in pseudocapacitive TiO<sub>2</sub> anatase nanosheets. *Journal of Physical Chemistry*  
3236 *C* **2011**, *115*, 4909–4915.
- 3237 (122) Dufils, T.; Jeanmairet, G.; Rotenberg, B.; Sprik, M.; Salanne, M. Simulating Electro-  
3238 chemical Systems by Combining the Finite Field Method with a Constant Potential  
3239 Electrode. *Physical Review Letters* **2019**, *123*, 195501.
- 3240 (123) Jorn, R.; Kumar, R.; Abraham, D. P.; Voth, G. A. Atomistic modeling of the electrode-  
3241 electrolyte interface in Li-ion energy storage systems: Electrolyte structuring. *Journal*  
3242 *of Physical Chemistry C* **2013**, *117*, 3747–3761.
- 3243 (124) Zhang, C.; Sayer, T.; Hutter, J.; Sprik, M. Modelling electrochemical systems with  
3244 finite field molecular dynamics. *Journal of Physics: Energy* **2020**, 0–21.

- 3245 (125) Cramer, C. J.; Truhlar, D. G. Implicit Solvation Models: Equilibria, Structure, Spec-  
3246 tra, and Dynamics. *Chemical Reviews* **1999**, *99*, 2161–2200.
- 3247 (126) Tomasi, J.; Mennucci, B.; Cammi, R. Quantum mechanical continuum solvation mod-  
3248 els. *Chemical Reviews* **2005**, *105*, 2999–3093.
- 3249 (127) Grochowski, P.; Trylska, J. Continuum molecular electrostatics, salt effects, and coun-  
3250 terion binding – A review of the Poisson-Boltzmann theory and its modifications.  
3251 *Biopolymers* **2008**, *89*, 93–113.
- 3252 (128) Jinnouchi, R.; Anderson, A. B. Electronic structure calculations of liquid-solid in-  
3253 terfaces: Combination of density functional theory and modified Poisson-Boltzmann  
3254 theory. *Phys. Rev. B* **2008**, *77*, 245417.
- 3255 (129) Gunceler, D.; Letchworth-Weaver, K.; Sundararaman, R.; Schwarz, K. A.; Arias, T. A.  
3256 The importance of nonlinear fluid response in joint density-functional theory studies  
3257 of battery systems. *Modelling and Simulation in Materials Science and Engineering*  
3258 **2013**, *21*.
- 3259 (130) Ringe, S.; Oberhofer, H.; Hille, C.; Matera, S.; Reuter, K. Function-Space-Based  
3260 Solution Scheme for the Size-Modified Poisson–Boltzmann Equation in Full-Potential  
3261 DFT. *Journal of Chemical Theory and Computation* **2016**, *12*, 4052–4066.
- 3262 (131) Nattino, F.; Truscott, M.; Marzari, N.; Andreussi, O. Continuum models of the elec-  
3263 trochemical diffuse layer in electronic-structure calculations. *The Journal of Chemical*  
3264 *Physics* **2019**, *150*, 41722.
- 3265 (132) Melander, M. M.; Kuisma, M. J.; Christensen, T. E. K.; Honkala, K. Grand-canonical  
3266 approach to density functional theory of electrocatalytic systems: Thermodynamics  
3267 of solid-liquid interfaces at constant ion and electrode potentials. *Journal of Chemical*  
3268 *Physics* **2019**, *150*, 041706.

- 3269 (133) Stein, C. J.; Herbert, J. M.; Head-Gordon, M. The Poisson-Boltzmann model for  
3270 implicit solvation of electrolyte solutions: Quantum chemical implementation and  
3271 assessment via Sechenov coefficients. *Journal of Chemical Physics* **2019**, *151*, 224111.
- 3272 (134) Womack, J. C.; Anton, L.; Dziedzic, J.; Hasnip, P. J.; Probert, M. I.; Skylaris, C. K.  
3273 DL-MG: A Parallel Multigrid Poisson and Poisson-Boltzmann Solver for Electronic  
3274 Structure Calculations in Vacuum and Solution. *Journal of Chemical Theory and*  
3275 *Computation* **2018**, *14*, 1412–1432.
- 3276 (135) Dziedzic, J.; Bhandari, A.; Anton, L.; Peng, C.; Womack, J. C.; Famili, M.;  
3277 Kramer, D.; Skylaris, C.-K. A Practical Approach to Large Scale Electronic Struc-  
3278 ture Calculations in Electrolyte Solutions via Continuum-Embedded Linear-Scaling  
3279 DFT. *The Journal of Physical Chemistry C* **2020**, *124*, 7860–7872.
- 3280 (136) Andreussi, O.; Dabo, I.; Marzari, N. Revised self-consistent continuum solvation in  
3281 electronic-structure calculations. *Journal of Chemical Physics* **2012**, *136*, 064102.
- 3282 (137) Fisicaro, G.; Genovese, L.; Andreussi, O.; Mandal, S.; Nair, N. N.; Marzari, N.;  
3283 Goedecker, S. Soft-Sphere Continuum Solvation in Electronic-Structure Calculations.  
3284 *Journal of Chemical Theory and Computation* **2017**, *13*, 3829–3845.
- 3285 (138) Sundararaman, R.; Letchworth-Weaver, K.; Schwarz, K. A. Improving accuracy of  
3286 electrochemical capacitance and solvation energetics in first-principles calculations.  
3287 *Journal of Chemical Physics* **2018**, *148*, 144105.
- 3288 (139) Dziedzic, J.; Helal, H. H.; Skylaris, C. K.; Mostofi, A. A.; Payne, M. C. Minimal  
3289 parameter implicit solvent model for ab initio electronic-structure calculations. *Epl*  
3290 **2011**, *95*, 1–6.
- 3291 (140) Jones, J. E. On the determination of molecular fields. —II. From the equation of state  
3292 of a gas. *Proceedings of the Royal Society of London. Series A, Containing Papers of*  
3293 *a Mathematical and Physical Character* **1924**, *106*, 463–477.



- 3294 (141) Gale, J. D. GULP fitting. 1996; [https://gulp.curtin.edu.au/local/docs/gulp/](https://gulp.curtin.edu.au/local/docs/gulp/gulp_31_manual/gulpnode38.html)  
3295 [gulp\\_31\\_manual/gulpnode38.html](https://gulp.curtin.edu.au/local/docs/gulp/gulp_31_manual/gulpnode38.html).
- 3296 (142) Gale, J. D. Empirical potential derivation for ionic materials. *Philosophical Magazine*  
3297 *B* **1996**, *73*, 3–19.
- 3298 (143) Stukowski, A.; Fransson, E.; Mock, M.; Erhart, P. Atomicrex—a general purpose  
3299 tool for the construction of atomic interaction models. *Modelling and Simulation in*  
3300 *Materials Science and Engineering* **2017**, *25*, 055003.
- 3301 (144) Ostrouchov, C. dftfit. <https://chrisostrouchov.com/dftfit>.
- 3302 (145) Wen, M.; Li, J.; Brommer, P.; Elliott, R. S.; Sethna, J. P.; Tadmor, E. B. A KIM-  
3303 compliant *potfit* for fitting sloppy interatomic potentials: application to the EDIP  
3304 model for silicon. *Modelling and Simulation in Materials Science and Engineering*  
3305 **2017**, *25*, 014001.
- 3306 (146) Wen, M.; Li, J.; Brommer, P.; Elliott, R. S.; Sethna, J. P.; Tadmor, E. B. potfit.  
3307 <https://www.potfit.net/wiki/doku.php>.
- 3308 (147) Lewis, G. V.; Catlow, C. R. A. Potential models for ionic oxides. *Journal of Physics*  
3309 *C: Solid State Physics* **1985**, *18*, 1149–1161.
- 3310 (148) Ledwaba, R. S.; Sayle, D. C.; Ngoepe, P. E. Atomistic Simulation and Characterization  
3311 of Spinel  $\text{Li}_{1+x}\text{Mn}_2\text{O}_4$  ( $0 \leq x \leq 1$ ) Nanoparticles. *ACS Applied Energy Materials*  
3312 **2020**, *3*, 1429–1438.
- 3313 (149) Sayle, T. X. T.; Catlow, C. R. A.; Maphanga, R. R.; Ngoepe, P. E.; Sayle, D. C. Gen-  
3314 erating  $\text{MnO}_2$  Nanoparticles Using Simulated Amorphization and Recrystallization.  
3315 *Journal of the American Chemical Society* **2005**, *127*, 12828–12837.
- 3316 (150) Dawson, J. A.; Tanaka, I. Oxygen Vacancy Formation and Reduction Properties of

- 3317  $\beta$ -MnO<sub>2</sub> Grain Boundaries and the Potential for High Electrochemical Performance.  
3318 *ACS Applied Materials & Interfaces* **2014**, *6*, 17776–17784.
- 3319 (151) Hart, F. X.; Bates, J. B. Lattice model calculation of the strain energy density and  
3320 other properties of crystalline LiCoO<sub>2</sub>. *Journal of Applied Physics* **1998**, *83*, 7560–  
3321 7566.
- 3322 (152) A. J. Fisher, C.; Saiful Islam, M.; Moriwake, H. Atomic Level Investigations of Lithium  
3323 Ion Battery Cathode Materials. *Journal of the Physical Society of Japan* **2010**, *79*,  
3324 59–64.
- 3325 (153) Ammundsen, B.; Burns, G. R.; Islam, M. S.; Kanoh, H.; Rozière, J. Lattice Dynamics  
3326 and Vibrational Spectra of Lithium Manganese Oxides: A Computer Simulation and  
3327 Spectroscopic Study. *The Journal of Physical Chemistry B* **1999**, *103*, 5175–5180.
- 3328 (154) Kerisit, S.; Chaka, A. M.; Droubay, T. C.; Ilton, E. S. Shell Model for Atomistic  
3329 Simulation of Lithium Diffusion in Mixed Mn/Ti Oxides. *The Journal of Physical*  
3330 *Chemistry C* **2014**, *118*, 24231–24239.
- 3331 (155) He, J.; Zhang, L.; Liu, L. Thermal transport in monocrystalline and polycrystalline  
3332 lithium cobalt oxide. *Physical Chemistry Chemical Physics* **2019**, *21*, 12192–12200.
- 3333 (156) Lee, S.; Park, S. S. Atomistic simulation study of mixed-metal oxide  
3334 (LiNi<sub>1/3</sub>Co<sub>1/3</sub>Mn<sub>1/3</sub>O<sub>2</sub>) cathode material for lithium ion battery. *The Journal of Phys-*  
3335 *ical Chemistry C* **2012**, *116*, 6484–6489.
- 3336 (157) Lindan, P. J. D.; Gillan, M. J. Shell-model molecular dynamics simulation of superionic  
3337 conduction in CaF<sub>2</sub>. *Journal of Physics: Condensed Matter* **1993**, *5*, 1019–1030.
- 3338 (158) Mitchell, P. J.; Fincham, D. Shell model simulations by adiabatic dynamics. *Journal*  
3339 *of Physics: Condensed Matter* **1993**, *5*, 1031–1038.

- 3340 (159) Wang, B.; Cormack, A. N. Molecular dynamics simulations of Mg-doped beta"-alumina  
3341 with potential models fitted for accurate structural response to thermal vibrations.  
3342 *Solid State Ionics* **2014**, *263*, 9–14.
- 3343 (160) Escribano, B.; Lozano, A.; Radivojević, T.; Fernández-Pendás, M.; Carrasco, J.;  
3344 Akhmatskaya, E. Enhancing sampling in atomistic simulations of solid-state mate-  
3345 rials for batteries: a focus on olivine NaFePO<sub>4</sub>. *Theoretical Chemistry Accounts* **2017**,  
3346 *136*, 43.
- 3347 (161) Lee, S.; Park, S. S. Lithium transition metal fluorophosphates (Li<sub>2</sub>CoPO<sub>4</sub>F and  
3348 Li<sub>2</sub>NiPO<sub>4</sub>F) as cathode materials for lithium ion battery from atomistic simulation.  
3349 *Journal of Solid State Chemistry* **2013**, *204*, 329 – 334.
- 3350 (162) Dai, J.; Chen, Q.; Glossmann, T.; Lai, W. Comparison of interatomic potential models  
3351 on the molecular dynamics simulation of fast-ion conductors: A case study of a Li  
3352 garnet oxide Li<sub>7</sub>La<sub>3</sub>Zr<sub>2</sub>O<sub>12</sub>. *Computational Materials Science* **2019**, *162*, 333–339.
- 3353 (163) Pedone, A.; Malavasi, G.; Menziani, M. C.; Cormack, A. N.; Segre, U. A New Self-  
3354 Consistent Empirical Interatomic Potential Model for Oxides, Silicates, and Silica-  
3355 Based Glasses. *The Journal of Physical Chemistry B* **2006**, *110*, 11780–11795.
- 3356 (164) Morgan, Lucy M. and Clarke, Matthew and Islam, M. Saiful and Morgan, Benjamin  
3357 J., PopOff: POtential Parameter Optimisation for Force-Fields. 2021; [https://doi.](https://doi.org/10.5281/zenodo.4773795)  
3358 [org/10.5281/zenodo.4773795](https://doi.org/10.5281/zenodo.4773795).
- 3359 (165) Fisher, C. A. J.; Hart Prieto, V. M.; Islam, M. S. Lithium Battery Materials LiMPO<sub>4</sub>  
3360 (M = Mn,Fe,Co,and Ni): Insights into Defect Association, Transport Mechanisms,  
3361 and Doping Behavior. *Chemistry of Materials* **2008**, *20*, 5907–5915.
- 3362 (166) Urban, A.; Seo, D.-H.; Ceder, G. Computational understanding of Li-ion batteries.  
3363 *npj Computational Materials* **2016**, *2*, 16002.

- 3364 (167) Ceder, G.; Van der Ven, A. Phase diagrams of lithium transition metal oxides: inves-  
3365 tigations from first principles. *Electrochimica Acta* **1999**, *45*, 131 – 150.
- 3366 (168) Van Der Ven, A.; Marianetti, C.; Morgan, D.; Ceder, G. Phase transformations and  
3367 volume changes in spinel  $\text{Li}_x\text{Mn}_2\text{O}_4$ . *Solid State Ionics* **2000**, *135*, 21–32.
- 3368 (169) Reynier, Y.; Graetz, J.; Swan-Wood, T.; Rez, P.; Yazami, R.; Fultz, B. Entropy of Li  
3369 intercalation in  $\text{Li}_x\text{CoO}_2$ . *Phys. Rev. B* **2004**, *70*, 174304.
- 3370 (170) Yazami, R.; Reynier, Y. Thermodynamics and crystal structure anomalies in lithium-  
3371 intercalated graphite. *Journal of Power Sources* **2006**, *153*, 312–318.
- 3372 (171) Atkins, P. W.; De Paula, J. *Atkins' Physical chemistry, 9th Ed.*; 2014.
- 3373 (172) Heitjans, P.; Kärger, J. *Diffusion in condensed matter: methods, materials, models*;  
3374 Springer Science & Business Media, 2006.
- 3375 (173) Heumann, T. *Diffusion in Metallen: Grundlagen, Theorie, Vorgänge in Reinmetallen*  
3376 *und Legierungen*; Springer-Verlag, 2013; Vol. 10.
- 3377 (174) Crank, J. *The mathematics of diffusion*; Oxford university press, 1979.
- 3378 (175) Einstein, A. The presumed movement of suspended particles in static fluids. *Ann.*  
3379 *Phys. Lpz* **1905**, *17*, 549–560.
- 3380 (176) Von Smoluchowski, M. Zur kinetischen theorie der brownschen molekularbewegung  
3381 und der suspensionen. *Annalen der physik* **1906**, *326*, 756–780.
- 3382 (177) Ladd, A. J.; Moran, B.; Hoover, W. G. Lattice thermal conductivity: A comparison of  
3383 molecular dynamics and anharmonic lattice dynamics. *Physical Review B* **1986**, *34*,  
3384 5058.

- 3385 (178) Turney, J.; Landry, E.; McGaughey, A.; Amon, C. Predicting phonon properties and  
3386 thermal conductivity from anharmonic lattice dynamics calculations and molecular  
3387 dynamics simulations. *Physical Review B* **2009**, *79*, 064301.
- 3388 (179) Seko, A.; Togo, A.; Hayashi, H.; Tsuda, K.; Chaput, L.; Tanaka, I. Prediction of low-  
3389 thermal-conductivity compounds with first-principles anharmonic lattice-dynamics  
3390 calculations and Bayesian optimization. *Physical review letters* **2015**, *115*, 205901.
- 3391 (180) Togo, A.; Chaput, L.; Tanaka, I. Distributions of Phonon Lifetimes in Brillouin Zones.  
3392 *Phys. Rev. B* **2015**, *91*, 094306.
- 3393 (181) Yang, H.; Yang, J.-y.; Savory, C. N.; Skelton, J. M.; Morgan, B. J.; Scanlon, D. O.;  
3394 Walsh, A. Highly Anisotropic Thermal Transport in LiCoO<sub>2</sub>. *The journal of physical*  
3395 *chemistry letters* **2019**, *10*, 5552–5556.
- 3396 (182) Yang, H.; Savory, C. N.; Morgan, B. J.; Scanlon, D. O.; Skelton, J. M.; Walsh, A.  
3397 Chemical Trends in the Lattice Thermal Conductivity of Li (Ni, Mn, Co) O<sub>2</sub> (NMC)  
3398 Battery Cathodes. *Chemistry of Materials* **2020**, *32*, 7542–7550.
- 3399 (183) Tadano, T.; Gohda, Y.; Tsuneyuki, S. Anharmonic force constants extracted from  
3400 first-principles molecular dynamics: applications to heat transfer simulations. *Journal*  
3401 *of Physics: Condensed Matter* **2014**, *26*, 225402.
- 3402 (184) Li, W.; Carrete, J.; Katcho, N. A.; Mingo, N. ShengBTE: a solver of the Boltzmann  
3403 transport equation for phonons. *Comp. Phys. Commun.* **2014**, *185*, 1747–1758.
- 3404 (185) Vetter, J.; Novák, P.; Wagner, M.; Veit, C.; Möller, K.-C.; Besenhard, J.; Winter, M.;  
3405 Wohlfahrt-Mehrens, M.; Vogler, C.; Hammouche, A. Ageing mechanisms in lithium-  
3406 ion batteries. *Journal of Power Sources* **2005**, *147*, 269 – 281.
- 3407 (186) Agubra, V.; Fergus, J. Lithium Ion Battery Anode Aging Mechanisms. *Materials*  
3408 **2013**, *6*, 1310–1325.

- 3409 (187) Yang, X.-G.; Leng, Y.; Zhang, G.; Ge, S.; Wang, C.-Y. Modeling of lithium plating  
3410 induced aging of lithium-ion batteries: Transition from linear to nonlinear aging.  
3411 *Journal of Power Sources* **2017**, *360*, 28 – 40.
- 3412 (188) Guerard, D.; Herold, A. Intercalation of lithium into graphite and other carbons.  
3413 *Carbon* **1975**, *13*, 337 – 345.
- 3414 (189) Woo, K. C.; Kamitakahara, W. A.; DiVincenzo, D. P.; Robinson, D. S.; Mertwoy, H.;  
3415 Milliken, J. W.; Fischer, J. E. Effect of In-Plane Density on the Structural and Elastic  
3416 Properties of Graphite Intercalation Compounds. *Phys. Rev. Lett.* **1983**, *50*, 182–185.
- 3417 (190) Basu, S.; Zeller, C.; Flanders, P.; Fuerst, C.; Johnson, W.; Fischer, J. Synthesis and  
3418 properties of lithium-graphite intercalation compounds. *Materials Science and Engi-*  
3419 *neering* **1979**, *38*, 275 – 283.
- 3420 (191) Besenhard, J. The electrochemical preparation and properties of ionic alkali metal-  
3421 and NR<sub>4</sub>-graphite intercalation compounds in organic electrolytes. *Carbon* **1976**, *14*,  
3422 111–115.
- 3423 (192) Yazami, R.; Touzain, P. A reversible graphite-lithium negative electrode for electro-  
3424 chemical generators. *Journal of Power Sources* **1983**, *9*, 365 – 371.
- 3425 (193) Fong, R.; von Sacken, U.; Dahn, J. R. Studies of Lithium Intercalation into Car-  
3426 bons Using Nonaqueous Electrochemical Cells. *Journal of The Electrochemical Society*  
3427 **1990**, *137*, 2009–2013.
- 3428 (194) Tarascon, J.; Guyomard, D. The Li<sub>1+x</sub>Mn<sub>2</sub>O<sub>4</sub>/C rocking-chair system: a review. *Elec-*  
3429 *trochimica Acta* **1993**, *38*, 1221 – 1231.
- 3430 (195) Dahn, J. R. Phase diagram of Li<sub>x</sub>C<sub>6</sub>. *Physical Review B* **1991**, *44*, 9170–9177.
- 3431 (196) Hazrati, E.; de Wijs, G. A.; Brocks, G. Li intercalation in graphite: A van der Waals  
3432 density-functional study. *Physical Review B* **2014**, *90*, 155448.

- 3433 (197) Konar, S.; Häusserman, U.; Svensson, G. Intercalation compounds from LiH and  
3434 graphite: Relative stability of metastable stages and thermodynamic stability of dilute  
3435 stage Id. *Chemistry of Materials* **2015**, *27*, 2566–2575.
- 3436 (198) Shi, H.; Barker, J.; Saïdi, M. Y.; Koksang, R. Structure and Lithium Intercalation  
3437 Properties of Synthetic and Natural Graphite. *Journal of The Electrochemical Society*  
3438 **1996**, *143*, 3466–3472.
- 3439 (199) Sethuraman, V. A.; Hardwick, L. J.; Srinivasan, V.; Kostecki, R. Surface structural  
3440 disordering in graphite upon lithium intercalation/deintercalation. *Journal of Power*  
3441 *Sources* **2010**, *195*, 3655–3660.
- 3442 (200) Ohzuku, T. Formation of Lithium-Graphite Intercalation Compounds in Nonaqueous  
3443 Electrolytes and Their Application as a Negative Electrode for a Lithium Ion (Shut-  
3444 tlecock) Cell. *Journal of The Electrochemical Society* **1993**, *140*, 2490.
- 3445 (201) He, H.; Huang, C.; Luo, C.-W.; Liu, J.-J.; Chao, Z.-S. Dynamic study of Li intercala-  
3446 tion into graphite by in situ high energy synchrotron XRD. *Electrochimica Acta* **2013**,  
3447 *92*, 148–152.
- 3448 (202) Trucano, P.; Chen, R. Structure of graphite by neutron diffraction. *Nature* **1975**, *258*,  
3449 136–137.
- 3450 (203) Okamoto, H. The C-Li (Carbon-Lithium) system. *Bulletin of Alloy Phase Diagrams*  
3451 **1989**, *10*, 69–72.
- 3452 (204) Billaud, D.; Henry, F.; Lelaurain, M.; Willmann, P. Revisited structures of dense  
3453 and dilute stage II lithium-graphite intercalation compounds. *Journal of Physics and*  
3454 *Chemistry of Solids* **1996**, *57*, 775–781.
- 3455 (205) Billaud, D.; Henry, F. Structural studies of the stage III lithium-graphite intercalation  
3456 compound. *Solid State Communications* **2002**, *124*, 299 – 304.

- 3457 (206) Didier, C.; Pang, W. K.; Guo, Z.; Schmid, S.; Peterson, V. K. Phase Evolution and  
3458 Intermittent Disorder in Electrochemically Lithiated Graphite Determined Using in  
3459 Operando Neutron Diffraction. *Chemistry of Materials* **2020**, *32*, 2518–2531.
- 3460 (207) Zheng, T.; Reimers, J. N.; Dahn, J. R. Effect of turbostratic disorder in graphitic  
3461 carbon hosts on the intercalation of lithium. *Physical Review B* **1995**, *51*, 734–741.
- 3462 (208) Senyshyn, A.; Dolotko, O.; Muhlbauer, M. J.; Nikolowski, K.; Fuess, H.; Ehrenberg, H.  
3463 Lithium Intercalation into Graphitic Carbons Revisited: Experimental Evidence for  
3464 Twisted Bilayer Behavior. *Journal of the Electrochemical Society* **2013**, *160*, A3198–  
3465 A3205.
- 3466 (209) Taminato, S. et al. Real-time observations of lithium battery reactions - Operando  
3467 neutron diffraction analysis during practical operation. *Scientific Reports* **2016**, *6*,  
3468 28843.
- 3469 (210) Thinius, S.; Islam, M. M.; Heitjans, P.; Bredow, T. Theoretical study of Li migration  
3470 in lithium–graphite intercalation compounds with dispersion-corrected DFT methods.  
3471 *The Journal of Physical Chemistry C* **2014**, *118*, 2273–2280.
- 3472 (211) Garcia, J. C.; Bloom, I.; Johnson, C.; Dees, D.; Iddir, H. Graphite Lithiation un-  
3473 der Fast Charging Conditions: Atomistic Modeling Insights. *The Journal of Physical*  
3474 *Chemistry C* **2020**, *124*, 8162–8169.
- 3475 (212) Olsson, E.; Cottom, J.; Au, H.; Guo, Z.; Jensen, A. C. S.; Alptekin, H.; Drew, A. J.;  
3476 Titirici, M.-M.; Cai, Q. Elucidating the Effect of Planar Graphitic Layers and Cylin-  
3477 drical Pores on the Storage and Diffusion of Li, Na, and K in Carbon Materials.  
3478 *Advanced Functional Materials* **2020**, *30*, 1908209.
- 3479 (213) Lenchuk, O.; Adelhelm, P.; Mollenhauer, D. Comparative study of density functionals  
3480 for the description of lithium-graphite intercalation compounds. *Journal of Computa-*  
3481 *tional Chemistry* **2019**, *40*, 2400–2412.



- 3482 (214) Ji, X.; Wang, Y.; Zhang, J. Understanding the anisotropic strain effects on lithium  
3483 diffusion in graphite anodes: A first-principles study. *Physica B: Condensed Matter*  
3484 **2018**, *539*, 66 – 71.
- 3485 (215) Wang, Z.; Ratvik, A. P.; Grande, T.; Selbach, S. M. Diffusion of alkali metals in the  
3486 first stage graphite intercalation compounds by vdW-DFT calculations. *RSC Adv.*  
3487 **2015**, *5*, 15985–15992.
- 3488 (216) Persson, K.; Sethuraman, V. A.; Hardwick, L. J.; Hinuma, Y.; Meng, Y. S.; Van  
3489 Der Ven, A.; Srinivasan, V.; Kostecki, R.; Ceder, G. Lithium diffusion in graphitic  
3490 carbon. *The journal of physical chemistry letters* **2010**, *1*, 1176–1180.
- 3491 (217) Otero, M.; Sigal, A.; Perassi, E.; Barraco, D.; Leiva, E. Statistical mechanical modeling  
3492 of the transition Stage II → Stage I of Li-ion storage in graphite. A priori vs induced  
3493 heterogeneity. *Electrochimica Acta* **2017**, *245*, 569 – 574.
- 3494 (218) Gavilán-Arriazu, E. M.; Pinto, O. A.; de Mishima, B. A. L.; Leiva, E. P. M.;  
3495 Oviedo, O. A. Grand Canonical Monte Carlo Study of Li Intercalation into Graphite.  
3496 *Journal of The Electrochemical Society* **2018**, *165*, A2019–A2025.
- 3497 (219) Gavilán Arriazu, E. M.; López de Mishima, B. A.; Oviedo, O. A.; Leiva, E. P. M.;  
3498 Pinto, O. A. Criticality of the phase transition on stage two in a lattice-gas model  
3499 of a graphite anode in a lithium-ion battery. *Phys. Chem. Chem. Phys.* **2017**, *19*,  
3500 23138–23145.
- 3501 (220) Gavilán-Arriazu, E.; Pinto, O.; López de Mishima, B.; Barraco, D.; Oviedo, O.;  
3502 Leiva, E. The kinetic origin of the Daumas-Hérolde model for the Li-ion/graphite in-  
3503 tercalation system. *Electrochemistry Communications* **2018**, *93*, 133 – 137.
- 3504 (221) Plett, G. L. Extended Kalman filtering for battery management systems of LiPB-based  
3505 HEV battery packs: Part 2. Modeling and identification. *Journal of Power Sources*  
3506 **2004**, *134*, 262 – 276.

- 3507 (222) Sole, C.; Drewett, N. E.; Hardwick, L. J. In situ Raman study of lithium-ion interca-  
3508 lation into microcrystalline graphite. *Faraday Discussions* **2014**, *172*, 223–237.
- 3509 (223) Allart, D.; Montaru, M.; Gualous, H. Model of Lithium Intercalation into Graphite  
3510 by Potentiometric Analysis with Equilibrium and Entropy Change Curves of Graphite  
3511 Electrode. *Journal of The Electrochemical Society* **2018**, *165*, A380–A387.
- 3512 (224) Markevich, E.; Levi, M. D.; Aurbach, D. New Insight into Studies of the Cycling  
3513 Performance of Li-Graphite Electrodes. *Journal of The Electrochemical Society* **2005**,  
3514 *152*, A778.
- 3515 (225) Reynier, Y.; Yazami, R.; Fultz, B. The entropy and enthalpy of lithium intercalation  
3516 into graphite. *Journal of Power Sources* **2003**, *119-121*, 850 – 855.
- 3517 (226) Liu, H.; Strobridge, F. C.; Borkiewicz, O. J.; Wiaderek, K. M.; Chapman, K. W.;  
3518 Chupas, P. J.; Grey, C. P. Capturing metastable structures during high-rate cycling  
3519 of LiFePO<sub>4</sub> nanoparticle electrodes. *Science* **2014**, *344*, 1252817–1–7.
- 3520 (227) Orikasa, Y.; Maeda, T.; Koyama, Y.; Murayama, H.; Fukuda, K.; Tanida, H.; Arai, H.;  
3521 Matsubara, E.; Uchimoto, Y.; Ogumi, Z. Direct Observation of a Metastable Crystal  
3522 Phase of Li<sub>x</sub>FePO<sub>4</sub> under Electrochemical Phase Transition. *Journal of the American*  
3523 *Chemical Society* **2013**, *135*, 5497–5500.
- 3524 (228) Gallagher, K. G.; Dees, D. W.; Jansen, A. N.; Abraham, D. P.; Kang, S.-H. A Vol-  
3525 ume Averaged Approach to the Numerical Modeling of Phase-Transition Intercalation  
3526 Electrodes Presented for Li<sub>x</sub>C<sub>6</sub>. *Journal of The Electrochemical Society* **2012**, *159*,  
3527 A2029–A2037.
- 3528 (229) Grimsman, F.; Gerbert, T.; Brauchle, F.; Gruhle, A.; Parisi, J.; Knipper, M. Hys-  
3529 teresis and current dependence of the graphite anode color in a lithium-ion cell and  
3530 analysis of lithium plating at the cell edge. *Journal of Energy Storage* **2018**, *15*, 17 –  
3531 22.

- 3532 (230) Osswald, P. J.; del Rosario, M.; Garche, J.; Jossen, A.; Hoster, H. E. Fast and accurate  
3533 measurement of entropy profiles of commercial lithium-ion cells. *Electrochimica Acta*  
3534 **2015**, *177*, 270–276.
- 3535 (231) Van der Ven, A.; Thomas, J.; Puchala, B.; Natarajan, A. First-Principles Statistical  
3536 Mechanics of Multicomponent Crystals. *Annual Review of Materials Research* **2018**,  
3537 *48*, 27–55.
- 3538 (232) Franco, A. A.; Rucci, A.; Brandell, D.; Frayret, C.; Gaberscek, M.; Jankowski, P.;  
3539 Johansson, P. Boosting Rechargeable Batteries R&D by Multiscale Modeling: Myth  
3540 or Reality? *Chemical Reviews* **2019**, *119*, 4569–4627.
- 3541 (233) Imai, Y.; Watanabe, A. Energetic evaluation of possible stacking structures of Li-  
3542 intercalation in graphite using a first-principle pseudopotential calculation. *Journal of*  
3543 *alloys and compounds* **2007**, *439*, 258–267.
- 3544 (234) Toyoura, K.; Koyama, Y.; Kuwabara, A.; Tanaka, I. Effects of off-stoichiometry of LiC<sub>6</sub>  
3545 on the lithium diffusion mechanism and diffusivity by first principles calculations. *The*  
3546 *Journal of Physical Chemistry C* **2010**, *114*, 2375–2379.
- 3547 (235) Yao, F.; Gunes, F.; Ta, H. Q.; Lee, S. M.; Chae, S. J.; Sheem, K. Y.; Cojocar, C. S.;  
3548 Xie, S. S.; Lee, Y. H. Diffusion mechanism of lithium ion through basal plane of layered  
3549 graphene. *Journal of the American Chemical Society* **2012**, *134*, 8646–8654.
- 3550 (236) NuLi, Y.; Yang, J.; Jiang, Z. Intercalation of lithium ions into bulk and powder highly  
3551 oriented pyrolytic graphite. *Journal of Physics and Chemistry of Solids* **2006**, *67*,  
3552 882–886.
- 3553 (237) Liu, T.; Lin, L.; Bi, X.; Tian, L.; Yang, K.; Liu, J.; Li, M.; Chen, Z.; Lu, J.; Amine, K.,  
3554 et al. In situ quantification of interphasial chemistry in Li-ion battery. *Nature nan-*  
3555 *otechnology* **2019**, *14*, 50–56.

- 3556 (238) Zhang, Z.; Smith, K.; Jarvis, R.; Shearing, P. R.; Miller, T. S.; Brett, D. J. Operando  
3557 Electrochemical Atomic Force Microscopy of Solid–Electrolyte Interphase Formation  
3558 on Graphite Anodes: The Evolution of SEI Morphology and Mechanical Properties.  
3559 *ACS applied materials & interfaces* **2020**, *12*, 35132–35141.
- 3560 (239) Thinius, S.; Islam, M. M.; Bredow, T. Reconstruction of low-index graphite surfaces.  
3561 *Surface Science* **2016**, *649*, 60–65.
- 3562 (240) Larciprete, R.; Lacovig, P.; Gardonio, S.; Baraldi, A.; Lizzit, S. Atomic Oxygen on  
3563 Graphite: Chemical Characterization and Thermal Reduction. *The Journal of Physical*  
3564 *Chemistry C* **2012**, *116*, 9900–9908.
- 3565 (241) Bernardo, P.; Le Meins, J.-M.; Vidal, L.; Dentzer, J.; Gadiou, R.; Märkle, W.;  
3566 Novák, P.; Spahr, M. E.; Vix-Guterl, C. Influence of graphite edge crystallographic  
3567 orientation on the first lithium intercalation in Li-ion battery. *Carbon* **2015**, *91*, 458–  
3568 467.
- 3569 (242) Toyoura, K.; Koyama, Y.; Kuwabara, A.; Oba, F.; Tanaka, I. First-principles approach  
3570 to chemical diffusion of lithium atoms in a graphite intercalation compound. *Physical*  
3571 *Review B* **2008**, *78*, 214303.
- 3572 (243) Takami, N.; Satoh, A.; Hara, M.; Ohsaki, T. Structural and kinetic characterization  
3573 of lithium intercalation into carbon anodes for secondary lithium batteries. *Journal of*  
3574 *the Electrochemical Society* **1995**, *142*, 371.
- 3575 (244) Yang, H.; Bang, H. J.; Prakash, J. Evaluation of electrochemical interface area and  
3576 lithium diffusion coefficient for a composite graphite anode. *Journal of the Electro-*  
3577 *chemical Society* **2004**, *151*, A1247.
- 3578 (245) Yu, P.; Popov, B. N.; Ritter, J. A.; White, R. E. Determination of the lithium ion  
3579 diffusion coefficient in graphite. *Journal of The Electrochemical Society* **1999**, *146*, 8.

- 3580 (246) Uthaisar, C.; Barone, V. Edge effects on the characteristics of Li diffusion in graphene.  
3581 *Nano letters* **2010**, *10*, 2838–2842.
- 3582 (247) Leggesse, E. G.; Chen, C.-L.; Jiang, J.-C. Lithium diffusion in graphene and graphite:  
3583 Effect of edge morphology. *Carbon* **2016**, *103*, 209–216.
- 3584 (248) Chan, T.-L.; Chelikowsky, J. R. Controlling diffusion of lithium in silicon nanostruc-  
3585 tures. *Nano letters* **2010**, *10*, 821–825.
- 3586 (249) Fujita, M.; Wakabayashi, K.; Nakada, K.; Kusakabe, K. Peculiar localized state at  
3587 zigzag graphite edge. *Journal of the Physical Society of Japan* **1996**, *65*, 1920–1923.
- 3588 (250) Lee, H.; Son, Y.-W.; Park, N.; Han, S.; Yu, J. Magnetic ordering at the edges of  
3589 graphitic fragments: Magnetic tail interactions between the edge-localized states.  
3590 *Physical Review B* **2005**, *72*, 174431.
- 3591 (251) Velický, M.; Toth, P. S.; Woods, C. R.; Novoselov, K. S.; Dryfe, R. A. Electrochemistry  
3592 of the Basal Plane versus Edge Plane of Graphite Revisited. *The Journal of Physical*  
3593 *Chemistry C* **2019**, *123*, 11677–11685.
- 3594 (252) Gerischer, H. An interpretation of the double layer capacity of graphite electrodes in  
3595 relation to the density of states at the Fermi level. *The Journal of Physical Chemistry*  
3596 **1985**, *89*, 4249–4251.
- 3597 (253) Weydanz, W.; Way, B.; Van Buuren, T.; Dahn, J. Behavior of Nitrogen-Substituted  
3598 Carbon ( $N_zC_{1-z}$ ) in Li/Li ( $N_zC_{+1-z}$ )<sub>6</sub> Cells. *Journal of the Electrochemical Society*  
3599 **1994**, *141*, 900.
- 3600 (254) Way, B.; Dahn, J. The effect of boron substitution in carbon on the intercalation of  
3601 lithium in  $Li_x(B_zC_{1-z})_6$ . *Journal of The Electrochemical Society* **1994**, *141*, 907.
- 3602 (255) Endo, M.; Hayashi, T.; Hong, S.-H.; Enoki, T.; Dresselhaus, M. S. Scanning tunneling

- 3603 microscope study of boron-doped highly oriented pyrolytic graphite. *Journal of Applied*  
3604 *Physics* **2001**, *90*, 5670–5674.
- 3605 (256) Gao, T.; Han, Y.; Fraggedakis, D.; Das, S.; Zhou, T.; Yeh, C. N.; Xu, S.; Chueh, W. C.;  
3606 Li, J.; Bazant, M. Z. Interplay of Lithium Intercalation and Plating on a Single  
3607 Graphite Particle. *Joule* **2021**, *5*, 393–414.
- 3608 (257) Peng, C.; Bhandari, A.; Dziejczak, J.; Owen, J. R.; Skylaris, C.-K.; Kramer, D. Mech-  
3609 anism of Li nucleation at graphite anodes and mitigation strategies. *J. Mater. Chem.*  
3610 *A* **2021**, *9*, 16798–16804.
- 3611 (258) Bhandari, A.; Peng, C.; Dziejczak, J.; Anton, L.; Owen, J. R.; Kramer, D.; Sky-  
3612 laris, C. K. Electrochemistry from first-principles in the grand canonical ensemble.  
3613 *Journal of Chemical Physics* **2021**, *155*, 1–14.
- 3614 (259) Winter, M. The solid electrolyte interphase—the most important and the least under-  
3615 stood solid electrolyte in rechargeable Li batteries. *Zeitschrift für physikalische Chemie*  
3616 **2009**, *223*, 1395–1406.
- 3617 (260) Verma, P.; Maire, P.; Novák, P. A review of the features and analyses of the solid  
3618 electrolyte interphase in Li-ion batteries. *Electrochimica Acta* **2010**, *55*, 6332 – 6341.
- 3619 (261) Haruyama, J.; Ikeshoji, T.; Otani, M. Analysis of lithium insertion/desorption reac-  
3620 tion at interfaces between graphite electrodes and electrolyte solution using density  
3621 functional+ implicit solvation theory. *The Journal of Physical Chemistry C* **2018**,  
3622 *122*, 9804–9810.
- 3623 (262) Yamada, Y.; Iriyama, Y.; Abe, T.; Ogumi, Z. Kinetics of Lithium Ion Transfer at the  
3624 Interface between Graphite and Liquid Electrolytes: Effects of Solvent and Surface  
3625 Film. *Langmuir* **2009**, *25*, 12766–12770.

- 3626 (263) Shi, S.; Lu, P.; Liu, Z.; Qi, Y.; Hector, L. G.; Li, H.; Harris, S. J. Direct calculation of  
3627 Li-ion transport in the solid electrolyte interphase. *Journal of the American Chemical*  
3628 *Society* **2012**, *134*, 15476–15487.
- 3629 (264) Larcher, D.; Beattie, S.; Morcrette, M.; Edstroem, K.; Jumas, J.-C.; Tarascon, J.-M.  
3630 Recent findings and prospects in the field of pure metals as negative electrodes for  
3631 Li-ion batteries. *Journal of Materials Chemistry* **2007**, *17*, 3759–3772.
- 3632 (265) Feng, K.; Li, M.; Liu, W.; Kashkooli, A. G.; Xiao, X.; Cai, M.; Chen, Z. Silicon-based  
3633 anodes for lithium-ion batteries: from fundamentals to practical applications. *Small*  
3634 **2018**, *14*, 1702737.
- 3635 (266) Nitta, N.; Yushin, G. High-capacity anode materials for lithium-ion batteries: choice  
3636 of elements and structures for active particles. *Particle & Particle Systems Charac-*  
3637 *terization* **2014**, *31*, 317–336.
- 3638 (267) Wagner, N. P.; Tron, A.; Tolchard, J. R.; Noia, G.; Bellmann, M. P. Silicon anodes for  
3639 lithium-ion batteries produced from recovered kerf powders. *Journal of Power Sources*  
3640 **2019**, *414*, 486–494.
- 3641 (268) Okamoto, H. The Li-Si (Lithium-Silicon) system. *Bulletin of Alloy Phase Diagrams*  
3642 **1990**, *11*, 306–312.
- 3643 (269) Gruber, T.; Thomas, D.; Röder, C.; Mertens, F.; Kortus, J. Raman spectroscopic  
3644 studies of  $\text{Li}_x\text{Si}_y$  compounds. *Journal of Raman Spectroscopy* **2013**, *44*, 934–938.
- 3645 (270) Jiang, Y.; Offer, G.; Jiang, J.; Marinescu, M.; Wang, H. Voltage Hysteresis Model  
3646 for Silicon Electrodes for Lithium Ion Batteries, Including Multi-Step Phase Transfor-  
3647 mations, Crystallization and Amorphization. *Journal of The Electrochemical Society*  
3648 **2020**, *167*, 130533.

- 3649 (271) Kuhn, A.; Sreeraj, P.; Pöttgen, R.; Wiemhöfer, H.-D.; Wilkening, M.; Heitjans, P.  
3650 Li Ion Diffusion in the Anode Material  $\text{Li}_{12}\text{Si}_7$ : Ultrafast Quasi-1D Diffusion and  
3651 Two Distinct Fast 3D Jump Processes Separately Revealed by  $^7\text{Li}$  NMR Relaxometry.  
3652 *Journal of the American Chemical Society* **2011**, *133*, 11018–11021.
- 3653 (272) Wang, D.; Gao, M.; Pan, H.; Wang, J.; Liu, Y. High performance amorphous-Si@  
3654  $\text{SiO}_x/\text{C}$  composite anode materials for Li-ion batteries derived from ball-milling and  
3655 in situ carbonization. *Journal of Power Sources* **2014**, *256*, 190–199.
- 3656 (273) Kirklin, S.; Meredig, B.; Wolverton, C. High-Throughput Computational Screening of  
3657 New Li-Ion Battery Anode Materials. *Advanced Energy Materials* **2013**, *3*, 252–262.
- 3658 (274) Fang, C.; Wang, X.; Meng, Y. S. Key issues hindering a practical lithium-metal anode.  
3659 *Trends in Chemistry* **2019**, *1*, 152–158.
- 3660 (275) Li, S.; Jiang, M.; Xie, Y.; Xu, H.; Jia, J.; Li, J. Developing high-performance lithium  
3661 metal anode in liquid electrolytes: challenges and progress. *Advanced Materials* **2018**,  
3662 *30*, 1706375.
- 3663 (276) Radin, M. D.; Alvarado, J.; Meng, Y. S.; Van der Ven, A. Role of Crystal Symmetry in  
3664 the Reversibility of Stacking–Sequence Changes in Layered Intercalation Electrodes.  
3665 *Nano Letters* **2017**, *17*, 7789–7795.
- 3666 (277) Vinckevičiūtė, J.; Radin, M. D.; Van der Ven, A. Stacking-Sequence Changes and  
3667 Na Ordering in Layered Intercalation Materials. *Chemistry of Materials* **2016**, *28*,  
3668 8640–8650.
- 3669 (278) Schmickler, W.; Santos, E. *Interfacial electrochemistry*, 2nd ed.; Springer-Verlag Berlin  
3670 Heidelberg, 2010; pp 1–272.
- 3671 (279) Bard, A. J.; Faulkner Larry R., *Electrochemical Methods: Fundamentals and Applica-*  
3672 *tions*, 2nd ed.; John Wiley & Sons, Ltd, 2010; pp 1–864.



- 3673 (280) Kralisch, D.; Stark, A.; Körsten, S.; Kreisel, G.; Ondruschka, B. Energetic, environ-  
3674 mental and economic balances: Spice up your ionic liquid research efficiency. *Green*  
3675 *Chemistry* **2005**, *7*, 301–309.
- 3676 (281) Smiglak, M.; Reichert, W. M.; Holbrey, J. D.; Wilkes, J. S.; Sun, L.; Thrasher, J. S.;  
3677 Kirichenko, K.; Singh, S.; Katritzky, A. R.; Rogers, R. D. Combustible ionic liquids  
3678 by design: is laboratory safety another ionic liquid myth? *Chemical Communications*  
3679 **2006**, 2554–2556.
- 3680 (282) Ding, F.; Xu, W.; Chen, X.; Zhang, J.; Engelhard, M. H.; Zhang, Y.; Johnson, B. R.;  
3681 Crum, J. V.; Blake, T. A.; Liu, X., et al. Effects of carbonate solvents and lithium  
3682 salts on morphology and coulombic efficiency of lithium electrode. *Journal of The*  
3683 *Electrochemical Society* **2013**, *160*, A1894.
- 3684 (283) Janek, J.; Zeier, W. G. A solid future for battery development. *Nature Energy* **2016**,  
3685 *1*, 16141.
- 3686 (284) Kazemiabnavi, S.; Zhang, Z.; Thornton, K.; Banerjee, S. Electrochemical stability  
3687 window of imidazolium-based ionic liquids as electrolytes for lithium batteries. *The*  
3688 *Journal of Physical Chemistry B* **2016**, *120*, 5691–5702.
- 3689 (285) Park, M.; Zhang, X.; Chung, M.; Less, G. B.; Sastry, A. M. A review of conduction  
3690 phenomena in Li-ion batteries. *Journal of Power Sources* **2010**, *195*, 7904–7929.
- 3691 (286) Kamaya, N.; Homma, K.; Yamakawa, Y.; Hirayama, M.; Kanno, R.; Yonemura, M.;  
3692 Kamiyama, T.; Kato, Y.; Hama, S.; Kawamoto, K.; Mitsui, A. A lithium superionic  
3693 conductor. *Nature materials* **2011**, *10*, 682–6.
- 3694 (287) Swift, M. W.; Swift, J. W.; Qi, Y. Modeling the electrical double layer at solid-state  
3695 electrochemical interfaces. *Nature Computational Science* **2021**, *1*, 212–220.

- 3696 (288) Xu, K.; von Cresce, A. Interfacing electrolytes with electrodes in Li ion batteries.  
3697 *Journal of Materials Chemistry* **2011**, *21*, 9849.
- 3698 (289) Yu, C.; Ganapathy, S.; van Eck, E. R. H.; Wang, H.; Basak, S.; Li, Z.; Wagemaker, M.  
3699 Accessing the bottleneck in all-solid state batteries, lithium-ion transport over the  
3700 solid-electrolyte-electrode interface. *Nature Communications* **2017**, *8*, 1086.
- 3701 (290) Xu, K. Nonaqueous Liquid Electrolytes for Lithium-Based Rechargeable Batteries.  
3702 *Chemical Reviews* **2004**, *104*, 4303–4418.
- 3703 (291) Xu, K. Electrolytes and interphases in Li-ion batteries and beyond. *Chemical Reviews*  
3704 **2014**, *114*, 11503–11618.
- 3705 (292) Maier, J. Ionic conduction in space charge regions. *Prog. Sol. Stat. Chem.* **1995**, *23*,  
3706 171 – 263.
- 3707 (293) Mebane, D. S. A variational approach to surface cation segregation in mixed conduct-  
3708 ing perovskites. *Comp. Mater. Sci.* **2015**, *103*, 231 – 236.
- 3709 (294) Mebane, D. S.; De Souza, R. A. A generalised space-charge theory for extended defects  
3710 in oxygen-ion conducting electrolytes: from dilute to concentrated solid solutions.  
3711 *Energy Environ. Sci.* **2015**, *8*, 2935–2940.
- 3712 (295) Tong, X.; Mebane, D. S.; De Souza, R. A. Analyzing the grain-boundary resistance  
3713 of oxide-ion conducting electrolytes: Poisson–Cahn vs Poisson–Boltzmann theories. *J.*  
3714 *Amer. Ceram. Soc.* **2020**, *103*, 5–22.
- 3715 (296) Lund, J.; Vikrant, K.; Bishop, C.; Rheinheimer, W.; García, R. Thermodynamically  
3716 consistent variational principles for charged interfaces. *Acta Materialia* **2021**, *205*,  
3717 116525.
- 3718 (297) Bazant, M. Z.; Storey, B. D.; Kornyshev, A. A. Double layer in ionic liquids: Over-  
3719 screening versus crowding. *Physical review letters* **2011**, *106*, 046102.

- 3720 (298) Perkin, S. Ionic liquids in confined geometries. *Phys. Chem. Chem. Phys.* **2012**, *14*,  
3721 5052–5062.
- 3722 (299) Groves, T. S.; Perez-Martinez, C. S.; Lhermerout, R.; Perkin, S. Surface Forces and  
3723 Structure in a Water-in-Salt Electrolyte. *The Journal of Physical Chemistry Letters*  
3724 **2021**, *12*, 1702–1707.
- 3725 (300) Bowers, J.; Vergara-Gutierrez, M. C.; Webster, J. R. P. Surface Ordering of Am-  
3726 phiphilic Ionic Liquids. *Langmuir* **2004**, *20*, 309–312.
- 3727 (301) Sloutskin, E.; Ocko, B. M.; Tamam, L.; Kuzmenko, I.; Gog, T.; Deutsch, M. Surface  
3728 Layering in Ionic Liquids: An X-ray Reflectivity Study. *Journal of the American*  
3729 *Chemical Society* **2005**, *127*, 7796–7804.
- 3730 (302) Dean, J. M.; Coles, S. W.; Saunders, W. R.; McCluskey, A. R.; Wolf, M. J.;  
3731 Walker, A. B.; Morgan, B. J. Overscreening and Underscreening in Solid-Electrolyte  
3732 Grain Boundary Space-Charge Layers. *arXiv preprint arXiv:2104.00623* **2021**,
- 3733 (303) Valøen, L. O.; Reimers, J. N. Transport properties of LiPF<sub>6</sub>-based Li-ion battery  
3734 electrolytes. *Journal of The Electrochemical Society* **2005**, *152*, A882.
- 3735 (304) Yamada, Y.; Yaegashi, M.; Abe, T.; Yamada, A. A superconcentrated ether electrolyte  
3736 for fast-charging Li-ion batteries. *Chem. Commun.* **2013**, *49*, 11194.
- 3737 (305) MacFarlane, D. R.; Tachikawa, N.; Forsyth, M.; Pringle, J. M.; Howlett, P. C.; El-  
3738 liott, G. D.; Davis, J. H.; Watanabe, M.; Simon, P.; Angell, C. A. Energy applications  
3739 of ionic liquids. *Energy & Environmental Science* **2014**, *7*, 232–250.
- 3740 (306) Suo, L.; Borodin, O.; Sun, W.; Fan, X.; Yang, C.; Wang, F.; Gao, T.; Ma, Z.;  
3741 Schroeder, M.; von Cresce, A., et al. Advanced high-voltage aqueous lithium-ion bat-  
3742 tery enabled by “water-in-bisalt” electrolyte. *Angewandte Chemie* **2016**, *128*, 7252–  
3743 7257.

- 3744 (307) Qian, J.; Henderson, W. A.; Xu, W.; Bhattacharya, P.; Engelhard, M.; Borodin, O.;  
3745 Zhang, J.-G. High rate and stable cycling of lithium metal anode. *Nature communi-*  
3746 *cations* **2015**, *6*, 1–9.
- 3747 (308) Kim, H.; Wu, F.; Lee, J. T.; Nitta, N.; Lin, H.-T.; Oschatz, M.; Cho, W. I.; Kaskel, S.;  
3748 Borodin, O.; Yushin, G. In situ formation of protective coatings on sulfur cathodes  
3749 in lithium batteries with LiFSI-based organic electrolytes. *Advanced energy materials*  
3750 **2015**, *5*, 1401792.
- 3751 (309) Zhou, X.; Zhou, J.; Yin, Y. *Modeling and Diagnostics of Polymer Electrolyte Fuel*  
3752 *Cells*; Springer, 2009; pp 307–380.
- 3753 (310) Enderby, J.; Neilson, G. The structure of electrolyte solutions. *Reports on Progress in*  
3754 *Physics* **1981**, *44*, 593.
- 3755 (311) Fujie, T.; Takenaka, N.; Suzuki, Y.; Nagaoka, M. Red Moon methodology compat-  
3756 ible with quantum mechanics/molecular mechanics framework: Application to solid  
3757 electrolyte interphase film formation in lithium-ion battery system. *The Journal of*  
3758 *Chemical Physics* **2018**, *149*, 044113.
- 3759 (312) Koch, V. R.; Dominey, L. A.; Nanjundiah, C.; Ondrechen, M. J. The Intrinsic Anodic  
3760 Stability of Several Anions Comprising Solvent-Free Ionic Liquids. *Journal of The*  
3761 *Electrochemical Society* **1996**, *143*, 798–803.
- 3762 (313) Ong, S. P.; Andreussi, O.; Wu, Y.; Marzari, N.; Ceder, G. Electrochemical windows  
3763 of room-temperature ionic liquids from molecular dynamics and density functional  
3764 theory calculations. *Chemistry of Materials* **2011**, *23*, 2979–2986.
- 3765 (314) Vuilleumier, R.; Sprik, M. Electronic properties of hard and soft ions in solution:  
3766 Aqueous Na<sup>+</sup> and Ag<sup>+</sup> compared. *The Journal of Chemical Physics* **2001**, *115*, 3454–  
3767 3468.

- 3768 (315) Blumberger, J.; Tavernelli, I.; Klein, M. L.; Sprik, M. Diabatic free energy curves  
3769 and coordination fluctuations for the aqueous  $\text{Ag}^+/\text{Ag}^{2+}$  redox couple: A biased  
3770 Born-Oppenheimer molecular dynamics investigation. *The Journal of chemical physics*  
3771 **2006**, *124*, 064507.
- 3772 (316) Blumberger, J.; Bernasconi, L.; Tavernelli, I.; Vuilleumier, R.; Sprik, M. Electronic  
3773 structure and solvation of copper and silver ions: a theoretical picture of a model  
3774 aqueous redox reaction. *Journal of the American Chemical Society* **2004**, *126*, 3928–  
3775 3938.
- 3776 (317) VandeVondele, J.; Sulpizi, M.; Sprik, M. From solvent fluctuations to quantitative  
3777 redox properties of quinones in methanol and acetonitrile. *Angewandte Chemie* **2006**,  
3778 *118*, 1970–1972.
- 3779 (318) Lynden-Bell, R. Can Marcus theory be applied to redox processes in ionic liquids?  
3780 A comparative simulation study of dimethylimidazolium liquids and acetonitrile. *The*  
3781 *Journal of Physical Chemistry B* **2007**, *111*, 10800–10806.
- 3782 (319) Ganesh, P.; Jiang, D.-E.; Kent, P. R. Accurate static and dynamic properties of liquid  
3783 electrolytes for Li-ion batteries from ab initio molecular dynamics. *Journal of Physical*  
3784 *Chemistry B* **2011**, *115*, 3085–3090.
- 3785 (320) Kameda, Y.; Umebayashi, Y.; Takeuchi, M.; Wahab, M. A.; Fukuda, S.; Ishiguro, S. I.;  
3786 Sasaki, M.; Amo, Y.; Usuki, T. Solvation structure of  $\text{Li}^+$  in concentrated  $\text{LiPF}_6$ -  
3787 propylene carbonate solutions. *Journal of Physical Chemistry B* **2007**, *111*, 6104–  
3788 6109.
- 3789 (321) Soetens, J.-C.; Millot, C.; Maignet, B. Molecular Dynamics Simulation of  $\text{Li}^+\text{BF}_4^-$   
3790 in Ethylene Carbonate, Propylene Carbonate, and Dimethyl Carbonate Solvents. *J.*  
3791 *Phys. Chem. A* **1998**, *102*, 1055–1061.

- 3792 (322) Lespes, N.; Filhol, J.-S. Using implicit solvent in *ab initio* electrochemical modeling:  
3793 investigating Li<sup>+</sup>/Li electrochemistry at a Li/solvent interface. *Journal of chemical*  
3794 *theory and computation* **2015**, *11*, 3375–3382.
- 3795 (323) Morgan, B. J.; Watson, G. W. Role of Lithium Ordering in the Li<sub>x</sub>TiO<sub>2</sub> Anatase →  
3796 Titanate Phase Transition. *J. Phys. Chem. Lett.* **2011**, *2*, 1657–1661.
- 3797 (324) Zhao, X.-G.; Dalpian, G. M.; Wang, Z.; Zunger, A. Polymorphous nature of cubic  
3798 halide perovskites. *Phys. Rev. B* **2020**, *101*, 155137.
- 3799 (325) Yeh, I.-C.; Hummer, G. System-Size Dependence of Diffusion Coefficients and Vis-  
3800 cosities from Molecular Dynamics Simulations with Periodic Boundary Conditions. *J.*  
3801 *Phys. Chem. B* **2004**, *108*, 15873–15879.
- 3802 (326) Botan, A.; Marry, V.; Rotenberg, B. Diffusion in bulk liquids: finite-size effects in  
3803 anisotropic systems. *Molecular Physics* **2015**, *113*, 2674–2679.
- 3804 (327) Horbach, J.; Kob, W.; Binder, K.; Angell, C. A. Finite size effects in simulations of  
3805 glass dynamics. *Phys. Rev. E* **1996**, *54*, R5897–R5900.
- 3806 (328) Coles, S. W.; Park, C.; Nikam, R.; Kanduč, M.; Dzubiella, J.; Rotenberg, B. Correla-  
3807 tion Length in Concentrated Electrolytes: Insights from All-Atom Molecular Dynamics  
3808 Simulations. *J. Phys. Chem. B* **2020**, *124*, 1778–1786.
- 3809 (329) Frenkel, D.; Smit, B. *Understanding molecular simulation*; Academic Press, 2002.
- 3810 (330) Lindahl,; Abraham,; Hess,; van der Spoel, GROMACS 2021 Manual. **2021**,
- 3811 (331) Canongia Lopes, J. N.; Pádua, A. A. H. CL&P: A generic and systematic force field  
3812 for ionic liquids modeling. *Theor Chem Acc* **2012**, *131*, 1129.
- 3813 (332) Jorgensen, W. L.; Maxwell, D. S.; Tirado-Rives, J. Development and Testing of the  
3814 OPLS All-Atom Force Field on Conformational Energetics and Properties of Organic  
3815 Liquids. *J. Am. Chem. Soc.* **1996**, *118*, 11225–11236.

- 3816 (333) Hess, B.; Bekker, H.; Berendsen, H. J. C.; Fraaije, J. G. E. M. LINCS: A linear con-  
3817 straint solver for molecular simulations. *Journal of Computational Chemistry* **1997**,  
3818 *18*, 1463–1472.
- 3819 (334) Ryckaert, J.-P.; Ciccotti, G.; Berendsen, H. J. C. Numerical integration of the cartesian  
3820 equations of motion of a system with constraints: molecular dynamics of n-alkanes.  
3821 *Journal of Computational Physics* **1977**, *23*, 327–341.
- 3822 (335) Andersen, H. C. Rattle: A “velocity” version of the shake algorithm for molecular  
3823 dynamics calculations. *Journal of Computational Physics* **1983**, *52*, 24–34.
- 3824 (336) Ewald, P. P. Die Berechnung optischer und elektrostatischer Gitterpotentiale. *Annalen*  
3825 *der Physik* **1921**, *369*, 253–287.
- 3826 (337) Darden, T.; York, D.; Pedersen, L. Particle mesh Ewald: An N.log(N) method for  
3827 Ewald sums in large systems. *J. Chem. Phys.* **1993**, *98*, 10089–10092.
- 3828 (338) Deserno, M.; Holm, C. How to mesh up Ewald sums. II. An accurate error estimate for  
3829 the particle–particle–particle-mesh algorithm. *J. Chem. Phys.* **1998**, *109*, 7694–7701.
- 3830 (339) Yeh, I.-C.; Berkowitz, M. L. Ewald summation for systems with slab geometry. *J.*  
3831 *Chem. Phys.* **1999**, *111*, 3155–3162.
- 3832 (340) Canongia Lopes, J. N.; Deschamps, J.; Pádua, A. A. H. Modeling Ionic Liquids Using  
3833 a Systematic All-Atom Force Field. *J. Phys. Chem. B* **2004**, *108*, 2038–2047.
- 3834 (341) Canongia Lopes, J. N.; Pádua, A. A. H. Molecular Force Field for Ionic Liquids Com-  
3835 posed of Triflate or Bistriflylimide Anions. *J. Phys. Chem. B* **2004**, *108*, 16893–16898.
- 3836 (342) Canongia Lopes, J. N.; Pádua, A. A. H. Molecular Force Field for Ionic Liquids III:  
3837 Imidazolium, Pyridinium, and Phosphonium Cations; Chloride, Bromide, and Di-  
3838 cyanamide Anions. *J. Phys. Chem. B* **2006**, *110*, 19586–19592.

- 3839 (343) Spackman, M. A. Potential derived charges using a geodesic point selection scheme.  
3840 *Journal of Computational Chemistry* **1996**, *17*, 1–18.
- 3841 (344) Breneman, C. M.; Wiberg, K. B. Determining atom-centered monopoles from molec-  
3842 ular electrostatic potentials. The need for high sampling density in formamide confor-  
3843 mational analysis. *Journal of Computational Chemistry* **1990**, *11*, 361–373.
- 3844 (345) Singh, U. C.; Kollman, P. A. An approach to computing electrostatic charges for  
3845 molecules. *Journal of Computational Chemistry* **1984**, *5*, 129–145.
- 3846 (346) Schröder, C. Comparing reduced partial charge models with polarizable simulations  
3847 of ionic liquids. *Phys. Chem. Chem. Phys.* **2012**, *14*, 3089–3102.
- 3848 (347) Schröder, C.; Lyons, A.; Rick, S. W. Polarizable MD simulations of ionic liquids:  
3849 How does additional charge transfer change the dynamics? *Phys. Chem. Chem. Phys.*  
3850 **2020**, *22*, 467–477.
- 3851 (348) Shimizu, K.; Freitas, A. A.; Atkin, R.; Warr, G. G.; FitzGerald, P. A.; Doi, H.;  
3852 Saito, S.; Ueno, K.; Umabayashi, Y.; Watanabe, M.; Lopes, J. N. C. Structural and  
3853 aggregate analyses of (Li salt + glyme) mixtures: the complex nature of solvate ionic  
3854 liquids. *Phys. Chem. Chem. Phys.* **2015**, *17*, 22321–22335.
- 3855 (349) Sangster, M.; Dixon, M. Interionic potentials in alkali halides and their use in simula-  
3856 tions of the molten salts. *Advances in Physics* **1976**, *25*, 247–342.
- 3857 (350) Madden, P. A.; Wilson, M. “Covalent” effects in “ionic” systems. *Chem. Soc. Rev.*  
3858 **1996**, *25*, 339–350.
- 3859 (351) Borodin, O. Polarizable Force Field Development and Molecular Dynamics Simulations  
3860 of Ionic Liquids. *J. Phys. Chem. B* **2009**, *113*, 11463–11478.
- 3861 (352) Borodin, O.; Smith, G. D. LiTFSI Structure and Transport in Ethylene Carbonate  
3862 from Molecular Dynamics Simulations. *J. Phys. Chem. B* **2006**, *110*, 4971–4977.



- 3863 (353) Bedrov, D.; Piquemal, J.-P.; Borodin, O.; MacKerell, A. D.; Roux, B.; Schröder, C.  
3864 Molecular Dynamics Simulations of Ionic Liquids and Electrolytes Using Polarizable  
3865 Force Fields. *Chem. Rev.* **2019**, *119*, 7940–7995.
- 3866 (354) Bedrov, D.; Borodin, O.; Li, Z.; Smith, G. D. Influence of Polarization on Structural,  
3867 Thermodynamic, and Dynamic Properties of Ionic Liquids Obtained from Molecular  
3868 Dynamics Simulations. *J. Phys. Chem. B* **2010**, *114*, 4984–4997.
- 3869 (355) Marin-Lafèche, A.; Haefele, M.; Scalfi, L.; Coretti, A.; Dufils, T.; Jeanmairet, G.;  
3870 Reed, S. K.; Alessandra, S.; Berthin, R.; Bacon, C.; Bonella, S.; Rotenberg, B.; Mad-  
3871 den, P. A.; Salanne, M. MetalWalls: A classical molecular dynamics software dedicated  
3872 to the simulation of electrochemical systems. *Journal of Open Source Software* **2020**,  
3873 *5*, 2373.
- 3874 (356) Mamatkulov, S.; Fyta, M.; Netz, R. R. Force fields for divalent cations based on  
3875 single-ion and ion-pair properties. *J. Chem. Phys.* **2013**, *138*, 024505.
- 3876 (357) Mamatkulov, S.; Schwierz, N. Force fields for monovalent and divalent metal cations in  
3877 TIP3P water based on thermodynamic and kinetic properties. *J. Chem. Phys.* **2018**,  
3878 *148*, 074504.
- 3879 (358) Pethes, I. A comparison of classical interatomic potentials applied to highly concen-  
3880 trated aqueous lithium chloride solutions. *Journal of Molecular Liquids* **2017**, *242*,  
3881 845–858.
- 3882 (359) Hanke, C. G.; Price, S. L.; Lynden-Bell, R. M. Intermolecular potentials for simulations  
3883 of liquid imidazolium salts. *Molecular Physics* **2001**, *99*, 801–809.
- 3884 (360) Tsuzuki, S.; Shinoda, W.; Saito, H.; Mikami, M.; Tokuda, H.; Watanabe, M. Molec-  
3885 ular Dynamics Simulations of Ionic Liquids: Cation and Anion Dependence of Self-  
3886 Diffusion Coefficients of Ions. *J. Phys. Chem. B* **2009**, *113*, 10641–10649.

- 3887 (361) Migliorati, V.; Serva, A.; Aquilanti, G.; Olivi, L.; Pascarelli, S.; Mathon, O.;  
3888 D'Angelo, P. Combining EXAFS spectroscopy and molecular dynamics simulations  
3889 to understand the structural and dynamic properties of an imidazolium iodide ionic  
3890 liquid. *Physical Chemistry Chemical Physics* **2015**, *17*, 2464–2474.
- 3891 (362) Chaudhari, M. I.; Muralidharan, A.; Pratt, L. R.; Rempe, S. B. Assessment of Simple  
3892 Models for Molecular Simulation of Ethylene Carbonate and Propylene Carbonate as  
3893 Solvents for Electrolyte Solutions. *Top Curr Chem (Z)* **2018**, *376*, 376.
- 3894 (363) Sergeev, A. V.; Chertovich, A. V.; Itkis, D. M.; Sen, A.; Gross, A.; Khokhlov, A. R.  
3895 Electrode/Electrolyte Interface in the Li–O<sub>2</sub> Battery: Insight from Molecular Dynam-  
3896 ics Study. *J. Phys. Chem. C* **2017**, *121*, 14463–14469.
- 3897 (364) Schröder, C. Collective translational motions and cage relaxations in molecular ionic  
3898 liquids. *J. Chem. Phys.* **2011**, *135*, 024502.
- 3899 (365) Schröder, C.; Steinhauser, O. On the dielectric conductivity of molecular ionic liquids.  
3900 *J. Chem. Phys.* **2009**, *131*, 114504.
- 3901 (366) Hayamizu, K.; Aihara, Y.; Arai, S.; Martinez, C. G. Pulse-gradient spin-echo <sup>1</sup>H, <sup>7</sup>Li,  
3902 and <sup>19</sup>F NMR diffusion and ionic conductivity measurements of 14 organic electrolytes  
3903 containing LiN(SO<sub>2</sub>CF<sub>3</sub>)<sub>2</sub>. *Journal of Physical Chemistry B* **1999**, *103*, 519–524.
- 3904 (367) Lesch, V.; Li, Z.; Bedrov, D.; Borodin, O.; Heuer, A. The influence of cations on  
3905 lithium ion coordination and transport in ionic liquid electrolytes: a MD simulation  
3906 study. *Phys. Chem. Chem. Phys.* **2015**, *18*, 382–392.
- 3907 (368) Borodin, O.; Smith, G. D.; Henderson, W. Li<sup>+</sup> Cation Environment, Transport, and  
3908 Mechanical Properties of the LiTFSI Doped N-Methyl-N-alkylpyrrolidinium<sup>+</sup>TFSI<sup>-</sup>  
3909 Ionic Liquids. *J. Phys. Chem. B* **2006**, *110*, 16879–16886.

- 3910 (369) Borodin, O.; Smith, G. D. Li<sup>+</sup> Transport Mechanism in Oligo(Ethylene Oxide)s Com-  
3911 pared to Carbonates. *J Solution Chem* **2007**, *36*, 803–813.
- 3912 (370) Skarmoutsos, I.; Ponnuchamy, V.; Vetere, V.; Mossa, S. Li<sup>+</sup> Solvation in Pure, Binary,  
3913 and Ternary Mixtures of Organic Carbonate Electrolytes. *J. Phys. Chem. C* **2015**,  
3914 *119*, 4502–4515.
- 3915 (371) Takeuchi, M.; Matubayasi, N.; Kameda, Y.; Minofar, B.; Ichi Ishiguro, S.; Ume-  
3916 bayashi, Y. Free-Energy and Structural Analysis of Ion Solvation and Contact Ion-Pair  
3917 Formation of Li<sup>+</sup> with BF<sub>4</sub><sup>-</sup> and PF<sub>6</sub><sup>-</sup> in Water and Carbonate Solvents. *J. Phys. Chem.*  
3918 *B* **2012**, *116*, 6476–6487.
- 3919 (372) Lazaridis, T. Inhomogeneous Fluid Approach to Solvation Thermodynamics. 1. The-  
3920 ory. *J. Phys. Chem. B* **1998**, *102*, 3531–3541.
- 3921 (373) Hall, D. S.; Self, J.; Dahn, J. R. Dielectric Constants for Quantum Chemistry and  
3922 Li-Ion Batteries: Solvent Blends of Ethylene Carbonate and Ethyl Methyl Carbonate.  
3923 *Journal of Physical Chemistry C* **2015**, *119*, 22322–22330.
- 3924 (374) Naejus, R.; Damas, C.; Lemordant, D.; Coudert, R.; Willmann, P. Excess thermody-  
3925 namic properties of the ethylene carbonate-trifluoroethyl methyl carbonate and propy-  
3926 lene carbonate-trifluoroethyl methyl carbonate systems at T = (298.15 or 315.15) K.  
3927 *Journal of Chemical Thermodynamics* **2002**, *34*, 795–806.
- 3928 (375) Stewart, S.; Newman, J. Measuring the salt activity coefficient in lithium-battery  
3929 electrolytes. *Journal of the Electrochemical Society* **2008**, *155*, 458–463.
- 3930 (376) Debye, P.; Hückel, E. On the theory of electrolytes. II Limiting law for electric con-  
3931 ductivity. *Physikalische Zeitschrift* **1923**, *24*, 305–325.
- 3932 (377) Merlet, C.; Péan, C.; Rotenberg, B.; Madden, P. A.; Simon, P.; Salanne, M. Simulating

- 3933 Supercapacitors: Can We Model Electrodes As Constant Charge Surfaces? *J. Phys.*  
3934 *Chem. Lett.* **2013**, *4*, 264–268.
- 3935 (378) Smith, A. M.; Lee, A. A.; Perkin, S. The Electrostatic Screening Length in Con-  
3936 centrated Electrolytes Increases with Concentration. *J. Phys. Chem. Lett.* **2016**, *7*,  
3937 2157–2163.
- 3938 (379) Coles, S. W.; Ivaništšev, V. B. Simulation of a Solvate Ionic Liquid at a Polarizable  
3939 Electrode with a Constant Potential. *J. Phys. Chem. C* **2019**, *123*, 3935–3943.
- 3940 (380) Scalfi, L.; Dufils, T.; Reeves, K. G.; Rotenberg, B.; Salanne, M. A semiclassical  
3941 Thomas–Fermi model to tune the metallicity of electrodes in molecular simulations.  
3942 *J. Chem. Phys.* **2020**, *153*, 174704.
- 3943 (381) Vatamanu, J.; Borodin, O. Ramifications of Water-in-Salt Interfacial Structure at  
3944 Charged Electrodes for Electrolyte Electrochemical Stability. *J. Phys. Chem. Lett.*  
3945 **2017**, *8*, 4362–4367.
- 3946 (382) Li, Z.; Jeanmairet, G.; Méndez-Morales, T.; Rotenberg, B.; Salanne, M. Capacitive  
3947 Performance of Water-in-Salt Electrolytes in Supercapacitors: A Simulation Study. *J.*  
3948 *Phys. Chem. C* **2018**, *122*, 23917–23924.
- 3949 (383) Vatamanu, J.; Borodin, O.; Smith, G. D. Molecular dynamics simulations of atomically  
3950 flat and nanoporous electrodes with a molten salt electrolyte. **2009**, *12*, 170–182.
- 3951 (384) Merlet, C.; Péan, C.; Rotenberg, B.; Madden, P. A.; Daffos, B.; Taberna, P.-L.; Si-  
3952 mon, P.; Salanne, M. Highly confined ions store charge more efficiently in supercapac-  
3953 itors. *Nature Communications* **2013**, *4*, 2701.
- 3954 (385) Merlet, C.; Rotenberg, B.; Madden, P. A.; Taberna, P.-L.; Simon, P.; Gogotsi, Y.;  
3955 Salanne, M. On the molecular origin of supercapacitance in nanoporous carbon elec-  
3956 trodes. *Nature Materials* **2012**, *11*, 306–310.

- 3957 (386) Vatamanu, J.; Cao, L.; Borodin, O.; Bedrov, D.; Smith, G. D. On the Influence of Sur-  
3958 face Topography on the Electric Double Layer Structure and Differential Capacitance  
3959 of Graphite/Ionic Liquid Interfaces. *J. Phys. Chem. Lett.* **2011**, *2*, 2267–2272.
- 3960 (387) Borodin, O.; Bedrov, D. Interfacial Structure and Dynamics of the Lithium Alkyl  
3961 Dicarboxylate SEI Components in Contact with the Lithium Battery Electrolyte. *J.*  
3962 *Phys. Chem. C* **2014**, *118*, 18362–18371.
- 3963 (388) Suo, L.; Borodin, O.; Gao, T.; Olguin, M.; Ho, J.; Fan, X.; Luo, C.; Wang, C.; Xu, K.  
3964 “Water-in-salt” electrolyte enables high-voltage aqueous lithium-ion chemistries. *Sci-*  
3965 *ence* **2015**, *350*, 938–943.
- 3966 (389) Chen, M.; Feng, G.; Qiao, R. Water-in-salt electrolytes: An interfacial perspective.  
3967 *Current Opinion in Colloid & Interface Science* **2020**, *47*, 99–110.
- 3968 (390) Li, Z.; Bouchal, R.; Mendez-Morales, T.; Rollet, A.-L.; Rizzi, C.; Le Vot, S.; Favier, F.;  
3969 Rotenberg, B.; Borodin, O.; Fontaine, O., et al. Transport properties of Li-TFSI water-  
3970 in-salt electrolytes. *The Journal of Physical Chemistry B* **2019**, *123*, 10514–10521.
- 3971 (391) McCurry, J. Samsung blames two separate battery faults for Galaxy Note  
3972 7 fires. 2017; [http://www.theguardian.com/technology/2017/jan/23/  
3973 samsung-blames-faulty-batteries-for-causing-galaxy-note-7-fires](http://www.theguardian.com/technology/2017/jan/23/samsung-blames-faulty-batteries-for-causing-galaxy-note-7-fires).
- 3974 (392) Zhang, S. S. Liquid electrolyte lithium/sulfur battery: Fundamental chemistry, prob-  
3975 lems, and solutions. *Journal of Power Sources* **2013**, *231*, 153–162.
- 3976 (393) Wu, X.; Pan, K.; Jia, M.; Ren, Y.; He, H.; Zhang, L.; Zhang, S. Electrolyte for lithium  
3977 protection: From liquid to solid. *Green Energy and Environment* **2019**, *4*, 360–374.
- 3978 (394) Kushima, A.; So, K. P.; Su, C.; Bai, P.; Kuriyama, N.; Maebashi, T.; Fujiwara, Y.;  
3979 Bazant, M. Z.; Li, J. Liquid cell transmission electron microscopy observation of

- 3980 lithium metal growth and dissolution: Root growth, dead lithium and lithium flot-  
3981 sams. *Nano Energy* **2017**, *32*, 271–279.
- 3982 (395) Lin, D.; Liu, Y.; Li, Y.; Li, Y.; Pei, A.; Xie, J.; Huang, W.; Cui, Y. Fast galvanic  
3983 lithium corrosion involving a Kirkendall-type mechanism. *Nature chemistry* **2019**, *11*,  
3984 382–389.
- 3985 (396) Hallinan Jr, D. T.; Balsara, N. P. Polymer electrolytes. *Annual review of materials*  
3986 *research* **2013**, *43*, 503–525.
- 3987 (397) Popovic, J. Chemistry of Soft Matter Battery Electrolytes. *Encyclopedia of Inorganic*  
3988 *and Bioinorganic Chemistry* **2011**, 1–11.
- 3989 (398) Simoncelli, M.; Ganfoud, N.; Sene, A.; Haefele, M.; Daffos, B.; Taberna, P.-L.;  
3990 Salanne, M.; Simon, P.; Rotenberg, B. Blue Energy and Desalination with Nanoporous  
3991 Carbon Electrodes: Capacitance from Molecular Simulations to Continuous Models.  
3992 *Phys. Rev. X* **2018**, *8*, 021024.
- 3993 (399) Shao, Y.; Knijff, L.; Dietrich, F. M.; Hermansson, K.; Zhang, C. Modelling Bulk  
3994 Electrolytes and Electrolyte Interfaces with Atomistic Machine Learning. *Batteries &*  
3995 *Supercaps* **2021**, *4*, 585–595.
- 3996 (400) Hellström, M.; Behler, J. Concentration-dependent proton transfer mechanisms in  
3997 aqueous NaOH solutions: From acceptor-driven to donor-driven and back. *The journal*  
3998 *of physical chemistry letters* **2016**, *7*, 3302–3306.
- 3999 (401) Tovey, S.; Narayanan Krishnamoorthy, A.; Sivaraman, G.; Guo, J.; Benmore, C.;  
4000 Heuer, A.; Holm, C. DFT Accurate Interatomic Potential for Molten NaCl from Ma-  
4001 chine Learning. *The Journal of Physical Chemistry C* **2020**, *124*, 25760–25768.
- 4002 (402) Fedkin, M. V.; Shin, Y. K.; Dasgupta, N.; Yeon, J.; Zhang, W.; Van Duin, D.;  
4003 Van Duin, A. C.; Mori, K.; Fujiwara, A.; Machida, M., et al. Development of the

- 4004 ReaxFF Methodology for Electrolyte–Water Systems. *The Journal of Physical Chem-*  
4005 *istry A* **2019**, *123*, 2125–2141.
- 4006 (403) Hossain, M. J.; Pawar, G.; Liaw, B.; Gering, K. L.; Dufek, E. J.; van Duin, A. C.  
4007 Lithium-electrolyte solvation and reaction in the electrolyte of a lithium ion battery:  
4008 A ReaxFF reactive force field study. *The Journal of chemical physics* **2020**, *152*,  
4009 184301.
- 4010 (404) Jeanmairet, G.; Rotenberg, B.; Borgis, D.; Salanne, M. Study of a water-graphene  
4011 capacitor with molecular density functional theory. *The Journal of chemical physics*  
4012 **2019**, *151*, 124111.
- 4013 (405) Forsman, J.; Woodward, C. E.; Trulsson, M. A Classical Density Functional Theory  
4014 of Ionic Liquids. *J. Phys. Chem. B* **2011**, *115*, 4606–4612.
- 4015 (406) Jeanmairet, G.; Rotenberg, B.; Levesque, M.; Borgis, D.; Salanne, M. A molecular  
4016 density functional theory approach to electron transfer reactions. *Chemical science*  
4017 **2019**, *10*, 2130–2143.
- 4018 (407) Jie, Y.; Ren, X.; Cao, R.; Cai, W.; Jiao, S. Advanced liquid electrolytes for rechargeable  
4019 Li metal batteries. *Advanced Functional Materials* **2020**, *30*, 1910777.
- 4020 (408) Francis, C. F.; Kyratzis, I. L.; Best, A. S. Lithium-Ion Battery Separators for Ionic-  
4021 Liquid Electrolytes: A Review. *Advanced Materials* **2020**, *32*, 1904205.
- 4022 (409) Xiong, S.; Regula, M.; Wang, D.; Song, J. Toward better lithium–sulfur batteries:  
4023 functional non-aqueous liquid electrolytes. *Electrochemical Energy Reviews* **2018**, *1*,  
4024 388–402.
- 4025 (410) Culver, S. P.; Koerver, R.; Krauskopf, T.; Zeier, W. G. Designing Ionic Conductors:  
4026 The Interplay between Structural Phenomena and Interfaces in Thiophosphate-Based  
4027 Solid-State Batteries. *Chemistry of Materials* **2018**, *30*, 4179–4192.

- 4028 (411) Famprakis, T.; Canepa, P.; Dawson, J. A.; Islam, M. S.; Masquelier, C. Fundamentals  
4029 of inorganic solid-state electrolytes for batteries. *Nature Materials* **2019**, *18*, 1278–  
4030 1291.
- 4031 (412) Goodenough, J. B.; Park, K.-S. The Li-Ion Rechargeable Battery: A Perspective.  
4032 *Journal of the American Chemical Society* **2013**, *135*, 1167–1176.
- 4033 (413) Dirican, M.; Yan, C.; Zhu, P.; Zhang, X. Composite solid electrolytes for all-solid-state  
4034 lithium batteries. *Materials Science and Engineering: R: Reports* **2019**, *136*, 27 – 46.
- 4035 (414) Han, L.; Lehmann, M. L.; Zhu, J.; Liu, T.; Zhou, Z.; Tang, X.; Heish, C.-T.;  
4036 Sokolov, A. P.; Cao, P.; Chen, X. C., et al. Recent Developments and Challenges  
4037 in Hybrid Solid Electrolytes for Lithium-Ion Batteries. *Frontiers in Energy Research*  
4038 **2020**, *8*, 202.
- 4039 (415) Manthiram, A.; Yu, X.; Wang, S. Lithium battery chemistries enabled by solid-state  
4040 electrolytes. *Nature Reviews Materials* **2017**, *2*, 1–16.
- 4041 (416) Faraday, M. IV. Experimental researches in electricity.–Third series. *Philosophical*  
4042 *Transactions of the Royal Society of London* **1833**, *123*, 23–54.
- 4043 (417) Armand, M.; Tarascon, J.-M. Building better batteries. *Nature* **2008**, *451*, 652–657.
- 4044 (418) Sudworth, J. The sodium/nickel chloride (ZEBRA) battery. *Journal of Power Sources*  
4045 **2001**, *100*, 149 – 163.
- 4046 (419) Oshima, T.; Kajita, M.; Okuno, A. Development of sodium-sulfur batteries. *Interna-*  
4047 *tional Journal of Applied Ceramic Technology* **2004**, *1*, 269–276.
- 4048 (420) Capasso, C.; Veneri, O. Experimental analysis of a zebra battery based propulsion  
4049 system for urban bus under dynamic conditions. *Energy Procedia* **2014**, *61*, 1138–  
4050 1141.



- 4051 (421) Dudney, N.; Bates, J.; Zuhr, R.; Luck, C.; Robertson, J. Sputtering of lithium com-  
4052 pounds for preparation of electrolyte thin films. *solid state ionics* **1992**, *53*, 655–661.
- 4053 (422) Bates, J.; Dudney, N.; Gruzalski, G.; Zuhr, R.; Choudhury, A.; Luck, C.; Robertson, J.  
4054 Electrical properties of amorphous lithium electrolyte thin films. *Solid state ionics*  
4055 **1992**, *53*, 647–654.
- 4056 (423) Inaguma, Y.; Liqun, C.; Itoh, M.; Nakamura, T.; Uchida, T.; Ikuta, H.; Wakihara, M.  
4057 High ionic conductivity in lithium lanthanum titanate. *Solid State Communications*  
4058 **1993**, *86*, 689–693.
- 4059 (424) Kasper, H. Series of rare earth garnets  $\text{Ln}_3^{3+}\text{M}_2\text{Li}_3^+\text{O}_{12}$  (M= Te, W). *Inorganic Chem-*  
4060 *istry* **1969**, *8*, 1000–1002.
- 4061 (425) Mazza, D. Remarks on a ternary phase in the  $\text{La}_2\text{O}_3\text{---}\text{Me}_2\text{O}_5\text{---}\text{Li}_2\text{O}$  system (Me= Nb,  
4062 Ta). *Materials Letters* **1988**, *7*, 205–207.
- 4063 (426) Kennedy, J. H.; Sahami, S.; Shea, S. W.; Zhang, Z. Preparation and conductivity  
4064 measurements of  $\text{SiS}_2\text{---}\text{Li}_2\text{S}$  glasses doped with LiBr and LiCl. *Solid State Ionics* **1986**,  
4065 *18*, 368–371.
- 4066 (427) Ivanov-Shits, A.; Sigaryov, S. Ionic conductivity in LISICON-type materials. *Solid*  
4067 *state ionics* **1988**, *27*, 89–100.
- 4068 (428) Lang, B.; Ziebarth, B.; Elsässer, C. Lithium ion conduction in  $\text{LiTi}_2(\text{PO}_4)_3$  and related  
4069 compounds based on the NASICON structure: a first-principles study. *Chemistry of*  
4070 *Materials* **2015**, *27*, 5040–5048.
- 4071 (429) De Klerk, N. J.; Rosłoń, I.; Wagemaker, M. Diffusion mechanism of Li argyrodite  
4072 solid electrolytes for Li-ion batteries and prediction of optimized halogen doping: the  
4073 effect of Li vacancies, halogens, and halogen disorder. *Chemistry of Materials* **2016**,  
4074 *28*, 7955–7963.

- 4075 (430) Dawson, J. A.; Attari, T. S.; Chen, H.; Emge, S. P.; Johnston, K. E.; Islam, M. S. Elu-  
4076 cidating lithium-ion and proton dynamics in anti-perovskite solid electrolytes. *Energy*  
4077 & *Environmental Science* **2018**, *11*, 2993–3002.
- 4078 (431) Ahiavi, E.; Dawson, J. A.; Kudu, U.; Courty, M.; Islam, M. S.; Clemens, O.; Masque-  
4079 lier, C.; Famprikis, T. Mechanochemical synthesis and ion transport properties of  
4080 Na<sub>3</sub>OX (X= Cl, Br, I and BH<sub>4</sub>) antiperovskite solid electrolytes. *Journal of Power*  
4081 *Sources* **2020**, *471*, 228489.
- 4082 (432) Fenton, D. Complexes of alkali metal ions with poly (ethylene oxide). *Polymer* **1973**,  
4083 *14*, 589.
- 4084 (433) Abraham, K.; Alamgir, M. Li<sup>+</sup>-conductive solid polymer electrolytes with liquid-like  
4085 conductivity. *J. Electrochem. Soc* **1990**, *137*, 1657.
- 4086 (434) Dautzenberg, G.; Croce, F.; Passerini, S.; Scrosati, B. Characterization of PAN-based  
4087 gel electrolytes. electrochemical stability and lithium cyclability. *Chemistry of mate-*  
4088 *rials* **1994**, *6*, 538–542.
- 4089 (435) Arcella, V.; Sanguineti, A.; Quartarone, E.; Mustarelli, P. Vinylidene fluoride–  
4090 hexafluoropropylene copolymers as hybrid electrolyte components for lithium batter-  
4091 ies. *Journal of power sources* **1999**, *81*, 790–794.
- 4092 (436) Kataoka, H.; Saito, Y.; Sakai, T.; Quartarone, E.; Mustarelli, P. Conduction mecha-  
4093 nisms of PVDF-type gel polymer electrolytes of lithium prepared by a phase inversion  
4094 process. *The Journal of Physical Chemistry B* **2000**, *104*, 11460–11464.
- 4095 (437) Li, W.; Zhu, Z.; Shen, W.; Tang, J.; Yang, G.; Xu, Z. A novel PVdF-based composite  
4096 gel polymer electrolyte doped with ionomer modified graphene oxide. *RSC Advances*  
4097 **2016**, *6*, 97338–97345.

- 4098 (438) Appetecchi, G.; Croce, F.; Scrosati, B. Kinetics and stability of the lithium electrode  
4099 in poly (methacrylate)-based gel electrolytes. *Electrochimica Acta* **1995**, *40*,  
4100 991–997.
- 4101 (439) Bohnke, O.; Frand, G.; Rezrazi, M.; Rousselot, C.; Truche, C. Fast ion transport in  
4102 new lithium electrolytes gelled with PMMA. 1. Influence of polymer concentration.  
4103 *Solid State Ionics* **1993**, *66*, 97–104.
- 4104 (440) Abbrent, S.; Plestil, J.; Hlavata, D.; Lindgren, J.; Tegenfeldt, J.; Wendsjö, Å. Crys-  
4105 tallinity and morphology of PVdF–HFP-based gel electrolytes. *Polymer* **2001**, *42*,  
4106 1407–1416.
- 4107 (441) Park, M.-S.; Hyun, S.-H.; Nam, S.-C.; Cho, S. B. Performance evaluation of printed  
4108 LiCoO<sub>2</sub> cathodes with PVDF-HFP gel electrolyte for lithium ion microbatteries. *Elec-  
4109 trochimica Acta* **2008**, *53*, 5523–5527.
- 4110 (442) Yang, C.-C.; Lian, Z.-Y.; Lin, S.; Shih, J.-Y.; Chen, W.-H. Preparation and application  
4111 of PVDF-HFP composite polymer electrolytes in LiNi<sub>0.5</sub>Co<sub>0.2</sub>Mn<sub>0.3</sub>O<sub>2</sub> lithium-polymer  
4112 batteries. *Electrochimica Acta* **2014**, *134*, 258–265.
- 4113 (443) Zhou, W.; Wang, S.; Li, Y.; Xin, S.; Manthiram, A.; Goodenough, J. B. Plating a  
4114 dendrite-free lithium anode with a polymer/ceramic/polymer sandwich electrolyte.  
4115 *Journal of the American Chemical Society* **2016**, *138*, 9385–9388.
- 4116 (444) Zhang, T.; He, W.; Zhang, W.; Wang, T.; Li, P.; Sun, Z.; Yu, X. Designing composite  
4117 solid-state electrolytes for high performance lithium ion or lithium metal batteries.  
4118 *Chem. Sci.* **2020**, *11*, 8686–8707.
- 4119 (445) Uvarov, N. Composite solid electrolytes: recent advances and design strategies. *Jour-  
4120 nal of Solid State Electrochemistry* **2011**, *15*, 367–389.

- 4121 (446) Wilkening, M.; Indris, S.; Heitjans, P. Heterogeneous lithium diffusion in nanocrys-  
4122 talline  $\text{Li}_2\text{O}:\text{Al}_2\text{O}_3$  composites. *Phys. Chem. Chem. Phys.* **2003**, *5*, 2225–2231.
- 4123 (447) Heitjans, P.; Indris, S. Diffusion and ionic conduction in nanocrystalline ceramics.  
4124 *Journal of Physics: Condensed Matter* **2003**, *15*, R1257–R1289.
- 4125 (448) Indris, S.; Heitjans, P.; Roman, H. E.; Bunde, A. Nanocrystalline versus Microcrys-  
4126 talline  $\text{Li}_2\text{O}:\text{B}_2\text{O}_3$  Composites: Anomalous Ionic Conductivities and Percolation The-  
4127 ory. *Phys. Rev. Lett.* **2000**, *84*, 2889–2892.
- 4128 (449) Indris, S.; Heitjans, P. Heterogeneous  $^7\text{Li}$  NMR relaxation in nanocrystalline  
4129  $\text{Li}_2\text{O}:\text{B}_2\text{O}_3$  composites. *Journal of Non-Crystalline Solids* **2002**, *307-310*, 555 – 564.
- 4130 (450) Blanchard, D.; Nale, A.; Sveinbjörnsson, D.; Eggenhuisen, T. M.; Verkuijlen, M. H.;  
4131 Vegge, T.; Kentgens, A. P.; de Jongh, P. E. Nanoconfined  $\text{LiBH}_4$  as a fast lithium ion  
4132 conductor. *Advanced Functional Materials* **2015**, *25*, 184–192.
- 4133 (451) Liang, C. Conduction characteristics of the lithium iodide-aluminum oxide solid elec-  
4134 trolytes. *Journal of the Electrochemical Society* **1973**, *120*, 1289.
- 4135 (452) Phipps, J.; Whitmore, D. Ion transport in  $\text{LiSiO}_2$  composites. *Solid State Ionics*  
4136 **1983**, *9*, 123–130.
- 4137 (453) Uvarov, N.; Isupov, V.; Sharma, V.; Shukla, A. Effect of morphology and particle size  
4138 on the ionic conductivities of composite solid electrolytes. *Solid State Ionics* **1992**, *51*,  
4139 41–52.
- 4140 (454) Pradel, A.; Ribes, M. Electrical properties of lithium conductive silicon sulfide glasses  
4141 prepared by twin roller quenching. *Solid State Ionics* **1986**, *18*, 351–355.
- 4142 (455) Kanno, R. Synthesis of a new lithium ionic conductor, thio-LISICON–lithium germa-  
4143 nium sulfide system. *Solid State Ionics* **2000**, *130*, 97–104.

- 4144 (456) Murayama, M. Synthesis of New Lithium Ionic Conductor Thio-LISICON—Lithium  
4145 Silicon Sulfides System. *Journal of Solid State Chemistry* **2002**, *168*, 140–148.
- 4146 (457) Murayama, M.; Sonoyama, N.; Yamada, A.; Kanno, R. Material design of new lithium  
4147 ionic conductor, thio-LISICON, in the  $\text{Li}_2\text{S}-\text{P}_2\text{S}_5$  system. *Solid State Ionics* **2004**, *170*,  
4148 173–180.
- 4149 (458) Minafra, N.; Culver, S. P.; Li, C.; Senyshyn, A.; Zeier, W. G. Influence of the  
4150 Lithium Substructure on the Diffusion Pathways and Transport Properties of the  
4151 Thio-LISICON  $\text{Li}_4\text{Ge}_{1-x}\text{Sn}_x\text{S}_4$ . *Chemistry of Materials* **2019**, *31*, 3794–3802.
- 4152 (459) Bron, P.; Johansson, S.; Zick, K.; Schmedt auf der Günne, J.; Dehnen, S.; Roling, B.  
4153  $\text{Li}_{10}\text{SnP}_2\text{S}_{12}$ : An Affordable Lithium Superionic Conductor. *Journal of the American*  
4154 *Chemical Society* **2013**, *135*, 15694–15697.
- 4155 (460) Whiteley, J. M.; Woo, J. H.; Hu, E.; Nam, K.-W.; Lee, S.-H. Empowering the Lithium  
4156 Metal Battery through a Silicon-Based Superionic Conductor. *Journal of The Elec-*  
4157 *trochemical Society* **2014**, *161*, A1812–A1817.
- 4158 (461) Huang, W.; Yoshino, K.; Hori, S.; Suzuki, K.; Yonemura, M.; Hirayama, M.; Kanno, R.  
4159 Superionic lithium conductor with a cubic argyrodite-type structure in the Li–Al–Si–S  
4160 system. *Journal of Solid State Chemistry* **2019**, *270*, 487–492.
- 4161 (462) Yamane, H.; Shibata, M.; Shimane, Y.; Junke, T.; Seino, Y.; Adams, S.; Minami, K.;  
4162 Hayashi, A.; Tatsumisago, M. Crystal structure of a superionic conductor,  $\text{Li}_7\text{P}_3\text{S}_{11}$ .  
4163 *Solid State Ionics* **2007**, *178*, 1163–1167.
- 4164 (463) Homma, K.; Yonemura, M.; Kobayashi, T.; Nagao, M.; Hirayama, M.; Kanno, R.  
4165 Crystal structure and phase transitions of the lithium ionic conductor  $\text{Li}_3\text{PS}_4$ . *Solid*  
4166 *State Ionics* **2011**, *182*, 53–58.

- 4167 (464) Minami, T.; Hayashi, A.; Tatsumisago, M. Recent progress of glass and glass-ceramics  
4168 as solid electrolytes for lithium secondary batteries. *Solid State Ionics* **2006**, *177*,  
4169 2715–2720.
- 4170 (465) Bai, X.; Duan, Y.; Zhuang, W.; Yang, R.; Wang, J. Research progress in Li-argyrodite-  
4171 based solid-state electrolytes. *Journal of Materials Chemistry A* **2020**, *8*, 25663–25686.
- 4172 (466) Minafra, N.; Hogrefe, K.; Barbon, F.; Helm, B.; Li, C.; Wilkening, H. M. R.;  
4173 Zeier, W. G. Two-Dimensional Substitution: Toward a Better Understanding of the  
4174 Structure–Transport Correlations in the Li-Superionic Thio-LISICONs. *Chemistry of*  
4175 *Materials* **2021**, *33*, 727–740.
- 4176 (467) Bhandari, A.; Bhattacharya, J. Origin of Fast Ion Conduction in  $Li_{10}GeP_2S_{12}$ , a  
4177 Superionic Conductor. *Journal of Physical Chemistry C* **2016**, *120*.
- 4178 (468) Mo, Y.; Ong, S. P.; Ceder, G. First Principles Study of the  $Li_{10}GeP_2S_{12}$  Lithium Super  
4179 Ionic Conductor Material. *Chemistry of Materials* **2012**, *24*, 15–17.
- 4180 (469) Kraft, M. A.; Ohno, S.; Zinkevich, T.; Koerver, R.; Culver, S. P.; Fuchs, T.;  
4181 Senyshyn, A.; Indris, S.; Morgan, B. J.; Zeier, W. G. Inducing High Ionic Conductivity  
4182 in the Lithium Superionic Argyrodites  $Li_{6+x}P_{1-x}Ge_xS_5I$  for All-Solid-State Batteries.  
4183 *Journal of the American Chemical Society* **2018**, *140*, 16330–16339.
- 4184 (470) Deiseroth, H.-J.; Kong, S.-T.; Eckert, H.; Vannahme, J.; Reiner, C.; Zaiß, T.;  
4185 Schlosser, M.  $Li_6PS_5X$ : A Class of Crystalline Li-Rich Solids With an Unusually High  
4186  $Li^+$  Mobility. *Angewandte Chemie International Edition* **2008**, *47*, 755–758.
- 4187 (471) Kraft, M. A.; Culver, S. P.; Calderon, M.; Böcher, F.; Krauskopf, T.; Senyshyn, A.;  
4188 Dietrich, C.; Zevalkink, A.; Janek, J.; Zeier, W. G. Influence of lattice polarizability  
4189 on the ionic conductivity in the lithium superionic argyrodites  $Li_6PS_5X$  ( $X = Cl, Br,$   
4190  $I$ ). *Journal of the American Chemical Society* **2017**, *139*, 10909–10918.

- 4191 (472) Minafra, N.; Culver, S. P.; Krauskopf, T.; Senyshyn, A.; Zeier, W. G. Effect of Si  
4192 substitution on the structural and transport properties of superionic Li-argyrodites.  
4193 *Journal of Materials Chemistry A* **2018**, *6*, 645–651.
- 4194 (473) Adeli, P.; Bazak, J. D.; Park, K. H.; Kochetkov, I.; Huq, A.; Goward, G. R.;  
4195 Nazar, L. F. Boosting solid-state diffusivity and conductivity in lithium superionic  
4196 argyrodites by halide substitution. *Angewandte Chemie International Edition* **2019**,  
4197 *58*, 8681–8686.
- 4198 (474) Kuhn, A.; Duppel, V.; Lotsch, B. V. Tetragonal  $\text{Li}_{10}\text{GeP}_2\text{S}_{12}$  – exploring the Li ion  
4199 dynamics in LGPS Li electrolytes. *Energy Environ. Sci.* **2013**, *6*, 3548–3552.
- 4200 (475) Xu, M.; Ding, J.; Ma, E. One-dimensional stringlike cooperative migration of lithium  
4201 ions in an ultrafast ionic conductor. *Applied Physics Letters* **2012**, *101*, 031901.
- 4202 (476) Adams, S.; Prasada Rao, R. Structural requirements for fast lithium ion migration in  
4203  $\text{Li}_{10}\text{GeP}_2\text{S}_{12}$ . *Journal of Materials Chemistry* **2012**, *22*, 7687.
- 4204 (477) Kuhn, A.; Köhler, J.; Lotsch, B. V. Single-crystal X-ray structure analysis of the  
4205 superionic conductor  $\text{Li}_{10}\text{GeP}_2\text{S}_{12}$ . *Phys. Chem. Chem. Phys.* **2013**, *15*, 11620–2.
- 4206 (478) Zhou, L.; Minafra, N.; Zeier, W. G.; Nazar, L. F. Innovative Approaches to Li-  
4207 Argyrodite Solid Electrolytes for All-Solid-State Lithium Batteries. *Accounts of Chem-  
4208 ical Research* **2021**, 19002–19013.
- 4209 (479) Bachman, J. C.; Muy, S.; Grimaud, A.; Chang, H.-H.; Pour, N.; Lux, S. F.;  
4210 Paschos, O.; Maglia, F.; Lupart, S.; Lamp, P., et al. Inorganic solid-state electrolytes  
4211 for lithium batteries: mechanisms and properties governing ion conduction. *Chemical  
4212 reviews* **2016**, *116*, 140–162.
- 4213 (480) Kuhs, W.; Nitsche, R.; Scheunemann, K. The argyrodites– A new family of tetrahe-  
4214 drally close-packed structures. *Materials Research Bulletin* **1979**, *14*, 241–248.

- 4215 (481) Ohno, S.; Helm, B.; Fuchs, T.; Dewald, G.; Kraft, M. A.; Culver, S. P.; Senyshyn, A.;  
4216 Zeier, W. G. Further Evidence for Energy Landscape Flattening in the Superionic  
4217 Argyrodites  $\text{Li}_{6+x}\text{P}_{1-x}\text{M}_x\text{S}_5\text{I}$  (M= Si, Ge, Sn). *Chemistry of Materials* **2019**, *31*, 4936–  
4218 4944.
- 4219 (482) Gautam, A.; Sadowski, M.; Ghidui, M.; Minafra, N.; Senyshyn, A.; Albe, K.;  
4220 Zeier, W. G. Engineering the Site-Disorder and Lithium Distribution in the Lithium  
4221 Superionic Argyrodite  $\text{Li}_6\text{PS}_5\text{Br}$ . *Advanced Energy Materials* *11*, 2003369.
- 4222 (483) Minafra, N.; Kraft, M.; Bernges, T.; Li, C.; Schlem, R.; Morgan, B.; Zeier, W. On the  
4223 Local Charge Inhomogeneity and Lithium Distribution in the Superionic Argyrodites  
4224  $\text{Li}_6\text{PS}_5\text{X}$  (X = Cl, Br, I). **2020**,
- 4225 (484) Morgan, B. Mechanistic Origin of Superionic Lithium Diffusion in Anion-Disordered  
4226  $\text{Li}_6\text{PS}_5\text{X}$  Argyrodites. *Chemistry of Materials* **2020**,
- 4227 (485) Deng, Z.; Zhu, Z.; Chu, I.-H.; Ong, S. P. Data-Driven First-Principles Methods for  
4228 the Study and Design of Alkali Superionic Conductors. *Chemistry of Materials* **2017**,  
4229 *29*, 281–288.
- 4230 (486) Yu, C. et al. Superionic conductivity in lithium argyrodite solid-state electrolyte by  
4231 controlled Cl-doping. *Nano Energy* **2020**, *69*, 104396.
- 4232 (487) Feng, X.; Chien, P.-H.; Wang, Y.; Patel, S.; Wang, P.; Liu, H.; Immediato-Scuotto, M.;  
4233 Hu, Y.-Y. Enhanced ion conduction by enforcing structural disorder in Li-deficient  
4234 argyrodites  $\text{Li}_{6-x}\text{PS}_{5-x}\text{Cl}_{1+x}$ . *Energy Storage Materials* **2020**, *30*, 67 – 73.
- 4235 (488) Yu, C.; Hageman, J.; Ganapathy, S.; van Eijck, L.; Zhang, L.; Adair, K. R.; Sun, X.;  
4236 Wagemaker, M. Tailoring  $\text{Li}_6\text{PS}_5\text{Br}$  ionic conductivity and understanding of its role  
4237 in cathode mixtures for high performance all-solid-state Li-S batteries. *Journal of*  
4238 *Materials Chemistry A* **2019**, *7*, 10412–10421.



- 4239 (489) Zhou, L.; Park, K.-H.; Sun, X.; Lalère, F.; Adermann, T.; Hartmann, P.; Nazar, L. F.  
4240 Solvent-Engineered Design of Argyrodite  $\text{Li}_6\text{PS}_5\text{X}$  ( $X = \text{Cl}, \text{Br}, \text{I}$ ) Solid Electrolytes  
4241 with High Ionic Conductivity. *ACS Energy Letters* **2019**, *4*, 265–270.
- 4242 (490) Murugan, R.; Thangadurai, V.; Weppner, W. Fast lithium ion conduction in garnet-  
4243 type  $\text{Li}_7\text{La}_3\text{Zr}_2\text{O}_{12}$ . *Angewandte Chemie - International Edition* **2007**, *46*, 7778–7781.
- 4244 (491) Ni, J. E.; Case, E. D.; Sakamoto, J. S.; Rangasamy, E.; Wolfenstine, J. B. Room  
4245 temperature elastic moduli and Vickers hardness of hot-pressed LLZO cubic garnet.  
4246 *Journal of Materials Science* **2012**, *47*, 7978–7985.
- 4247 (492) Zhu, Y.; He, X.; Mo, Y. First principles study on electrochemical and chemical stability  
4248 of solid electrolyte-electrode interfaces in all-solid-state Li-ion batteries. *Journal of*  
4249 *Materials Chemistry A* **2016**, *4*, 3253–3266.
- 4250 (493) Binninger, T.; Marcolongo, A.; Mottet, M.; Weber, V.; Laino, T. Comparison of com-  
4251 putational methods for the electrochemical stability window of solid-state electrolyte  
4252 materials. *Journal of Materials Chemistry A* **2020**, *8*, 1347–1359.
- 4253 (494) Geiger, C. A.; Alekseev, E.; Lazic, B.; Fisch, M.; Armbruster, T.; Langner, R.;  
4254 Fechtelkord, M.; Kim, N.; Pettke, T.; Weppner, W. Crystal chemistry and stability of  
4255 “ $\text{Li}_7\text{La}_3\text{Zr}_2\text{O}_{12}$ ” garnet: A fast lithium-ion conductor. *Inorganic Chemistry* **2011**, *50*,  
4256 1089–1097.
- 4257 (495) Rangasamy, E.; Wolfenstine, J.; Sakamoto, J. The role of Al and Li concentration on  
4258 the formation of cubic garnet solid electrolyte of nominal composition  $\text{Li}_7\text{La}_3\text{Zr}_2\text{O}_{12}$ .  
4259 *Solid State Ionics* **2012**, *206*, 28–32.
- 4260 (496) Ren, Y.; Shen, Y.; Lin, Y.; Nan, C. W. Direct observation of lithium dendrites inside  
4261 garnet-type lithium-ion solid electrolyte. *Electrochemistry Communications* **2015**, *57*,  
4262 27–30.

- 4263 (497) Sudo, R.; Nakata, Y.; Ishiguro, K.; Matsui, M.; Hirano, A.; Takeda, Y.; Yamamoto, O.;  
4264 Imanishi, N. Interface behavior between garnet-type lithium-conducting solid elec-  
4265 trolyte and lithium metal. *Solid State Ionics* **2014**, *262*, 151–154.
- 4266 (498) Cheng, E. J.; Sharafi, A.; Sakamoto, J. Intergranular Li metal propagation through  
4267 polycrystalline  $\text{Li}_{6.25}\text{Al}_{0.25}\text{La}_3\text{Zr}_2\text{O}_{12}$  ceramic electrolyte. *Electrochimica Acta* **2017**,  
4268 *223*, 85–91.
- 4269 (499) Kim, S.; Jung, C.; Kim, H.; Thomas-Alyea, K. E.; Yoon, G.; Kim, B.; Badding, M. E.;  
4270 Song, Z.; Chang, J. M.; Kim, J.; Im, D.; Kang, K. The Role of Interlayer Chemistry in  
4271 Li-Metal Growth through a Garnet-Type Solid Electrolyte. *Advanced Energy Materials*  
4272 **2020**, *10*, 1903993.
- 4273 (500) Canepa, P.; Dawson, J. A.; Sai Gautam, G.; Statham, J. M.; Parker, S. C.; Islam, M. S.  
4274 Particle Morphology and Lithium Segregation to Surfaces of the  $\text{Li}_7\text{La}_3\text{Zr}_2\text{O}_{12}$  Solid  
4275 Electrolyte. *Chemistry of Materials* **2018**, *30*, 3019–3027.
- 4276 (501) Tian, H. K.; Xu, B.; Qi, Y. Computational study of lithium nucleation tendency in  
4277  $\text{Li}_7\text{La}_3\text{Zr}_2\text{O}_{12}$  (LLZO) and rational design of interlayer materials to prevent lithium  
4278 dendrites. *Journal of Power Sources* **2018**, *392*, 79–86.
- 4279 (502) Gao, B.; Jalem, R.; Tateyama, Y. Surface-Dependent Stability of the Interface between  
4280 Garnet  $\text{Li}_7\text{La}_3\text{Zr}_2\text{O}_{12}$  and the Li Metal in the All-Solid-State Battery from First-  
4281 Principles Calculations. *ACS Applied Materials & Interfaces* **2020**, *12*, 16350–16358.
- 4282 (503) Ma, C.; Cheng, Y.; Yin, K.; Luo, J.; Sharafi, A.; Sakamoto, J.; Li, J.; More, K. L.;  
4283 Dudney, N. J.; Chi, M. Interfacial Stability of Li Metal–Solid Electrolyte Elucidated  
4284 via in Situ Electron Microscopy. *Nano Letters* **2016**, *16*, 7030–7036.
- 4285 (504) Rettenwander, D.; Wagner, R.; Reyer, A.; Bonta, M.; Cheng, L.; Doeff, M. M.;  
4286 Limbeck, A.; Wilkening, M.; Amthauer, G. Interface instability of fe-stabilized  
4287  $\text{Li}_7\text{La}_3\text{Zr}_2\text{O}_{12}$  versus li metal. *Journal of Physical Chemistry C* **2018**, *122*, 3780–3785.

- 4288 (505) Shen, F.; Dixit, M. B.; Xiao, X.; Hatzell, K. B. Effect of Pore Connectivity on Li  
4289 Dendrite Propagation within LLZO Electrolytes Observed with Synchrotron X-ray  
4290 Tomography. *ACS Energy Letters* **2018**, *3*, 1056–1061.
- 4291 (506) Aguesse, F.; Manalastas, W.; Buannic, L.; Del Amo, J. M. L.; Singh, G.; Llordés, A.;  
4292 Kilner, J. Investigating the dendritic growth during full cell cycling of garnet elec-  
4293 trolyte in direct contact with Li metal. *ACS Applied Materials and Interfaces* **2017**,  
4294 *9*, 3808–3816.
- 4295 (507) Krauskopf, T.; Hartmann, H.; Zeier, W. G.; Janek, J. Toward a Fundamental Un-  
4296 derstanding of the Lithium Metal Anode in Solid-State Batteries - An Electrochemo-  
4297 Mechanical Study on the Garnet-Type Solid Electrolyte  $\text{Li}_{6.25}\text{Al}_{0.25}\text{La}_3\text{Zr}_2\text{O}_{12}$ . *ACS*  
4298 *Applied Materials and Interfaces* **2019**, *11*, 14463–14477.
- 4299 (508) Zhu, Y.; Connell, J. G.; Tepavcevic, S.; Zapol, P.; Garcia-Mendez, R.; Tay-  
4300 lor, N. J.; Sakamoto, J.; Ingram, B. J.; Curtiss, L. A.; Freeland, J. W.; Fong, D. D.;  
4301 Markovic, N. M. Dopant-Dependent Stability of Garnet Solid Electrolyte Interfaces  
4302 with Lithium Metal. *Advanced Energy Materials* **2019**, *9*, 1–11.
- 4303 (509) Tsai, C.-L.; Roddatis, V.; Chandran, C. V.; Ma, Q.; Uhlenbruck, S.; Bram, M.; Heit-  
4304 jans, P.; Guillon, O.  $\text{Li}_7\text{La}_3\text{Zr}_2\text{O}_{12}$  Interface Modification for Li Dendrite Prevention.  
4305 *ACS Applied Materials & Interfaces* **2016**, *8*, 10617–10626.
- 4306 (510) Thompson, T.; Yu, S.; Williams, L.; Schmidt, R. D.; Garcia-Mendez, R.; Wolfen-  
4307 stine, J.; Allen, J. L.; Kioupakis, E.; Siegel, D. J.; Sakamoto, J. Electrochemical  
4308 Window of the Li-Ion Solid Electrolyte  $\text{Li}_7\text{La}_3\text{Zr}_2\text{O}_{12}$ . *ACS Energy Letters* **2017**, *2*,  
4309 462–468.
- 4310 (511) Yu, S.; Schmidt, R. D.; Garcia-Mendez, R.; Herbert, E.; Dudney, N. J.; Wolfen-  
4311 stine, J. B.; Sakamoto, J.; Siegel, D. J. Elastic Properties of the Solid Electrolyte  
4312  $\text{Li}_7\text{La}_3\text{Zr}_2\text{O}_{12}$  (LLZO). *Chemistry of Materials* **2016**, *28*, 197–206.

- 4313 (512) Wang, Y.; Lv, J.; Zhu, L.; Ma, Y. CALYPSO: A method for crystal structure predic-  
4314 tion. *Computer Physics Communications* **2012**, *183*, 2063–2070.
- 4315 (513) Gao, B.; Gao, P.; Lu, S.; Lv, J.; Wang, Y.; Ma, Y. Interface structure prediction via  
4316 CALYPSO method. *Science Bulletin* **2019**, *64*, 301–309.
- 4317 (514) Han, F.; Westover, A. S.; Yue, J.; Fan, X.; Wang, F.; Chi, M.; Leonard, D. N.;  
4318 Dudney, N. J.; Wang, H.; Wang, C. High electronic conductivity as the origin of  
4319 lithium dendrite formation within solid electrolytes. *Nature Energy* **2019**, *4*, 187–196.
- 4320 (515) Squires, A.; Davies, D.; Kim, S.; Scanlon, D.; Walsh, A.; Morgan, B. Low Electronic  
4321 Conductivity of  $\text{Li}_7\text{La}_3\text{Zr}_2\text{O}_{12}$  (LLZO) Solid Electrolytes from First Principles. **2020**,
- 4322 (516) Xu, M.; Park, M. S.; Lee, J. M.; Kim, T. Y.; Park, Y. S.; Ma, E. Mechanisms of  $\text{Li}^+$   
4323 transport in garnet-type cubic  $\text{Li}_{3+x}\text{La}_3\text{M}_2\text{O}_{12}$  ( $M = \text{Te}, \text{Nb}, \text{Zr}$ ). *Physical Review B*  
4324 **2012**, *85*, 052301.
- 4325 (517) Burbano, M.; Carlier, D.; Boucher, F.; Morgan, B. J.; Salanne, M. Sparse Cyclic Exci-  
4326 tations Explain the Low Ionic Conductivity of Stoichiometric  $\text{Li}_7\text{La}_3\text{Zr}_2\text{O}_{12}$ . *Physical*  
4327 *Review Letters* **2016**, *116*, 1–6.
- 4328 (518) Meier, K.; Laino, T.; Curioni, A. Solid-state electrolytes: Revealing the mechanisms  
4329 of Li-Ion conduction in tetragonal and cubic LLZO by first-principles calculations.  
4330 *Journal of Physical Chemistry C* **2014**, *118*, 6668–6679.
- 4331 (519) Jalem, R.; Yamamoto, Y.; Shiiba, H.; Nakayama, M.; Munakata, H.; Kasuga, T.;  
4332 Kanamura, K. Concerted migration mechanism in the Li ion dynamics of garnet-type  
4333  $\text{Li}_7\text{La}_3\text{Zr}_2\text{O}_{12}$ . *Chemistry of Materials* **2013**, *25*, 425–430.
- 4334 (520) Rettenwander, D.; Blaha, P.; Laskowski, R.; Schwarz, K.; Bottke, P.; Wilkening, M.;  
4335 Geiger, C. A.; Amthauer, G. DFT study of the role of  $\text{Al}^{3+}$  in the fast ion-conductor  
4336  $\text{Li}_{7-3x}\text{Al}_{3+x}\text{La}_3\text{Zr}_2\text{O}_{12}$  garnet. *Chemistry of Materials* 2617–2623.

- 4337 (521) Rettenwander, D.; Redhammer, G.; Preishuber-Pflügl, F.; Cheng, L.; Miara, L.; Wag-  
4338 ner, R.; Welzl, A.; Suard, E.; Doeff, M. M.; Wilkening, M.; Fleig, J.; Amthauer, G.  
4339 Structural and Electrochemical Consequences of Al and Ga Cosubstitution in  
4340  $\text{Li}_7\text{La}_3\text{Zr}_2\text{O}_{12}$  Solid Electrolytes. *Chemistry of Materials* **2016**, *28*, 2384–2392.
- 4341 (522) Bonilla, M. R.; García Daza, F. A.; Carrasco, J.; Akhmatskaya, E. Exploring Li-ion  
4342 conductivity in cubic, tetragonal and mixed-phase Al-substituted  $\text{Li}_7\text{La}_3\text{Zr}_2\text{O}_{12}$  using  
4343 atomistic simulations and effective medium theory. *Acta Materialia* **2019**, *175*, 426–  
4344 435.
- 4345 (523) Islam, M. M.; Bredow, T.; Heitjans, P. The ionic conductivity in lithium-boron oxide  
4346 materials and its relation to structural, electronic and defect properties: insights from  
4347 theory. *Journal of Physics: Condensed Matter* **2012**, *24*, 203201.
- 4348 (524) Islam, M. M.; Bredow, T.; Indris, S.; Heitjans, P. Enhanced Conductivity at the  
4349 Interface of  $\text{Li}_2\text{O}:\text{B}_2\text{O}_3$  Nanocomposites: Atomistic Models. *Phys. Rev. Lett.* **2007**,  
4350 *99*, 145502.
- 4351 (525) Baggio, B. F.; Grunder, Y. In Situ X-Ray Techniques for Electrochemical Interfaces.  
4352 *Annual Review of Analytical Chemistry* **2021**, *14*, DOI: 10.1146/annurev-anchem-  
4353 091020-100631.
- 4354 (526) Claessen, R.; Sing, M.; Paul, M.; Berner, G.; Wetscherek, A.; Müller, A.; Drube, W.  
4355 Hard x-ray photoelectron spectroscopy of oxide hybrid and heterostructures: a new  
4356 method for the study of buried interfaces. *New Journal of Physics* **2009**, *11*, 125007.
- 4357 (527) Anomalous High Ionic Conductivity of Nanoporous  $\beta\text{-Li}_3\text{PS}_4$ . *Journal of the American*  
4358 *Chemical Society* **2013**, *135*, 975–978.
- 4359 (528) Han, F.; Gao, T.; Zhu, Y.; Gaskell, K. J.; Wang, C. A Battery Made from a Single  
4360 Material. *Advanced Materials* **2015**, *27*, 3473–3483.

- 4361 (529) Thangadurai, V.; Weppner, W.  $\text{Li}_6\text{A}\text{La}_2\text{Ta}_2\text{O}_{12}$  (A=Sr, Ba): Novel garnet-like oxides  
4362 for fast lithium ion conduction. *Advanced Functional Materials* **2005**, *15*, 107–112.
- 4363 (530) Kobayashi, T.; Yamada, A.; Kanno, R. Interfacial reactions at electrode/electrolyte  
4364 boundary in all solid-state lithium battery using inorganic solid electrolyte, thio-  
4365 LISICON. *Electrochimica Acta* **2008**, *53*, 5045–5050.
- 4366 (531) Takada, K.; Ohta, N.; Zhang, L.; Fukuda, K.; Sakaguchi, I.; Ma, R.; Osada, M.;  
4367 Sasaki, T. Interfacial modification for high-power solid-state lithium batteries. *Solid*  
4368 *State Ionics* 1333–1337.
- 4369 (532) Sakuda, A.; Hayashi, A.; Tatsumisago, M. Interfacial observation between  $\text{LiCoO}_2$   
4370 electrode and  $\text{Li}_2\text{S-P}_2\text{S}_5$  solid electrolytes of all-solid-state lithium secondary batteries  
4371 using transmission electron microscopy. *Chemistry of Materials* **2010**, *22*, 949–956.
- 4372 (533) Okuno, Y.; Haruyama, J.; Tateyama, Y. Comparative study on sulfide and oxide  
4373 electrolyte interfaces with cathodes in all-solid-state battery via first-principles calcu-  
4374 lations. *ACS Applied Energy Materials* **2020**, *3*, 11061–11072.
- 4375 (534) Sharafi, A.; Kazyak, E.; Davis, A. L.; Yu, S.; Thompson, T.; Siegel, D. J.; Das-  
4376 gupta, N. P.; Sakamoto, J. Surface Chemistry Mechanism of Ultra-Low Interfacial  
4377 Resistance in the Solid-State Electrolyte  $\text{Li}_7\text{La}_3\text{Zr}_2\text{O}_{12}$ . *Chemistry of Materials* **2017**,  
4378 *29*, 7961–7968.
- 4379 (535) Jiang, Z.; Han, Q.; Wang, S.; Wang, H. Reducing the Interfacial Resistance in  
4380 All-Solid-State Lithium Batteries Based on Oxide Ceramic Electrolytes. *ChemElec-*  
4381 *troChem* **2019**, *6*, 2970–2983.
- 4382 (536) Lepley, N. D.; Holzwarth, N. A. Modeling interfaces between solids: Application to  
4383 Li battery materials. *Physical Review B - Condensed Matter and Materials Physics*  
4384 **2015**, *92*, 1–15.

- 4385 (537) Zhang, Y. Q.; Tian, Y.; Xiao, Y.; Miara, L. J.; Aihara, Y.; Tsujimura, T.; Shi, T.;  
4386 Scott, M. C.; Ceder, G. Direct Visualization of the Interfacial Degradation of Cathode  
4387 Coatings in Solid State Batteries: A Combined Experimental and Computational  
4388 Study. *Advanced Energy Materials* **2020**, *10*.
- 4389 (538) Xiao, Y.; Miara, L. J.; Wang, Y.; Ceder, G. Computational Screening of Cathode  
4390 Coatings for Solid-State Batteries. *Joule* **2019**, *3*, 1252–1275.
- 4391 (539) Sang, J.; Yu, Y.; Wang, Z.; Shao, G. Theoretical formulation of  $\text{Li}_{3a+b}\text{N}_a\text{X}_b$  (X =  
4392 halogen) as a potential artificial solid electrolyte interphase (ASEI) to protect the Li  
4393 anode. *Physical Chemistry Chemical Physics* **2020**, *22*, 12918–12928.
- 4394 (540) Glass, C. W.; Oganov, A. R.; Hansen, N. USPEX-Evolutionary crystal structure pre-  
4395 diction. *Computer Physics Communications* **2006**, *175*, 713–720.
- 4396 (541) Oganov, A. R.; Glass, C. W. Crystal structure prediction using ab initio evolutionary  
4397 techniques: Principles and applications. *Journal of Chemical Physics* **2006**, *124*.
- 4398 (542) Parlinski, K.; Li, Z. Q.; Kawazoe, Y. First-principles determination of the soft mode  
4399 in cubic  $\text{ZrO}_2$ . *Physical Review Letters* **1997**, *78*, 4063–4066.
- 4400 (543) Togo, A.; Oba, F.; Tanaka, I. First-principles calculations of the ferroelastic transi-  
4401 tion between rutile-type and  $\text{CaCl}_2$ -type  $\text{SiO}_2$  at high pressures. *Physical Review B -*  
4402 *Condensed Matter and Materials Physics* **2008**, *78*, 1–9.
- 4403 (544) Hart, G. L.; Forcade, R. W. Algorithm for generating derivative structures. *Physical*  
4404 *Review B - Condensed Matter and Materials Physics* **2008**, *77*, 1–12.
- 4405 (545) Schnell, J.; Knörzer, H.; Imbsweiler, A. J.; Reinhart, G. Solid versus Liquid—A  
4406 Bottom-Up Calculation Model to Analyze the Manufacturing Cost of Future High-  
4407 Energy Batteries. *Energy Technology* **2020**, *8*, 1901237.

- 4408 (546) Kato, Y.; Hori, S.; Saito, T.; Suzuki, K.; Hirayama, M.; Mitsui, A.; Yonemura, M.;  
4409 Iba, H.; Kanno, R. High-power all-solid-state batteries using sulfide superionic con-  
4410 ductors. *Nature Energy* **2016**, *1*, 1–7.
- 4411 (547) Kim, K. J.; Balaish, M.; Wadaguchi, M.; Kong, L.; Rupp, J. L. Solid-State Li–Metal  
4412 Batteries: Challenges and Horizons of Oxide and Sulfide Solid Electrolytes and Their  
4413 Interfaces. *Advanced Energy Materials* **2021**, *11*, 2002689.
- 4414 (548) Albertus, P.; Babinec, S.; Litzelman, S.; Newman, A. Status and challenges in enabling  
4415 the lithium metal electrode for high-energy and low-cost rechargeable batteries. *Nature*  
4416 *Energy* **2018**, *3*, 16–21.
- 4417 (549) Rodney, D.; Ventelon, L.; Clouet, E.; Pizzagalli, L.; Willaime, F. Ab initio modeling  
4418 of dislocation core properties in metals and semiconductors. *Acta Materialia* **2017**,  
4419 *124*, 633–659.
- 4420 (550) Clouet, E. In *Handbook of Materials Modeling: Methods: Theory and Modeling*; An-  
4421 dreoni, W., Yip, S., Eds.; Springer International Publishing, 2020; pp 1503–1524.
- 4422 (551) Chen, H.; Liu, Q. Y.; Jing, M. X.; Chen, F.; Yuan, W. Y.; Ju, B. W.; Tu, F. Y.;  
4423 Shen, X. Q.; Qin, S. B. Improved Interface Stability and Room-Temperature Per-  
4424 formance of Solid-State Lithium Batteries by Integrating Cathode/Electrolyte and  
4425 Graphite Coating. *ACS Applied Materials and Interfaces* **2020**, *12*, 15120–15127.
- 4426 (552) Ito, Y.; Yamakawa, S.; Hayashi, A.; Tatsumisago, M. Effects of the microstructure  
4427 of solid-electrolyte-coated LiCoO<sub>2</sub> on its discharge properties in all-solid-state lithium  
4428 batteries. *Journal of Materials Chemistry A* **2017**, *5*, 10658–10668.
- 4429 (553) Yin, Y.; Jiang, C.-S.; Guthrey, H.; Xiao, C.; Seitzman, N.; Ban, C.; Al-Jassim, M.  
4430 Improved Stability and Cyclability of Ceramic Solid Electrolyte by Coating Polymer.  
4431 *Journal of The Electrochemical Society* **2020**, *167*, 020519.



- 4432 (554) Ji, X.; Hou, S.; Wang, P.; He, X.; Piao, N.; Chen, J.; Fan, X.; Wang, C. Solid-State  
4433 Electrolyte Design for Lithium Dendrite Suppression. *Advanced Materials* **2020**, *32*.
- 4434 (555) Li, H.; Lian, F.; Meng, N.; Xiong, C.; Wu, N.; Xu, B.; Li, Y. Constructing Elec-  
4435 tronic and Ionic Dual Conductive Polymeric Interface in the Cathode for High-Energy-  
4436 Density Solid-State Batteries. *Advanced Functional Materials* **2021**, *31*, 2008487.
- 4437 (556) Yi, J.; He, P.; Liu, H.; Ni, H.; Bai, Z.; Fan, L. Z. Manipulating interfacial stability  
4438 of  $\text{LiNi}_{0.5}\text{Co}_{0.3}\text{Mn}_{0.2}\text{O}_2$  cathode with sulfide electrolyte by nanosized LLTO coating to  
4439 achieve high-performance all-solid-state lithium batteries. *Journal of Energy Chem-*  
4440 *istry* **2021**, *52*, 202–209.
- 4441 (557) Dai, H.; Chen, Y.; Xu, W.; Hu, Z.; Gu, J.; Wei, X.; Xie, F.; Zhang, W.; Wei, W.;  
4442 Guo, R.; Zhang, G. A Review of Modification Methods of Solid Electrolytes for All-  
4443 Solid-State Sodium-Ion Batteries. *Energy Technology* **2021**, *9*, 1–13.
- 4444 (558) High Voltage Stable Polyoxalate Catholyte with Cathode Coating for All-Solid-State  
4445 Li-Metal/NMC622 Batteries. *Advanced Energy Materials* **2020**, *10*, 1–11.
- 4446 (559) Jing, M. X.; Yuan, W. Y.; Shen, X. Q.; Zhang, L. K.; Yang, H.; Liu, Q. Y.; Chen, F.;  
4447 Liu, M. Q.; Ji, Y. S. Highly efficient interface modification between poly(propylene  
4448 carbonate)-based solid electrolytes and a lithium anode by facile graphite coating.  
4449 *ACS Sustainable Chemistry and Engineering* **2020**, *8*, 17106–17115.
- 4450 (560) Wang, C.; Sun, X.; Yang, L.; Song, D.; Wu, Y.; Ohsaka, T.; Matsumoto, F.; Wu, J.  
4451 In Situ Ion-Conducting Protective Layer Strategy to Stable Lithium Metal Anode for  
4452 All-Solid-State Sulfide-Based Lithium Metal Batteries. *Advanced Materials Interfaces*  
4453 **2021**, *8*, 1–10.
- 4454 (561) Zhao, F. et al. Tuning bifunctional interface for advanced sulfide-based all-solid-state  
4455 batteries. *Energy Storage Materials* **2020**, *33*, 139–146.

- 4456 (562) Zhao, B.; Feng, X.; Yu, M.; Wang, W.; Hao, S.; Chen, H.; Huang, Y.; Gong, W.;  
4457 Liu, L.; Qiu, H. Interfacial modification enabled room temperature solid-state lithium–  
4458 metal batteries. *Ionics* **2021**, *27*, 1569–1578.
- 4459 (563) Liang, J. et al. Stabilizing and understanding the interface between nickel-rich cathode  
4460 and PEO-based electrolyte by lithium niobium oxide coating for high-performance all-  
4461 solid-state batteries. *Nano Energy* **2020**, *78*, 105107.
- 4462 (564) Zhang, Q.; Bruck, A. M.; Stavola, A. M.; Liang, W.; Aurora, P.; Gallaway, J. W.  
4463 Enhanced Electrochemical Stability of Sulfide-Based  $\text{LiNi}_{0.8}\text{Mn}_{0.1}\text{Co}_{0.1}\text{O}_2$  All-Solid-  
4464 State Batteries by Ti Surface Doping. *Batteries & Supercaps* **2020**, 1–8.
- 4465 (565) Mizushima, K.; Jones, P.; Wiseman, P.; Goodenough, J. B.  $\text{Li}_x\text{CoO}_2$  ( $0 < x < -1$ ): A  
4466 new cathode material for batteries of high energy density. *Materials Research Bulletin*  
4467 **1980**, *15*, 783–789.
- 4468 (566) Rozier, P.; Tarascon, J. M. Li-rich layered oxide cathodes for next-generation Li-ion  
4469 batteries: chances and challenges. *Journal of The Electrochemical Society* **2015**, *162*,  
4470 A2490.
- 4471 (567) Whittingham, M. S. Materials challenges facing electrical energy storage. *MRS Bul-*  
4472 *letin* **2008**, *33*, 411–419.
- 4473 (568) Dunn, B.; Kamath, H.; Tarascon, J.-M. Electrical energy storage for the grid: a battery  
4474 of choices. *Science* **2011**, *334*, 928–935.
- 4475 (569) Liu, J.; Zhang, J.-G.; Yang, Z.; Lemmon, J. P.; Imhoff, C.; Graff, G. L.; Li, L.;  
4476 Hu, J.; Wang, C.; Xiao, J., et al. Materials science and materials chemistry for large  
4477 scale electrochemical energy storage: from transportation to electrical grid. *Advanced*  
4478 *Functional Materials* **2013**, *23*, 929–946.

- 4479 (570) Palacin, M. R. Recent advances in rechargeable battery materials: a chemist's per-  
4480 spective. *Chemical Society Reviews* **2009**, *38*, 2565–2575.
- 4481 (571) Masquelier, C.; Croguennec, L. Polyanionic (phosphates, silicates, sulfates) frame-  
4482 works as electrode materials for rechargeable Li (or Na) batteries. *Chemical Reviews*  
4483 **2013**, *113*, 6552–6591.
- 4484 (572) Bruce, P. G.; Freunberger, S. A.; Hardwick, L. J.; Tarascon, J.-M. Li–O<sub>2</sub> and Li–S  
4485 batteries with high energy storage. *Nature materials* **2012**, *11*, 19.
- 4486 (573) Scrosati, B.; Hassoun, J.; Sun, Y.-K. Lithium-ion batteries. A look into the future.  
4487 *Energy & Environmental Science* **2011**, *4*, 3287–3295.
- 4488 (574) Etacheri, V.; Marom, R.; Elazari, R.; Salitra, G.; Aurbach, D. Challenges in the  
4489 development of advanced Li-ion batteries: a review. *Energy & Environmental Science*  
4490 **2011**, *4*, 3243–3262.
- 4491 (575) Takada, K. Progress and prospective of solid-state lithium batteries. *Acta Materialia*  
4492 **2013**, *61*, 759–770.
- 4493 (576) Fergus, J. W. Recent developments in cathode materials for lithium ion batteries.  
4494 *Journal of power sources* **2010**, *195*, 939–954.
- 4495 (577) Ellis, B. L.; Lee, K. T.; Nazar, L. F. Positive electrode materials for Li-ion and Li-  
4496 batteries. *Chemistry of materials* **2010**, *22*, 691–714.
- 4497 (578) He, P.; Yu, H.; Zhou, H., et al. Layered lithium transition metal oxide cathodes towards  
4498 high energy lithium-ion batteries. *Journal of Materials Chemistry* **2012**, *22*, 3680–  
4499 3695.
- 4500 (579) Zaghbi, K.; Guerfi, A.; Hovington, P.; Vijh, A.; Trudeau, M.; Mauger, A.; Good-  
4501 enough, J.; Julien, C. Review and analysis of nanostructured olivine-based lithium

- 4502 rechargeable batteries: Status and trends. *Journal of Power Sources* **2013**, *232*,  
4503 357–369.
- 4504 (580) Ellis, B. L.; Nazar, L. F. Sodium and sodium-ion energy storage batteries. *Current*  
4505 *Opinion in Solid State and Materials Science* **2012**, *16*, 168–177.
- 4506 (581) Kim, S.-W.; Seo, D.-H.; Ma, X.; Ceder, G.; Kang, K. Electrode materials for recharge-  
4507 able sodium-ion batteries: potential alternatives to current lithium-ion batteries. *Ad-*  
4508 *vanced Energy Materials* **2012**, *2*, 710–721.
- 4509 (582) Palomares, V.; Serras, P.; Villaluenga, I.; Hueso, K. B.; Carretero-González, J.;  
4510 Rojo, T. Na-ion batteries, recent advances and present challenges to become low cost  
4511 energy storage systems. *Energy & Environmental Science* **2012**, *5*, 5884–5901.
- 4512 (583) Fergus, J. W. Ion transport in sodium ion conducting solid electrolytes. *Solid State*  
4513 *Ionics* **2012**, *227*, 102–112.
- 4514 (584) Yabuuchi, N.; Kajiyama, M.; Iwatate, J.; Nishikawa, H.; Hitomi, S.; Okuyama, R.;  
4515 Usui, R.; Yamada, Y.; Komaba, S. P2-type  $\text{Na}_x[\text{Fe}_{1/2}\text{Mn}_{1/2}]\text{O}_2$  made from earth-  
4516 abundant elements for rechargeable Na batteries. *Nature materials* **2012**, *11*, 512–517.
- 4517 (585) Daniel, C.; Mohanty, D.; Li, J.; Wood, D. L. Cathode materials review. **2014**, *1597*,  
4518 26–43.
- 4519 (586) Islam, M. S.; Fisher, C. A. Lithium and sodium battery cathode materials: computa-  
4520 tional insights into voltage, diffusion and nanostructural properties. *Chemical Society*  
4521 *Reviews* **2014**, *43*, 185–204.
- 4522 (587) Myung, S.-T.; Maglia, F.; Park, K.-J.; Yoon, C. S.; Lamp, P.; Kim, S.-J.; Sun, Y.-K.  
4523 Nickel-rich layered cathode materials for automotive lithium-ion batteries: achieve-  
4524 ments and perspectives. *ACS Energy Letters* **2017**, *2*, 196–223.

- 4525 (588) Mo, J. Y.; Jeon, W. The impact of electric vehicle demand and battery recycling on  
4526 price dynamics of lithium-ion battery cathode materials: A vector error correction  
4527 model (VECM) analysis. *Sustainability* **2018**, *10*, 2870.
- 4528 (589) Goonetilleke, D.; Sharma, N.; Pang, W. K.; Peterson, V. K.; Petibon, R.;  
4529 Li, J.; Dahn, J. Structural Evolution and High-Voltage Structural Stability of  
4530  $\text{Li}(\text{Ni}_x\text{Mn}_y\text{Co}_z)\text{O}_2$  Electrodes. *Chemistry of Materials* **2018**, *31*, 376–386.
- 4531 (590) Chen, Z.; Lu, Z.; Dahn, J. Staging phase transitions in  $\text{Li}_x\text{CoO}_2$ . *Journal of the Elec-*  
4532 *trochemical Society* **2002**, *149*, A1604.
- 4533 (591) Min, K.; Kim, K.; Jung, C.; Seo, S.-W.; Song, Y. Y.; Lee, H. S.; Shin, J.; Cho, E. A  
4534 comparative study of structural changes in lithium nickel cobalt manganese oxide as  
4535 a function of Ni content during delithiation process. *Journal of Power Sources* **2016**,  
4536 *315*, 111–119.
- 4537 (592) Tian, Z.; Yu, H.; Zhang, Z.; Xu, X. Performance Improvements of Cobalt Oxide  
4538 Cathodes for Rechargeable Lithium Batteries. *ChemBioEng Reviews* **2018**, *5*, 111–  
4539 118.
- 4540 (593) Paulsen, J.; Thomas, C.; Dahn, J.  $\text{O}_2$  Structure  $\text{Li}_{2/3}[\text{Ni}_{1/3}\text{Mn}_{2/3}]\text{O}_2$ : A New Layered  
4541 Cathode Material for Rechargeable Lithium Batteries. I. Electrochemical Properties.  
4542 *Journal of the Electrochemical Society* **2000**, *147*, 861.
- 4543 (594) Paulsen, J.; Dahn, J.  $\text{O}_2$ -Type  $\text{Li}_{2/3}[\text{Ni}_{1/3}\text{Mn}_{2/3}]\text{O}_2$ : A New Layered Cathode Mate-  
4544 rial for Rechargeable Lithium Batteries II. Structure, Composition, and Properties.  
4545 *Journal of the Electrochemical Society* **2000**, *147*, 2478.
- 4546 (595) Lu, Z.; MacNeil, D.; Dahn, J. Layered  $\text{Li}[\text{Ni}_x\text{Co}_{1-2x}\text{Mn}_x]\text{O}_2$  Cathode materials for  
4547 lithium-ion batteries. *Electrochemical and Solid State Letters* **2001**, *4*, A200.

- 4548 (596) Ohzuku, T.; Makimura, Y. Layered lithium insertion material of  $\text{LiNi}_{1/2}\text{Mn}_{1/2}\text{O}_2$ : A  
4549 possible alternative to  $\text{LiCoO}_2$  for advanced lithium-ion batteries. *Chemistry Letters*  
4550 **2001**, *30*, 744–745.
- 4551 (597) Duan, Y.; Yang, L.; Zhang, M.-J.; Chen, Z.; Bai, J.; Amine, K.; Pan, F.; Wang, F.  
4552 Insights into Li/Ni ordering and surface reconstruction during synthesis of Ni-rich  
4553 layered oxides. *Journal of Materials Chemistry A* **2019**, *7*, 513–519.
- 4554 (598) Zhang, N.; Li, J.; Li, H.; Liu, A.; Huang, Q.; Ma, L.; Li, Y.; Dahn, J. R. Structural,  
4555 Electrochemical, and Thermal Properties of Nickel-Rich  $\text{LiNi}_x\text{Mn}_y\text{Co}_z\text{O}_2$  Materials.  
4556 *Chemistry of Materials* **2018**, *30*, 8852–8860.
- 4557 (599) Azevedo, M.; Campagnol, N.; Hagenbruch, T.; Hoffman, K.; Lala, A.; Ramsbot-  
4558 tom, O. *Metals and Mining* **2018**, [https://www.mckinsey.com/industries/metals-and-](https://www.mckinsey.com/industries/metals-and-mining/our-insights/lithium-and-cobalt-a-tale-of-two-commodities)  
4559 [mining/our-insights/lithium-and-cobalt-a-tale-of-two-commodities](https://www.mckinsey.com/industries/metals-and-mining/our-insights/lithium-and-cobalt-a-tale-of-two-commodities).
- 4560 (600) Sathiya, M.; Rousse, G.; Ramesha, K.; Laisa, C.; Vezin, H.; Sougrati, M. T.; Dou-  
4561 blet, M.-L.; Foix, D.; Gonbeau, D.; Walker, W., et al. Reversible anionic redox chem-  
4562 istry in high-capacity layered-oxide electrodes. *Nature materials* **2013**, *12*, 827–835.
- 4563 (601) Lee, J.; Urban, A.; Li, X.; Su, D.; Hautier, G.; Ceder, G. Unlocking the potential of  
4564 cation-disordered oxides for rechargeable lithium batteries. *Science* **2014**, *343*, 519–  
4565 522.
- 4566 (602) Oishi, M.; Yogi, C.; Watanabe, I.; Ohta, T.; Orikasa, Y.; Uchimoto, Y.; Ogumi, Z.  
4567 Direct observation of reversible charge compensation by oxygen ion in Li-rich man-  
4568 ganese layered oxide positive electrode material,  $\text{Li}_{1.16}\text{Ni}_{0.15}\text{Co}_{0.19}\text{Mn}_{0.50}\text{O}_2$ . *Journal of*  
4569 *Power Sources* **2015**, *276*, 89–94.
- 4570 (603) Seo, D.-H.; Lee, J.; Urban, A.; Malik, R.; Kang, S.; Ceder, G. The structural and  
4571 chemical origin of the oxygen redox activity in layered and cation-disordered Li-excess  
4572 cathode materials. *Nature Chemistry* **2016**, *8*, 692–697.

- 4573 (604) Gent, W. E. et al. Coupling between oxygen redox and cation migration explains un-  
4574 usual electrochemistry in lithium-rich layered oxides. *Nature Communications* **2017**,  
4575 **8**, 2091.
- 4576 (605) Assat, G.; Tarascon, J.-M. Fundamental understanding and practical challenges of  
4577 anionic redox activity in Li-ion batteries. *Nature Energy* **2018**, **3**, 373–386.
- 4578 (606) Naylor, A. J.; Makkos, E.; Maibach, J.; Guerrini, N.; Sobkowiak, A.; Björklund, E.;  
4579 Lozano, J. G.; Menon, A. S.; Younesi, R.; Roberts, M. R., et al. Depth-dependent  
4580 oxygen redox activity in lithium-rich layered oxide cathodes. *Journal of Materials*  
4581 *Chemistry A* **2019**, **7**, 25355–25368.
- 4582 (607) House, R. A.; Maitra, U.; Pérez-Osorio, M. A.; Lozano, J. G.; Jin, L.; Somerville, J. W.;  
4583 Duda, L. C.; Nag, A.; Walters, A.; Zhou, K.-J.; Roberts, M. R.; Bruce, P. G. Super-  
4584 structure control of first-cycle voltage hysteresis in oxygen-redox cathodes. *Nature*  
4585 **2020**, *577*, 502–508.
- 4586 (608) House, R. A.; Rees, G. J.; Pérez-Osorio, M. A.; Marie, J. J.; Boivin, E.; Robert-  
4587 son, A. W.; Nag, A.; Garcia-Fernandez, M.; Zhou, K. J.; Bruce, P. G. First-cycle  
4588 voltage hysteresis in Li-rich 3d cathodes associated with molecular O<sub>2</sub> trapped in the  
4589 bulk. *Nature Energy* **2020**, **5**, 777–785.
- 4590 (609) Hy, S.; Liu, H.; Zhang, M.; Qian, D.; Hwang, B.-J.; Meng, Y. S. Performance and  
4591 design considerations for lithium excess layered oxide positive electrode materials for  
4592 lithium ion batteries. *Energy & Environmental Science* **2016**, **9**, 1931–1954.
- 4593 (610) Urban, A.; Lee, J.; Ceder, G. The Configurational Space of Rocksalt-Type Oxides  
4594 for High-Capacity Lithium Battery Electrodes. *Advanced Energy Materials* **2014**, **4**,  
4595 1400478.
- 4596 (611) Lee, J.; Seo, D.-H.; Balasubramanian, M.; Twu, N.; Li, X.; Ceder, G. A new

- 4597 class of high capacity cation-disordered oxides for rechargeable lithium batteries:  
4598 Li–Ni–Ti–Mo oxides. *Energy & Environmental Science* **2015**, *8*, 3255–3265.
- 4599 (612) Yabuuchi, N.; Nakayama, M.; Takeuchi, M.; Komaba, S.; Hashimoto, Y.; Mukai, T.;  
4600 Shiiba, H.; Sato, K.; Kobayashi, Y.; Nakao, A.; Yonemura, M.; Yamanaka, K.; Mit-  
4601 suhara, K.; Ohta, T. Origin of stabilization and destabilization in solid-state redox  
4602 reaction of oxide ions for lithium-ion batteries. *Nature Communications* **2016**, *7*, 1–  
4603 10.
- 4604 (613) Freire, M.; Kosova, N. V.; Jordy, C.; Chateigner, D.; Lebedev, O. I.; Maignan, A.;  
4605 Pralong, V. A new active Li–Mn–O compound for high energy density Li-ion batteries.  
4606 *Nature Materials* **2016**, *15*, 173–177.
- 4607 (614) Yao, Z.; Kim, S.; He, J.; Hegde, V. I.; Wolverton, C. Interplay of cation and anion redox  
4608 in  $\text{Li}_4\text{Mn}_2\text{O}_5$  cathode material and prediction of improved  $\text{Li}_4(\text{Mn},\text{M})_2\text{O}_5$  electrodes  
4609 for Li-ion batteries. *Science Advances* **2018**, *4*, eaao6754.
- 4610 (615) Bhandari, A.; Jindal, P.; Bhattacharya, J. Discovery of new ground state structures  
4611 for  $\text{Li}_4\text{Mn}_2\text{O}_5$  and  $\text{V}_2\text{O}_5$  from first principles. *Computational Materials Science* **2019**,  
4612 *159*, 454–459.
- 4613 (616) Nakajima, M.; Yabuuchi, N. Lithium-Excess Cation-Disordered Rocksalt-Type Oxide  
4614 with Nanoscale Phase Segregation:  $\text{Li}_{1.25}\text{Nb}_{0.25}\text{V}_{0.5}\text{O}_2$ . *Chemistry of Materials* **2017**,  
4615 *29*, 6927–6935.
- 4616 (617) Yabuuchi, N.; Takeuchi, M.; Nakayama, M.; Shiiba, H.; Ogawa, M.; Nakayama, K.;  
4617 Ohta, T.; Endo, D.; Ozaki, T.; Inamasu, T.; Sato, K.; Komaba, S. High-capacity  
4618 electrode materials for rechargeable lithium batteries:  $\text{Li}_3\text{NbO}_4$ -based system with  
4619 cation-disordered rocksalt structure. *Proceedings of the National Academy of Sciences*  
4620 **2015**, *112*, 7650–7655.



- 4621 (618) Wang, R.; Li, X.; Liu, L.; Lee, J.; Seo, D.-H.; Bo, S.-H.; Urban, A.; Ceder, G. A  
4622 disordered rock-salt Li-excess cathode material with high capacity and substantial  
4623 oxygen redox activity:  $\text{Li}_{1.25}\text{Nb}_{0.25}\text{Mn}_{0.5}\text{O}_2$ . *Electrochemistry Communications* **2015**,  
4624 *60*, 70–73.
- 4625 (619) Sharpe, R.; House, R. A.; Clarke, M. J.; Forstermann, D.; Marie, J.-J.; Cibir, G.;  
4626 Zhou, K.-J.; Playford, H. Y.; Bruce, P. G.; Islam, M. S. Redox Chemistry and the  
4627 Role of Trapped Molecular  $\text{O}_2$  in Li-Rich Disordered Rocksalt Oxyfluoride Cathodes.  
4628 *J. Am. Chem. Soc.* **2020**, *142*, 21799–21809.
- 4629 (620) House, R. A.; Jin, L.; Maitra, U.; Tsuruta, K.; Somerville, J. W.; Förstermann, D. P.;  
4630 Massel, F.; Duda, L.; Roberts, M. R.; Bruce, P. G. Lithium manganese oxyfluoride  
4631 as a new cathode material exhibiting oxygen redox. *Energy & Environmental Science*  
4632 **2018**, *11*, 926–932.
- 4633 (621) Lun, Z.; Ouyang, B.; Cai, Z.; Clément, R. J.; Kwon, D.-H.; Huang, J.; Papp, J. K.;  
4634 Balasubramanian, M.; Tian, Y.; McCloskey, B. D.; Ji, H.; Kim, H.; Kitchaev, D. A.;  
4635 Ceder, G. Design Principles for High-Capacity Mn-Based Cation-Disordered Rocksalt  
4636 Cathodes. *Chem* 153–168.
- 4637 (622) Chen, R.; Ren, S.; Yavuz, M.; Guda, A. A.; Shapovalov, V.; Witter, R.; Fichtner, M.;  
4638 Hahn, H.  $\text{Li}^+$  intercalation in isostructural  $\text{Li}_2\text{VO}_3$  and  $\text{Li}_2\text{VO}_2\text{F}$  with  $\text{O}^{2-}$  and mixed  
4639  $\text{O}^{2-}/\text{F}^-$  anions. *Physical Chemistry Chemical Physics* **2015**, *17*, 17288–17295.
- 4640 (623) Chen, R.; Ren, S.; Knapp, M.; Wang, D.; Witter, R.; Fichtner, M.; Hahn, H. Dis-  
4641 ordered Lithium-Rich Oxyfluoride as a Stable Host for Enhanced  $\text{Li}^+$  Intercalation  
4642 Storage. *Advanced Energy Materials* **2015**, *5*, 1401814.
- 4643 (624) Baur, C. et al. Improved cycling stability in high-capacity Li-rich vanadium containing  
4644 disordered rock salt oxyfluoride cathodes. *Journal of Materials Chemistry A* **2019**, *7*,  
4645 21244–21253.

- 4646 (625) Cambaz, M. A.; Vinayan, B. P.; Pervez, S. A.; Johnsen, R. E.; Geßwein, H.;  
4647 Guda, A. A.; Rusalev, Y. V.; Kinyanjui, M. K.; Kaiser, U.; Fichtner, M. Suppress-  
4648 ing Dissolution of Vanadium from Cation-Disordered  $\text{Li}_{2-x}\text{VO}_2\text{F}$  via a Concentrated  
4649 Electrolyte Approach. *Chemistry of Materials* **2019**, *31*, 7941–7950.
- 4650 (626) Baur, C.; Lacatusu, M.-E.; Fichtner, M.; Johnsen, R. E. Insights into Structural Trans-  
4651 formations in the Local Structure of  $\text{Li}_2\text{VO}_2\text{F}$  Using Operando X-ray Diffraction and  
4652 Total Scattering: Amorphization and Recrystallization. *ACS Applied Materials & In-*  
4653 *terfaces* **2020**, *12*, 27010–27016.
- 4654 (627) Källquist, I.; Naylor, A. J.; Baur, C.; Chable, J.; Kullgren, J.; Fichtner, M.; Ed-  
4655 ström, K.; Brandell, D.; Hahlin, M. Degradation Mechanisms in  $\text{Li}_2\text{VO}_2\text{F}$  Li-Rich  
4656 Disordered Rock-Salt Cathodes. *Chemistry of Materials* **2019**, *31*, 6084–6096.
- 4657 (628) Chang, J. H.; Baur, C.; Mba, J.-M. A.; Arçon, D.; Mali, G.; Alwast, D.; Behm, R. J.;  
4658 Fichtner, M.; Vegge, T.; Lastra, J. M. G. Superoxide Formation in  $\text{Li}_2\text{VO}_2\text{F}$  Cathode  
4659 Material – a Combined Computational and Experimental Investigation of Anionic  
4660 Redox Activity. *Journal of Materials Chemistry A* **2020**, *8*, 16551–16559.
- 4661 (629) Lee, J.; Kitchaev, D. A.; Kwon, D.-H.; Lee, C.-W.; Papp, J. K.; Liu, Y.-S.; Lun, Z.; Clé-  
4662 ment, R. J.; Shi, T.; McCloskey, B. D.; Guo, J.; Balasubramanian, M.; Ceder, G. Re-  
4663 versible  $\text{Mn}^{2+}/\text{Mn}^{4+}$  double redox in lithium-excess cathode materials. *Nature* **2018**,  
4664 *556*, 185–190.
- 4665 (630) Freire, M.; Lebedev, O.; Maignan, A.; Jordy, C.; Pralong, V. Nanostructured  $\text{Li}_2\text{MnO}_3$ :  
4666 a disordered rock salt type structure for high energy density Li ion batteries. *Journal*  
4667 *of Materials Chemistry A* **2017**, *5*, 21898–21902.
- 4668 (631) Jacquet, Q.; Iadecola, A.; Saubanere, M.; Li, H.; Berg, E. J.; Rouse, G.; Cabana, J.;  
4669 Doublet, M. L.; Tarascon, J. M. Charge Transfer Band Gap as an Indicator of Hys-

- 4670 teresis in Li-Disordered Rock Salt Cathodes for Li-Ion Batteries. *J. Am. Chem. Soc.*  
4671 **2019**, *141*, 11452–11464.
- 4672 (632) Clément, R.; Lun, Z.; Ceder, G. Cation-disordered rocksalt transition metal oxides and  
4673 oxyfluorides for high energy lithium-ion cathodes. *Energy & Environmental Science*  
4674 **2020**, *13*, 345–373.
- 4675 (633) Nyttén, A.; Abouimrane, A.; Armand, M.; Gustafsson, T.; Thomas, J. O. Electrochem-  
4676 ical performance of  $\text{Li}_2\text{FeSiO}_4$  as a new Li-battery cathode material. *Electrochemistry*  
4677 *communications* **2005**, *7*, 156–160.
- 4678 (634) Sirisopanaporn, C.; Dominko, R.; Masquelier, C.; Armstrong, A. R.; Mali, G.;  
4679 Bruce, P. G. Polymorphism in  $\text{Li}_2(\text{Fe,Mn})\text{SiO}_4$ : A combined diffraction and NMR  
4680 study. *Journal of Materials Chemistry* **2011**, *21*, 17823–17831.
- 4681 (635) Islam, M. S.; Dominko, R.; Masquelier, C.; Sirisopanaporn, C.; Armstrong, A. R.;  
4682 Bruce, P. G. Silicate cathodes for lithium batteries: alternatives to phosphates? *Jour-*  
4683 *nal of Materials Chemistry* **2011**, *21*, 9811–9818.
- 4684 (636) Padhi, A.; Nanjundaswamy, K.; Masquelier, C.; Goodenough, J. Mapping of transition  
4685 metal redox energies in phosphates with NASICON structure by lithium intercalation.  
4686 *Journal of the Electrochemical Society* **1997**, *144*, 2581.
- 4687 (637) Tygesen, A. S.; Chang, J. H.; Vegge, T.; García-Lastra, J. M. Computational frame-  
4688 work for a systematic investigation of anionic redox process in Li-rich compounds. *npj*  
4689 *Computational Materials* **2020**, *6*, 1–9.
- 4690 (638) Armstrong, A. R.; Bruce, P. G. Synthesis of layered  $\text{LiMnO}_2$  as an electrode for  
4691 rechargeable lithium batteries. *Nature* **1996**, *381*, 499–500.
- 4692 (639) Mosbah, A.; Verbaere, A.; Tournoux, M. Phases  $\text{Li}_x\text{MnO}_{2\lambda}$  rattachees au type spinelle.  
4693 *Materials research bulletin* **1983**, *18*, 1375–1381.

- 4694 (640) Dittrich, G.; Hoppe, R. Zur Kristallstruktur von  $\text{LiMnO}_2$ . *Zeitschrift für anorganische*  
4695 *und allgemeine Chemie* **1969**, *368*, 262–270.
- 4696 (641) Gao, P.; Ishikawa, R.; Tochigi, E.; Kumamoto, A.; Shibata, N.; Ikuhara, Y. Atomic-  
4697 Scale Tracking of a Phase Transition from Spinel to Rocksalt in Lithium Manganese  
4698 Oxide. *Chemistry of Materials* **2017**, *29*, 1006–1013.
- 4699 (642) Chen, B.; Ben, L.; Yu, H.; Chen, Y.; Huang, X. Understanding Surface Structural  
4700 Stabilization of the High-Temperature and High-Voltage Cycling Performance of  $\text{Al}^{3+}$ -  
4701 Modified  $\text{LiMn}_2\text{O}_4$  Cathode Material. *ACS Applied Materials & Interfaces* **2018**, *10*,  
4702 550–559.
- 4703 (643) Reed, J.; Ceder, G.; Van Der Ven, A. Layered-to-spinel phase transition in  $\text{Li}_x\text{MnO}_2$ .  
4704 *Electrochemical and Solid State Letters* **2001**, *4*, A78.
- 4705 (644) Bruce, P. G.; Scrosati, B.; Tarascon, J.-M. Nanomaterials for rechargeable lithium  
4706 batteries. *Angewandte Chemie International Edition* **2008**, *47*, 2930–2946.
- 4707 (645) Franger, S.; Benoit, C.; Bourbon, C.; Le Cras, F. Chemistry and electrochemistry of  
4708 composite  $\text{LiFePO}_4$  materials for secondary lithium batteries. *Journal of Physics and*  
4709 *Chemistry of Solids* **2006**, *67*, 1338–1342.
- 4710 (646) Ellis, B.; Kan, W. H.; Makahnouk, W.; Nazar, L. Synthesis of nanocrystals and mor-  
4711 phology control of hydrothermally prepared  $\text{LiFePO}_4$ . *Journal of Materials Chemistry*  
4712 **2007**, *17*, 3248–3254.
- 4713 (647) Malik, R.; Burch, D.; Bazant, M.; Ceder, G. Particle size dependence of the ionic  
4714 diffusivity. *Nano letters* **2010**, *10*, 4123–4127.
- 4715 (648) Ledwaba, R. S.; Ngoepe, P.; Sayle, D. Modeling Diffusion-Induced Stress In Li-Mn-O  
4716 Nanocomposite Cathode Materials. APS March Meeting Abstracts. 2018; p E20.006.

- 4717 (649) Sayle, T. X.; Maphanga, R. R.; Ngoepe, P. E.; Sayle, D. C. Predicting the electrochem-  
4718 ical properties of MnO<sub>2</sub> nanomaterials used in rechargeable Li batteries: simulating  
4719 nanostructure at the atomistic level. *Journal of the American Chemical Society* **2009**,  
4720 *131*, 6161–6173.
- 4721 (650) Gupta, P. K.; Bhandari, A.; Bhattacharya, J.; Pala, R. G. S. Correlating Voltage  
4722 Profile to Molecular Transformations in Ramsdellite MnO<sub>2</sub> and Its Implication for  
4723 Polymorph Engineering of Lithium Ion Battery Cathodes. *The Journal of Physical*  
4724 *Chemistry C* **2018**, *122*, 11689–11700.
- 4725 (651) Gupta, P. K.; Bhandari, A.; Bhattacharya, J.; Ganesh S Pala, R. Higher voltage,  
4726 wider voltage plateau, longer cycle life, and faster kinetics via thermally modulated  
4727 interfaces between Ramsdellite and Pyrolusite MnO<sub>2</sub> for lithium-ion battery cathodes.  
4728 *Journal of Power Sources* **2020**, *450*, 227619.
- 4729 (652) Moriwake, H.; Kuwabara, A.; Fisher, C. A.; Huang, R.; Hitosugi, T.; Ikuhara, Y. H.;  
4730 Oki, H.; Ikuhara, Y. First-Principles Calculations of Lithium-Ion Migration at a Co-  
4731 herent Grain Boundary in a Cathode Material, LiCoO<sub>2</sub>. *Advanced Materials* **2013**,  
4732 *25*, 618–622.
- 4733 (653) Dixit, M.; Engel, H.; Eitan, R.; Aurbach, D.; Levi, M. D.; Kosa, M.; Major, D. T.  
4734 Classical and Quantum Modeling of Li and Na Diffusion in FePO<sub>4</sub>. *The Journal of*  
4735 *Physical Chemistry C* **2015**, *119*, 15801–15809.
- 4736 (654) Morgan, D.; Van der Ven, A.; Ceder, G. Li Conductivity in Li<sub>x</sub>MPO<sub>4</sub>  
4737 (M=Mn,Fe,Co,Ni) Olivine Materials. *Electrochemical and Solid-State Letters* **2004**,  
4738 *7*, A30–A32.
- 4739 (655) Ouyang, C.; Shi, S.; Wang, Z.; Huang, X.; Chen, L. First-principles study of Li ion  
4740 diffusion in LiFePO<sub>4</sub>. *Physical Review B* **2004**, *69*, 104303.

- 4741 (656) Islam, M. S.; Driscoll, D. J.; Fisher, C. A. J.; Slater, P. R. Atomic-scale investigation of  
4742 defects, dopants, and lithium transport in the  $\text{LiFePO}_4$  olivine-type battery material.  
4743 *Chemistry of Materials* **2005**, *17*, 5085–5092.
- 4744 (657) Amin, R.; Balaya, P.; Maier, J. Anisotropy of electronic and ionic transport in  $\text{LiFePO}_4$   
4745 single crystals. *Electrochemical and Solid State Letters* **2006**, *10*, A13.
- 4746 (658) Van der Ven, A.; Ceder, G. Lithium diffusion in layered  $\text{Li}_x\text{CoO}_2$ . *Electrochemical and*  
4747 *Solid State Letters* **2000**, *3*, 301.
- 4748 (659) Thackeray, M. M. Manganese oxides for lithium batteries. *Progress in Solid State*  
4749 *Chemistry* **1997**, *25*, 1–71.
- 4750 (660) Proell, J.; Kohler, R.; Mangang, A.; Ulrich, S.; Ziebert, C.; Pfleging, W. 3D structures  
4751 in battery materials. *Journal of Laser Micro Nanoengineering* **2012**, *7*, 97.
- 4752 (661) Nishimura, S.-i.; Kobayashi, G.; Ohoyama, K.; Kanno, R.; Yashima, M.; Yamada, A.  
4753 Experimental visualization of lithium diffusion in  $\text{Li}_x\text{FePO}_4$ . *Nature materials* **2008**,  
4754 *7*, 707–711.
- 4755 (662) Van der Ven, A.; Thomas, J. C.; Xu, Q.; Swoboda, B.; Morgan, D. Nondilute diffusion  
4756 from first principles: Li diffusion in  $\text{Li}_x\text{TiS}_2$ . *Physical Review B* **2008**, *78*, 104306.
- 4757 (663) Bhattacharya, J.; Van der Ven, A. First-principles study of competing mechanisms of  
4758 nondilute Li diffusion in spinel  $\text{Li}_x\text{TiS}_2$ . *Physical Review B* **2011**, *83*, 144302.
- 4759 (664) Bhattacharya, J.; Van der Ven, A. Phase stability and nondilute Li diffusion in spinel  
4760  $\text{Li}_{1+x}\text{Ti}_2\text{O}_4$ . *Physical Review B* **2010**, *81*, 104304.
- 4761 (665) Van Der Ven, A.; Bhattacharya, J.; Belak, A. A. Understanding Li diffusion in Li-  
4762 intercalation compounds. *Accounts of Chemical Research* **2013**, *46*, 1216–1225.
- 4763 (666) Van der Ven, A.; Ceder, G. Lithium diffusion mechanisms in layered intercalation  
4764 compounds. *Journal of power sources* **2001**, *97*, 529–531.

- 4765 (667) Choi, S. H.; Shlyakhtin, O.; Kim, J.; Yoon, Y. S. Structural and electrochemical  
4766 properties of  $\text{Li}_{1+x}\text{Ni}_{0.5}\text{Mn}_{0.5}\text{O}_{2+\delta}$  ( $0 \leq x \leq 0.7$ ) cathode materials for lithium-ion  
4767 batteries. *Journal of power sources* **2005**, *140*, 355–360.
- 4768 (668) Kang, K.; Meng, Y. S.; Breger, J.; Grey, C. P.; Ceder, G. Electrodes with high power  
4769 and high capacity for rechargeable lithium batteries. *Science* **2006**, *311*, 977–980.
- 4770 (669) Laubach, S.; Laubach, S.; Schmidt, P. C.; Gröting, M.; Albe, K.; Jaegermann, W.;  
4771 Wolf, W. Structure, Electronic Structure and Defect Formation Energies of  
4772  $\text{Li}_x\text{Co}_{1-y}\text{Ni}_y\text{O}_2$  as a Function of  $x$  ( $0 < x < 1$ ) and  $y$  ( $y = 0, 0.5, 1$ ). *Zeitschrift*  
4773 *für Physikalische Chemie* **2009**, *223*, 1327–1340.
- 4774 (670) Lee, E.; Persson, K. A. Solid-Solution Li Intercalation as a Function of Cation Or-  
4775 der/Disorder in the High-Voltage  $\text{Li}_x\text{Ni}_{0.5}\text{Mn}_{1.5}\text{O}_4$  Spinel. *Chemistry of Materials*  
4776 **2013**, *25*, 2885–2889.
- 4777 (671) Hao, S.; Lu, Z.; Wolverton, C. Quaternary phase diagrams of spinel  
4778  $\text{Li}_y\text{Mn}_{1-y}\text{Ni}_x\text{O}_4$  and composite cathode voltages for concentration gradient ma-  
4779 terials. *Physical Review B* **2016**, *94*, 014114.
- 4780 (672) Capsoni, D.; Bini, M.; Chiodelli, G.; Mustarelli, P.; Massarotti, V.; Azzoni, C. B.;  
4781 Mozzati, M. C.; Linati, L. Inhibition of Jahn-Teller Cooperative Distortion in  $\text{LiMn}_2\text{O}_4$   
4782 Spinel by  $\text{Ga}^{3+}$  Doping. *The Journal of Physical Chemistry B* **2002**, *106*, 7432–7438.
- 4783 (673) Singh, G.; Gupta, S.; Prasad, R.; Auluck, S.; Gupta, R.; Sil, A. Suppression of Jahn-  
4784 Teller distortion by chromium and magnesium doping in spinel  $\text{LiMn}_2\text{O}_4$ : A first-  
4785 principles study using GGA and GGA+U. *Journal of Physics and Chemistry of Solids*  
4786 **2009**, *70*, 1200–1206.
- 4787 (674) Padhi, A.; Nanjundaswamy, K.; Goodenough, J. Phospho-olivines as positive-electrode  
4788 materials for rechargeable lithium batteries. *Journal of the Electrochemical Society*  
4789 **1997**, *144*, 1188–1194.

- 4790 (675) Thackeray, M. M.; David, W. I. F.; Bruce, P. G.; Goodenough, P. G. Lithium Insertion  
4791 into Manganese Spinel. *Materials Research Bulletin* **1983**, *18*, 461–472.
- 4792 (676) Koga, H.; Croguennec, L.; Menetrier, M.; Douhiol, K.; Belin, S.; Bourgeois, L.;  
4793 Suard, E.; Weill, F. Reversible Oxygen Participation to the Redox Processes Revealed  
4794 for  $\text{Li}_{1.20}\text{Mn}_{0.54}\text{Co}_{0.13}\text{Ni}_{0.13}\text{O}_2$ . *J. Electrochem. Soc.* **2013**, *160*, A786–A792.
- 4795 (677) Sathiya, M.; Lerich, J.-B.; Salager, E.; Gourier, D.; Tarascon, J.-M.; Vezin, H. Electron  
4796 paramagnetic resonance imaging for real-time monitoring of Li-ion batteries. *Nat.*  
4797 *Commun.* **2015**, *6*, 6276.
- 4798 (678) McCalla, E.; Abakumov, A. M.; Saubanère, M.; Foix, D.; Berg, E. J.; Rouse, G.;  
4799 Doublet, M.-L.; Gonbeau, D.; Novák, P.; Van Tendeloo, G., et al. Visualization of OO  
4800 peroxo-like dimers in high-capacity layered oxides for Li-ion batteries. *Science* **2015**,  
4801 *350*, 1516–1521.
- 4802 (679) Cao, T.; Shi, C.; Zhao, N.; He, C.; Li, J.; Liu, E. Understanding the Electrochemi-  
4803 cal Properties of Li-Rich Cathode Materials from First-Principles Calculations. *The*  
4804 *Journal of Physical Chemistry C* **2015**, *119*, 28749–28756.
- 4805 (680) Shimoda, K.; Minato, T.; Nakanishi, K.; Komatsu, H.; Matsunaga, T.; Tanida, H.;  
4806 Arai, H.; Ukyo, Y.; Uchimoto, Y.; Ogumi, Z. Oxidation behaviour of lattice oxygen  
4807 in Li-rich manganese-based layered oxide studied by hard X-ray photoelectron spec-  
4808 troscopy. *J. Mater. Chem. A* **2016**, *4*, 5909–5916.
- 4809 (681) Chen, H.; Islam, M. S. Lithium Extraction Mechanism in Li-Rich  $\text{Li}_2\text{MnO}_3$  Involving  
4810 Oxygen Hole Formation and Dimerization. *Chemistry of Materials* **2016**, *28*, 6656–  
4811 6663.
- 4812 (682) Luo, K.; Roberts, M. R.; Hao, R.; Guerrini, N.; Pickup, D. M.; Liu, Y.-S.; Edström, K.;  
4813 Guo, J.; Chadwick, A. V.; Duda, L. C.; Bruce, P. G. Charge-compensation in 3d-



- 4814 transition-metal-oxide intercalation cathodes through the generation of localized elec-  
4815 tron holes on oxygen. *Nature Chemistry* **2016**, *8*, 684–691.
- 4816 (683) Muhammad, S.; Kim, H.; Kim, Y.; Kim, D.; Song, J. H.; Yoon, J.; Park, J.-H.;  
4817 Ahn, S.-J.; Kang, S.-H.; Thackeray, M. M.; Yoon, W.-S. Evidence of reversible oxy-  
4818 gen participation in anomalously high capacity Li- and Mn-rich cathodes for Li-ion  
4819 batteries. *Nano Energy* **2016**, *21*, 172–184.
- 4820 (684) Zhan, C. et al. Enabling the high capacity of lithium-rich anti-fluorite lithium iron  
4821 oxide by simultaneous anionic and cationic redox. *Nature Energy* **2017**, *2*, 963–971.
- 4822 (685) Zheng, J.; Myeong, S.; Cho, W.; Yan, P.; Xiao, J.; Wang, C.; Cho, J.; Zhang, J. G. Li-  
4823 and Mn-Rich Cathode Materials: Challenges to Commercialization. **2017**, *7*, 1601284.
- 4824 (686) Ben Yahia, M.; Vergnet, J.; Saubanère, M.; Doublet, M.-L. Unified picture of anionic  
4825 redox in Li/Na-ion batteries. *Nature Materials* **2019**, *18*, 496–502.
- 4826 (687) Hua, W.; Wang, S.; Knapp, M.; Leake, S. J.; Senyshyn, A.; Richter, C.; Yavuz, M.;  
4827 Binder, J. R.; Grey, C. P.; Ehrenberg, H.; Indris, S.; Schwarz, B. Structural insights  
4828 into the formation and voltage degradation of lithium- and manganese-rich layered  
4829 oxides. *Nature Communications* **2019**, *10*, 5365.
- 4830 (688) Li, L.; Castro, F. C.; Park, J. S.; Li, H.; Lee, E.; Boyko, T. D.; Freeland, Z., J.  
4831 W. and Yao; Fister, T. T.; Vinson, J.; Shirley, E. L.; Wolverton, C.; Cabana, J.;  
4832 Dravid, V. P.; M., T. M.; Chan, M. K. Y. Probing Electrochemically Induced Struc-  
4833 tural Evolution and Oxygen Redox Reactions in Layered Lithium Iridate. *Chem.*  
4834 *Mater.* **2019**, *31*, 4341–4352.
- 4835 (689) Eum, D.; Kim, B.; Kim, S. J.; Park, H.; Wu, J.; Cho, S.-P.; Yoon, G.; Lee, M. H.;  
4836 Jung, S.-K.; Yang, W., et al. Voltage decay and redox asymmetry mitigation by re-  
4837 versible cation migration in lithium-rich layered oxide electrodes. *Nature materials*  
4838 **2020**, *19*, 419–427.

- 4839 (690) Gent, W. E.; Abate, I. I.; Yang, W.; Nazar, L. F.; Chueh, W. C. Design Rules for  
4840 High-Valent Redox in Intercalation Electrodes. **2020**, *4*, 1369–1397.
- 4841 (691) Sathiya, M.; Ramesha, K.; Rouse, G.; Foix, D.; Gonbeau, D.; Prakash, A. S.; Dou-  
4842 blet, M. L.; Hemalatha, K.; Tarascon, J. M. High performance  $\text{Li}_2\text{Ru}_{1-y}\text{Mn}_y\text{O}_3$  ( $0.2 \leq$   
4843  $y \leq 0.8$ ) cathode materials for rechargeable lithium-ion batteries: Their understand-  
4844 ing. *Chemistry of Materials* **2013**, *25*, 1121–1131.
- 4845 (692) Xiao, R.; Li, H.; Chen, L. Density functional investigation on  $\text{Li}_2\text{MnO}_3$ . *Chemistry of*  
4846 *Materials* **2012**, *24*, 4242–4251.
- 4847 (693) Hong, J. et al. Metal–oxygen decoordination stabilizes anion redox in Li-rich oxides.  
4848 *Nature Materials* **2019**, *18*, 256–265.
- 4849 (694) Davies, D. W.; Morgan, B. J.; Scanlon, D. O.; Walsh, A. Low-cost descriptors of  
4850 electrostatic and electronic contributions to anion redox activity in batteries. *IOP*  
4851 *SciNotes* **2020**, *1*, 024805.
- 4852 (695) Xiao, Y.; Liu, T.; Liu, J.; He, L.; Chen, J.; Zhang, J.; Luo, P.; Lu, H.; Wang, R.;  
4853 Zhu, W., et al. Insight into the origin of lithium/nickel ions exchange in layered Li  
4854  $(\text{Ni}_x\text{Mn}_y\text{Co}_z)\text{O}_2$  cathode materials. *Nano Energy* **2018**, *49*, 77–85.
- 4855 (696) Sun, H.; Zhao, K. Electronic Structure and Comparative Properties of  $\text{LiNi}_x\text{Mn}_y\text{Co}_z\text{O}_2$   
4856 Cathode Materials. *The Journal of Physical Chemistry C* **2017**, *121*, 6002–6010.
- 4857 (697) Dixit, M.; Markovsky, B.; Schipper, F.; Aurbach, D.; Major, D. T. Origin of struc-  
4858 tural degradation during cycling and low thermal stability of Ni-rich layered transition  
4859 metal-based electrode materials. *The Journal of Physical Chemistry C* **2017**, *121*,  
4860 22628–22636.
- 4861 (698) Hoang, K.; Johannes, M. Defect physics and chemistry in layered mixed transition

- 4862 metal oxide cathode materials:(Ni, Co, Mn) vs (Ni, Co, Al). *Chemistry of Materials*  
4863 **2016**, *28*, 1325–1334.
- 4864 (699) Dixit, M.; Markovsky, B.; Aurbach, D.; Major, D. T. Unraveling the effects of Al  
4865 doping on the electrochemical properties of  $\text{LiNi}_{0.5}\text{Co}_{0.2}\text{Mn}_{0.3}\text{O}_2$  using first principles.  
4866 *Journal of The Electrochemical Society* **2017**, *164*, A6359.
- 4867 (700) Du, T.; Xu, B.; Wu, M.; Liu, G.; Ouyang, C. Insight into the vibrational and ther-  
4868 modynamic properties of layered lithium transition-metal oxides  $\text{LiMO}_2$  (M= Co, Ni,  
4869 Mn): a first-principles study. *The Journal of Physical Chemistry C* **2016**, *120*, 5876–  
4870 5882.
- 4871 (701) Shang, S.; Wang, Y.; Mei, Z.; Hui, X.; Liu, Z. Lattice dynamics, thermodynamics,  
4872 and bonding strength of lithium-ion battery materials  $\text{LiMPO}_4$  (M= Mn, Fe, Co, and  
4873 Ni): a comparative first-principles study. *Journal of Materials Chemistry* **2012**, *22*,  
4874 1142–1149.
- 4875 (702) Sagotra, A. K.; Chu, D.; Cazorla, C. Influence of lattice dynamics on lithium-ion  
4876 conductivity: A first-principles study. *Physical Review Materials* **2019**, *3*, 035405.
- 4877 (703) Puligheddu, M.; Xia, Y.; Chan, M.; Galli, G. Computational prediction of lattice  
4878 thermal conductivity: A comparison of molecular dynamics and Boltzmann transport  
4879 approaches. *Physical Review Materials* **2019**, *3*, 085401.
- 4880 (704) Mattila, N.; Karttunen, A. J. Lattice thermal conductivity of  $\text{NaCoO}_2$  and  $\text{LiCoO}_2$   
4881 intercalation materials studied by hybrid density functional theory. *Materials Research*  
4882 *Express* **2020**, *7*, 075502.
- 4883 (705) Feng, T.; O’Hara, A.; Pantelides, S. T. Quantum prediction of ultra-low thermal  
4884 conductivity in lithium intercalation materials. *Nano Energy* **2020**, 104916.

- 4885 (706) Qian, X.; Gu, X.; Dresselhaus, M. S.; Yang, R. Anisotropic tuning of graphite ther-  
4886 mal conductivity by lithium intercalation. *The Journal of Physical Chemistry Letters*  
4887 **2016**, *7*, 4744–4750.
- 4888 (707) Wei, Z.; Yang, F.; Bi, K.; Yang, J.; Chen, Y. Tunable Anisotropic Thermal Conduc-  
4889 tivity and Elastic Properties in Intercalated Graphite via Lithium Ions. *The Journal*  
4890 *of Physical Chemistry C* **2018**, *122*, 1447–1455.
- 4891 (708) Xia, Y.; Hegde, V. I.; Pal, K.; Hua, X.; Gaines, D.; Patel, S.; He, J.; Aykol, M.; Wolver-  
4892 ton, C. High-Throughput Study of Lattice Thermal Conductivity in Binary Rocksalt  
4893 and Zinc Blende Compounds Including Higher-Order Anharmonicity. *Physical Review*  
4894 *X* **2020**, *10*, 041029.
- 4895 (709) Zhang, Q.; Uchaker, E.; Candelaria, S. L.; Cao, G. Nanomaterials for energy conversion  
4896 and storage. *Chemical Society Reviews* **2013**, *42*, 3127–3171.
- 4897 (710) Kramer, D.; Ceder, G. Tailoring the morphology of LiCoO<sub>2</sub>: a first principles study.  
4898 *Chemistry of Materials* **2009**, *21*, 3799–3809.
- 4899 (711) Xu, B.; Fell, C. R.; Chi, M.; Meng, Y. S. Identifying surface structural changes in  
4900 layered Li-excess nickel manganese oxides in high voltage lithium ion batteries: A  
4901 joint experimental and theoretical study. *Energy & Environmental Science* **2011**, *4*,  
4902 2223–2233.
- 4903 (712) Dahéron, L.; Martinez, H.; Dedryvere, R.; Baraille, I.; Ménétrier, M.; Denage, C.;  
4904 Delmas, C.; Gonbeau, D. Surface properties of LiCoO<sub>2</sub> investigated by XPS analyses  
4905 and theoretical calculations. *The Journal of Physical Chemistry C* **2009**, *113*, 5843–  
4906 5852.
- 4907 (713) Kim, Y.; Lee, H.; Kang, S. First-principles and experimental investigation of the  
4908 morphology of layer-structured LiNiO<sub>2</sub> and LiCoO<sub>2</sub>. *Journal of Materials Chemistry*  
4909 **2012**, *22*, 12874–12881.

- 4910 (714) Benedek, R.; Thackeray, M. Simulation of the surface structure of lithium manganese  
4911 oxide spinel. *Physical Review B* **2011**, *83*, 195439.
- 4912 (715) Karim, A.; Fosse, S.; Persson, K. A. Surface structure and equilibrium particle shape  
4913 of the  $\text{LiMn}_2\text{O}_4$  spinel from first-principles calculations. *Physical Review B* **2013**, *87*,  
4914 075322.
- 4915 (716) Leung, K. First-principles modeling of the initial stages of organic solvent decompo-  
4916 sition on  $\text{Li}_x\text{Mn}_2\text{O}_4$  (100) surfaces. *The Journal of Physical Chemistry C* **2012**, *116*,  
4917 9852–9861.
- 4918 (717) Tompsett, D. A.; Parker, S. C.; Bruce, P. G.; Islam, M. S. Nanostructuring of  $\beta\text{-MnO}_2$ :  
4919 The important role of surface to bulk ion migration. *Chemistry of materials* **2013**, *25*,  
4920 536–541.
- 4921 (718) Qian, D.; Hinuma, Y.; Chen, H.; Du, L.-S.; Carroll, K. J.; Ceder, G.; Grey, C. P.;  
4922 Meng, Y. S. Electronic spin transition in nanosize stoichiometric lithium cobalt oxide.  
4923 *Journal of the American Chemical Society* **2012**, *134*, 6096–6099.
- 4924 (719) Hong, L.; Hu, L.; Freeland, J. W.; Cabana, J.; Ögüt, S.; Klie, R. F. Electronic Struc-  
4925 ture of  $\text{LiCoO}_2$  Surfaces and Effect of Al Substitution. *The Journal of Physical Chem-*  
4926 *istry C* **2019**, *123*, 8851–8858.
- 4927 (720) Abbaspour-Tamijani, A.; Bennett, J. W.; Jones, D. T.; Cartagena-Gonzalez, N.;  
4928 Jones, Z. R.; Laudadio, E. D.; Hamers, R. J.; Santana, J. A.; Mason, S. E. DFT  
4929 and thermodynamics calculations of surface cation release in  $\text{LiCoO}_2$ . *Applied Surface*  
4930 *Science* **2020**, *515*, 145865.
- 4931 (721) Deng, Y.-P.; Yin, Z.-W.; Wu, Z.-G.; Zhang, S.-J.; Fu, F.; Zhang, T.; Li, J.-  
4932 T.; Huang, L.; Sun, S.-G. Layered/spinel heterostructured and hierarchical mi-  
4933 cro/nanostructured Li-rich cathode materials with enhanced electrochemical prop-  
4934 erties for Li-ion batteries. *ACS applied materials & interfaces* **2017**, *9*, 21065–21070.

- 4935 (722) Deng, Y.-P.; Fu, F.; Wu, Z.-G.; Yin, Z.-W.; Zhang, T.; Li, J.-T.; Huang, L.; Sun, S.-G.  
4936 Layered/spinel heterostructured Li-rich materials synthesized by a one-step solvother-  
4937 mal strategy with enhanced electrochemical performance for Li-ion batteries. *Journal*  
4938 *of Materials Chemistry A* **2016**, *4*, 257–263.
- 4939 (723) Long, B. R.; Croy, J. R.; Park, J. S.; Wen, J.; Miller, D. J.; Thackeray, M. M. Advances  
4940 in stabilizing ‘layered-layered’  $x\text{Li}_2\text{MnO}_3 \cdot (1-x)\text{LiMO}_2$  (M= Mn, Ni, Co) electrodes  
4941 with a spinel component. *Journal of the Electrochemical Society* **2014**, *161*, A2160.
- 4942 (724) Wang, D.; Belharouak, I.; Zhou, G.; Amine, K. Nanoarchitecture multi-structural  
4943 cathode materials for high capacity lithium batteries. *Advanced Functional Materials*  
4944 **2013**, *23*, 1070–1075.
- 4945 (725) Warburton, R. E.; Castro, F. C.; Deshpande, S.; Madsen, K. E.; Bassett, K. L.;  
4946 Dos Reis, R.; Gewirth, A. A.; Dravid, V. P.; Greeley, J. Oriented  $\text{LiMn}_2\text{O}_4$  Particle  
4947 Fracture from Delithiation-Driven Surface Stress. *ACS applied materials & interfaces*  
4948 **2020**, *12*, 49182–49191.
- 4949 (726) Liang, C.; Longo, R. C.; Kong, F.; Zhang, C.; Nie, Y.; Zheng, Y.; Cho, K. Ab  
4950 Initio Study on Surface Segregation and Anisotropy of Ni-Rich  $\text{LiNi}_{1-2y}\text{Co}_y\text{Mn}_y\text{O}_2$   
4951 (NCM)( $y \leq 0.1$ ) Cathodes. *ACS applied materials & interfaces* **2018**, *10*, 6673–6680.
- 4952 (727) Chen, G.; Song, X.; Richardson, T. J. Electron microscopy study of the  $\text{LiFePO}_4$  to  
4953  $\text{FePO}_4$  phase transition. *Electrochemical and Solid State Letters* **2006**, *9*, A295.
- 4954 (728) Islam, M. S. Recent atomistic modelling studies of energy materials: batteries in-  
4955 cluded. *Philosophical Transactions of the Royal Society A: Mathematical, Physical*  
4956 *and Engineering Sciences* **2010**, *368*, 3255–3267.
- 4957 (729) Tankhilsaikhon, B.; Gorfman, S.; Tungalag, N.; Tuvjargal, N.; Davaasambuu, J.;  
4958 Pietsch, U. *Solid State Phenomena*; 2019; Vol. 288; pp 98–103.

- 4959 (730) Xu, G.; Zhong, K.; Yang, Y.; Zhang, J.-M.; Huang, Z. Insight into delithiation process  
4960 on the  $\text{LiFePO}_4$  (010) surface from a novel viewpoint of the work function. *Solid State*  
4961 *Ionics* **2019**, *338*, 25–30.
- 4962 (731) Zhang, Y.; Alarco, J. A.; Nerkar, J. Y.; Best, A. S.; Snook, G. A.; Talbot, P. C.;  
4963 Cowie, B. C. Observation of preferential cation doping on the surface of  $\text{LiFePO}_4$   
4964 particles and its effect on properties. *ACS Applied Energy Materials* **2020**, *3*, 9158–  
4965 9167.
- 4966 (732) Li, Y.; Chen, H.; Lim, K.; Deng, H. D.; Lim, J.; Fraggedakis, D.; Attia, P. M.;  
4967 Lee, S. C.; Jin, N.; Moškon, J., et al. Fluid-enhanced surface diffusion controls intra-  
4968 particle phase transformations. *Nature materials* **2018**, *17*, 915–922.
- 4969 (733) Edström, K.; Gustafsson, T.; Thomas, J. O. The cathode-electrolyte interface in the  
4970 Li-ion battery. *Electrochimica Acta* **2004**, *50*, 397–403.
- 4971 (734) Bhandari, A.; Bhattacharya, J.; Pala, R. G. S. Adsorption Preference of HF over  
4972 Ethylene Carbonate Leads to Dominant Presence of Fluoride Products in  $\text{LiFePO}_4$   
4973 Cathode–Electrolyte Interface in Li-Ion Batteries. *The Journal of Physical Chemistry*  
4974 *C* **2020**, *124*, 9170–9177.
- 4975 (735) Tebbe, J. L.; Fuerst, T. F.; Musgrave, C. B. Mechanism of hydrofluoric acid forma-  
4976 tion in ethylene carbonate electrolytes with fluorine salt additives. *Journal of Power*  
4977 *Sources* **2015**, *297*, 427–435.
- 4978 (736) Tebbe, J. L.; Holder, A. M.; Musgrave, C. B. Mechanisms of  $\text{LiCoO}_2$  Cathode Degrada-  
4979 tion by Reaction with HF and Protection by Thin Oxide Coatings. *ACS Applied*  
4980 *Materials and Interfaces* **2015**, *7*, 24265–24278.
- 4981 (737) Bhandari, A.; Gupta, P. K.; Bhattacharya, J.; Pala, R. G. S. Higher Energy Barrier  
4982 for Interfacial Li-Ion Transfer from EC/ $\text{LiPF}_6$  Electrolyte into (010)  $\text{LiFePO}_4$  Cathode

- 4983 Surface than Bulk Li-Ion Diffusion within Both Cathode and Electrolyte. *Journal of*  
4984 *The Electrochemical Society* **2019**, *166*, A2966–A2972.
- 4985 (738) Tebbe, J. L.; Fuerst, T. F.; Musgrave, C. B. Degradation of Ethylene Carbonate  
4986 Electrolytes of Lithium Ion Batteries via Ring Opening Activated by LiCoO<sub>2</sub> Cath-  
4987 ode Surfaces and Electrolyte Species. *ACS Applied Materials and Interfaces* **2016**, *8*,  
4988 26664–26674.
- 4989 (739) Xu, S.; Luo, G.; Jacobs, R.; Fang, S.; Mahanthappa, M. K.; Hamers, R. J.; Morgan, D.  
4990 Ab Initio Modeling of Electrolyte Molecule Ethylene Carbonate Decomposition Reac-  
4991 tion on Li(Ni,Mn,Co)O<sub>2</sub> Cathode Surface. *ACS Applied Materials & Interfaces* **2017**,  
4992 *9*, 20545–20553.
- 4993 (740) Malmgren, S.; Rensmo, H.; Gustafsson, T.; Gorgoi, M.; Edström, K. Non-destructive  
4994 depth profiling of the solid electrolyte interphase on LiFePO<sub>4</sub> and graphite electrodes.  
4995 *ECS Transactions* **2010**, *25*, 201–210.
- 4996 (741) Dathar, G. K. P.; Sheppard, D.; Stevenson, K. J.; Henkelman, G. Calculations of  
4997 Li-Ion Diffusion in Olivine Phosphates. *Chemistry of Materials* **2011**, *23*, 4032–4037.
- 4998 (742) Li, W.; Erickson, E. M.; Manthiram, A. High-nickel layered oxide cathodes for lithium-  
4999 based automotive batteries. *Nature Energy* **2020**, *5*, 26–34.
- 5000 (743) Li, W.; Dolocan, A.; Oh, P.; Celio, H.; Park, S.; Cho, J.; Manthiram, A. Dynamic  
5001 behaviour of interphases and its implication on high-energy-density cathode materials  
5002 in lithium-ion batteries. *Nature communications* **2017**, *8*, 1–10.
- 5003 (744) Li, W.; Liu, X.; Celio, H.; Smith, P.; Dolocan, A.; Chi, M.; Manthiram, A. Mn versus  
5004 Al in layered oxide cathodes in lithium-ion batteries: a comprehensive evaluation on  
5005 long-term cyclability. *Advanced Energy Materials* **2018**, *8*, 1703154.



- 5006 (745) Middlemiss, L. A.; Rennie, A. J.; Sayers, R.; West, A. R. Characterisation of batteries  
5007 by electrochemical impedance spectroscopy. *Energy Reports* **2020**, *6*, 232–241.
- 5008 (746) Li, J.; Murphy, E.; Winnick, J.; Kohl, P. Studies on the cycle life of commercial lithium  
5009 ion batteries during rapid charge–discharge cycling. *Journal of Power Sources* **2001**,  
5010 *102*, 294–301.
- 5011 (747) Song, J.; Lee, H.; Wang, Y.; Wan, C. Two-and three-electrode impedance spectroscopy  
5012 of lithium-ion batteries. *Journal of Power Sources* **2002**, *111*, 255–267.
- 5013 (748) Li, J.; Manthiram, A. A Comprehensive Analysis of the Interphasial and Structural  
5014 Evolution over Long-Term Cycling of Ultrahigh-Nickel Cathodes in Lithium-Ion Bat-  
5015 teries. *Advanced Energy Materials* **2019**, *9*, 1902731.
- 5016 (749) Kim, J.-S.; Johnson, C. S.; Vaughey, J. T.; Thackeray, M. M.; Hackney, S. A.;  
5017 Yoon, W.; Grey, C. P. Electrochemical and Structural Properties of  $x\text{Li}_2\text{M}'\text{O}_3 \cdot (1 -$   
5018  $x)\text{LiMn}_{0.5}\text{Ni}_{0.5}\text{O}_2$  Electrodes for Lithium Batteries ( $\text{M}' = \text{Ti, Mn, Zr}$ ;  $0 \leq x \leq 0.3$ ).  
5019 *Chemistry of Materials* **2004**, *16*, 1996–2006.
- 5020 (750) Armstrong, A. R.; Holzapfel, M.; Novák, P.; Johnson, C. S.; Kang, S.-H.; Thack-  
5021 eray, M. M.; Bruce, P. G. Demonstrating oxygen loss and associated structural reorga-  
5022 nization in the lithium battery cathode  $\text{Li}[\text{Ni}_{0.2}\text{Li}_{0.2}\text{Mn}_{0.6}]\text{O}_2$ . *Journal of the American*  
5023 *Chemical Society* **2006**, *128*, 8694–8698.
- 5024 (751) Bhandari, A.; Bhattacharya, J. Review—Manganese Dissolution from Spinel Cathode:  
5025 Few Unanswered Questions. *Journal of The Electrochemical Society* **2016**, *164*, A106–  
5026 A127.
- 5027 (752) Nakayama, K.; Ishikawa, R.; Kobayashi, S.; Shibata, N.; Ikuhara, Y. Dislocation and  
5028 oxygen-release driven delithiation in  $\text{Li}_2\text{MnO}_3$ . *Nature Communications* **2020**, *11*,  
5029 4452.

- 5030 (753) Deringer, V. L.; Caro, M. A.; Csányi, G. Machine learning interatomic potentials as  
5031 emerging tools for materials science. *Advanced Materials* **2019**, *31*, 1902765.
- 5032 (754) Assat, G.; Glazier, S. L.; Delacourt, C.; Tarascon, J.-M. Probing the thermal effects  
5033 of voltage hysteresis in anionic redox-based lithium-rich cathodes using isothermal  
5034 calorimetry. *Nature Energy* **2019**, *4*, 647–656.
- 5035 (755) Grimsman, F.; Brauchle, F.; Gerbert, T.; Gruhle, A.; Knipper, M.; Parisi, J. Hystere-  
5036 sis and current dependence of the thickness change of lithium-ion cells with graphite  
5037 anode. *Journal of Energy Storage* **2017**, *12*, 132–137.
- 5038 (756) Zheng, T.; McKinnon, W. R.; Dahn, J. R. Hysteresis during Lithium Insertion in  
5039 Hydrogen-Containing Carbons. *Journal of The Electrochemical Society* **1996**, *143*,  
5040 2137–2145.
- 5041 (757) Edge, J. S.; O’Kane, S.; Prosser, R.; Kirkaldy, N. D.; Patel, A. N.; Hales, A.; Ghosh, A.;  
5042 Ai, W.; Chen, J.; Jiang, J., et al. Lithium ion battery degradation: what you need to  
5043 know. *Physical Chemistry Chemical Physics* **2021**, *23*, 8200–8221.
- 5044 (758) Birkl, C. R.; Roberts, M. R.; McTurk, E.; Bruce, P. G.; Howey, D. A. Degradation  
5045 diagnostics for lithium ion cells. *Journal of Power Sources* **2017**, *341*, 373–386.
- 5046 (759) Zülke, A.; Li, Y.; Keil, P.; Burrell, R.; Belaisch, S.; Nagarathinam, M.; Mercer, M. P.;  
5047 Hoster, H. E. High-Energy Nickel-Cobalt-Aluminium Oxide (NCA) Cells on Idle:  
5048 Anode- versus Cathode-Driven Side Reactions. *Batteries & Supercaps* **2021**, *4*, 934–  
5049 947.
- 5050 (760) Symington, A. R.; Molinari, M.; Dawson, J. A.; Statham, J. M.; Purton, J.; Canepa, P.;  
5051 Parker, S. C. Elucidating the nature of grain boundary resistance in lithium lanthanum  
5052 titanate. *Journal of Materials Chemistry A* **2021**, *9*, 6487–6498.

- 5053 (761) Vicent-Luna, J. M.; Ortiz-Roldan, J. M.; Hamad, S.; Tena-Zaera, R.; Calero, S.;  
5054 Anta, J. A. Quantum and classical molecular dynamics of ionic liquid elec-  
5055 trolytes for Na/Li-based batteries: molecular origins of the conductivity behavior.  
5056 *ChemPhysChem* **2016**, *17*, 2473–2481.
- 5057 (762) Choi, Y.-S.; Park, J.-H.; Ahn, J.-P.; Lee, J.-C. Interfacial reactions in the Li/Si diffu-  
5058 sion couples: origin of anisotropic lithiation of crystalline Si in Li–Si batteries. *Scien-  
5059 tific reports* **2017**, *7*, 1–9.